SYNTHESIS AND ENVIRONMENTAL ASSESSMENT OF ARSENIC-CONTAINING COPPER CHALCOGENIDES FOR PHOTOVOLTAIC APPLICATIONS

by

Joseph Andler

A Dissertation

Submitted to the Faculty of Purdue University

In Partial Fulfillment of the Requirements for the Degree of

Doctor of Philosophy

School of Materials Engineering

West Lafayette, Indiana

August 2020

THE PURDUE UNIVERSITY GRADUATE SCHOOL

STATEMENT OF COMMITTEE APPROVAL

Dr. Carol Handwerker, Chair

School of Materials Engineering

Dr. Rakesh Agrawal, Co-Chair

Davidson School of Chemical Engineering

Dr. John Blendell

School of Materials Engineering

Dr. Fu Zhao

School of Mechanical Engineering

Dr. Eric Kvam

School of Materials Engineering

Approved by:

Dr. David Bahr

Head of the Graduate Program

ACKNOWLEDGMENTS

My progress throughout this endeavor physically, intellectually, and emotionally could not have been as successful as it was without help from some notable individuals who I would like to recognize.

I would like to thank my primary advisor, Carol Handwerker for a few things. First, you have genuinely impacted my development as a researcher, mentor, and person. Your insights and mentoring style continually motivate me to achieve more, and I have benefited from your constructive criticism and encouraging feedback. Next, I am grateful for your willingness to open your home for parties and social events. The benefits of having a good work-life balance are apparent in the increased productivity both inside and outside the lab. Lastly, I appreciated your encouraging role regarding the IGERT program by molding whatever ideas we had into successful content. Although we demonstrated self-motivated behavior, I believe your leadership was key to building that motivation. I hope every grant of yours can be as successful for your students as the IGERT was for me.

I would like to thank my co-adviser, Dr. Agrawal for his encouraging attitude and healthy skepticism. Your curiosity to determine how the world works has been elightening and has guided my thought process regarding scientific rigor. I have also appreciated your attention to safety, which I will carry with me throughout my career. My other committee members, Drs. John Blendell, Fu Zhao, and Eric Kvam, have also been helpful during my time here. John, every time I interact with you I feel as though I learn something new; I aspire to explain how the world works with clarity like you do. Dr. Zhao, I appreciate your helpful feedback when we were developing the LCA and I look forward to continuing to work with you, especially this summer. Dr. Kvam, your calm demeanor and thorough explanations resonate with me; I have and will continue to apply this teaching style in future interactions.

Regarding the solar energy research group, if an outsider visited for one meeting it would not take them long to recognize there are emerging world experts in the group. It is one thing to be taught how to solve problems, but watching how many of you developed into researchers through your inquisitive nature and thirst for comprehension was truly informative. Scott McClary,

I have learned from your natural ability to lead. You have been an active mentor to me and I am sincerely grateful to have spent so much time with you. I am honored to have shared the lab with all other group members, especially Ruihong Zhang, Mark Koeper, Caleb Miskin, Brian Graeser, Steven McLeod, Xin Zhao, Robert Boyne, Xin Zhao, Xianyi Hu, Robert Boyne, Essam AlRuqobah, Swapnil Deshmukh, Ryan Ellis, David Rokke, Kyle Weideman, Anna Murray, Apurva Pradhan, Jonathan Turnley, and Daniel Hayes. Although we did not spend lab time together, I want to thank the MSE group members for mentoring me during our weekly meetings and tolerating my repeated questioning. I especially thank Thomas Reeve, David Lowing, John Holaday, Matt Michie, Xi Chen, Kei Yazawa, Congying Wang, Yaohui Fan, Alyssa Yaeger, Ruwen Zhang, Elizabeth McClamrock, Ziyun Huang, Yifan Wu, Hannah Fowler, and John Obamedo.

To my IGERT fellows both at Purdue and Tuskegee University I wish to express gratitude for our time together spent learning, tolerating innumerable technical problems, and ultimately designing the program. I would like to particularly thank those who helped me to recognize the synergistic value of interdisciplinary groups. Christina Young, Aiesha Etheridge, Matt Korey, Caitlyn Clarkson, Ying Wang, Kali Frost, Kristen Quade, Nick Winovich, and Nehika Mathur, I learned much more from all of you than the material we developed together, and I treasure our shared experiences. Matt, thank you for your support as my roommate throughout this journey and with helping to host departmental gatherings which made my position as social chair much more enjoyable. Our conversations have expanded my understanding of politics, social issues, and cooking, and I wish you the best of luck in our next marathon together. I'm looking forward to seeing the leader you become.

I cannot thank my family and friends enough for their encouragement. Mom and dad, I certainly would not be in this position if you were not so nurturing. Your endless love and support continues to shape me, and I am so grateful for the lessons you have taught me. Jason, your enthusiasm for always putting family first is inspiring, and your mix of intelligence and tough love during our childhood has driven me to achieve more than I otherwise would. I would lastly like to thank all my friends who have indulged in shared interests such as intramural sports, breweries, poker, traveling, and more recently - puppies.

TABLE OF CONTENTS

LIST OF TABLES

LIST OF FIGURES

LIST OF ABBREVIATIONS

AEGL	Acute exposure guideline level
AT	Averaging time
BOS	Balance of system
CdTe	Cadmium telluride
CIGS	Copper indium gallium diselenide
CZTS(Se)	Copper zinc tin sulfide (selenide)
CV	Coefficient of variation
DQI	Data quality indicator
ITO	tin-doped indium oxide
LCA	Life cycle assessment
LCI	Life cycle inventory
mc-Si	Multicrystalline silicon
MHNC	Maximum hourly normalized concentration
PEFCR	Product environmental footprint category rules
PF	Persistence factor
PV	Photovoltaic
SLG	Soda-lime glass
TCLP	Toxicity Characteristic Leaching Procedure
TCO	Transparent conducting oxide

ABSTRACT

As the demand for energy increases, competition for a sustainable alternative to non-renewable energy resources has resulted in the growth of the photovoltaic industry. Although most photovoltaic technologies are based on crystalline silicon, thin film technologies have been developed with the expectation of generating a comparably high-performing product with lower processing costs. These materials have demonstrated sufficiently high optoelectronic performance to enable commercialization but concerns such as material scarcity limit terawatt level power production.

In the continuous pursuit of earth abundant solar absorber materials appropriate for thin film technologies, enargite Cu_3AsS_4 has been identified as a promising material due to its ideal direct band gap, stability, and high absorption. Recent efforts have demonstrated this class of copper chalcogenides exhibits band gap tunability and has solution processing capabilities for potentially scalable manufacturing. Furthermore, recent first-principles calculations of enargite Cu_3AsS_4 have hypothesized this material may have high carrier mobility and defect-tolerant optoelectronic properties, which further support investigation into this material.

In this dissertation, a novel reactive deposition processing route has been developed which has produced dense, single-phase enargite thin films. A champion device efficiency of 0.54% was achieved following a post deposition etching procedure on these films, which demonstrates the density and observable secondary phases were not limiting to initial nanoparticle-based device performances. Together with recent modeling efforts, the non-ideal band alignment with both the back contact and diode junction is concluded to be the primary limiting factor for high efficiency devices.

As this technology contains arsenic, concerns have been raised about its potential carcinogenicity and toxicity. Similar concerns were raised during the development of cadmium telluride technology, but these concerns have been mitigated through careful life cycle analyses and identifying strategies for responsible life cycle management. Therefore, a life cycle analysis and two risk assessments

have been completed on Cu_3AsS_4 systems. Although emissions of arsenic and its contributions to life cycle impacts are expected to be low due to the small quantity required, hot spots have been identified to reduce waste and emissions. Reduction strategies for this material system are found to be applicable to other PV systems and include minimizing molybdenum sputter waste, reusing and recycling balance of system components, and investigating low-energy processing routes on thin substrates. This work serves to establish a basis on which the potential environmental implications of this thin film technology are understood.

This dissertation will serve as a guide toward the technical and environmental development of Cu_3AsS_4 thin films. Having a life cycle perspective during the systematic development of a technology will enable sustainable engineering. Furthermore, the processing and characterization methods detailed herein are expected to be generally applicable to other copper chalcogenide systems.

CHAPTER 1. INTRODUCTION

1.1 Solar technology

Renewable energy technologies offer a sustainable alternative for supplying the growing energy demand. Although all renewable technologies have benefits and disadvantages, solar energy is the largest exploitable resource given the relatively large irradiance compared to global power consumption (Lewis and Nocera, 2006). Solar energy can be harnessed through techniques such as photoelectrochemical, photothermic, or photovoltaic, and enabling ubiquitous application of solar energy requires achieving global grid parity. Although photovoltaic approaches lack dispatchability, they have demonstrated functionality suitable for both small- and large-scale applications. With further development, photovoltaics can be a sustainable alternative to competitively meet global power demand.

Photovoltaic cells are created with multiple designs, chemistries, and layers that optimize performance for various applications. Monofacial, thin film, single-junction solar cells sacrifice moderate efficiency gains for the expectation of high throughput, low-cost manufacturing and installation. Commercially available technologies in this category include amorphous silicon (α-Si), gallium arsenide (GaAs), cadmium telluride (CdTe), and copper indium gallium diselenide (CIGS). Although improvements are continually made regarding device performance, limitations such as high cost and material scarcity have prompted research into alternative earth abundant thin film solar absorber materials. The compound Cu_3AsS_4 has been identified as a promising potential absorber for single-junction thin film applications, the fabrication of which is discussed extensively in this dissertation.

1.2 Arsenic-based chalcogenides

Luzonite and enargite are two polymorphs of the stoichiometry Cu_3AsS_4. Aside from being comprised of earth-abundant elements, Cu_3AsS_4 solar absorbers are promising due to their ideal

direct band gaps and subsequent high absorption (Durant and Parkinson, 2016, Shi et al., 2013, Yu et al., 2013), stability (Wallace et al., 2017), solution processing capabilities (McClary et al., 2017), band gap tunability (Balow et al., 2016), expected high carrier mobility (Wallace et al., 2017), and possible defect-tolerant optoelectronic properties (Wallace et al., 2017). Benefits of these attributes include: ideal direct band gaps are necessary for single-junction solar cell maximum efficiencies exceeding 30%, solution processing capabilities may reduce capital costs which can increase competitiveness in an economically-driven market, band gap tunability facilitates band bending which can increase photon absorption and can be used to limit undesirable Shockley-Read-Hall recombination at the back contact, having high carrier mobility is helpful for extracting the maximum amount of photocurrent from a p-n junction, and because defects are pervasive in all materials, having optoelectronic properties such as diffusion length and minority carrier lifetime that are not dependent on defects at grain boundaries (for example) can be attractive for reproducibility and facile synthesizability. It has also been proposed that enargite's polar structure will lead to ferroelectric domains that may enhance exciton separation, decrease carrier recombination, and increase defect-tolerant carrier transport (Wallace et al., 2017), which has also been simulated in perovskite solar cells (Rossi et al., 2018). These properties are all expected to increase photocarrier collection, which will ultimately increase solar cell efficiency. Recent experimental work has shown that the observed structural disorder in enargite (Pósfai and Sundberg, 1998, Pósfai and Buseck, 1998) can be overcome by annealing at temperatures above the luzonite-enargite transition region, which resulted in the first report of this material in a solar cell architecture that demonstrated a non-zero photoconversion efficiency of 0.18% (McClary et al., 2017). The limiting factor in this device has been determined to be the non-ideal band alignment of this material with the CdS buffer layer (McClary et al., 2019), and recent work has identified non-conventional buffer layers (Wallace et al., 2019) that are expected to produce efficiencies closer to the spectroscopic limited maximum efficiency ($>$25%, (Yu et al., 2013)) which is expected to make this technology competitive with commercial photovoltaic technology.

Regarding photovoltaic performance, Cu_3AsSe_4 has received little attention due to having a band gap that is smaller than what is ideal for single-junction thin film technology, between

0.3 and 0.9 eV (Berger and Prochukhan, 1969, Yu et al., 2013). However, as solar technology is continually decreasing costs to achieve global grid parity, it is possible new single-junction photovoltaic technologies like Cu_3AsS_4 may not be able to compete economically with established technologies unless notable capital, processing, or installation costs are eliminated. Therefore, preliminary investigations into Cu_3AsSe_4 has been reported in the context of applying it as a bottom layer in tandem devices.

1.3 Environmental analyses

Enargite and luzonite have significant promise for single-junction, thin-film photovoltaics. These materials have theoretically promising and experimentally determined optoelectronic properties that suit this application well enough to warrant further investigation. However, since these materials contain arsenic, which is a known human carcinogen, it is important to assess the potential life cycle impacts of these materials should they develop into thoroughly researched or commercial absorbers. A life cycle assessment (LCA) is a tool used to quantify the environmental impact over the life cycle of a product and will contribute to understanding the life cycle impacts of this potential technology. Data from LCA analyses will also be able to compare the life cycle impact to other photovoltaic technologies to determine key processes unique to these systems. It follows that performing a cradle-to-grave life cycle assessment on Cu_3AsS_4 absorbers will provide insights into the key areas of development for this technology.

Although LCAs are powerful tools for life cycle modeling, not all aspects of a system can be included in the system boundary. Specifically, risk assessments quantifying the potential human impact from anomalous behavior such as fires and during decommissioning are not included in LCA studies. Therefore, corresponding assessments have been completed to determine the severity of the prospective risk of this technology.

1.4 Structure of this dissertation

At the beginning of each methods section, I list the quantity of chemicals that are used for

various syntheses, treatments, depositions, and reactions in each chapter. The motivation for this list is not only for repeatability, but also to inform both technological development and life cycle analyses. Many of the syntheses performed require solvents and chemicals that are hazardous or produce significant waste. It is my hope that the life cycle impacts of the technologies being developed at the lab scale do not outweigh the life cycle benefits of producing the product if it comes to fruition. To decrease the likelihood of this scenario, either the impacts at lab scale must be relatively small or the benefits of the product must be relatively large. Small burdens will come by minimizing waste and using environmentally non-hazardous chemicals; large benefits will come with more time devoted to developing and improving the technology. However, the relationship between understanding the correct, non-hazardous chemicals to use and time spent developing the technology is proportional. The implication is that the more time spent developing a technology to understand the ideal chemicals to use consequently increases the impacts of developing the technology. Life cycle assessment is a tool that can identify chemicals that have a relatively smaller life cycle burden, but performing LCAs during the development stage of a product is uncommon since a trade-off exists between obtaining the knowledge to decrease life cycle impacts and devoting the resources to develop the technology. Therefore, building a collective knowledge of the non-hazardous chemicals and processing routes that are known to minimize waste can inform developers of a technology the routes to investigate that may be less impactful for their in-progress product. Although an LCA was not performed on the lab scale processes during this investigation, listing the quantity of chemicals used at the beginning of each section is a first step toward this goal, and will hopefully motivate others to do the same.

Chapter 2 investigates the formation of enargite thin films from luzonite nanoparticles by offering supporting data for the preliminary investigations into this technology (McClary et al., 2017). The cited work assumed that having a condensing arsenic sulfide phase on the surface of the film would be beneficial for the microstructural evolution of the film. However, no knowledge of an arsenic sulfide atmosphere or the benefits of achieving an arsenic sulfide melt was provided. The beginning of this chapter addresses this information and follows with an understanding of how the luzonite nanoparticles structurally and chemically break down upon heating. Lastly, four main issues with the films are identified that motivates subsequent chapters.

Chapter 3 demonstrates a novel processing route to the development of enargite thin films that bypasses the necessity of nanoparticle precursors. This technique is introduced through two main processing routes beginning from evaporated copper films. After forming either copper (I) sulfide or copper (II) sulfide, the films are prepared in the same way as the initial nanoparticle-based films and produce similar enargite films but without an IR active secondary phase.

Chapter 4 associates the influence of added arsenic sulfide powders on various film characteristics as an attempt to identify trends associated with observed qualities. Through this analysis, conditions to synthesize a dense film were identified. Together with the elimination of the IR active secondary phase, these films are used to test the hypothesis that either the observed film porosity or secondary phase significantly contributed to the low device performance in preliminary enargite-based devices. Furthermore, a post-deposition procedure is developed to improve the performance which has resulted in the highest reported short circuit current and efficiency. Chapter 5 addresses the band alignment of enargite in the current architecture, which is thought to be the primary limiting factor in enargite-based solar cells. The enargite band alignment with Mo and MoS_2 has been modeled and suggests the formation of MoS_2 is detrimental to device performance. Furthermore, the documented poor alignment with CdS (McClary et al., 2019) is addressed thorough investigating deposition routes for ZnS thin films. Chemical bath deposition, sulfurization of sputtered ZnO films, and the synthesis and deposition of ZnS nanoparticles are investigated.

Chapter 6 covers three environmental assessments performed on Cu_3AsS_4 PV technology. The first is a life cycle assessment on a prospective system which is aimed at reducing the life cycle impact of this technology by identifying material and processing hot spots. The second is an investigation into the potential risk of this technology if it were to be burned in a small house fire as a conservative estimate. Lastly, a scaled Toxicity Characteristic Leaching Procedure is performed that identifies the potential risk of discarding this technology into a landfill environment.

Chapter 7 shares insights on the development of Cu_3AsSe_4 nanoparticles and thin films. Specifically, nanoparticles are investigated through extracting and analyzing aliquots during syntheses. A strong texture is observed in mesoparticles formed through modifying the reported synthesis method. The degradation of Cu_3AsSe_4 nanoparticles is reported through both thermal and selenium-induced arsenic volatility.

Chapter 8 focuses on the development of the graduate student researcher in an interdisciplinary environment. Two studies were performed to shed light on the factors that resulted in the third cohort of the IGERT program in sustainable electronics exhibiting self-motivated behavior consistent with the goals of the IGERT program. One study investigates a method used by the program to identify and discuss cultural and personal biases and reports best practices for use in future contexts. The other study uses indicators based on self-determination theory and the expectancy-value theory to identify key attributes of the program that may be useful to model in future interdisciplinary projects.

1.5 References

Balow, R. B., Tomlinson, E. P., Abu-Omar, M. M., Boudouris, B. W., and Agrawal, R. (2016). Solution-based synthesis and characterization of earth abundant Cu3(As,Sb)Se4 nanocrystal alloys: towards scalable room-temperature thermoelectric devices. *Journal of Materials Chemistry A*, 4(6):2198–2204.

Berger, L. I. and Prochukhan, V. D. (1969). *Ternary diamond-like semiconductors*. Consultants Bureau, New York.

Durant, B. and Parkinson, B. A. (2016). Photovoltaic response of naturally occurring semiconducting sulfide minerals. In *Conference Record of the IEEE Photovoltaic Specialists Conference*.

Lewis, N. S. and Nocera, D. G. (2006). Powering the planet: Chemical challenges in solar energy utilization. *Proceeding of the National Academy of Sciences*, 103(43):15729–15736.

McClary, S. A., Andler, J., Handwerker, C. A., and Agrawal, R. (2017). Solution-processed copper arsenic sulfide thin films for photovoltaic applications. *Journal of Materials Chemistry C*, 5(28):6913–6916.

McClary, S. A., Li, S., Yin, X., Dippo, P., Kuciauskas, D., Yan, Y., Baxter, J. B., and Agrawal, R. (2019). Optoelectronic Characterization of Emerging Solar Absorber Cu3AsS4. In *IEEE Photovoltaics Specialists Conference Proceedings*, pages 3–7.

Pósfai, M. and Buseck, P. R. (1998). Relationships between microstructure and composition in enargite and luzonite. *American Mineralogist*, 83(3-4):373–382.

Pósfai, M. and Sundberg, M. (1998). Stacking disorder and polytypism in enargite and luzonite. *American Mineralogist*, 83:365–372.

Rossi, D., Pecchia, A., der Maur, M. A., Leonhard, T., Röhm, H., Hoffmann, M. J., Colsmann, A., and Carlo, A. D. (2018). On the importance of ferroelectric domains for the performance of perovskite solar cells. *Nano Energy*, 48(March):20–26.

Shi, T., Yin, W.-J., Al-Jassim, M., and Yan, Y. (2013). Structural, electronic, and optical properties of Cu3-V-VI4 compound semiconductors. *Applied Physics Letters*, 103(15):152105.

Wallace, S. K., Butler, K. T., Hinuma, Y., and Walsh, A. (2019). Finding a junction partner for candidate solar cell absorbers enargite and bournonite from electronic band and lattice matching. *Journal of Applied Physics*, 125(5):1–8.

Wallace, S. K., Svane, K., Huhn, W. P., Zhu, T., Mitzi, D. B., Blum, V., and Walsh, A. (2017). Candidate photoferroic absorber materials for thin-film solar cells from naturally occurring minerals: enargite, stephanite, and bournonite. *Sustainable Energy & Fuels*, 1(6):1339–1350.

Yu, L., Kokenyesi, R. S., Keszler, D. A., and Zunger, A. (2013). Inverse design of high absorption thin-film photovoltaic materials. *Advanced Energy Materials*, 3(1):43–48.

CHAPTER 2. SYNTHESIS OF Cu_3AsS_4 ENARGITE FILMS FROM Cu_3AsS_4 LUZONITE NANOPARTICLES

2.1 Introduction

Before beginning to explore thin film synthesis methods, it is helpful to understand what ideal films should look like for solar cell absorber layers. Porous films are not ideal in theory for three reasons: incomplete absorption of incident radiation which decreases short circuit current, increased surface area to facilitate surface-induced minority carrier recombination, and facilitating the formation of electrical shunts that decrease open circuit voltage and reduce the number of carriers able to perform work in an external circuit. In practice, pores have been identified in high efficiency devices and therefore are not the most crucial factor in determining device performance in some systems. Ideal films do not have significant impurities, structurally or otherwise, that negatively contribute to the performance of the device. Impurities can act as point, planar, or bulk limitations for optoelectronic performance in films and devices. Point defects, such as atomic anti-site or vacancies, can change the local electronic structure and induce minority carrier recombination. This type of defect can reduce open circuit voltage and is prevalent in copper zinc tin sulfo-selenide (CZT(S,Se)) solar cells (Yuan et al., 2015). Planar defects, such as at a terminating surface or grain boundaries, are relatively high energy regions that subsequently have different electronic states than the bulk. These states typically act as Shockley-Read-Hall recombination centers and can decrease the open circuit voltage in devices. Bulk impurities, such as secondary phases, can physically intercede with subsequent layer deposition to inhibit strong p-n junction formation and can also decrease short circuit current through parasitic absorption of incident irradiation. The ideal thickness of films varies from system to system but is generally about 1 to 5 micrometers thick for direct band gap absorbers used in solar cells. Example images of copper indium gallium diselenide (CIGS) films are provided in Figures 2.1 (a) – (c). Co-evaporation techniques result in highly dense microstructures throughout the thickness of the film, such as in Figures 2.1 (a) and (b) (Ramanathan et al., 2003). For solution processed techniques, morphologies

with more pores and horizontal grain boundaries have also produced high efficiency devices, but these devices typically have inferior optoelectronic properties. A side view image from a high efficiency CIGS film from solution processing is shown in Figure 2.1 (c), obtained using hydrazine (Zhang et al., 2016). These films have notable similarities that we aim to obtain in our films: single phase, contiguous particles larger than 100 nm, and relatively low porosity.

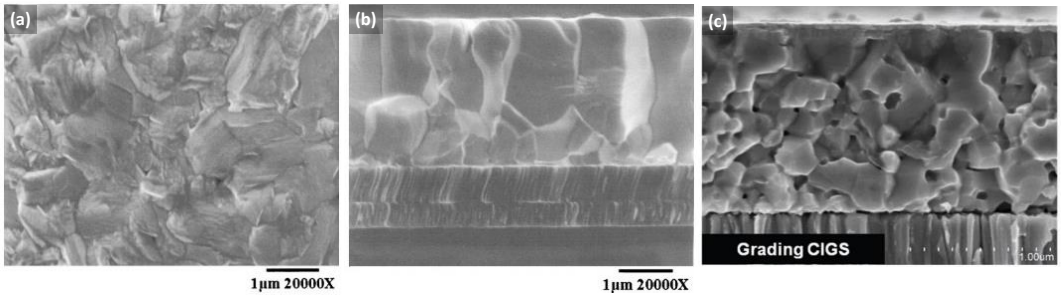

Figure 2.1. Plan and side view SEM images of high efficiency CIGS solar cells. (a) and (b) are produced from evaporation techniques from this reference (Ramanathan et al., 2003). (c) is an image of a film produced through solution processing from this reference (Zhang et al., 2016).

Much of the information extracted from preliminary Cu_3AsS_4 film fabrication has been compiled and published (McClary et al., 2017), but a brief synopsis is described here to provide context for this chapter. Our solution processed film formation pathway began using nanoparticles to satisfy local chemical stoichiometry to reduce the likelihood that elemental mass transport throughout the film would be a limiting factor constraining formation and growth of large particles. At temperatures necessary to grow large grains, we observed mass loss that corresponded to the volatilization of arsenic and sulfur. Therefore, we treated nanoparticles in an atmosphere of arsenic and sulfur to suppress volatilization and found the Cu_3AsS_4 enargite phase to be the prevalent and stable phase formed at a range of times and temperatures. However, film contiguity and porosity were dependent on processing temperature. Small, faceted, needle and plate-like particles were observed to form at relatively low temperatures and large, faceted, isolated particles was observed at relatively high temperatures, likely due to enhanced mass transport through a liquid medium. Under relatively moderate processing conditions using As_2S_5 powder as an arsenic and sulfur

source, contiguous films were formed with a grain size on the order of one micrometer. A solar cell was fabricated and demonstrated a non-zero photoconversion efficiency, which was the first reported use of Cu_3AsS_4 enargite as the absorber layer in a solar cell architecture.

This chapter provides data not included in the above publication, but also support its findings and conclusions. As described above, films were treated with an As_2S_5 powder to minimize volatilization. Understanding when this arsenic sulfide phase breaks down, when it supplies an atmosphere, and the nature of the volatile products is important information to consider when building an accurate model of the system. However, we were not able to find thermal data for this phase in literature. Therefore, TGA and DSC analyses were completed on As_2S_5 powder and is reported in section 2.3.1. Subsequently in the publication, we hypothesized that a sulfur-rich arsenic sulfide binary phase could provide the environment necessary to facilitate grain growth. Notably, a liquid phase capable of enhancing mass transport by dissolution and reprecipitation of particles during a liquid phase sintering process. To test this hypothesis, an experiment is discussed in Section 2.3.2. where one film is exposed to a liquid during this growth process and one is not. To investigate the conditions present during the initial stages of film development, luzonite nanoparticles are heated and a short-time film treatment study is analyzed in Section 2.3.3. Lastly, data are provided in Section 2.3.4. which demonstrate non-optimal film characteristics of the thin films and motivate subsequent chapters of this dissertation.

2.2 Experimental methods

2.2.1 Materials

The chemicals and materials used to complete the investigations in this chapter are listed in Table 2.1.

Table 2.1. *List of products used in this chapter*

Chemicals / equipment	**Purity / type**	**Source**	**Quantity***
Ampule (10 mL)	Borosilicate glass	Chemglass Life Sciences	$\approx$ 13 g / treatment
Arsenic (III) chloride (AsCl3)	>99.99%	Sigma-Aldrich	$\approx$ 0.018 mL / synthesis
Arsenic (V) sulfide	>98%	Santa Cruz Biotechnology	$\approx$ 30 mg / treatment
Centrifuge	Allegra X-30	Beckman Coulter	1 used indefinitely
Copper (I) chloride (CuCl)	>99.99%	Strem Chemicals	$\approx$ 60 mg / synthesis
Ethanol	200 proof	Decon Labs	$\approx$ 30 mL / synthesis
Hexanes	>98.5% / ACS	Fisher Scientific	$\approx$ 8 mL / synthesis
1-hexanethiol	>95%	Sigma-Aldrich	$\approx$ 0.004 mL / treatment
Molybdenum target	>99.95%	Kurt J. Lesker	$\approx$ 85 mg deposited**
Oleylamine (OLA)***	>98% primary amine	Sigma-Aldrich	$\approx$ 15 mL / synthesis
Stir bar	3/8" PTFE	VWR International	1 used indefinitely
Sulfur flakes	>99.99%	Sigma-Aldrich	$\approx$ 38 mg / synthesis
Vortex Mixer	Analog	VWR International	1 used indefinitely

**Hexane, IPA, water, soap, and nitric acid used for glassware cleaning between each synthesis is not included.*
***Deposition area is one 4"x4" substrate per deposition. Over the life of the target (about 8 depositions), the total target utilization for this lab scale deposition process is approximately 5%, measured empirically. Most molybdenum ($\approx$ 90%, empirically deduced) is sputtered onto chamber walls resulting in a total material utilization of approximately 0.5%.*
****OLA stock solution was degassed using three freeze-pump-thaw (FPT) cycles and stored under nitrogen.*

2.2.2 Luzonite nanoparticle synthesis

The nanoparticle synthesis used in these analyses has been previously reported (Balow, 2015, Balow et al., 2017, McClary, 2019). I report below only the information necessary to facilitate the transferring of data into a life cycle or similar analysis that requires specific quantities of chemicals to be reported. The sulfur precursor is 1 M in FPT OLA (160 mg in 5 mL). The copper arsenic precursor is 0.2 M in 5 mL FPT OLA with an approximate Cu:As ratio of 2.8:1 (99 mg CuCl and 30.1 μL $AsCl_3$). Non-FPT OLA (10.5 mL) is refluxed at 120 °C for one hour before increasing the reaction temperature to 175 °C. At this temperature, 1.2 mL of sulfur precursor is injected followed by 3.0 mL of the copper-arsenic precursor and left to react for ten minutes. After cooling and the reaction mixture is pipette into a centrifuge tube, the nanoparticles are washed by topping with ethanol and centrifuging at 14,000 rpm for five minutes and discarding the supernatant. Then, two additional washes with approximately 4 mL hexane mixed with 12 mL ethanol are completed before the nanoparticles are dried under a nitrogen flow and stored dry for later use.

2.2.3 Film fabrication

Dried nanoparticles are suspended in hexanethiol with a concentration of 250 mg per mL in a glass vial. This vial is vortexed for approximately two minutes before coating onto a molybdenum-coated soda-lime glass (Mo-SLG) substrate using a doctor blade technique with a clean glass rod. The amount of liquid used is dependent on the surface area covered but requires 11.6 mL per square meter of substrate. Typically, a lab scale setting requires anywhere from 1 to 12 μL. The coating procedure proceeds as follows in a fume hood: A substrate is placed with the molybdenum side facing upwards between home-made taped glass rails that allows the rod to pass over the substrate without making direct contact. The nanoparticle suspension is pipette across the width of one end of the substrate. A glass rod is used to push the nanoparticle suspension across the length of the substrate and is returned to its original position in a process that is repeated once more. The freshly coated substrate is placed upwards at an angle such as to minimize the spreading that

occurs due to the build-up of solution where the glass rod had been removed. Drying is determined through visual inspection, but typically lasts several minutes. Afterwards, the substrate is again placed between the glass rails and the coating procedure as above is repeated once more with 66% of the original ink. Unless the films are immediately used, they are stored in a nitrogen environment.

2.2.4 Ampule preparation

Ampules used in this study have a neck diameter of approximately 1/4" so nanoparticle-coated substrate samples must be at least this small in one dimension. The substrate sample size used in all ampule treatments mentioned in this chapter is 1/4" x 1" unless otherwise noted. If treatments are performed under a controlled-vapor environment, the appropriate chemicals are first put into the ampule in a nitrogen ambient. The nanoparticle-coated substrates are then loaded into the ampule and sealed from oxygen with a valve. The ampule is then connected to a Schlenk line which is purged three times with argon. The valve is opened and the ampule is purged three times with argon. When under a vacuum of approximately 0.2 torr, a butane torch is used to yield the glass at the neck until an airtight seal is formed. The resulting total volume of the ampule is approximately 13 mL.

2.2.5 Heat Treatments

Treatments of the nanoparticle-containing ampules in this chapter were performed in a three-zone tube furnace. From one end, a K-type thermocouple protrudes into the center of the three zones to monitor temperature of the ampule ambient. The other end is installed with a pushrod. The furnace is sealed and purged three times with argon. Under an argon flow of about 10 sccm, the furnace is then stabilized at operating temperature before the ampule is pushed into the center of the three zones. Cooling occurs naturally after opening the top of the furnace unless otherwise noted.

2.2.5.1 Heating profile of furnace

The ramp rate of the furnace was not observed to change over the course of this dissertation. The heating curve below represents a typical heating curve of the ambient during a heat treatment. These data measured with a thermocouple inserted into an ampule with a molybdenum coated soda-lime glass sample. The thermocouple arrangement was sturdy enough to support the ampule and sample to ensure no contact was made with the tube (i.e. no heating was conductive). The initial temperature was 21 °C.

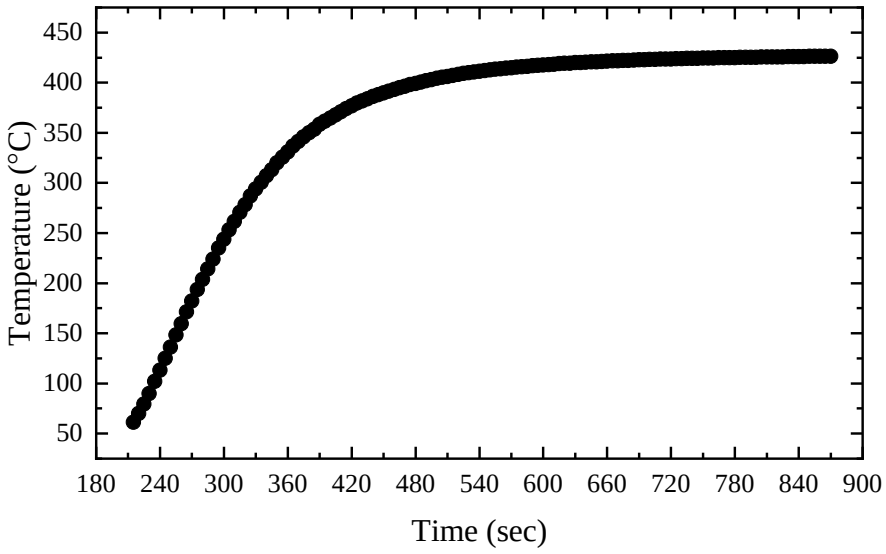

Figure 2.2. Heating profile of the ambient conditions inside of the three-zone furnace used for the treatments performed in this study.

2.2.5.2 Cooling profile of furnace

Different techniques for convective cooling will alter the cooling rate of the ampules. Six different techniques were assessed to 300 °C and three of these techniques were assessed to 200 °C. Throughout the course of this dissertation, no relationship was found between cooling rate and film quality when characterizing films with XRD, Raman spectroscopy, and SEM.

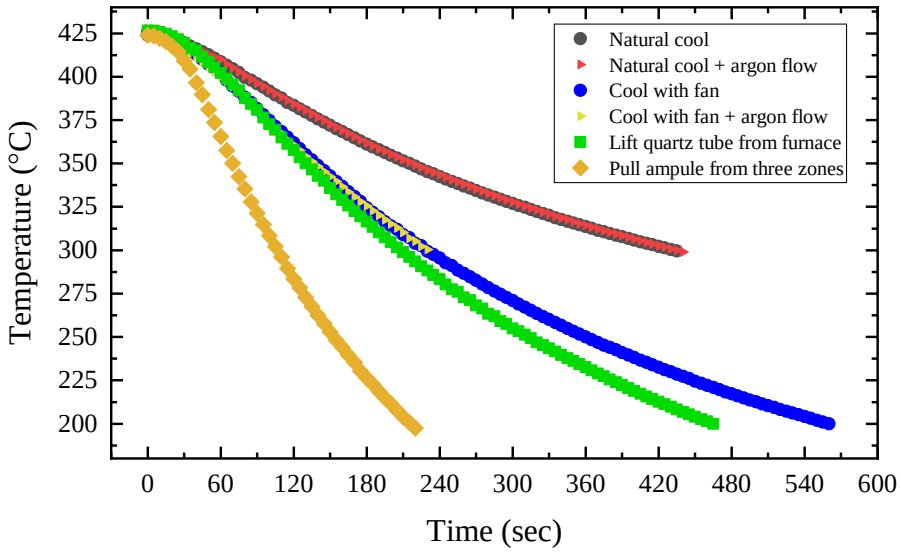

Figure 2.3. Cooling techniques to control cooling rate of ampules after treatments in the three-zone furnace.

2.2.6 Characterization details

A FEI quanta 3D dual-beam field emission scanning electron microscope (SEM) was used to capture nanoparticle and film morphology. Energy-dispersive X-ray spectroscopy (EDS) was collected with an accelerating voltage of 20 kV on the same SEM with a silicon drift detector. Elemental compositions were determined through AZtec software using standardless quantitative analysis. X-ray diffraction (XRD) data were collected on a Rigaku SmartLab diffractometer using a copper Kα X-ray source with a Kβ filter in Bragg-Brentano mode. Raman spectra were collected using a Horiba/Jobin-Yvon LabRAM HR800 confocal microscope system with a 17 mW 633 nm He:Ne laser. Thermogravimetric analysis (TGA) was conducted using a TA Instruments SDT Q600 system in a 100 mL/min helium flow with a ramp rate of 10 °C/min. A TA Instruments Q2000 differential scanning calorimetry (DSC) instrument was used for controlling the heating and cooling rate of the arsenic sulfide powder. DSC measurements were completed with 50 mL flowing nitrogen and a heating and cooling rate of 10 °C/min. Scanning transmission electron microscopy (STEM) (EDS) data were collected on a Talos 200X TEM using a SiN grid.

2.3 Results and discussion

2.3.1 Thermal analysis of As_2S_5 powder

Glasses are known to exist in pnictogen-chalcogenide systems (Borisova, 1981, Ewen, 1978). For arsenic sulfides, mixtures of over 60% at. sulfur have a high tendency of forming glasses, which has made it notably difficult to determine the liquidus temperature, if any, of arsenic-sulfide mixtures in this composition range (Blachnik et al., 1980, Jonker, 1909). Therefore, crystalline As_2S_5 may best be characterized as a glass upon heating.

TGA analyses were completed on 34.7 mg As_2S_5 powder. Corresponding data are plotted in Figure 2.4 and indicate this powder does not lose mass until about 200 °C. This result is expected since sulfur has been reported to follow a similar trend in TGA analyses with almost about 30 - 70% of sulfur volatilizing by about 300 °C (Jia et al., 2019, Ryu et al., 2013). Sulfur may be expected to form from the decomposition of As_2S_5 into the more stable As_2S_3 phase. However, the mass leaving the system is less than is expected if all excess sulfur were to volatilize from this decomposition. Given the molar mass of As_2S_3 is approximately 80% that of As_2S_5, a scenario where 50% excess sulfur volatilizes will result in approximately a 10% mass loss. Since less than 5% of mass is lost in this system by 300 °C, these data imply that relative to As_2S_3, sulfur is retained in the arsenic-sulfur system. Therefore, it is inaccurate to model the initial stages of ampule treatments as if the amount of sulfur in the atmosphere is equal to the amount available if As_2S_5 undergoes complete decomposition into As_2S_3 and S.

DSC analyses were completed on 9.9 mg As_2S_5 powder hermetically sealed in ambient conditions in an aluminum pan. The resulting curve is displayed in Figure 2.5 (a) and corresponds with the equilibrium phase diagram in Figure 2.5 (b). Note that As_2S_5 (71 at.% S) is metastable under ambient conditions and is consequently not provided on the diagram. DSC analysis indicates a crystalline As_2S_5 melting peak at approximately 70 °C. A subsequent endothermic event is noted at 102 °C, and a melting peak with an onset temperature of 116 °C is attributed to sulfur. Since elemental sulfur is observed in this system, we speculate the event at 102 °C is related to the phase

segregation of sulfur. A broad endotherm is identified after this melting event and is attributed to arsenic incorporation into the sulfur melt which forms a sulfur-rich arsenic sulfide glass. A small, broad exotherm is noted with an onset at approximately 215 °C and a peak at approximately 230 °C. We note that these data coincide with a mass-loss stabilization event in the TGA data. A small glass transition is noted between 303 – 304 °C, and an unidentified sharp endotherm is noted at 327 °C. Post-treatment inspection determined the sample lid remained intact. No crystallization peak was observed upon cooling and, interestingly, no melting or glass transition was observed when reheating of the sample to 350 °C.

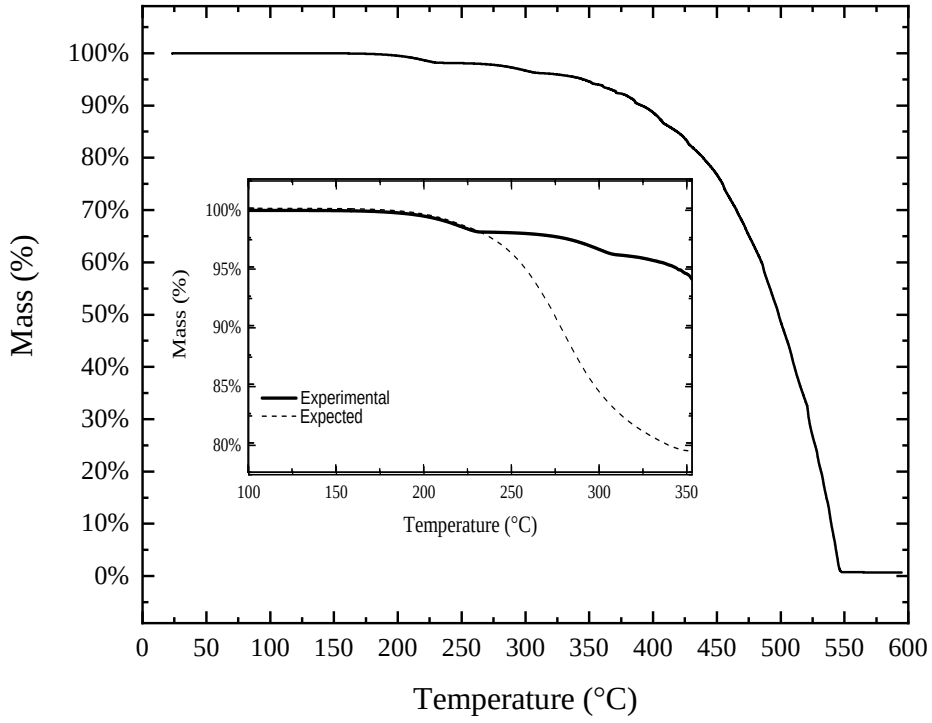

Figure 2.4. Thermogravimetric analysis on 34.7 mg of As_2S_5 powder.

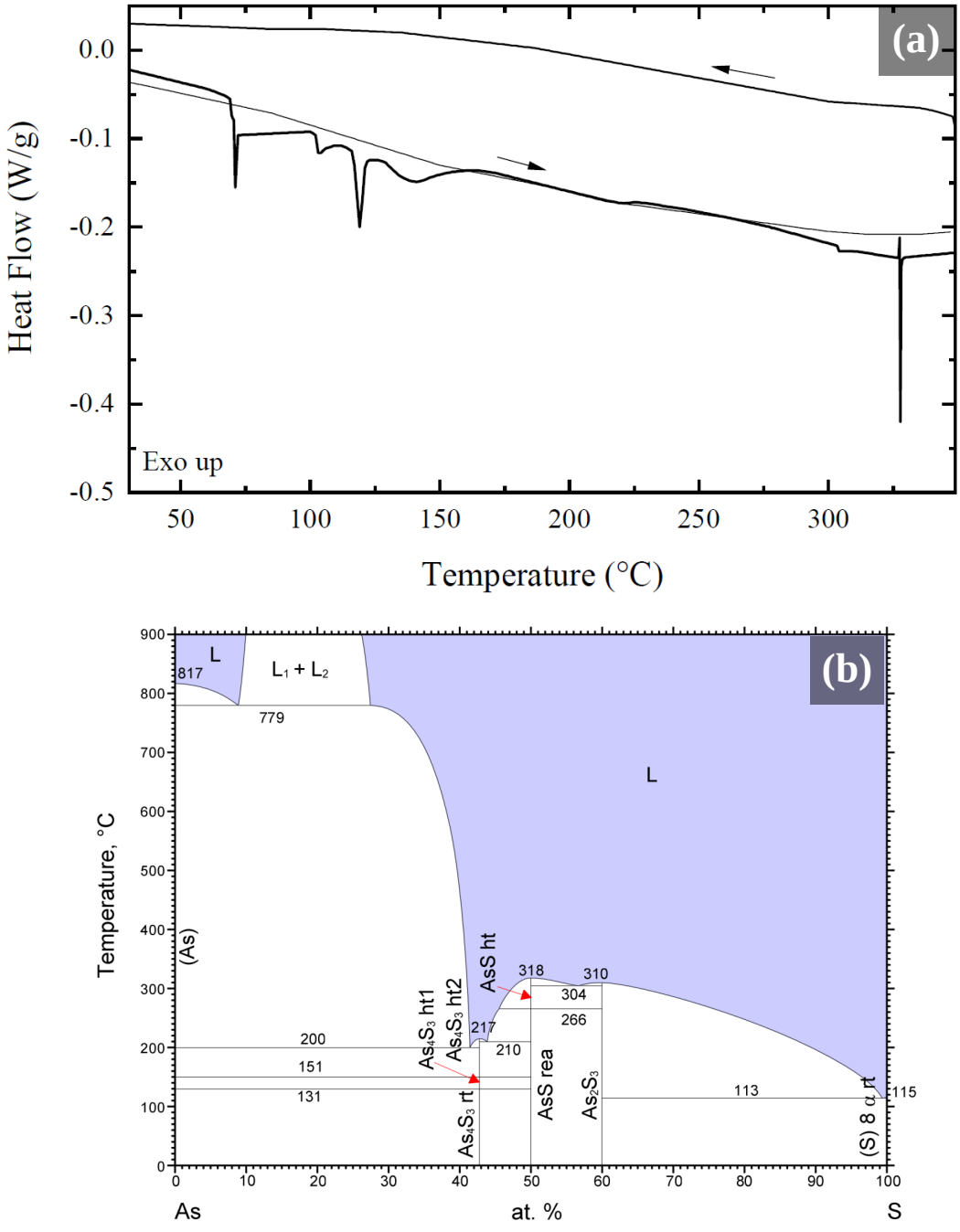

Figure 2.5. (a) Differential scanning calorimetry data on 9.9 mg of As_2S_5 powder. (b) The arsenic sulfide binary phase diagram (Okamoto, 2006). Reprinted with permission of ASM International. All rights reserved. www.asminternational.org

Together with TGA, these data provide the understanding that As_2S_5 powder melts at approximately 70 °C and, at least partially, phase segregates into sulfur that melts and incorporates arsenic to form a sulfur-rich arsenic sulfide glass. As heating continues and sulfur begins to volatilize from the melt, a mass loss stabilization event occurs at approximately 225 °C. Since arsenic sulfide glasses in this composition range have been found to become more viscous with increasing arsenic content (Jonker, 1909), it is possible this stabilization may be the result of the sulfur-rich arsenic sulfide glass stabilizing with increasing arsenic content. This volatilization-stabilization event may occur again around 300 °C. Nevertheless, these data suggest sulfur does not completely volatilize from the system in the early stages of heating. Arsenic and sulfur will volatilize over time, however, as this was readily observed throughout experiments performed during this dissertation.

2.3.2 Effect of annealing environment on film quality

Time and temperature effects on film quality are discussed in the publication (McClary et al., 2017). Briefly, at 375 °C, rod and needle-like particles were observed which prevented a dense packing of the film and resulted in a porous structure. At 500 °C, rapid growth and coarsening was observed resembling Ostwald ripening behavior where mass transport occurred from small to large particles and created large void spaces in the film. At 425 °C, grains formed with a lower aspect ratio than the 375 °C films and with higher surface coverage than the 500 °C films. Time did not appear to play a significant role in determining grain size, morphology, or density when temperatures 425 °C and lower were used.

In the above report, we also determined that a binary arsenic-sulfur atmosphere was required to form a film of unimodal, micron size particles suitable for thin film applications. In all cases, films were sealed facing upwards in an ampule with powder that was expected to vaporize and condense on the film. In Figure 2.6, the resulting morphology of this technique is portrayed against a sample exposed to the same conditions except the sample was placed up-side down to ensure a persistent arsenic-sulfide melt. Sample A was annealed under the above conditions whereas sample B was annealed face-down in the arsenic sulfide powder. Sample B is observed

to have a denser morphology than Sample A, with less pores and a qualitatively similar grain size. Although Sample B still contains needle and plate-like particles, these particles are arranged to share boundaries with their nearest neighbors much more frequently than observed in Sample A. Therefore, the presence of a melt may help densify the structure through particle rearrangement rather than modifying the morphology of the particles. This experiment underlines the importance of having an arsenic-sulfide melt to assist with dense film formation.

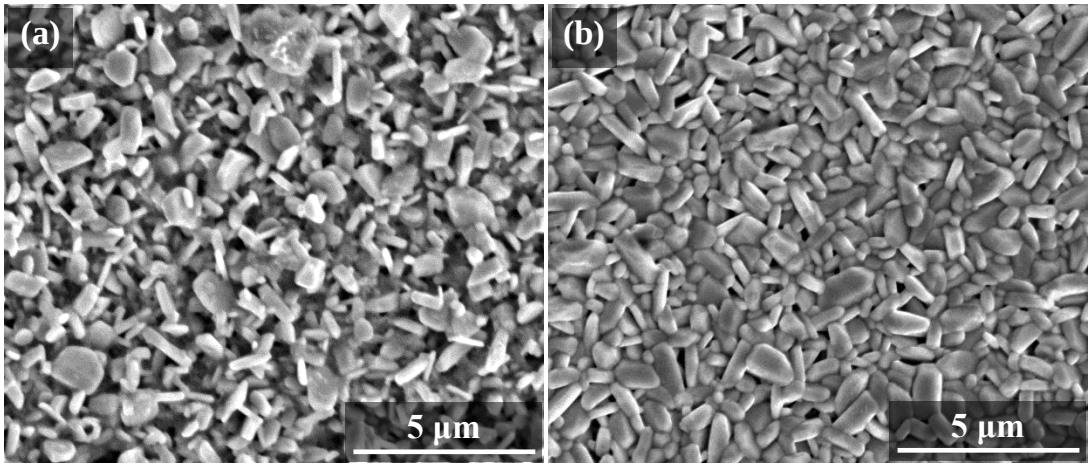

Figure 2.6. Plan-view SEM images of an enargite film formed from luzonite nanoparticles treated in an ampule (a) surface up and (b) surface down in arsenic (V) sulfide powders at 400 °C for 30 minutes.

2.3.3 Investigation into early-stage luzonite nanoparticle film characteristics upon heating

Before investigating Cu_3AsS_4 thin films, an understanding of the formation behavior of similar thin-film chalcogenide materials is addressed for comparison. A proposed film formation mechanism for CZTSe thin films in a selenium ambient (Hages et al., 2016) begins with a structural and chemical breaking down of nanoparticles when exposed to selenium liquid on the surface of the film. Copper diffuses to the surface where copper selenide nucleates and subsequently incorporates tin and zinc. The growth front drives the CZTSe grains into the film as cations from small grains are incorporated into the larger surface grains. A bottom fine-grain layer comprised of a rejected

carbon and selenium complex induces a stagnation of the growth front which results in a bilayer film structure. Similarly, a proposed film formation mechanism for CIGS films in a selenium ambient (McLeod et al., 2019) asserts a rapid formation of CIGSe grains on the surface of the film that grow into the film through cation incorporation. The CIGS nanoparticles under the grains incorporate selenium and grow through a liquid assisted densification process. The growth of the nanoparticles is hindered due to carbon incorporation, but the growth is enough to decrease the driving force for mass diffusion and stagnate the bulk CIGSe growth. The CIGSe films formed from nanoparticle precursors also result in a bilayer morphology with a large grain CIGSe region and a fine-grain region of mostly carbon and selenium.

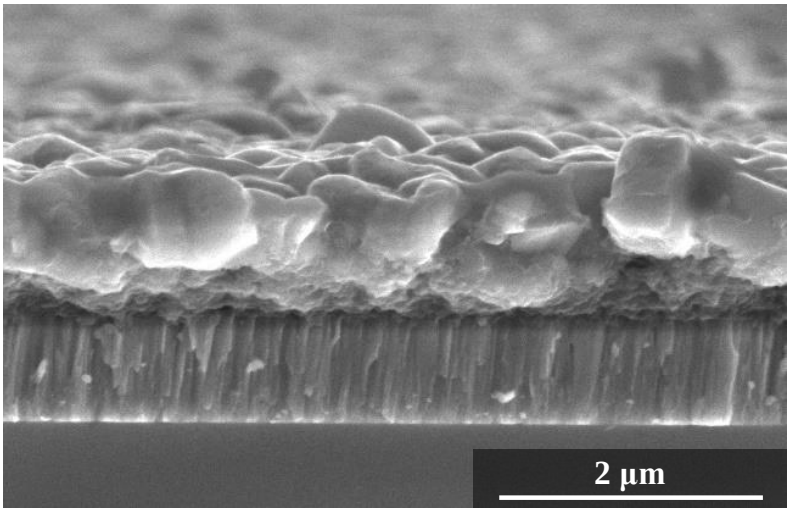

Figure 2.7. Side-view SEM image of an enargite film formed from luzonite nanoparticles at 400 °C for 90 minutes.

For Cu_3AsS_4 enargite films, SEM side view in Figure 2.7 reveals a bilayer morphology with a fine-grain layer underneath a large grain region, like CZTSe and CIGSe systems. This bilayer suggests it is possible the formation mechanisms between these three systems have film evolution similarities. Therefore, a working hypothesis is developed that asserts the film formation pathway is like that of CZTSe and CIGSe systems, where grains form on the surface of the film and grow towards the substrate. To test this hypothesis, the film formation process was analyzed for the Cu_3AsS_4 system. Section 2.3.3.1. tests this hypothesis by investigating the structural

and chemical integrity of the luzonite nanoparticles quenched from a temperature that exceeds the luzonite stability range of 300 °C (Maske and Skinner, 1971). Section 2.3.3.1. tests this hypothesis through analyzing the microstructure and composition throughout the film during the film formation process via side-view TEM-EDS.

2.3.3.1 Thermal treatment of luzonite nanoparticles in sealed, ambient conditions

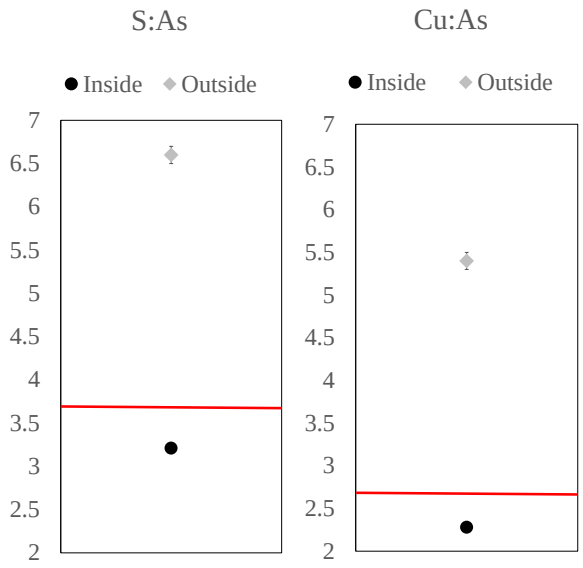

Figure 2.8. SEM-EDS data corresponding to compositions inside and outside a nanoparticle agglomerate after heating to 330 °C and quenching at approximately 90 °C per minute. The red lines indicate the composition of the original nanoparticles.

The conclusions from TGA and EDS analyses from the published paper note that luzonite nanoparticles become thermally destabilized and release sulfur by 315 °C, while arsenic is retained (McClary et al., 2017). Luzonite nanoparticle agglomerates were heated in a hermetically sealed aluminum pan sealed under ambient conditions. These nanoparticles were heated to 330 °C and quenched at approximately 90 °C/min. The agglomerates were mechanically fractured and analyzed with SEM-EDS, XRD, and Raman spectroscopy. EDS results are illustrated in Figure 2.8, which indicate a relatively arsenic rich composition on the inside of the agglomerate while

the surface was observed to be arsenic poor. XRD data in Figure 2.9 (a) indicate luzonite is the primary crystalline structure in the sample. Raman analyses in Figure 2.9 (b) indicate that although luzonite is present in the sample, copper sulfide is also observed. Even though sulfur is reported to volatilize from luzonite films at temperatures below 315 °C, these data support the published data by verifying that luzonite is the most prevalent phase at these conditions. Additionally, these data indicate mass transport can occur throughout the film at these conditions, and that copper sulfide is observed at temperatures as low as 330 °C.

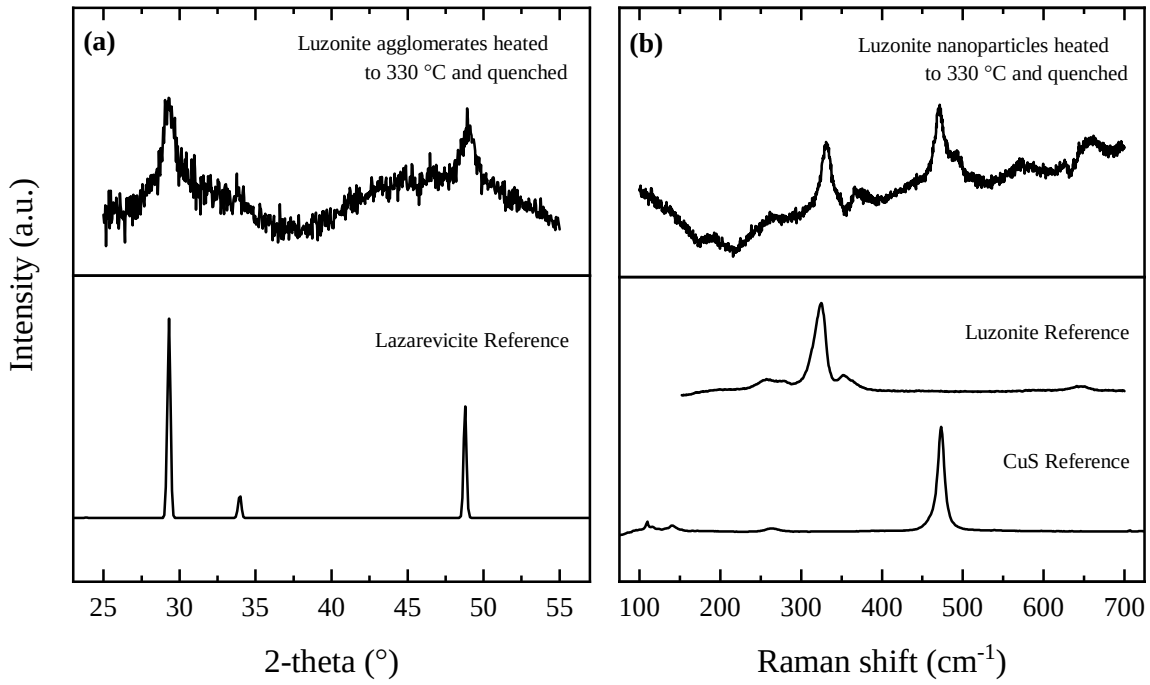

Figure 2.9. (a) XRD and (b) Raman data corresponding to nanoparticle agglomerates after heating to 330 °C and quenching at approximately 90 °C per minute. Lazarevicite reference is ICSD 42516, the luzonite reference is RRUFF ID R070247, and the CuS reference is RRUFF ID R060306. To the best of our knowledge, no pure luzonite XRD reference exists without some antimony contamination since luzonite free of antimony tends to form enargite. Lazarevicite, cubic Cu_3AsS_4, is used since the calculated luzonite {112} d-spacing from this study (Kanazawa, 1984) is better represented by the lazarevicite {111} than antimony-contaminated luzonite references.

The data presented thus far can be summarized as follows. Cu_3AsS_4 luzonite nanoparticles become thermally destabilized over the melting temperature of sulfur. DSC analyses from Section 2.3.1 concluded that liquid sulfur can incorporate arsenic to form a sulfur-rich arsenic sulfide melt, in agreement with the binary equilibrium phase diagram. According to the ternary equilibrium phase diagram, this arsenic sulfide melt has increasing copper solubility with increasing temperature. Therefore, it is likely that an initially pure sulfur melt can incorporate both arsenic and copper. Although luzonite is structurally the only phase identified after quenching from 330 °C, Raman analyses suggest CuS may also be present. Evidence for CuS is also present in SEM-EDS analyses, which indicates the surface of nanoparticle agglomerates is arsenic-poor. We speculate the arsenic may be expelled from the melt in nanoparticle agglomerates when copper sulfide forms, both inwards through phase segregation and outwards through evaporation.

2.3.3.2 Thermal treatment of luzonite nanoparticles under low vacuum

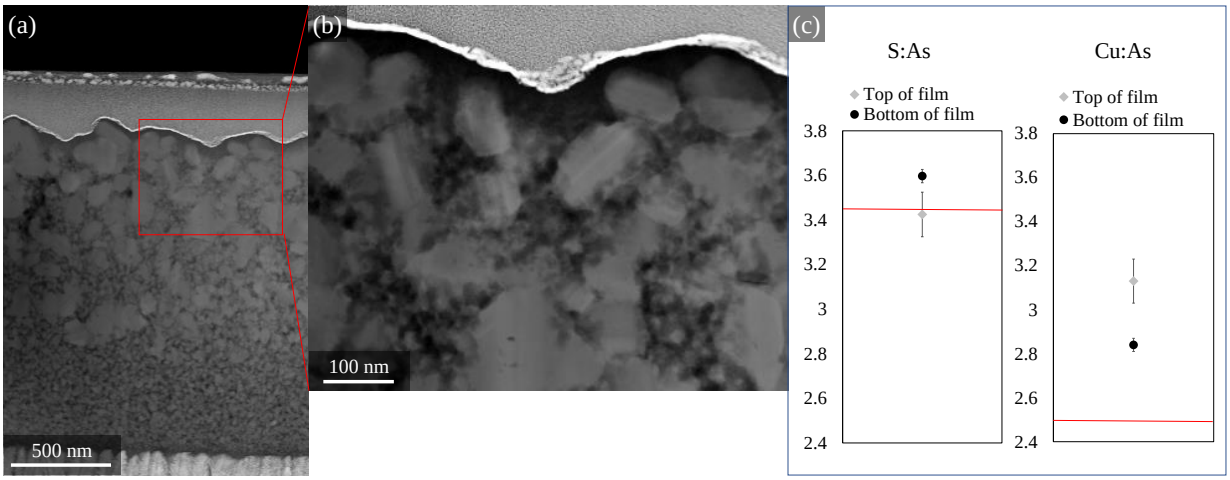

Figure 2.10. (a) and (b) Side-view TEM on a luzonite nanoparticle film after heating in a vacuum with As_2S_5 powder to approximately 330 °C and cooling approximately 10 °C/min.

To investigate the growth process of thin films, Cu_3AsS_4 luzonite nanoparticles were heated in an As_2S_5 environment at short times and their films were analyzed with TEM-EDS, XRD, Raman spectroscopy, and photoluminescence. Grains are observed to grow as a gradient throughout

the thickness of the film, as portrayed in Figure 2.10 (a). A closer look at the grains in Figure 2.10 (b) reveals stacking faults, which are commonly observed in the enargite-luzonite system when grains form around their polymorphic transition temperature (Pósfai and Sundberg, 1998). XRD analyses in Figure 2.11 (a) indicate a luzonite phase with enargite {210} planes, supporting this observation. EDS analyses in Figure 2.10 (c) indicates the large grain region is relatively rich in copper and poor in arsenic. Luzonite is observed together with a sulfur complex (McClary et al., 2017) in Raman analyses portrayed in Figure 2.11.

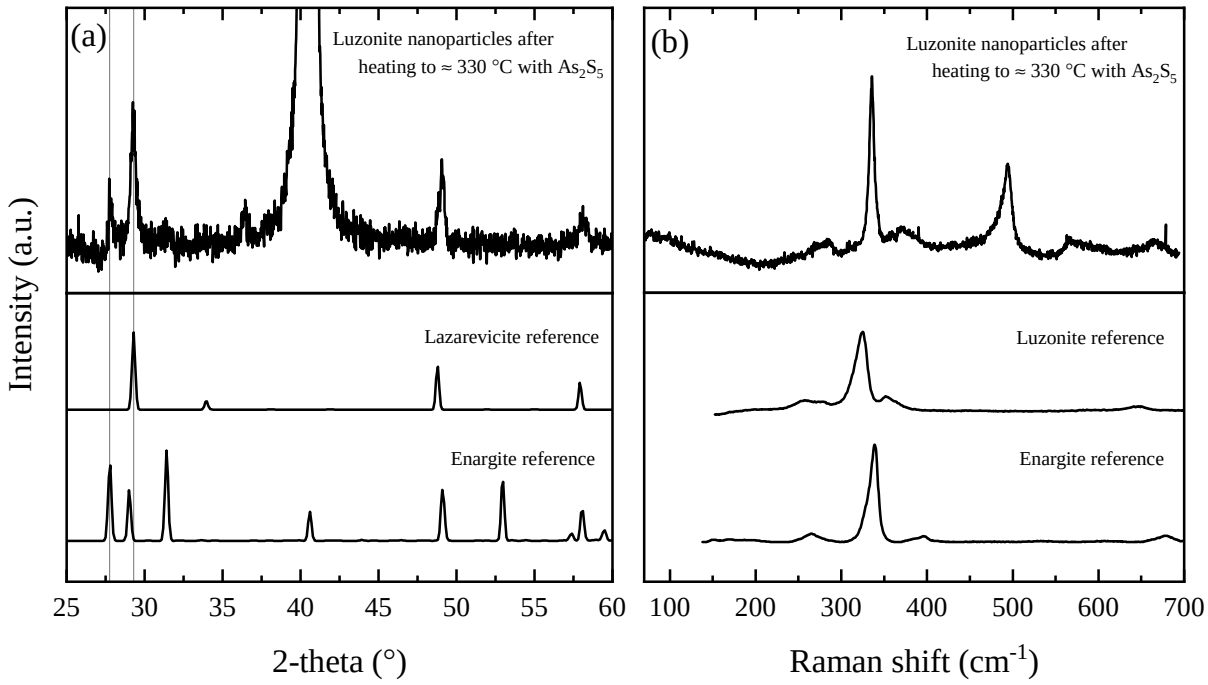

Figure 2.11. (a) XRD and (b) Raman data corresponding to a luzonite nanoparticle film after heating in a vacuum with As_2S_5 powder to approximately 330 °C and cooling approximately 10 °C/min. The peaks observed in Raman spectra (approximately 494 and 560 cm^{-1}) are attributed to a secondary phase discussed here (McClary et al., 2017). Lazarevicite reference is ICSD 42516, the luzonite reference is RRUFF ID R070247, and the enargite references are ICSD 14285 and RRUFF ID R060306. To the best of our knowledge, no pure luzonite XRD reference exists without some antimony contamination since luzonite free of antimony tends to form enargite. Lazarevicite, cubic Cu_3AsS_4, is used since the calculated luzonite {112} d-spacing from this study (Kanazawa, 1984) is better represented by the lazarevicite {111} than antimony-contaminated luzonite references.

Like the data provided when heating under ambient conditions, these data suggest similar findings when heated in a low vacuum. The approximate heating profile of the sample is shown below in Figure 2.12, measured in a separate experiment where a thermocouple was pushed into the furnace in place of a film under the same conditions. From the data above, luzonite nanoparticles become thermally destabilized and begin to form relatively large grains as a gradient toward the bottom of the film, corresponding to the presumed thermal gradient induced from radiative and convective processes. Copper sulfide is not observed in these samples through Raman spectroscopy, likely due to the extended cooling curve permitting the reincorporation of arsenic to form a ternary phase. Although arsenic reincorporation during cooling is speculative, evidence of this ternary phase is structurally observed in XRD. Separately, chemical quantification indicates a relatively arsenic poor region near the surface of the sample. Compared to the treatment under ambient conditions, the arsenic content near the substrate does not relatively increase in the same manner. These data suggest the arsenic content near the surface may be low due to increased volatilization due to the surrounding vacuum, which was likely suppressed during the treatment under higher pressure. Alternatively, arsenic may have diffused back into the upper layer, driven by diffusion after arsenic incorporation in the ternary phase. This speculation is only substantiated by the relative arsenic concentrations, so more analyses are required to confirm this alternative scenario. Either way a relatively arsenic poor surface with large grains results.

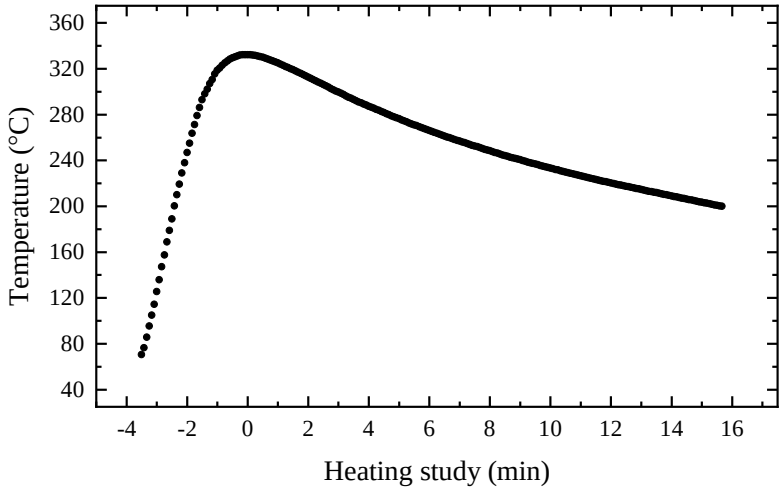

Figure 2.12. Approximate temperature profile of the sample examined in this section.

2.3.4 Identification of non-optimal film characteristics

As identified in Section 2.1., some qualifications for a high-quality thin film include phase purity and a dense morphology. For high-efficiency solar cells, a robust p-n junction with proper band alignment throughout the device is necessary. Actual or potential shortcomings regarding Cu_3AsS_4 films and devices have been identified and are discussed below.

Through the characterization techniques used on initial films (XRD, XRF, Raman spectroscopy, FTIR), the only apparent secondary phase was observed in Raman spectra, like that observed in Figure 2.11 (b). This secondary phase was observed and detailed in the journal publication (McClary et al., 2017) as belonging to sulfur bonds perturbed through interaction with the carbonaceous ligands surrounding the nanoparticles. This carbon-sulfur secondary phase may contribute to poor optoelectronic performance through parasitic absorption, introduction of shunt pathways and prevention of a robust p-n junction. One method to remove this secondary phase by means of a ligand exchange has been documented (McClary, 2019). In Chapter 3 of this dissertation, I outline another method to circumvent the formation of this phase.

Although 425 °C conditions were utilized to reduce porosity relative to other conditions, pores still remained in the system. A comparison of plan-view SEM images between $Cu_2Zn(Sn,Ga)Se_4$ and Cu_3AsS_4 in Figures 2.13 (a) and (b), respectively, illustrates this difference. Many grains in the $Cu_2Zn(Sn,Ga)Se_4$ material system are observed to form a common grain boundary with their neighbors, which is depicted with a red arrow in Figure 2.13 (a). This behavior is expected as surface energies are relatively high energy compared to the bulk and forming one boundary for both particles is energetically more favorable than forming two independent boundaries. Although this behavior is observable in some regions of Cu_3AsS_4 films, many particles are observed to form facetted planes instead of forming relatively low energy grain boundaries with their neighbors. The formation of these independent, distinct facets does not facilitate a continuous pathway for electrons to move freely from one grain to the next. Therefore, faceting behavior is generally undesirable in thin film solar cells. In addition to pores, an amorphous, non-IR active, chemically indistinct thin film was observed on the surface of some samples, indicated in Figure 2.13 (c) with red arrows. The existence of a film on the surface of enargite thin films are likely

to introduce weak junctions that may not effectively separate charge carriers. Efforts to reduce porosity and eliminate the observed surface film are detailed in Chapter 4 of this dissertation.

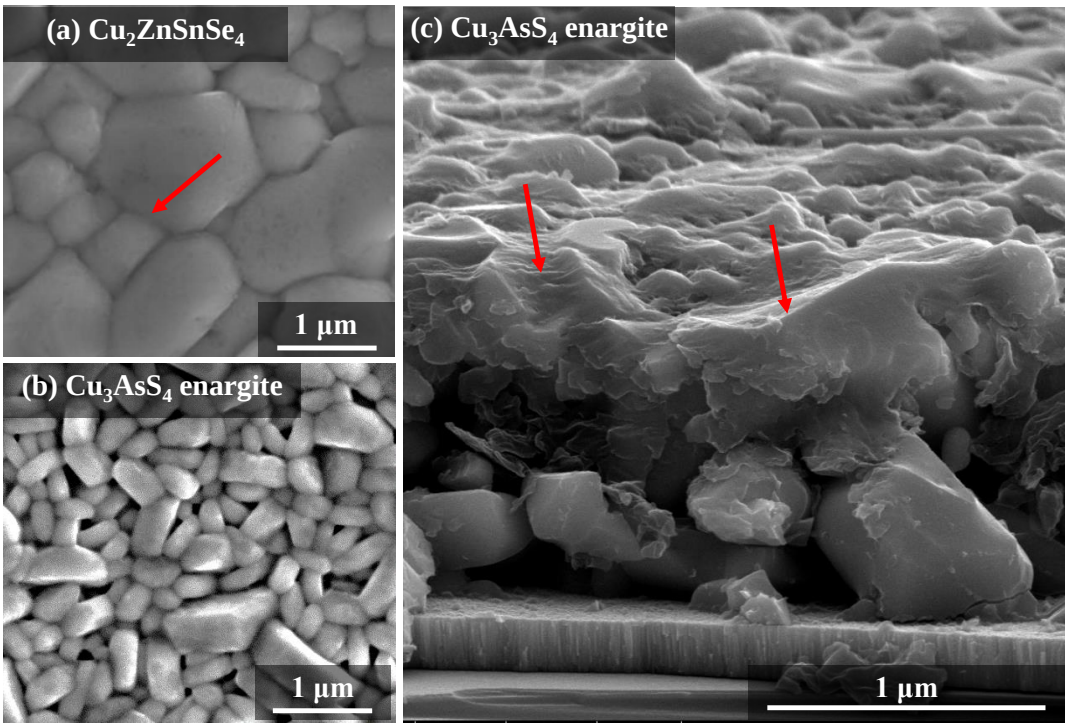

Figure 2.13. (a) plan-view CZTSe film from this reference (Hages, 2015). (b) plan-view and (c) side-view of two different enargite films displaying non-ideal characteristics of porosity and a secondary phase, respectively. The arrow in (a) notes conformal grain boundaries and the arrows in (b) highlight an observed secondary phase.

Utilizing Cu_3AsS_4 thin films toward photovoltaic applications is a relatively new concept (McClary et al., 2017, Yu et al., 2013). Therefore, optimization regarding device architecture is not well-studied. Initial devices used existing architecture from similar thin film technologies and used molybdenum as a back contact together with cadmium sulfide as an n-type junction partner to fabricate the diode. Materials for ideal n-type partner band alignment have been calculated elsewhere and have suggested ZnS in addition to other nonconventional materials like ZnTe or WO_3 to be promising avenues for investigation (McClary et al., 2019, Wallace et al., 2019). However, the alignment with the molybdenum interface has not yet been modeled. In addition to modeling the Mo interface, Chapter 5 of this dissertation investigates initial attempts at ZnS film formation.

2.4 Summary and conclusions

This chapter has provided additional context and data for the formation of Cu_3AsS_4 thin films. Specifically, three areas were addressed that together focused on the ambient conditions during film formation and problems with the resulting films. The thermal characteristics of As_2S_5 upon heating demonstrate that although sulfur is formed, most of this phase dissolves arsenic sulfide after melting and is retained in the melt through arsenic incorporation for some amount of time. The presence of an arsenic sulfide melt during Cu_3AsS_4 thin film development has revealed its effectiveness for increasing the densification of these films. Investigation into the early stage processes during thermal treatment provide evidence supporting the understanding that luzonite nanoparticles form a gradient of binary and/or ternary intermediate phases before growing large enargite grains. Lastly, the limitations of preliminary films have been identified and have guided future research that is introduced and discussed in the following chapters.

2.5 Acknowledgements

J.A. would like to acknowledge financial support from the NSF under grant #1144843 (Purdue-Tuskegee IGERT on globally sustainable electronics) and laboratory support from the NSF under grant #1534691-DMR (DMREF: Rapid Design of Earth Abundant Inorganic Materials for Future PVs). He thanks Dr. Scott McClary for providing TGA data and assistance and training on Raman spectroscopy, Dr. Md Nuruddin for assistance and training with the differential scanning calorimeter, Dr. Chris Gilpin and Jameson Root for assistance and training with scanning electron microscopy, and Dr. Brian Graeser, Dr. Xianyi Hu and Essam Alruqoba for training and assistance with providing molybdenum-coated soda-lime glass.

2.6 References

Balow, R. B. (2015). *Low-cost and earth-abundant nanocrystal synthesis for solar energy conversion and thermoelectric device applications*. Ph.d., Purdue.

Balow, R. B., Miskin, C. K., Abu-Omar, M. M., and Agrawal, R. (2017). Synthesis and Characterization of Cu3(Sb1-xAsx)S4 Semiconducting Nanocrystal Alloys with Tunable Properties for Optoelectronic Device Applications. *Chemistry of Materials*, 29(2):573–578.

Blachnik, R., Hoppe, A., and Wickel, U. (1980). Die Systeme Arsen-Schwefel und Arsen-Selen und die thermodynamischen Daten ihrer Verbindungen. *ZAAC - Journal of Inorganic and General Chemistry*, 463(1):78–90.

Borisova, Z. U. (1981). Glasses in Binary Systems. *Glassy Semiconductors*, pages 37–168.

Ewen, P. J. S. (1978). *THE RAMAN SPECTRA AND STRUCTURE OF GLASSES IN THE ARSENIC-SULPHUR AND ARSENIC-SELENIUM SYSTEMS BY Thesis presented for the degree of Doctor of Philosophy of the University of Edinburgh October 1978*. Ph.d., Edinburgh.

Hages, C. J. (2015). *DEVELOPMENT AND CHARACTERIZATION OF NANOPARTICLE-BASED KESTERITE SOLAR CELLS*. PhD thesis, Purdue University.

Hages, C. J., Koeper, M. J., Miskin, C. K., Brew, K. W., and Agrawal, R. (2016). Controlled Grain Growth for High Performance Nanoparticle-Based Kesterite Solar Cells. *Chemistry of Materials*, 28.

Jia, X., Bennett, T. D., and Cowan, M. G. (2019). Gas permeation of sulfur thin-films and potential as a barrier material. *Membranes*, 9(6):28–30.

Jonker, W. P. A. (1909). Untersuchungen uber das System: Schwefel und Arsen. *Zeitschrift fur anorganische und allgemeine Chemie*, 62(1):89–107.

Kanazawa, Y. (1984). Synthesis and lattice constants of luzonite-famatinite crystals.

Maske, S. and Skinner, B. J. (1971). Studies of the Sulfosalts of Copper I. Phases and Phase Relations in the System Cu-As-S. *Economic Geology*, 66:901–918.

McClary, S. A. (2019). *SYNTHESIS AND CHARACTERIZATION OF COPPER ARSENIC SULFIDE FOR SOLUTION-PROCESSED PHOTOVOLTAICS*. PhD thesis, Purdue University.

McClary, S. A., Andler, J., Handwerker, C. A., and Agrawal, R. (2017). Solution-processed copper arsenic sulfide thin films for photovoltaic applications. *Journal of Materials Chemistry C*, 5(28):6913–6916.

McClary, S. A., Li, S., Yin, X., Dippo, P., Kuciauskas, D., Yan, Y., Baxter, J. B., and Agrawal, R. (2019). Optoelectronic Characterization of Emerging Solar Absorber Cu3AsS4. In *IEEE Photovoltaics Specialists Conference Proceedings*, pages 3–7.

McLeod, S., Alruqobah, E., and Agrawal, R. (2019). Liquid assisted grain growth in solution processed Cu(In,Ga)(S,Se) 2. *Solar Energy Materials and Solar Cells*, 195(February):12–23.

Okamoto, H. (2006). As-S (Arsenic-Sulfur). In *Binary Alloy Phase Diagrams*, pages 314–315. ASM International.

Pósfai, M. and Sundberg, M. (1998). Stacking disorder and polytypism in enargite and luzonite. *American Mineralogist*, 83:365–372.

Ramanathan, K., Contreras, M. A., Perkins, C. L., Asher, S., Hasoon, F. S., Keane, J., Young, D., Romero, M., Metzger, W., Noufi, R., Ward, J., and Duda, A. (2003). Properties of 19.2% Efficiency ZnO/CdS/CuInGaSe2 Thin-film Solar Cells. *Progress in Photovoltaics: Research and Applications*, 11:225–230.

Ryu, H. S., Park, J. W., Park, J., Ahn, J. P., Kim, K. W., Ahn, J. H., Nam, T. H., Wang, G., and Ahn, H. J. (2013). High capacity cathode materials for Li-S batteries. *Journal of Materials Chemistry A*, 1(5):1573–1578.

Wallace, S. K., Butler, K. T., Hinuma, Y., and Walsh, A. (2019). Finding a junction partner for candidate solar cell absorbers enargite and bournonite from electronic band and lattice matching. *Journal of Applied Physics*, 125(5):1–8.

Yu, L., Kokenyesi, R. S., Keszler, D. A., and Zunger, A. (2013). Inverse design of high absorption thin-film photovoltaic materials. *Advanced Energy Materials*, 3(1):43–48.

Yuan, Z. K., Chen, S., Xiang, H., Gong, X. G., Walsh, A., Park, J. S., Repins, I., and Wei, S. H. (2015). Engineering Solar Cell Absorbers by Exploring the Band Alignment and Defect Disparity: The Case of Cu- and Ag-Based Kesterite Compounds. *Advanced Functional Materials*, 25(43):6733–6743.

Zhang, T., Yang, Y., Liu, D., Tse, S. C., Cao, W., Feng, Z., Chen, S., and Qian, L. (2016). High efficiency solution-processed thin-film Ci(In,Ga)(Se,S)2 solar cells. *Energy & Environmental Science*, 9:3674–3681.

CHAPTER 3. SYNTHESIS OF Cu_3AsS_4 ENARGITE FILMS FROM EVAPORATED COPPER SUBSTRATES

3.1 Introduction

As demonstrated in the last chapter, methods to synthesize Cu_3AsS_4 enargite thin films from nanoparticles precursors have demonstrated an IR-active secondary phase and notable porosity. The secondary phase has been attributed to a carbonaceous phase introduced from carbon ligands surrounding precursor nanoparticles (McClary et al., 2017). These film characteristics are hypothesized to be a significant contributor hindering the performance of current devices. Efforts have been made to remove this secondary phase by exchanging the nanoparticle ligands with inorganic arsenic sulfide ligands, but contiguous thin films appropriate for device applications have yet to be fabricated (McClary, 2019).

In this chapter I demonstrate that the IR-active secondary phase can be avoided through a novel thin film enargite synthesis technique that bypasses the necessity of a nanoparticle synthesis. I also observe the formation of the IR-active secondary phase in precursor copper (II) sulfide thin films without the formation of carbon, indicating that although carbon ligands may facilitate the formation of this phase, it remains a phase distinct from carbon. Precursor copper and copper sulfide films are characterized and compared and resulting enargite films are further analyzed to contrast similarities between these processing routes. This approach to enargite fabrication demonstrates the first phase pure synthesis route to these thin films suitable for photovoltaic device applications.

3.2 Experimental methods

3.2.1 Materials

The chemicals used to complete the investigations in this chapter are listed in Table 3.1.

Table 3.1. *List of products used in this chapter*

Chemicals / equipment	**Purity / type**	**Source**	**Quantity***
Aluminum pellets	>99.999%	Kurt J. Lesker	≈ 3.5 mg / 2 μm Al**
Ammonium hydroxide	30%	Sigma-aldrich	≈ 30 mL / CdS deposition
ampule (10 mL)	Borosilicate glass	Chemglass Life Sciences	≈ 13 g / treatment
Arsenic (III) sulfide	>99.9%	Strem Chemicals	≈ 17 mg / treatment
Cadmium sulfate hydrate	>99.996%	Alfa Aesar	≈ 85 mg / CdS deposition
Copper pellet	>99.99%	Kurt J Lesker	≈ 2 mg / 300 nm**
Indium oxide (ITO) target	>99.99%	Kurt J Lesker	≈ 1 mg / 220 nm**
Hydrogen sulfide (H2S) gas	1% and 3% bal. Ar	Airgas	Tanks used indefinitely
Molybdenum target	>99.95%	Kurt J. Lesker	≈ 85 mg deposited***
Nickel pellets	>99.999%	Kurt J. Lesker	≈ 0.6 mg / 100 nm Ni**
Sulfur flakes	99.99%	Sigma-Aldrich	≈ 8 mg / treatment
Thiourea	>99% ACS	Sigma-Aldrich	≈ 1.3 g / CdS deposition
Ultrapure water	18.2 MΩ-cm	Direct-Q3 UV (in-house)	≈ 150 mL / CdS deposition
Zinc oxide target	>99.9%	Kurt J Lesker	≈ 0.3 mg / 80 nm**

**Hexane, IPA, water, soap, and nitric acid used for glassware cleaning between each synthesis is not included*
***OLA stock solution was degassed using three freeze-pump-thaw (FPT) cycles and stored under nitrogen*
****Deposition area is one 4"x4" substrate per deposition. Over the life of the target (about 8 depositions), the total target utilization for this lab scale deposition process is approximately 5%, measured empirically. Most molybdenum (≈ 90%, empirically deduced) is sputtered onto chamber walls resulting in a total material utilization of approximately 0.5%.*

3.2.2 Film deposition and fabrication

3.2.2.1 Thermal evaporation of copper films on Mo-SLG

Substrates, typically cut into 1" x 1/4" areas, were adhered to a target holder approximately 30 cm from the evaporation source. The base pressure and operating conditions for all samples was less than 1E-3 Pa (1E-5 mbar). Thermal depositions were completed with a copper pellet placed on a tungsten boat and resistively heated to its melting point. The deposition rate and thickness of these films were controlled using a quartz crystal microbalance. Deposited thicknesses were verified with side-view SEM when appropriate, and typically demonstrated $\pm 30\%$ and $\pm 10\%$ accuracy with 25 - 30% and 5 - 10% thickness uniformity when depositing with new and old pure copper pellets, respectively. We speculate the increased non-uniformity when using new pellets is due to the inconsistent melting behavior observed. This behavior is most likely due to spatially nonuniform heating between regions of copper in physical contact with the tungsten boat and regions not in contact with the boat. The thermal evaporator is housed in a dry environment (water and oxygen less than approximately 5 ppm), so resulting copper films are stored in this environment as well.

3.2.2.2 Fabrication of CuS thin films

Six copper films total were sealed under argon in two ampules with ampules containing different quantities of sulfur (1 mg and 6.8 mg). The lower of these values was chosen as the approximate minimum stoichiometrically necessary quantity of sulfur for each ampule. Two copper films in each ampule were deposited on Mo-SLG substrates and one was deposited on a bare SLG substrate. These ampules were sealed under argon at pressures between about 145-170 mTorr and placed in a horizontal tube furnace. The furnace was equilibrated at 300 °C before the samples were pushed in and held for 40 minutes before the furnace was shut off and the lid was opened. All samples were allowed to cool naturally to room temperature.

3.2.2.3 Fabrication of Cu_2S thin films

Copper films were exposed to ambient conditions for approximately 5 minutes while samples were staged and loaded into a vertical tube furnace. After loading, the furnace was purged three times with argon and the furnace was heated to 300 °. When approximately stabilized (≈ 20 minutes), hydrogen sulfide gas was introduced into the chamber until the bubbler solution on the exhaust system began to react with the gas. The flow rate of H_2S gas varied between 25 – 100 sccm depending on gas concentration (1% or 3%). The samples were then pushed into the center of the furnace and left to react for 30 - 120 minutes depending on the thickness of the copper film being reacted (300 - 900 nm). During cooling, hydrogen sulfide gas was replaced with an argon flow until the furnace reached room temperature. Samples were removed from the furnace and stored in a dry environment until used.

3.2.3 ampule preparation

Ampules used in this study have a neck diameter of approximately 1/4" so copper sulfide films samples must be at least this small in one dimension. The substrate sample size used in all ampule treatments mentioned in this chapter is 1/4" x 1" unless otherwise noted. Sulfur flakes and arsenic sulfide powders are loaded into the ampule in a nitrogen ambient. Typically, two copper sulfide films are loaded into the ampule and sealed with a valve. One film is usually used for characterization and the other is used for device or other purposes. This valve is then connected to a Schlenk line which is purged three times with argon. The valve is opened and the ampule is purged three times with argon. When under a vacuum of at least 0.2 torr, a butane torch is used to yield the glass at the neck until an airtight seal is formed. The resulting total volume of the ampule is approximately 13 mL.

Arsenic sulfide and other fine powders often electrostatically adhere to the neck of the ampule during filling. These powders volatilize when sealing with a butane torch and can react with the substrates. Copper sulfide films are used to mitigate this effect. CuS films, fabricated by reacting copper films with elemental sulfur in an ampule, did not demonstrate observable spatial non-uniformity since there were no particles electrostatically held on the neck of the ampule to

volatilize. Spatial nonuniformity for both CuS and Cu_2S films were not observed when sealing with arsenic sulfide powders.

3.2.4 Heat Treatments

Treatments of CuS and Cu_2S films were performed in a three-zone tube furnace. From one end, a K-type thermocouple protrudes into the center of the three zones to monitor temperature of the ampule ambient. The other end is installed with a pushrod. The furnace is sealed and purged three times with argon. Under an argon flow of about 10 sccm, the furnace is then stabilized at operating temperature ($\approx$ 10 min) before the ampule is pushed into the center of the three zones. Cooling occurs naturally after opening the top of the furnace unless otherwise noted. Typically, a yellow gas is observed until arsenic sulfide vapors condense on the top of the ampule due to convective cooling. These condensing species were observed to change color during cooling from dark red to yellow, with shades of orange throughout, which is expected for liquid sulfur and arsenic sulfide solutions. Copper species were never observed with Raman spectroscopy, photoluminescence, and X-ray fluorescence when analyzing these condensed species, indicating it remained in the film. Therefore, calculations involving mass balance can assume all copper remained in the film.

3.2.5 Device fabrication

Enargite films were retrieved by scribing around the neck of the ampule and mechanically fracturing the glass along the scribe. Samples were formed into devices by first depositing approximately 50 nm CdS via chemical bath deposition. Approximately 80 nm of slightly n-type ZnO was deposited through RF sputtering with an ambient oxygen content of 2% in argon. Approximately 220 nm ITO was deposited by the same sputter system, but fully in an argon ambient. Electron beam evaporation of patterned Ni/Al grids was used to deposit the top contact. Cells were electrically isolated by individually scribing with a dull blade capable of penetrating through the enargite film, but not capable of scratching the molybdenum surface. These cells result in an area of approximately 0.1 cm^2.

3.2.6 Characterization details

A FEI quanta 3D dual-beam field emission scanning electron microscope (SEM) was used to capture film morphology. Energy-dispersive X-ray spectroscopy (EDS) was collected with an accelerating voltage of 20 kV on the same SEM with a silicon drift detector. Elemental compositions were determined through AZtec software using standardless quantitative analysis. X-ray diffraction (XRD) data were collected on a Rigaku SmartLab diffractometer using a copper Kα X-ray source in parallel beam mode with a grazing incidence angle of 0.5°. Raman spectra were collected using a Horiba/Jobin-Yvon LabRAM HR800 confocal microscope system with a 17 mW 633 nm He:Ne laser. Unit cell modelling was performed using VESTA version 3.4.8. Time-resolved photoluminescence (TRPL) measurements were collected on a custom optical setup using a 447 nm diode laser for excitation and a PDM photon counting module for signal detection. A Bruker MultiMode 8 was used to complete the atomic force microscopy (AFM) measurements. Current-voltage (J-V) measurements were acquired with an Oriel Sol3A solar simulator with the AM1.5G spectrum calibrated to 100 mW/cm^2 using a certified silicon reference cell.

3.3 Results and discussion

3.3.1 Cu film characteristics

Structural analysis in Figure 3.1 indicates the thermally evaporated copper is not oriented on the textured molybdenum surfaces. A small peak is observed at approximately 41.5°, which does not correspond to known oxides of the metals, and its source has not been identified. A slight shifting of the XRD pattern to higher 2-theta is noted, suggesting these films have a smaller lattice constant than what is expected. These features are assumed not to influence the development of copper sulfide or copper arsenic sulfide thin films and were not investigated further.

These copper films are sealed together with arsenic sulfide powders in an evacuated ampule using a butane torch. When the ampule is filled with powders, small particles can be electrostatically adhered to the neck of the ampule. The sealing process volatilizes these powders,

which were observed to react with the copper film creating a non-uniform substrate prior to thermal treatment. Mechanically displacing the powders can reduce the effect, but not eliminate it. Therefore, stabilizing the copper film by first forming copper (II) sulfide and copper (I) sulfide films was completed.

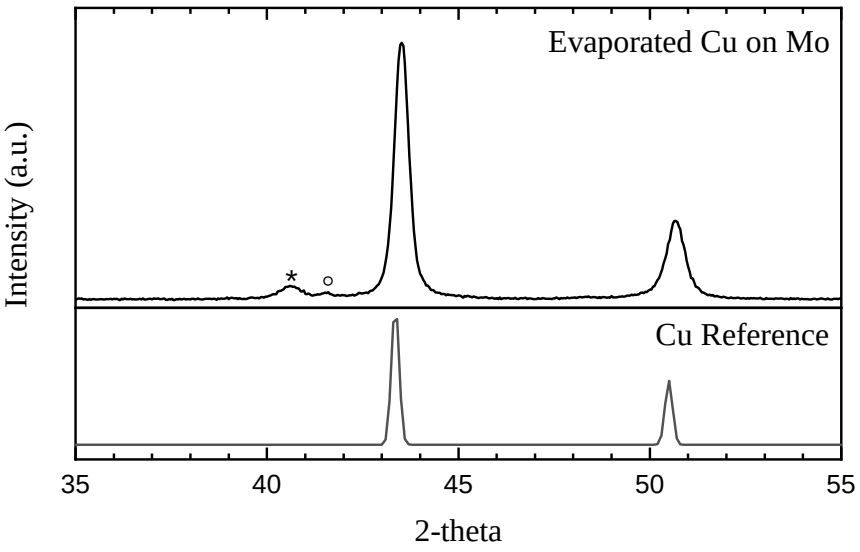

Figure 3.1. XRD analysis of evaporated copper films deposited onto a molybdenum-coated SLG substrate. The (*) indicates the {110} planes of the Mo substrate. (°) is an unidentified peak not known to correspond to either of the metals or their oxides. The reference spectrum for copper is ISCD 43493.

3.3.2 CuS film characteristics

Copper films on SLG and Mo-SLG were exposed to elemental sulfide in a sealed ampule at elevated temperatures. For Mo-SLG samples, XRD data in Figure 3.2 (a) indicate CuS to be the only crystalline phase. Raman spectra in Figure 3.2 (b) indicate CuS is primarily present with a secondary phase that has a main peak at 494 cm^{-1} and broad vibrations at 360 cm^{-1} and 560 cm^{-1}. A secondary phase with these characteristic vibrations were previously reported and shown to be associated with carbonaceous ligands on precursor nanoparticles (McClary et al., 2017). However, a carbon impurity capable of producing these vibrations is unlikely given these films were not

exposed to carbon or ambient conditions after the copper film deposition. Although the formation of this secondary phase may be facilitated through exposure to carbonaceous species, we find it is also correlated with the formation of copper (II) sulfide thin films produced under low vacuum from elemental precursors on a Mo-SLG substrate at 300 °C for 30 minutes.

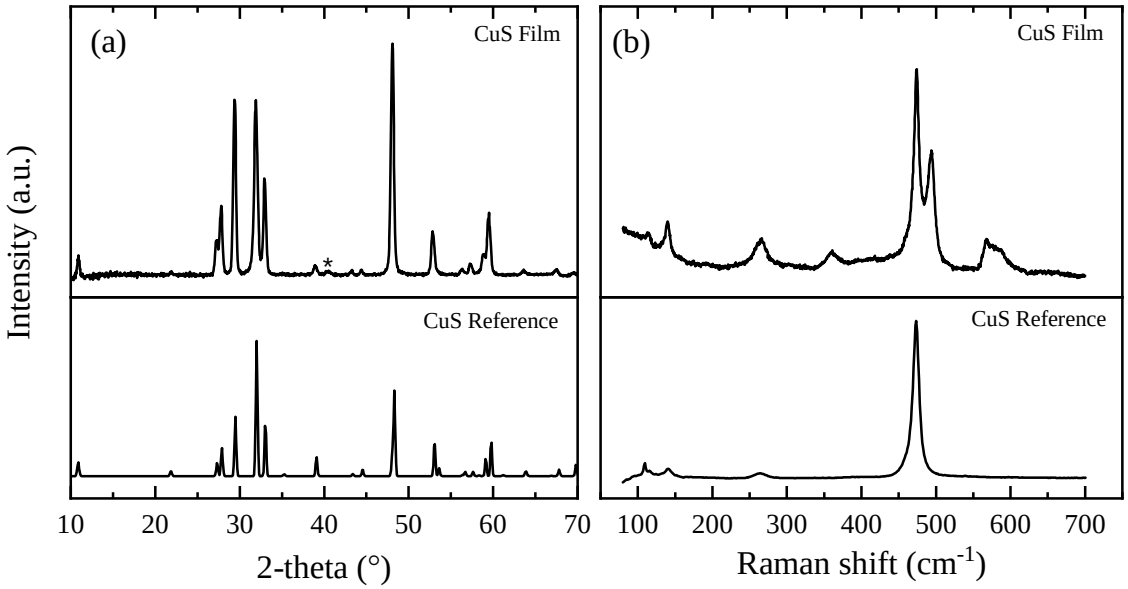

Figure 3.2. Characterization of CuS films through (a) XRD and (b) Raman analyses. The peak denoted by (*) is due to the substrate Mo. The XRD reference spectrum for CuS is ISCD 32105 and the Raman reference is RRUFF ID R060306.

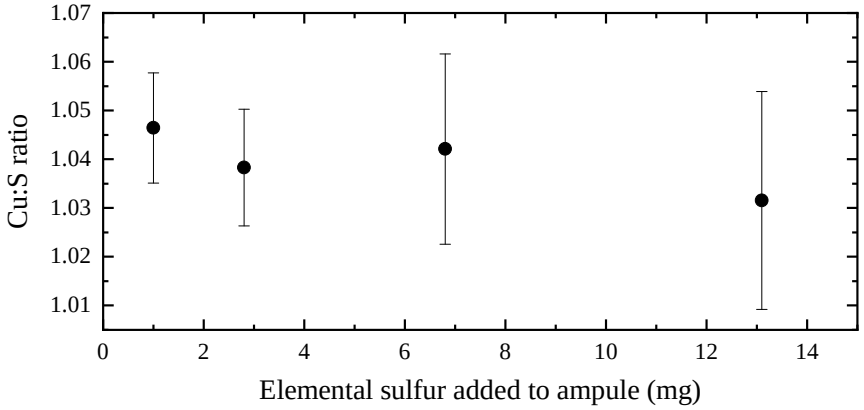

Figure 3.3. Chemical characterization of CuS films with SEM-EDS. These films were analyzed on bare SLG so that sulfur characteristic peaks would not overlap with molybdenum.

Compositional data for all films are provided in Figure 3.3 and suggest similar Cu:S ratios for all samples tested. When an excess of sulfur is used, films may be expected to incorporate this excess sulfur. However, this analysis indicates that a sulfur melt is not likely to persist in these films.

Similar film thickness, grain size, and morphology were observed for these samples, and representative images are shown in Figures 3.4 (a) – (c). A bimorphological film is observed generally consisting of large, faceted particles with a high aspect ratio, and smaller, sphere-like particles that demonstrate high relative contrast. Smaller particles are observed throughout the film, based on side-view SEM imaging, indicating that these particles are not only a surface phenomenon. These films have spatial uniformity and are not observed to contain cracks.

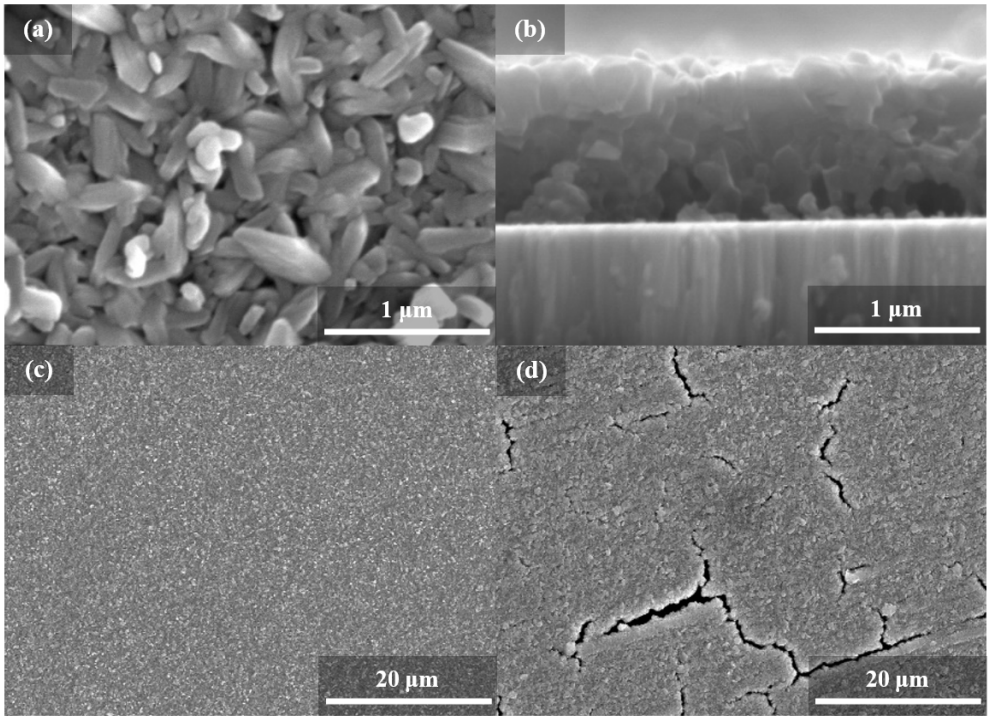

Figure 3.4. SEM images of CuS thin films. (a) plan view and (b) side view images demonstrate small, spherical particles coexisting with faceted grains. A comparison of CuS films fabricated on (c) Mo-SLG and (d) bare SLG demonstrate severe cracking with films fabricated on bare SLG.

Photoluminescence measurements were performed to obtain the band gap and defect characteristics of the film, illustrated in Figure 3.5. Although reported band gaps of CuS vary, they

are generally above 2 eV and exceed the detection limit of our instrumentation (Nemade and Waghuley, 2015, Santos Cruz et al., 2013). However, copper sulfide secondary phases that are more rich in copper generally have a lower band gap, which can be detected (Quintana-ramirez et al., 2014). We observe a sharp peak corresponding to a transition of approximately 1.8 eV, which cannot be associated with any specific secondary phase. However, the presence of a broad photoemission region may indicate the presence of defects throughout the structure. Therefore, due to the PL and Raman data, these precursor films are identified not to be single-phase CuS.

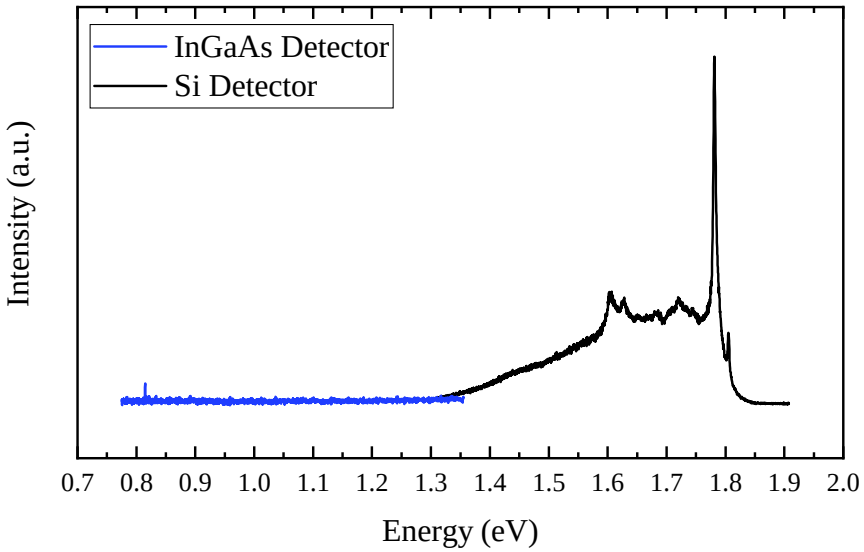

Figure 3.5. Photoluminescence of CuS films excited by a 632 nm He:Ne laser. Two detectors were used during subsequent scans.

Samples prepared on SLG substrates were observed to contain numerous throughout the films, represented in Figure 3.4 (d). Differences in coefficient of thermal expansion are known to cause delamination and cracking, however, the expansion in these temperature ranges of molybdenum (Hidnert, 1924) is less than glass (Scholze, 1991), which are both less than the thermal expansion of copper sulfide (Selivanov et al., 2007). Thermal expansion discrepancies suggest cracking should be more severe on molybdenum than glass. Evaporation of sulfur during cooling could also induce cracking, but given these samples were in the same ampules, the films

are expected to be exposed to the same conditions. Even so, a slower cooling rate will reduce cracking from an evaporation event, but we expect the sample with molybdenum to cool at a faster rate given its superior thermal transport properties. The origin of the film cracking on bare SLG has not been further investigated. Nevertheless, copper sulfide films were observed to crack more readily on SLG than on Mo-SLG substrates. For all quantities of elemental sulfur added to ampules containing copper films, resulting CuS films were observed to have similar structures, bonding behavior, thickness, chemical composition, grain size, and morphology compared to other samples prepared on the same substrates.

3.3.3 Cu_2S film characteristics

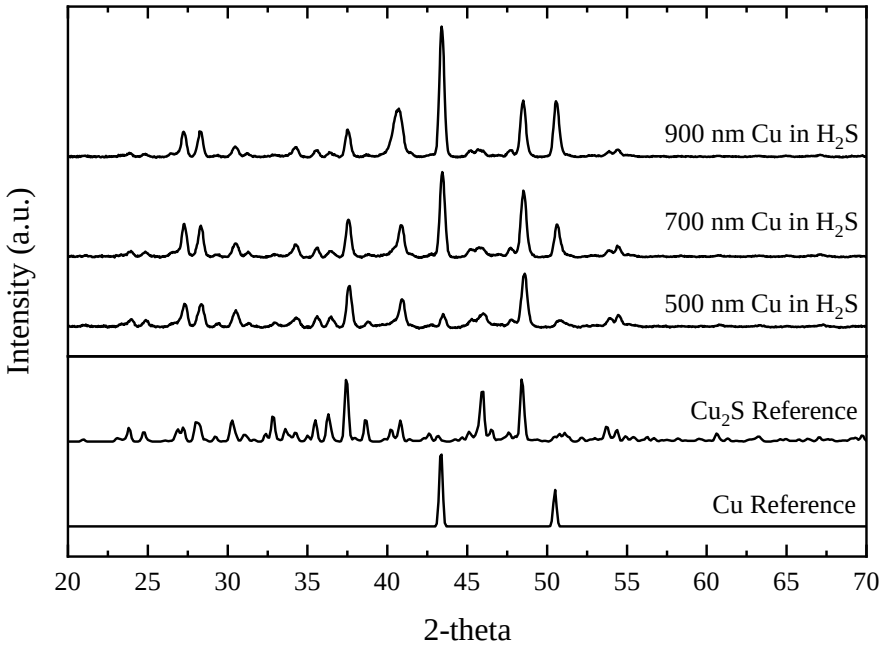

Figure 3.6. XRD patterns resulting from copper films treated in H_2S gas. The XRD reference spectrum for copper is ISCD 43493 and Cu_2S is ISCD 23596.

As a copper film is reacting with gaseous H_2S, we expect these films to nucleate copper sulfide on the surface. Copper sulfide is expected to either grow toward the substrate as a planar

front or act as a blocking layer to H_2S to prevent further growth. To observe the development of these films, 500, 700, and 900 nm Cu films were exposed to 3% H_2S gas for 30 minutes at 300 °C with a flow rate of 30 – 40 sccm. An incomplete structural transformation was observed according to XRD analysis of Figure 3.6, and a planar growth front was observed in side-view SEM. Figures 3.7 (a), (b), and (c) depict starting film thicknesses of 500, 700, and 900 nm, respectively. We note that with a treatment time of 120 minutes, 300, 500, and 700 nm copper films were observed to fully transform to Cu_2S (900 nm was not tested). For the thicknesses tested, H_2S is observed to penetrate through the copper sulfide grains and react with the copper layer underneath. Regarding H_2S concentration, thirty minutes was found to be enough to fully convert a 300 nm Cu film under these conditions with both 1% and 3% H_2S gas.

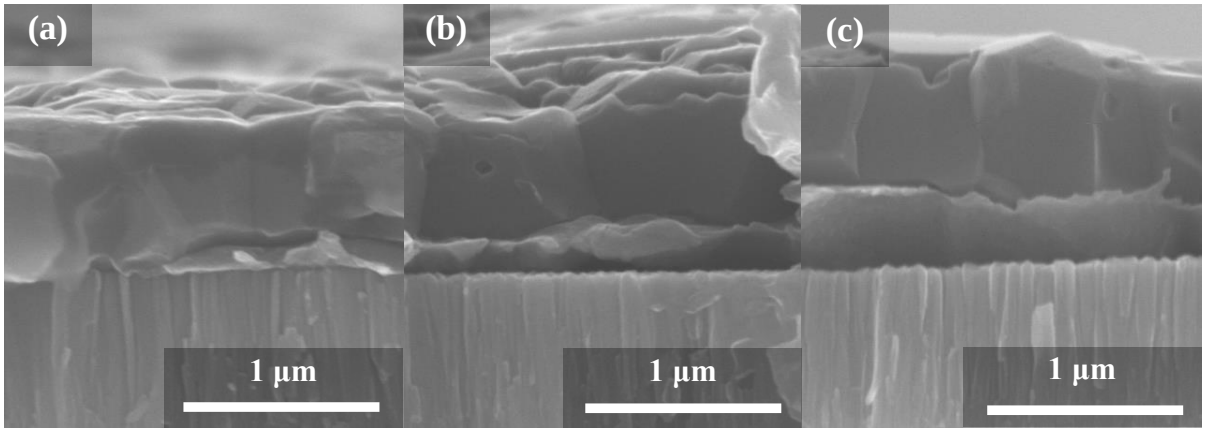

Figure 3.7. Side-view SEM images of copper films in H_2S gas with the same treatment conditions. Initial copper thicknesses were (a) 500 nm, (b) 700 nm, and (c) 900 nm.

Figures 3.7 indicate Cu_2S forms as a growth front toward the substrate with single grain thickness. Plan-view SEM in Figure 3.8 indicates these films are densely packed, faceted films. No secondary particles were observed during imaging of these films; however, some circular features were detected that influenced the growth of the film. These features were approximately 0.1 to 0.5 mm in diameter and are attributed to particulate contamination during processing. For fully treated Cu_2S films, XRD data in Figure 3.9 (a) demonstrate a single phase is formed. Raman spectra are provided in Figure 3.9 (b) for fabricated Cu_2S films relative to various Cu_2S references.

The source of the different vibrations observed and reported is unclear, but peaks around 280 and 600 cm^{-1} are generally reported and are observed in our Cu_2S films. Conclusions made from Raman spectra in this system are inconclusive. However, a distinct stretch at approximately 474 cm^{-1} is sometimes reported (Minceva-Sukarova et al., 1997) and results from sulfur-sulfur stretching modes (Ewen, 1978, Scott et al., 1961, Ward, 1968). Therefore, the lack of observed disulfide bonds indicates the sulfur present in the film is bound to copper. No further investigations were completed on with Raman spectra on Cu_2S films.

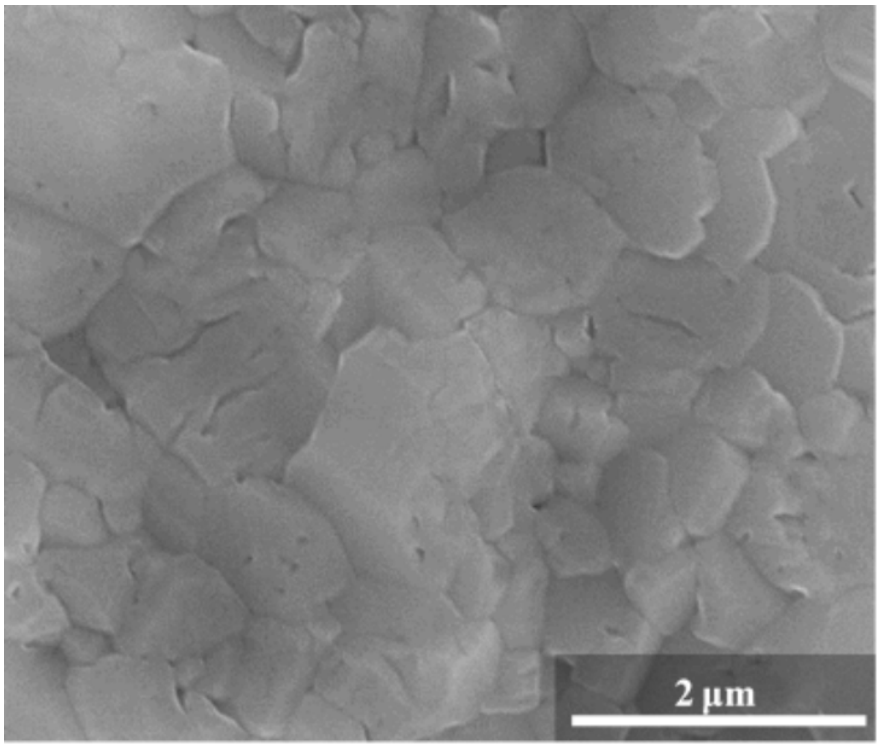

Figure 3.8. Plan-view SEM image of a copper film treated in H_2S gas

The band gap of Cu_2S from absorption data is reported to vary widely from about 1.2 eV to 2.4 eV (Das et al., 1978, Grozdanov and Najdoski, 1995, Pathan et al., 2002). Here, photoluminescence is used to capture this value and an approximated band gap of 1.24 eV has been determined for these films, demonstrated in Figure 3.10. A relatively small, broad optical emission is observed in the Cu_2S data beginning at approximately 1.8 eV. Although this region corresponds to CuS emission observed in the last section, we do not believe this represents Cu_xS

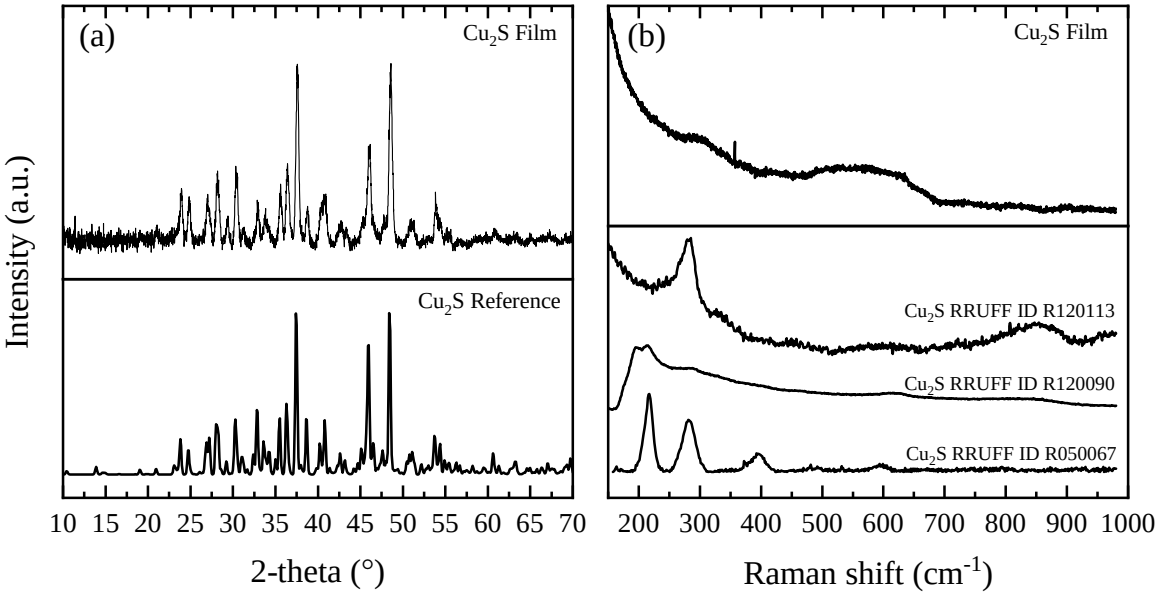

Figure 3.9. Characterization of Cu_2S films through (a) XRD and (b) Raman analyses. Many different Raman spectra are reported, and a few of them are provided here for reference. The XRD reference spectrum for Cu_2S is ISCD 23596.

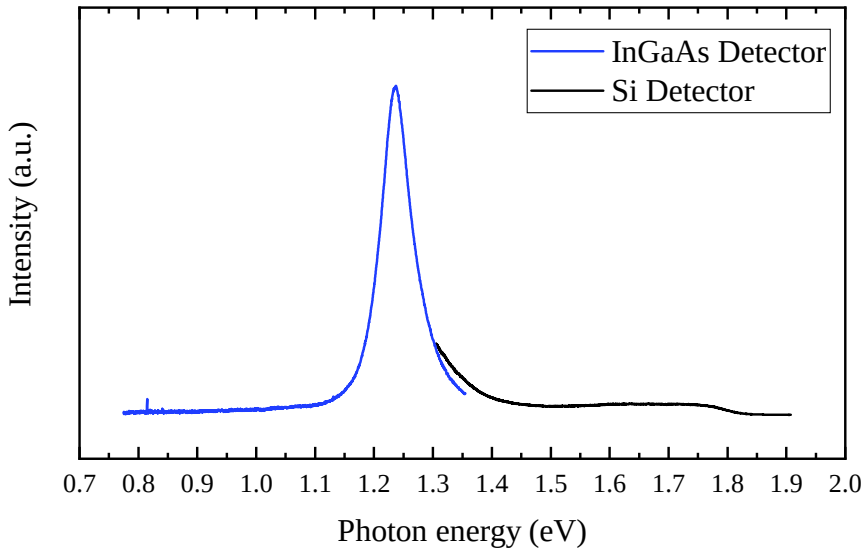

Figure 3.10. Photoluminescence of Cu_2S films excited by a 632 nm He:Ne laser. Two detectors were used during subsequent scans.

impurities due to the lack of distinctive peaks. Rather, a broad, nondistinctive peak was commonly acquired in this region for many different samples. Therefore, we believe these data to reflect an artifact of our measurement technique that has not yet been corrected. However, we do report observed photoemission above the band edge of Cu_2S, and the presence of Cu_xS is inconclusive. Due to no other phases observed in Raman spectra, XRD, or SEM, we report this film to be single-phase Cu_2S.

3.3.4 Cu_3AsS_4 enargite film characteristics fabricated from CuS films

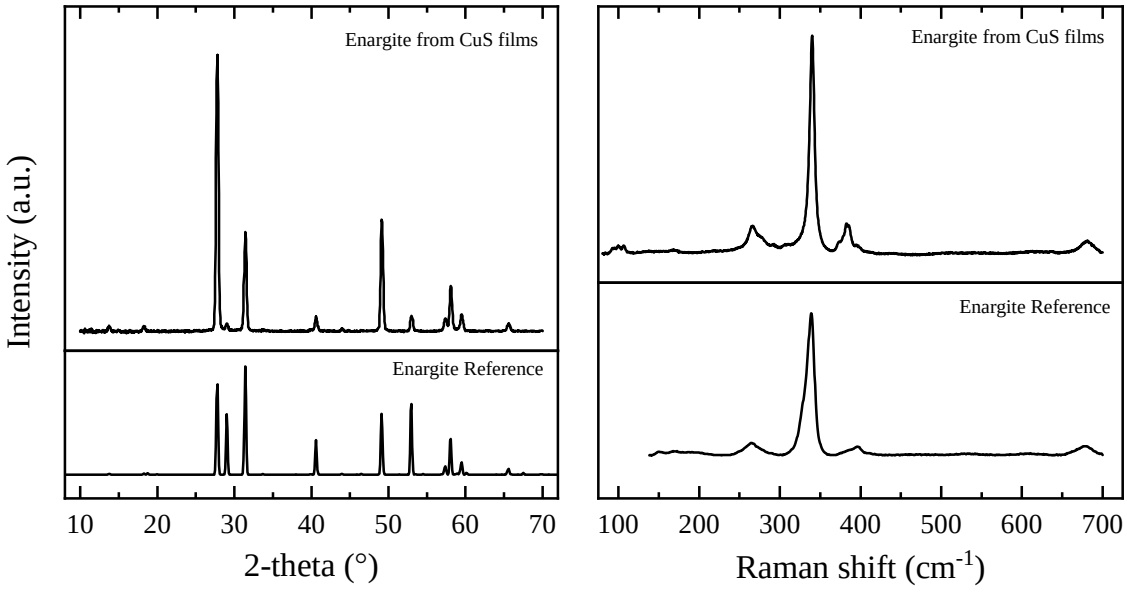

Figure 3.11. (a) XRD and (b) Raman analyses of Cu_3AsS_4 formed from treating CuS films. The XRD reference spectrum for Cu_3AsS_4 is ICSD 14285 and the Raman reference spectrum is RRUFF ID R070176.

From XRD and Raman analyses in Figures 3.11 (a) and (b), respectively, Cu_3AsS_4 enargite is the only observed phase. Orientation relative to the reference spectrum is noted along the {210} planes, which is consistent with films grown from Cu_3AsS_4 luzonite nanoparticles in an ampule with As_2S_5 powders. However, low relative intensity along the {002} planes has not

yet been observed for this system. Modeling of the enargite unit cell in Figure 3.12 indicates the $\{002\}$ planes are sulfur rich planes. In the presence of excess sulfur during growth, these planes could become thermodynamically preferred similar to the behavior observed for pyrite (Arrouvel and Eon, 2019). However, a CuS precursor film with sulfur flakes and arsenic sulfide powders should be enough to provide a sulfur-rich ambient. Here, the preferred orientation regarding the $\{002\}$ planes has not been found to change with the addition of more sulfur in the ampule with the conditions studied. In this chapter, we focus on the characteristics of enargite thin films and delay further discussion on enargite orientation to Chapter 4.

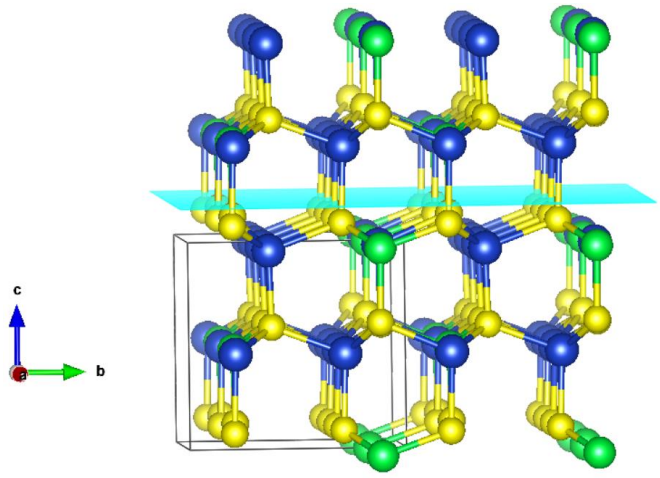

Figure 3.12. Enargite unit cell with the (002) plane highlighted.

Regarding film morphology, side-view SEM in Figure 3.13 (a) reveals dense grains flush with the molybdenum substrate. Although facets are visible, neighboring grains appear to mostly develop conformal grain boundaries with a high degree of necking. Similar behavior is observed in the plan-view SEM images for these particles in Figures 3.13 (b) and (c). However, a bimorphological film is observed consisting of large, faceted grains together with smaller, partly sintered particles. A closer inspection of these faceted grains reveals what may be intraparticle grain boundaries, suggesting these grains may be the product of sintered particles. On one hand, materials that undergo densification through sintering are beneficial for thin film semiconductors since porosity and grain boundaries are reduced. However, densification resulting in faceted grains

may not be beneficial if the grains grow vertically from the substrate and establish independent, distinct facets that do not facilitate electron transport. Furthermore, if the facets introduce surface-level trap states, these morphologies could increase surface recombination velocities and lead to a reduced open circuit voltage through increased minority carrier recombination in the depletion region.

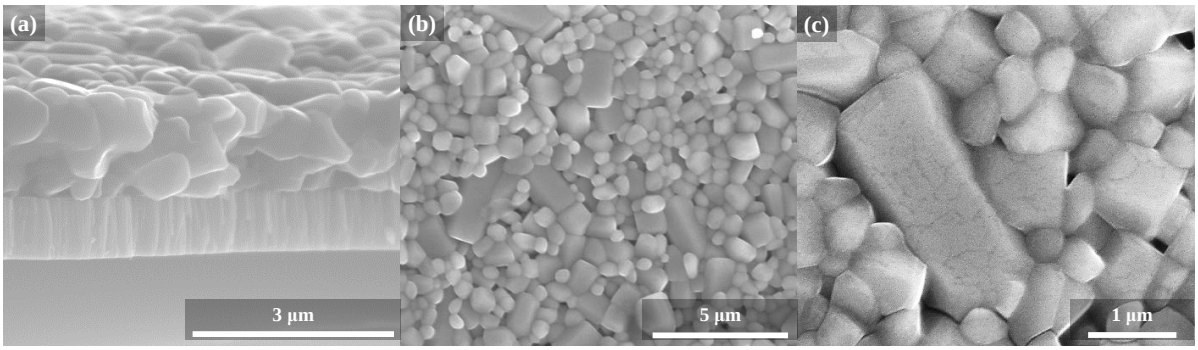

Figure 3.13. SEM images of an enargite film formed from a CuS film.

Time-resolved PL measurements on films from CuS can be fit by a single exponential with a decay constant of 0.61 ns, reported in Figure 3.14. This minority carrier lifetime is low compared to commercial thin film solar cells, but it is unclear if this lifetime corresponds to bulk or surface-limited radiative recombination. We note that this lifetime is similar to the 0.42 ns carrier lifetime reported for presumed surface-limited recombination for films formed from nanoparticle precursor (McClary et al., 2019). Photoluminescence measurements on these enargite films demonstrate a material with approximately a 1.43 eV band gap, shown in Figure 3.15. Photoemission shoulders are observed slightly above and below the band gap. Subtle mid-gap emissions are observed at approximately 0.4 – 0.5 eV from the band edge, possibly indicating the presence of deep level trap states, but these emissions are relatively low intensity compared to the band-to-band emission. Comparative analysis of large, faceted particles reveals largely the same behavior but a relatively more pronounced contribution of the shallow defect to the photoemission compared to band-to-band recombination. Future efforts can investigate the source of this phenomenon.

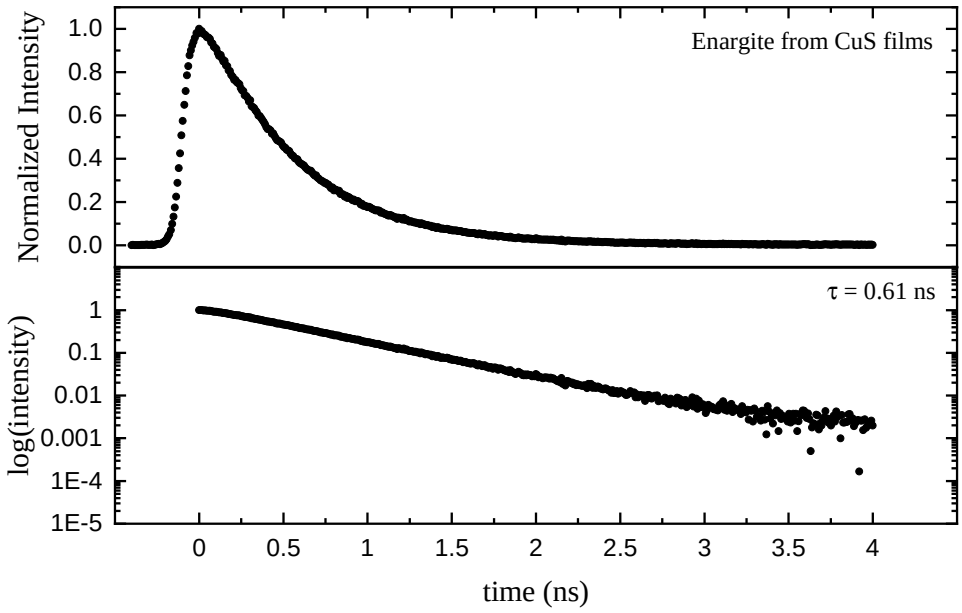

Figure 3.14. TRPL data collected on an enargite film fabricated from CuS films. The decay was fit with a single exponential.

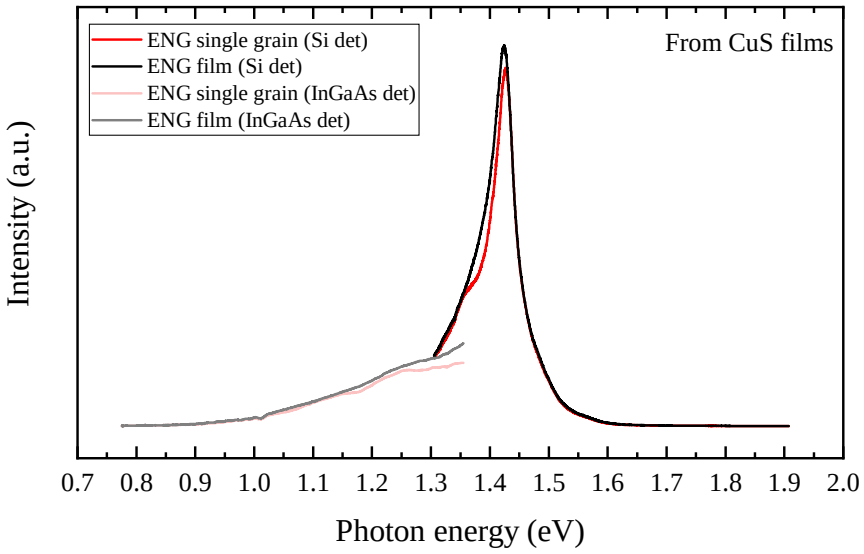

Figure 3.15. Photoluminescence of enargite films excited by a 632 nm He:Ne laser. Two detectors were used during subsequent scans.

3.3.5 Cu_3AsS_4 enargite film characteristics fabricated from Cu_2S films

XRD and Raman analyses for enargite films fabricated from Cu_2S films are presented in Figures 3.16 (a) and (b), respectively, and display strong similarities to the films produced from CuS films. Orientation along the {210} planes is preferred and a low relative intensity of the {002} planes is observed. PL data in Figure 3.17 demonstrates the same 1.43 eV band gap as enargite films synthesized from CuS. Large, faceted grains demonstrate similar photoemission to the rest of the film, but have a relatively less pronounced contribution of the shallow defect to the photoemission, contrary to films synthesized from CuS. This result may be due to the larger contribution to the luminescence of shallow defects. The peak observed around 1.3 eV is attributed to a detector artifact, but photoemission in this energy range is still observed.

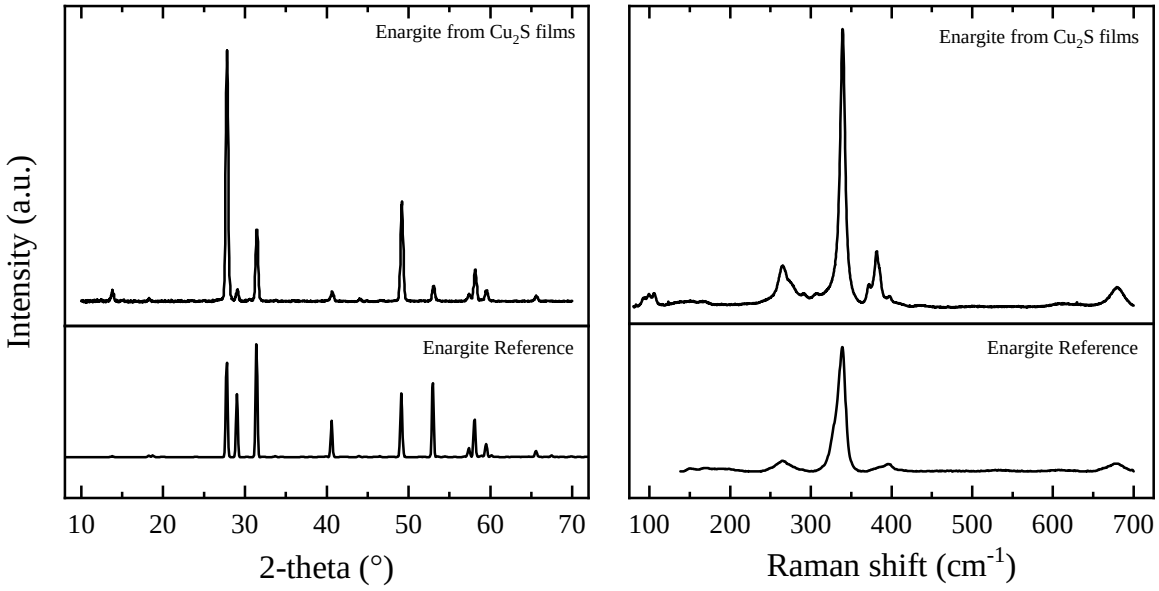

Figure 3.16. (a) XRD and (b) Raman analyses of Cu_3AsS_4 formed from treating Cu_2S films. The XRD reference spectrum for Cu_3AsS_4 is ICSD 14285 and the Raman reference spectrum is RRUFF ID R070176.

TRPL data on these films can also be fit by a single exponential, but have a decay constant of 0.51 nanoseconds, which is shown in in Figure 3.18. This minority carrier lifetime is shorter

than the lifetime extracted for enargite films formed from CuS. If the relatively short lifetimes for these enargite films are due to surface-limiting effects, a passivation of the surfaces should improve carrier lifetime. Passivation is usually completed through adding a small amount of dopant that preferentially accumulates at the grain boundaries and donates an electron to fill the defect state, which is typically an alkali metal. If these short lifetimes are due to bulk recombination, these lifetimes are expected to increase with the formation of a p-n junction due to increased separation of the electron-hole pairs in the depletion region. Wavelength-dependent TRPL can be used to investigate the lifetime as a function of photon penetration depth, which can give a better indication as to the nature of this decay lifetime. This measurement is left for future studies.

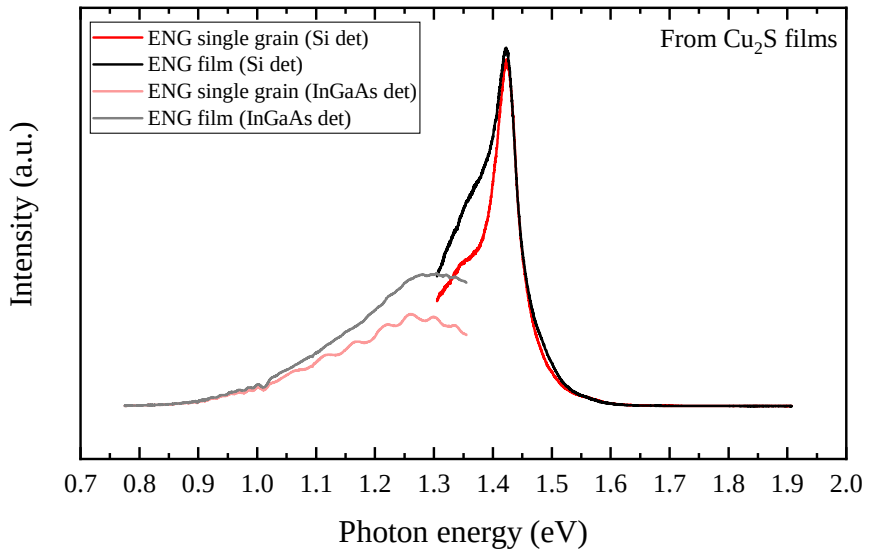

Figure 3.17. Photoluminescence of enargite films excited by a 632 nm He:Ne laser. Two detectors were used during subsequent scans.

To investigate the microstructural evolution of the film during the formation of enargite, short time studies were performed and are presented in Figures 3.19 (a) – (h). Nucleation of small, rounded grains were observed at the shortest time interval. Notably, these grains are observed to be of similar size to the small CuS grains observed in Section 3.3.2., which may indicate that nucleation of CuS grains from the volatilized sulfur flakes is the initial event. The grain size

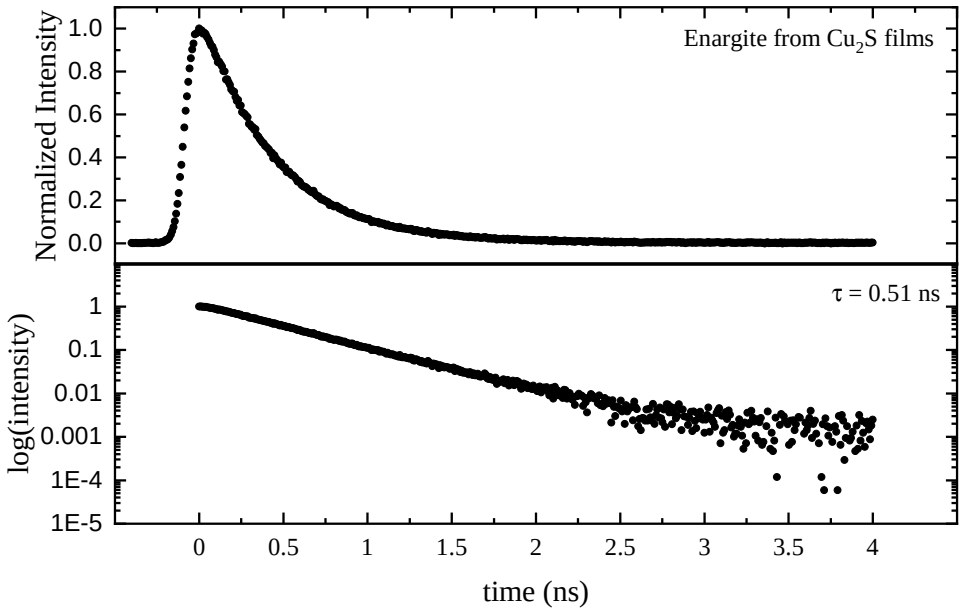

Figure 3.18. TRPL data collected on an enargite film fabricated from Cu_2S films. The decay was fit with a single exponential

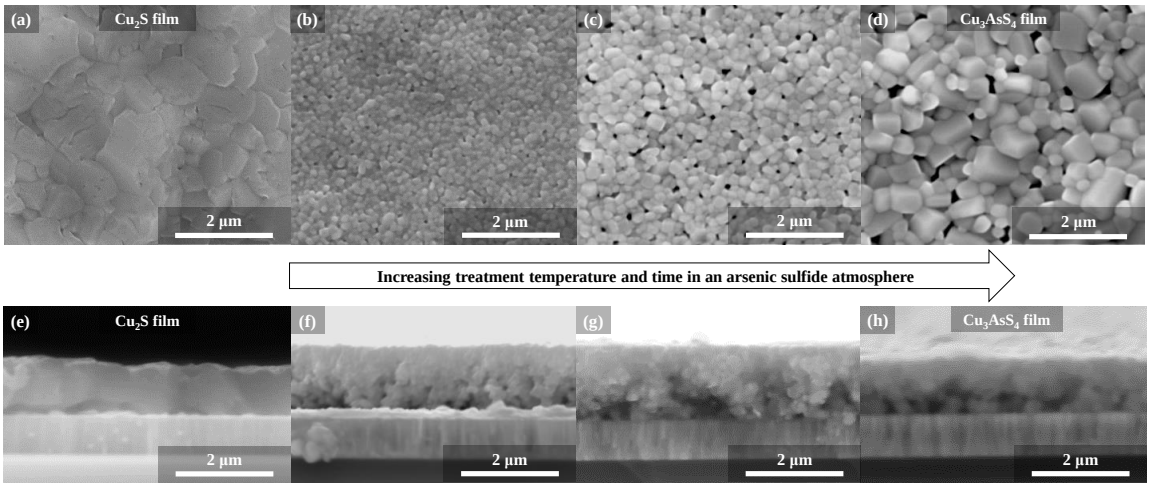

Figure 3.19. SEM images of Cu_3AsS_4 enargite films formed from Cu_2S precursor films. (a) and (e) are SEM images of a Cu_2S film formed from a 500 nm copper film. The images (b) - (d) and (f) - (h) are films from 300 nm copper films. The image for (h) was taken on the edge of the film, which explains the slightly thinner resulting film.

is observed to increase while the particles become more faceted, demonstrating faceted particles form early during the development of these thin films. These observations are consistent with the observations in the previous section which suggested the faceted particles may be the product of sintered smaller particles. Regarding side-view SEM, voids are observed to develop near the back contact at earliest stages of the film formation process. We speculate this mass transport is the result of a diffusion gradient established by excess condensed sulfur on the surface of the film, which nucleates CuS particles and locally depletes the available copper.

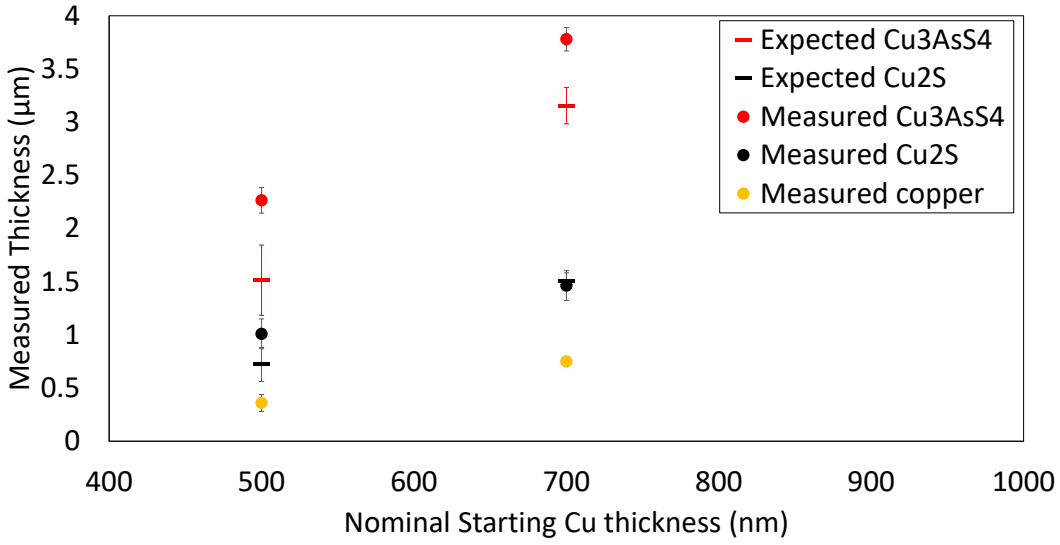

Figure 3.20. Copper, Cu_2S, and Cu_3AsS_4 thickness measurements from side-view SEM. These films were formed from the same sample throughout the process for both the 500 and 700 nm films.

The film packing density is helpful to know when optimally designing solar absorbers so that parameters such as thickness can be tuned to optimize characteristics such as photon absorption. To estimate the packing density of the copper sulfide and enargite films, side view SEM measurements were made after depositing copper, forming copper sulfide, and forming an enargite film. Based on initial copper measurements, the expected thickness of copper sulfide and enargite

were calculated assuming a 100% dense structure. The packing density was then calculated by dividing the expected value by the measured value. The study results are illustrated in Figure 3.20, where the error bars represent the variability from at least six total measurements taken from at least three different areas of the film. Copper sulfide packing densities determined for Samples A and B were 0.7 ± 0.3 and 1.0 ± 0.10, respectively. Sample A corresponds to the film with a nominal starting copper thickness of 500 nm, and Sample B corresponds to the film with a nominal starting copper thickness of 700 nm. Subsequent enargite packing densities were calculated to be 0.7 ± 0.2 and 0.83 ± 0.06, respectively. Sample B suggests the packing density of the enargite film is less than the copper sulfide film it was formed from, but these results are inconclusive for sample A. These data will inform the calculations concerning the optimal thickness of enargite films formed in this manner when approximate diffusion length is determined.

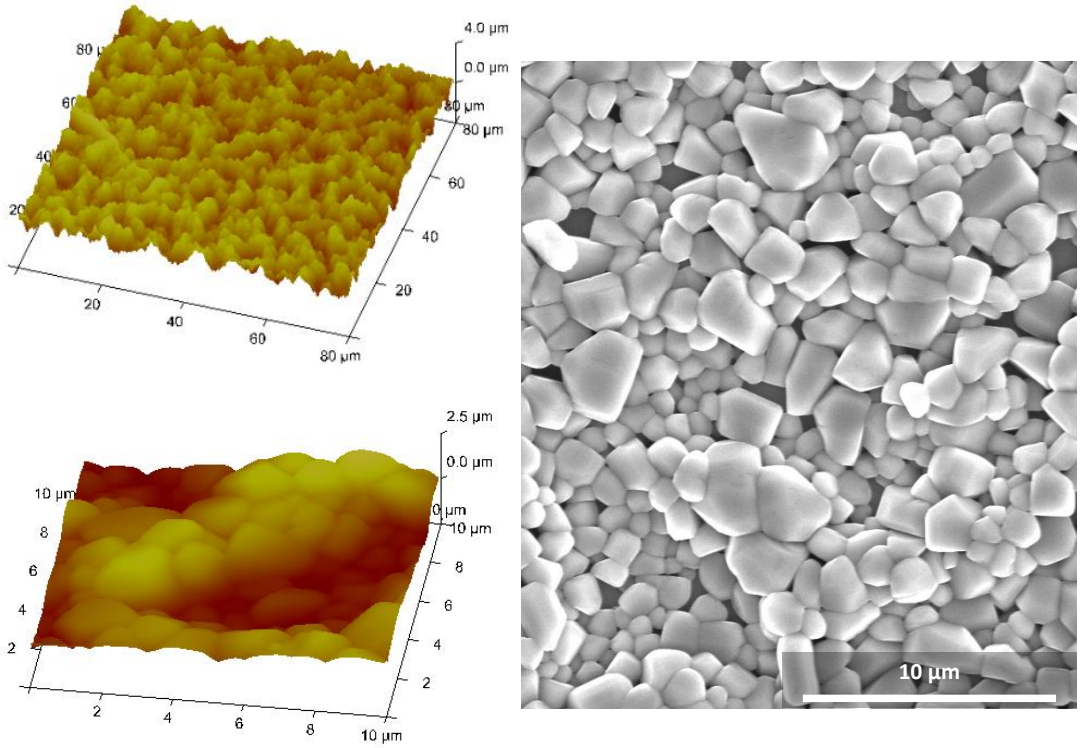

Figure 3.21. AFM scans and plan-view SEM images depicting transgranular mounds that contribute to the surface roughness of many enargite thin films.

Surface roughness of the substrates was investigated with AFM using rms as the roughness quantification. Topology maps are provided for enargite films in Figure 3.21. The scan area for Cu_2S films is 2500 μm^2 and the scan area for enargite is 6400 μm^2. Cu_2S films are calculated to have a roughness of 82 nm and enargite films are calculated to have a roughness of 524 nm. The increase in surface roughness due to the formation of transgranular mounds, which are also observed in enargite films with SEM. Reinspection of Figures 3.19 (a) – (d) confirms that these films also demonstrate signs of transgranular mounds. These mounds may originate from two different phenomena. It is possible these features are remnants of preexisting Cu_2S mounds, but if enargite grains are modeled to form from Cu_2S in a closed system the calculated roughness is less than that observed. Therefore, in this scenario it is implied that mass from thin regions must diffuse to thicker regions. Given the presumed high diffusivity implied from Figures 3.19 (f) – (g), this requirement will likely not present an obstacle.

Alternatively, these preexisting mounds may not influence the resulting enargite mounds. In this case, the roughness could be a consequence of the locally available arsenic sulfide melt, which grows grains preferentially where arsenic is present. In this case the mounds are remnants of regions rich in arsenic and sulfur. The origin of these mounds, and enargite surface roughness, may likely be a combination of the two proposed scenarios.

3.4 Conclusions and future directions

In this chapter, we first noted the emergence of a secondary phase in CuS thin films fabricated from evaporated copper substrates and sulfur flakes. The formation of this secondary phase was previously identified to be facilitated by the incorporation of carbon ligands into a nanoparticle film, but here we observe this phase in the absence of carbon. This phase is not observed in Cu_2S films fabricated from evaporated copper substrates in H_2S gas. The formation of Cu_3AsS_4 enargite films eliminate this phase from the Raman spectra from both precursor films. All enargite films were observed to be oriented along the $\{210\}$ planes with very little stability of the sulfur-rich $\{002\}$ planes. These films demonstrate a band gap of 1.43 eV at room temperature and both shallow and deep defects were observed but with relatively low photoemission.

Bimorphological films of large, faceted particles and smaller, partly sintered particles. Plan-view SEM images provide evidence that these faceted enargite grains were likely from the densification of smaller particles. These small particles were observed to form at early stages during the film formation process, concurrent with an increasing average grain size and transgranular mound formation. The source of these mounds is unknown but can possibly originate from precursor film roughness or from nonuniform condensation of the arsenic sulfide atmosphere. Due to similarities morphologically, in XRD, Raman, and PL analyses, and the observation that Cu_2S films likely form small CuS grains, the rest of this thesis does not distinguish between films made through either method. However, we note that defect characteristics between the films may be slightly different so analyses concerning these features should consider precursor films.

3.5 Acknowledgements

J.A. would like to acknowledge financial support from the NSF under grant #1144843 (Purdue-Tuskegee IGERT on globally sustainable electronics) and laboratory support from the NSF under grant #1534691-DMR (DMREF: Rapid Design of Earth Abundant Inorganic Materials for Future PVs). He thanks Dr. Scott McClary for XRD and Raman training and assistance as well as informative discussions during the development of this chapter, Kei Yazawa for assistance and training on AFM, Dr. Chris Gilpin and Jameson Root for assistance and training with scanning electron microscopy, Dr. Brian Graeser, Dr. Xianyi Hu, Essam Alruqoba, and Jonathan Turnley for training and assistance with providing molybdenum-coated soda-lime glass, David Rokke for assistance and training with PL, Kyle Weideman for assistance and training on the thermal evaporator, and Ryan Ellis, Swapnil Deshmukh, Essam Alruqoba, Apurva Pradhan, and Jonathan Turnley, for their assistance with E-beam depositions.

3.6 References

Arrouvel, C. and Eon, J.-g. (2019). Understanding the Surfaces and Crystal Growth of Pyrite FeS2. *Materials Research*, 22(1):1–9.

Das, S. R., Vankar, V. D., Nath, P., and Chopra, K. L. (1978). The preparation of Cu2S films for solar cells. *Thin Solid Films*, 51:257–264.

Ewen, P. J. S. (1978). *THE RAMAN SPECTRA AND STRUCTURE OF GLASSES IN THE ARSENIC-SULPHUR AND ARSENIC-SELENIUM SYSTEMS BY Thesis presented for the degree of Doctor of Philosophy of the University of Edinburgh October 1978*. Ph.d., Edinburgh.

Grozdanov, I. and Najdoski, M. (1995). Optical and electrical properties of copper sulfide films of variable composition.

Hidnert, P. (1924). Thermal expansion of molybdenum. *Scientific Papers of the Bureau of Standards*, 19:429–444.

McClary, S. A. (2019). *SYNTHESIS AND CHARACTERIZATION OF COPPER ARSENIC SULFIDE FOR SOLUTION-PROCESSED PHOTOVOLTAICS*. PhD thesis, Purdue University.

McClary, S. A., Andler, J., Handwerker, C. A., and Agrawal, R. (2017). Solution-processed copper arsenic sulfide thin films for photovoltaic applications. *Journal of Materials Chemistry C*, 5(28):6913–6916.

McClary, S. A., Li, S., Yin, X., Dippo, P., Kuciauskas, D., Yan, Y., Baxter, J. B., and Agrawal, R. (2019). Optoelectronic Characterization of Emerging Solar Absorber Cu3AsS4. In *IEEE Photovoltaics Specialists Conference Proceedings*, pages 3–7.

Minceva-Sukarova, B., Najdoski, M., Grozdanov, I., and Chunnilall, C. J. (1997). Raman spectra of thin solid films of some metal sulfides. *Journal of Molecular Structure*, 410-411(96):267–270.

Nemade, K. R. and Waghuley, S. A. (2015). Band gap engineering of CuS nanoparticles for artificial photosynthesis. *Materials Science in Semiconductor Processing*, 39:781–785.

Pathan, H. M., Desai, J. D., and Lokhande, C. D. (2002). Modified chemical deposition and physico-chemical properties of copper sulphide (Cu 2 S) thin films. *Applied Surface Science*, 202(1-2):47–56.

Quintana-ramirez, P. V., Arenas-arrocena, M. C., Santos-cruz, J., Vega-gonzález, M., Martínez-alvarez, O., Castaño-meneses, V. M., Acosta-torres, L. S., and Fuente-hernández, J. D. (2014). Growth evolution and phase transition from chalcocite to digenite in nanocrystalline copper sulfide : Morphological , optical and electrical properties. *Bilstein Journal of Nanotechnology*, 5:1542–1552.

Santos Cruz, J., Mayén Hernández, S. A., Paraguay Delgado, F., Zelaya Angel, O., Castanedo Pérez, R., and Torres Delgado, G. (2013). Optical and electrical properties of thin films of CuS nanodisks ensembles annealed in a vacuum and their photocatalytic activity. *International Journal of Photoenergy*.

Scholze, H. (1991). Properties of Glass. In *Glass*, pages 156–364. Springer, New York, NY.

Scott, D. W., McCullough, J. P., and Kruse, F. H. (1961). Vibrational assignment and force constants of S8 from a normal-coordinate treatment. *Journal of Molecular Spectroscopy*, 6(C):372–378.

Selivanov, E. N., Gulyaeva, R. I., and Vershinin, A. D. (2007). Thermal Expansion and Phase Transformations of Copper Sulfides. *Inorganic Materials*, 43(6):653–658.

Ward, A. T. (1968). Raman spectroscopy of sulfur, sulfur-selenium, and sulfur-arsenic mixtures. *Journal of Physical Chemistry*, 72(12):4133–4139.

CHAPTER 4. INSIGHTS INTO THE OPTIMIZATION OF Cu_3AsS_4 FILM PROCESSING

4.1 Introduction

The previous chapter introduced a novel synthesis method for the fabrication of thin enargite films suitable for photovoltaic applications. However, no optimization was performed regarding the quantity of arsenic or sulfur used for its fabrication. Optimization of film quality regarding morphology, orientation, and density is expected to improved optoelectronics properties such as short circuit current and open circuit voltage which will consequently enhance device performance. Previous work has demonstrated an arsenic sulfide binary is necessary to facilitate the development of contiguous thin films, but does not discuss the implications of utilizing combinations of arsenic and sulfur elements and binaries (McClary et al., 2017).

Evidence is presented in this chapter testing the hypothesis that altering the elemental composition of the added powder will systematically change the morphology and orientation of the resulting films. Optimization of these films though this method will enable testing of the hypothesis that the secondary phase and/or the porosity of the film were limitations to high device performance in the previous report (McClary et al., 2017). Subsequently, this chapter investigates a solution etching procedure to clean the surface of enargite thin films before the deposition of an n-type layer. Optoelectronic characterization of these films is completed to demonstrate the viability of these films for photovoltaic applications.

4.2 Experimental Methods

4.2.1 Materials

The chemicals and materials used to complete the investigations in this chapter are listed in Table 4.1.

Table 4.1. *List of products used in this chapter*

Chemicals / equipment	**Purity / type**	**Source**	**Quantity***
Aluminum pellets	>99.999%	Kurt J. Lesker	≈ 3.5 mg / 2 μm Al**
Ammonium hydroxide	30%	Sigma-aldrich	≈ 30 mL / CdS deposition
ampule (10 mL)	Borosilicate glass	Chemglass Life Sciences	≈ 13 g / treatment
Arsenic (III) sulfide	>99.9%	Strem Chemicals	≈ 17 mg / treatment
Arsenic (V) sulfide	>99.99%	Sigma-Aldrich	≈ 20 mg / treatment
Cadmium sulfate hydrate	>99.996%	Alfa Aesar	≈ 85 mg / CdS deposition
Copper pellet	>99.99%	Kurt J Lesker	≈ 2 mg / 300 nm**
Diammonium sulfide	40-48 wt. %	Sigma-Aldrich	≈ 4 mL / 1" x 1/4" film
Indium oxide (ITO) target	>99.99%	Kurt J Lesker	≈ 1 mg / 220 nm**
Hydrogen sulfide (H_2S) gas	1% and 3% bal. Ar	Airgas	Tanks used indefinitely
Molybdenum target	>99.95%	Kurt J. Lesker	≈ 85 mg deposited***
Nickel pellets	>99.999%	Kurt J. Lesker	≈ 0.6 mg / 100 nm Ni**
Sulfur flakes	99.99%	Sigma-Aldrich	≈ 8 mg / treatment
Thiourea	>99% ACS	Sigma-Aldrich	≈ 1.3 g / CdS deposition
Ultrapure water	18.2 MΩ-cm	Direct-Q3 UV (in-house)	≈ 150 mL / CdS deposition
Zinc oxide target	>99.9%	Kurt J Lesker	≈ 0.3 mg / 80 nm**

**Hexane, IPA, water, soap, and nitric acid used for glassware cleaning between each synthesis is not included*
***Assumed deposition area is a 1"x1" substrate. Waste material not included.*
****Deposition area is one 4"x4" substrate per deposition. Over the life of the target (about 8 depositions), the total target utilization for this lab scale deposition process is approximately 5%, measured empirically. Most molybdenum (≈ 90%, empirically deduced) is sputtered onto chamber walls resulting in a total material utilization of approximately 0.5%.*

4.2.2 Substrate film deposition and fabrication

Soda-lime glass (SLG) substrates were cleaned with isopropanol, ethanol, sonication with a Liquinox-based solvent followed by ultrapure water, and then ozone cleaned before being placed as the substrate into a DC magnetron sputter system. Approximately 800 nm of molybdenum was sputtered onto the substrate to serve as the back contact. The deposition rate and thickness were monitored using a quartz crystal microbalance, and the resulting films were measured to be within 15% accurate and demonstrated a relative standard deviation of approximately 5% regarding thickness uniformity (N = 11 spots, 1 measurement per spot over a 2" x 1" substrate). To deposit copper films, these Mo-SLG substrates were cut into 1" x 1/4" areas and adhered to a target holder approximately 30 cm from the copper evaporation source in a thermal evaporator system. The base pressure and operating conditions for all samples was less than or equal to 1E-3 Pa (1E-5 mbar). Thermal depositions were completed with a copper pellet placed on a tungsten boat and resistively heated to its melting point. The deposition rate and thickness of these films were controlled using a quartz crystal microbalance. Deposited thicknesses were verified with side-view SEM when appropriate, and typically demonstrated $\pm$30% and $\pm$10% accuracy with a relative standard deviation of approximately 20% and 5% regarding thickness when depositing with new and old pure copper pellets, respectively (N = 3 spots, 2-3 measurements per spot over a 2" x 1" substrate for new pellets and N = 11 spots, 1 measurement per spot over a 2" x 1" substrate for old pellets). We speculate the increased non-uniformity when using new pellets is due to the inconsistent melting behavior observed. This behavior is most likely due to spatially nonuniform heating between regions of copper in physical contact with the tungsten boat and regions not in contact with the boat. The thermal evaporator is housed in a dry environment (water and oxygen were continuously monitored to be less than approximately 5 ppm), so resulting copper films (Cu-Mo-SLG) are stored in this environment until used.

4.2.3 Fabrication of Cu_xS thin films

Copper sulfide films are made following the treatment conditions described in Chapter 3.

4.2.4 Ampule preparation

The ampule preparation is similar to that described in Section 3.2.3. Sulfur flakes and arsenic sulfide powders are loaded into an ampule in a nitrogen ambient. Two copper sulfide films, one for characterization and one for device or other purposes, are subsequently loaded into the ampule. The substrate sample size used in all ampule treatments mentioned in this chapter is 1/4" x 1" unless otherwise noted. After purging three times with argon, a butane torch is used to yield the glass at the neck under a vacuum of at least 0.2 torr until an airtight seal is formed.

4.2.5 Heat treatments

Treatments of copper, CuS, and Cu_2S films sealed in an ampule were performed in a three-zone tube furnace, which is further described in Section 3.2.4. The ampule is pushed into the center of the furnace after it equilibrates and cools naturally after turning off and opening the furnace. Some samples used a fan to more rapidly cool, and this technique is described more in Section 2.2.5.2. Condensed vapors were observed on the inside of ampule upon cooling, and analysis of these condensed vapors did not reveal copper species. Although these observations suggest copper remained in the film, not all ampules were tested post-treatment.

We note the devices made in this chapter did not originate from synthesized copper sulfide films, but rather sealed Cu-Mo-SLG films together with arsenic sulfide powder and sulfur flakes. Non-uniformity due to the sealing process was minimized by using one large grain of arsenic sulfide ($\approx$ 29 mg) instead of a powder. These grains were formed from natural processes after sitting in dry conditions for more than one year.

4.2.6 Device fabrication

Enargite films were retrieved by scribing around the neck of the ampule and mechanically fracturing the glass along the scribe. Devices were formed by depositing approximately 50 nm CdS via chemical bath deposition, approximately 80 nm of slightly n-type ZnO through RF sputtering

with an ambient oxygen content of 2% in argon, approximately 220 nm ITO through RF sputtering in an argon ambient, and patterned Ni/Al grids evaporated from an electron beam. Cells were electrically isolated by mechanical scribing and had an area of approximately 0.1 cm^2.

4.2.7 Characterization details

A FEI quanta 3D dual-beam field emission scanning electron microscope (SEM) was used to capture film morphology. Energy-dispersive X-ray spectroscopy (EDS) was collected with an accelerating voltage of 5 kV on the same SEM with a silicon drift detector. Elemental compositions were determined through AZtec software using standardless quantitative analysis. X-ray diffraction (XRD) data were collected on a Rigaku SmartLab diffractometer using a copper Kα X-ray source in parallel beam mode with a grazing incidence angle of 0.5°. Temperature dependent photoluminescence (TDPL) and Raman spectroscopy (TDRS) measurements were performed using a Horiba/Jobin-Yvon LabRAM HR800 confocal microscope system with a 633 nm He:Ne laser with a nominal power of 17 mW (about 8.5 mW exposed to the sample). The system setup for TDPL used a diffraction grating of 300 grooves/mm and both silicon and InGaAs detectors depending on the wavelengths assessed. The system setup for TDRS used a diffraction grating of 1800 grooves/mm and a silicon detector. Current-voltage (J-V) measurements were acquired with an Oriel Sol3A solar simulator with the AM1.5G spectrum calibrated to 100 mW/cm^2 using a certified silicon reference cell. External quantum efficiency (EQE) measurements were performed at 160 Hz and zero bias using a lock-in amplifier and preamplifier for signal processing.

4.2.8 Band alignment modeling

Adept 2.1 was used to model the band alignments in this study (Gray et al., 2011). The parameter values used to model the CdS-As_2S_3 and As_2S_3-Cu_3AsS_4 interfaces are tabulated in Table 4.2. The front layer (Layer 1 in Adept) is modeled with CdS and the backmost layer is modeled with Cu_3AsS_4.

Table 4.2. *List of values and sources used for modeling the band structure with ADEPT 2.1.*

Parameter	**Value (CdS)**	**Source**	**Value (As_2S_3)**	**Source**	**Value (Cu_3AsS_4)**	**Source**
Layer thickness (μm)	0.05	SEM	0.05	assumption	1	SEM
Doping type	n-type	assumption	p-type	assumption	p-type	Hot probe
Dopant dens. (cm^{-3})	1E18	(Chirilă et al., 2011)	1E12	assumption	8E15	(McClary, 2019)
Band gap (eV)	2.4	(Chirilă et al., 2011)	2.35	(Tsiulyanu, 2004)	1.43	PL
Electron affinity (eV)	4.45	(Chirilă et al., 2011)	3.5	(Tsiulyanu, 2004)	3.61	(McClary, 2019)
Dielectric Constant	10	(Chirilă et al., 2011)	6.3	(Tsiulyanu, 2004)	5.83	(Wallace et al., 2017)
CB eff. DOS (cm^{-3})	1E18	(Chirilă et al., 2011)	1E18	assumption	1E18	(McClary, 2019)
VB eff. DOS (cm^{-3})	1E19	(Chirilă et al., 2011)	1E19	assumption	1E19	(McClary, 2019)
Electron mobility ($cm^2\ V^{-1}\ s^{-1}$)	100	(Chirilă et al., 2011)	1	(Madelung, 2004)	7	(McClary, 2019)
Hole mobility ($cm^2\ V^{-1}\ s^{-1}$)	25	(Chirilă et al., 2011)	10E-5	(Tsiulyanu, 2004)	1.5	(McClary, 2019)
SRH electron lifetime (ns)	160	(Madelung, 2004)	1	assumption	1.8	TRPL and assumption
SRH hole lifetime (ns)	15	(Madelung, 2004)	0.01	assumption	18	assumption
Auger electron recomb. coef ($cm^6\ s^{-1}$)	0	assumption	0	assumption	0	assumption
Auger hole recomb. coef ($cm^6\ s^{-1}$)	0	assumption	0	assumption	0	assumption
Radiative recomb. coef ($cm^3\ s^{-1}$)	0	assumption	0	assumption	0	assumption
Acceptor energy (eV)	0	assumption	0	assumption	0	assumption
Donor energy (eV)	0	assumption	0	assumption	0	assumption

4.3 Results and discussion

4.3.1 Influence of treatment atmosphere on film characteristics

For thin films suitable for photovoltaic applications, densification parallel to the substrate is preferred to increase photon absorption and decrease the likelihood of forming electrical shunt pathways. If a small number of nuclei are formed but they can grow in the direction perpendicular to the substrate, then their growth will result in a film comprised of large grains in loose contact, if contacting at all. In this case, the mass transport away from the substrate surface will decrease the densification along the substrate axis and result in electrical shunting when subsequent layers are deposited. As demonstrated in chapter 3 the number of faceted grains and morphology of the film may be dictated at early stages of film development. As such, the ambient conditions will be expected to influence the final film characteristics. Compared to arsenic (V) sulfide, similar moles of arsenic and sulfur using sulfur flakes and arsenic (III) sulfide powder can be used. This scenario has the conceptual advantage of volatilizing more sulfur during early film development since it is no longer in physical contact with the arsenic sulfide powder. This additional volatilized sulfur will be able to nucleate small grains of copper sulfide which will increase the relative number of nuclei present in the film that can compete for arsenic when it begins to volatilize. The hypothesis is that a greater abundance of stable nuclei will limit the mass transport perpendicular to the substrate which will result in a relatively denser film along the substrate axis, assuming the arsenic incorporates uniformly across the film surface.

To test this hypothesis, precursor films consisting of luzonite nanoparticles and copper sulfide films were exposed to similar treatment conditions but with different precursor films and atmospheres. The SEM images in Figure 4.1 demonstrate that films formed a greater number of smaller grains when elemental sulfur is present in the ampule compared to when only binary arsenic sulfides are used. More faceted grains with a larger size are observed in the scenario where As_2S_3 and As_2S_5 powders are used. These films also demonstrate more porosity compared to the films synthesized with elemental sulfur. The films previously reported using only arsenic (V)

sulfide powder results in films resembling Figures 4.1 (c) and (d) (McClary et al., 2017). These results support the hypothesis that a greater number of small nuclei are formed with elemental sulfur, and that resulting films are qualitatively denser. Therefore, the films discussed in the following parts of this dissertation have been completed using arsenic (III) sulfide powder and sulfur flakes unless otherwise noted.

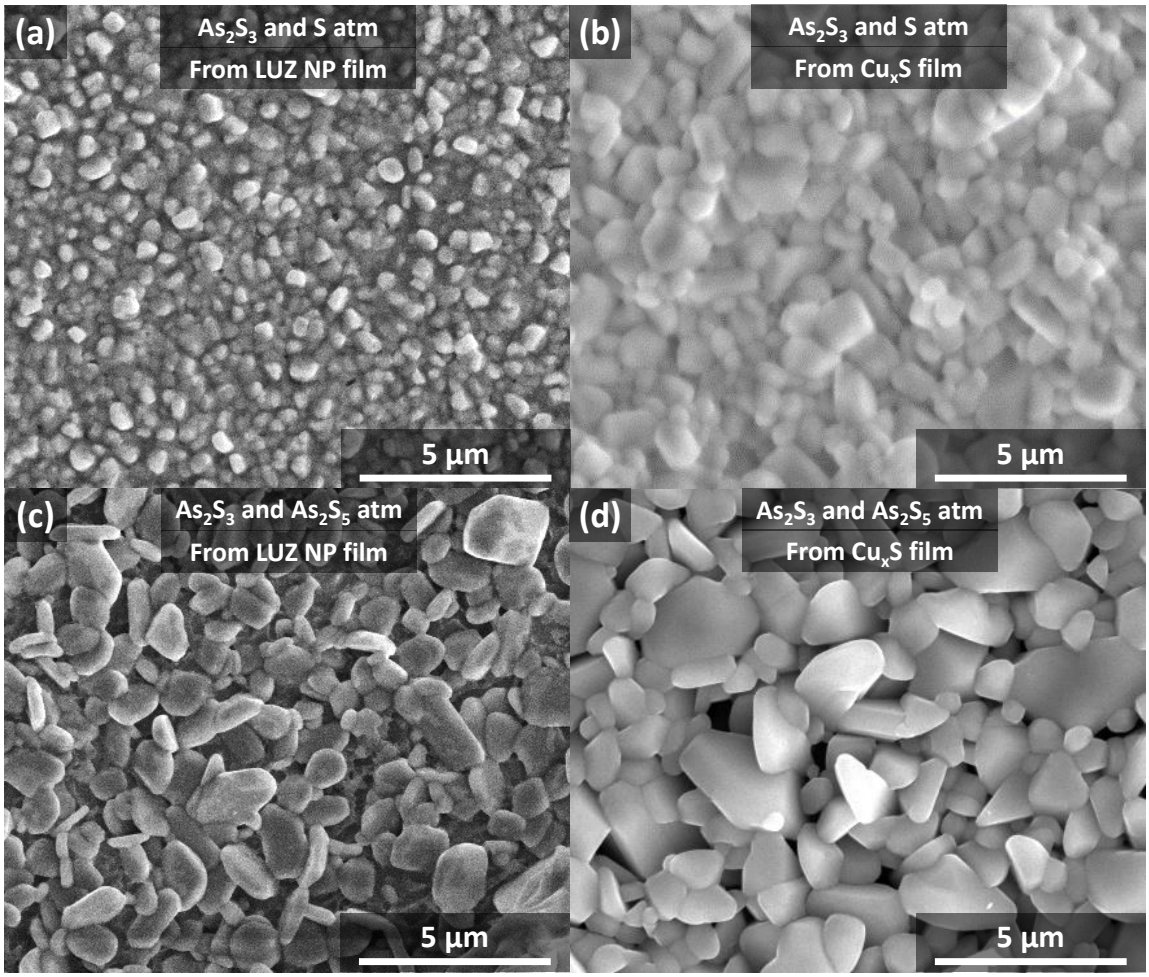

Figure 4.1. Plan-view SEM images of films from (a) (c) luzonite nanoparticles and (b) (d) copper sulfide treated in (a) (b) As_2S_3 powder and sulfur flakes and (c) (d) As_2S_3 and As_2S_5 powders.

The SEM images also demonstrate that films treated under similar conditions appear to result in similar morphologies, even when films begin with different compositions and structures.

This result suggests that enargite films formed from ampule treatments with arsenic sulfide binaries may undergo similar film formation mechanisms regardless of precursor film. Therefore, we hypothesize the formation of enargite films can be carried out on a variety of copper and copper sulfide films including electroplated copper, copper nanoparticles, copper sulfide nanoparticles, etc. Testing of this hypothesis has not yet been completed.

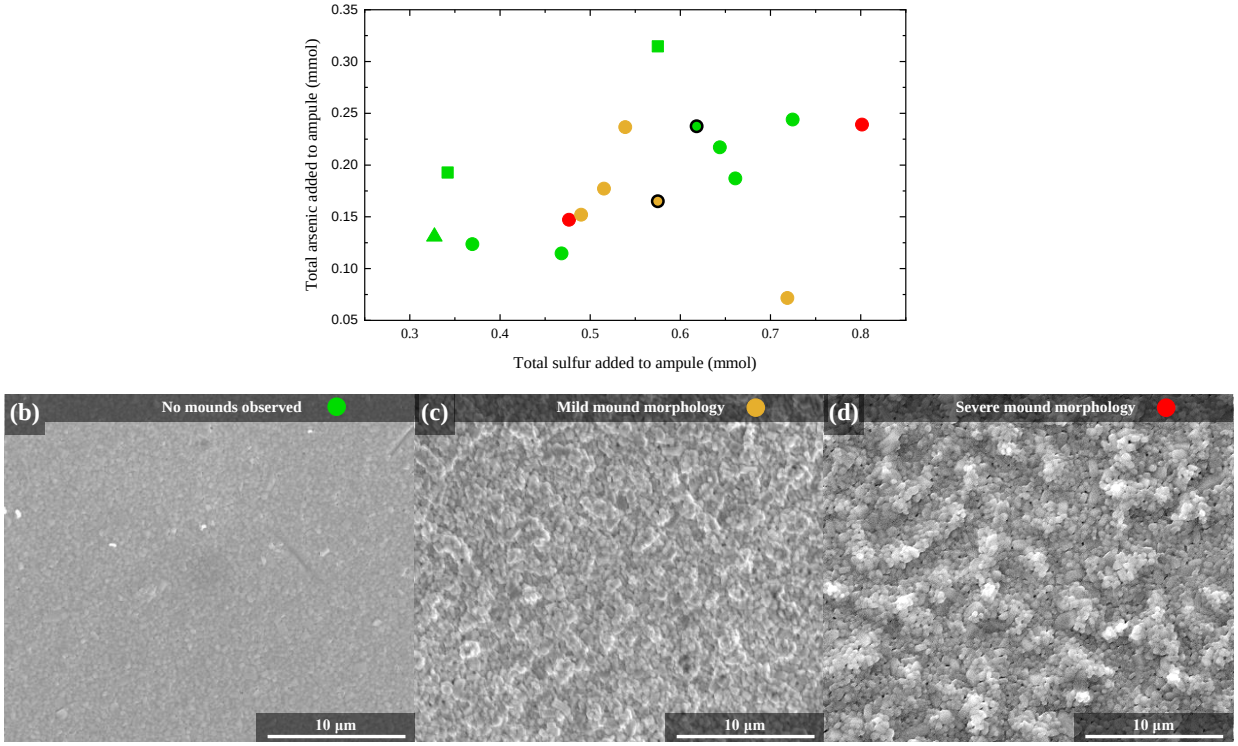

Figure 4.2. (a) qualitative plot identifying the relationship between moles of constituents and film morphology. (b) - (d) plan-view SEM images displaying the characteristics plotted in (a). Data represented with a black boundary represent champion devices fabricated during this dissertation.

To investigate a systematic densification of enargite films, multiple samples were exposed to the same treatment conditions except a different relative amount of arsenic sulfide powder (or grains) and sulfur flakes. The hypothesis under investigation is that the film morphology, porosity, and orientation will systematically depend on the relative amount of arsenic and sulfur used even if the source is the same. Analyses were performed by plotting the film characteristics as a

function of the moles of the constituents. Characteristics investigated were relative quantity of large, faceted grains, quality of surface topology regarding mound formation, and abundance of pores, and orientation. These data are plotted in Figures 4.2 (a), 4.3 (a), 4.4 (a), and 5 respectively. Squares, triangles, and circles represent films formed from As_2S_3 and As_2S_5 powders, As_2S_5 powder only, and As_2S_3 powder and S flakes, respectively. Circles with boundaries represent the two champion performing substrates regarding photoconversion efficiency. All films were synthesized by 425 °C, 30-minute treatment conditions on a Mo-SLG substrate from evaporated copper films. SEM images are displayed for each subjective category to give the reader a clear understanding of categorized characteristics.

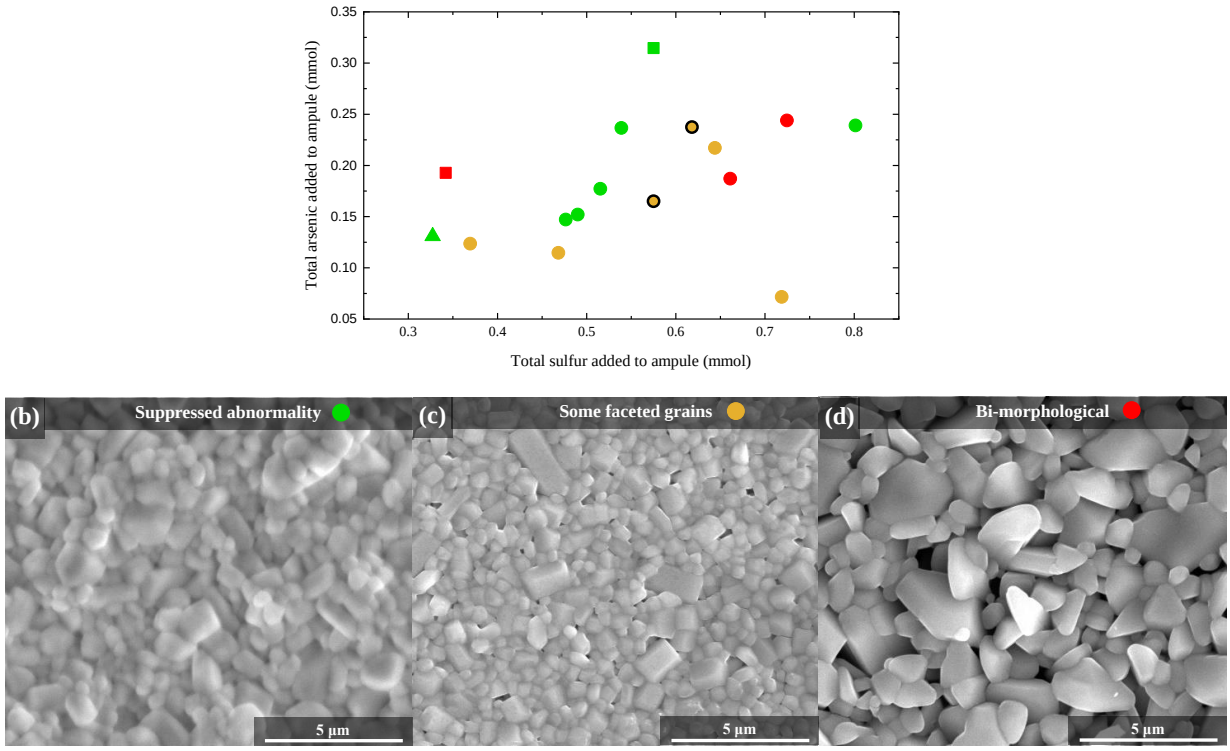

Figure 4.3. (a) qualitative plot identifying the relationship between moles of constituents and growth of faceted grains. (b) - (d) plan-view SEM images displaying the characteristics plotted in (a). Data represented with a black boundary represent champion devices fabricated during this dissertation.

We observe that for a system with arsenic sulfide powder and sulfur pellets, films that form single morphologies generally have an issue with developing mound-like topologies. Conversely,

films that form bimorphological films generally have fewer observable mounds. These data suggest these morphologies may originate from similar driving forces, and that the formation of large, faceted grains may help reduce the formation of mounds. However, the source of this behavior is left for future investigations. The formation of faceted grains and mounds do not appear to be correlated with the formation of pores. We note that an arsenic sulfide powder with sulfur flakes was observed to produce fewer observable pores compared with other arsenic sulfide systems, even when single morphologies and flat topology were present in the other system. Since films are designed to reduce the number of pores, free sulfur was used in most treatments during this study.

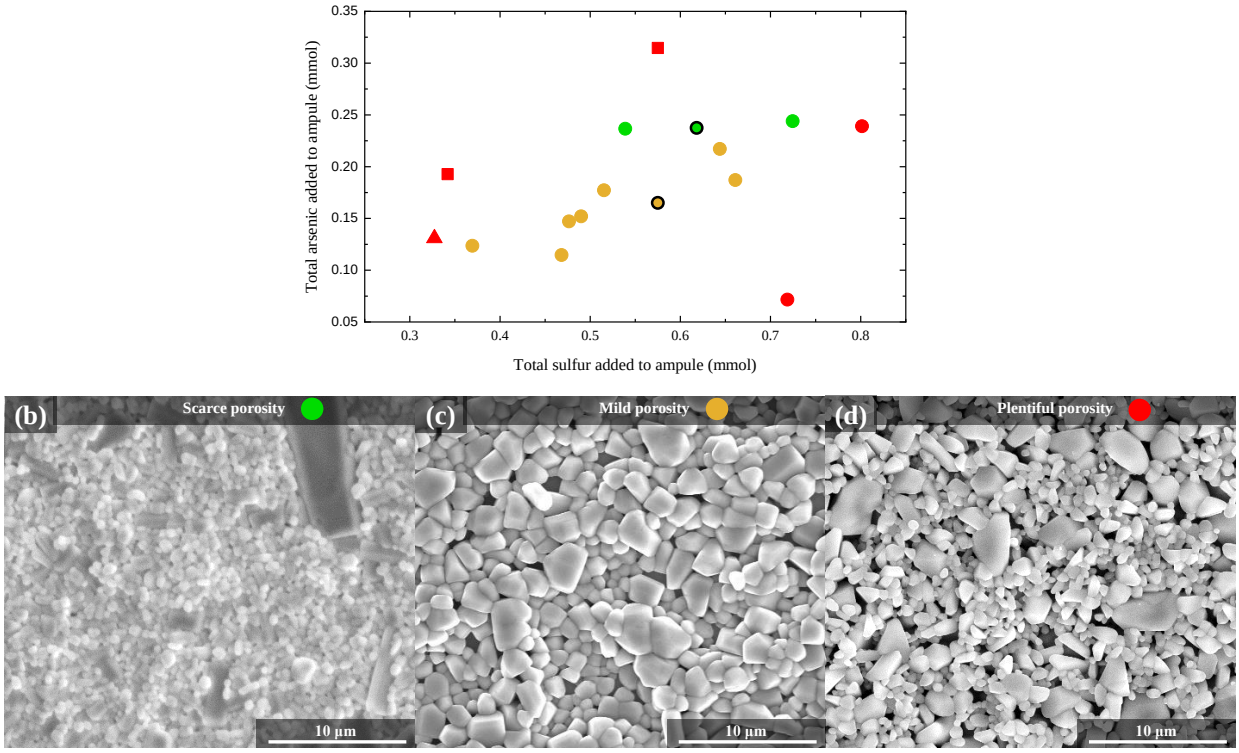

Figure 4.4. (a) qualitative plot identifying the relationship between moles of constituents and abundance of pores. (b) - (d) plan-view SEM images displaying the characteristics plotted in (a). Data represented with a black boundary represent champion devices fabricated during this dissertation.

Orientation of enargite thin films has been discussed in the context of the incorporation of sodium into the film (McClary, 2019). Here, film orientation is investigated as a function of ambient arsenic sulfide treatment conditions. The orientation of the film may be expected

to correlate with the number or size of observed faceted particles. Since no direct correlation was observed between number of faceted particles and treatment condition, we do not expect a correlation of orientation with treatment condition. However, the corresponding data in Figure A demonstrate a correlation of non-oriented growth (green) with an increasing arsenic to sulfur ratio. These data imply that enough free sulfur available during heating can increase the orientation of the films along the {210} planes. Future studies may look to introduce a treatment process entailing high relative arsenic content if non-oriented behavior is preferred. However, the champion device outlined in Figure 4.5 may suggest that an oriented film is preferable.

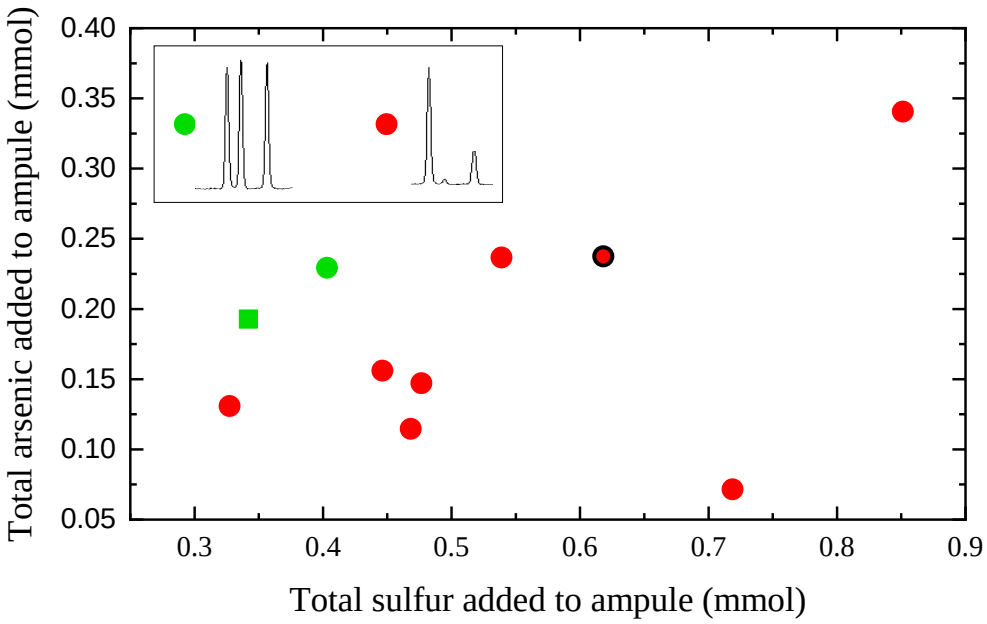

Figure 4.5. Qualitative plot identifying the relationship between moles of constituents and resulting film texture. The datum represented with a black boundary represents a champion device fabricated during this dissertation.

4.3.2 Cu_3AsS_4 enargite device characteristics without post deposition treatment

Enargite films made from copper films that demonstrated the least amount of porosity are able to provide a platform to test the hypothesis that either the secondary phase or the observable

porosity are a primary limitation to high performance Cu_3AsS_4-based photovoltaics. Evaporated copper films provide an avenue to create enargite films that are free from the secondary phase identified in Raman spectra. The addition of elemental sulfur into the ampule to provide an initial sulfur-rich environment to facilitate copper sulfide nucleation provides relative densification. Therefore, devices were made from the substitution of these processing steps and the characteristics of the devices are reported Table 4.3. Data for each cell are averaged results of two subsequent runs. These results represent a relatively low degree of variation compared to the cells that produced a photoefficiency in the first publication (McClary et al., 2017). The reduced variation from evaporated copper techniques may be attributable to the elimination of the IR-active secondary phase or a relative densification of the film. However, the efficiency of the devices is consistent with the previous report. Therefore, with the improvements in phase purity and film densification, these data demonstrate these factors were not the primary bottleneck for high efficiency devices.

4.3.3 Post deposition treatments

One hypothesis that could lead to the prevention of a robust p-n junction was mentioned in Chapter 2. Since the treatment is occurring in a closed environment with volatilized arsenic and sulfur, it is likely the atmosphere will partly condense on the surface of the substrate instead of all condensing on the top surface of the ampule which is being cooled fastest. In this case, an arsenic sulfide film may result on the surface of the film. If this film is deposited on the surface of enargite, it will likely prevent the formation of a robust p-n junction and will ultimately decrease the performance of the cell. To explore the potential impact of this film on device performance, a band diagram was constructed and is illustrated in Figure 4.6. This analysis demonstrates the arsenic sulfide film may have a small spike offset in the conduction band and a hole blocking feature in the valence band. These features are not themselves limiting, however, the high quantity of shallow recombination-inducing defects has been reported to limit carrier mobility in glassy As_2S_3 (Tsiulyanu, 2004) so avoiding the formation of this phase may be advantageous. From this perspective, thermal treatments and solution etching are investigated to remove the film.

Table 4.3. *Device characteristics of films fabricated with minimal porosity and without the previously identified IR-active secondary phase.*

Cell Number	**Voc (V)**	**Jsc (mA/cm^2)**	**Fill Factor (%)**	**Efficiency (%)**	**R$_{Sh}$ (Ω)**	**R$_S$(Ω)**
1	0.05	3.4	24.5	0.04	130	40
2	0.13	4.0	25.5	0.13	310	40
3	0.14	3.9	25.9	0.14	340	60
4	0.12	4.2	25.5	0.13	260	140
5	0.07	4.1	25.4	0.07	160	50
Average	0.10	3.9	25.4	0.10	240	70
Standard deviation	0.04	0.3	0.5	0.04	80	40

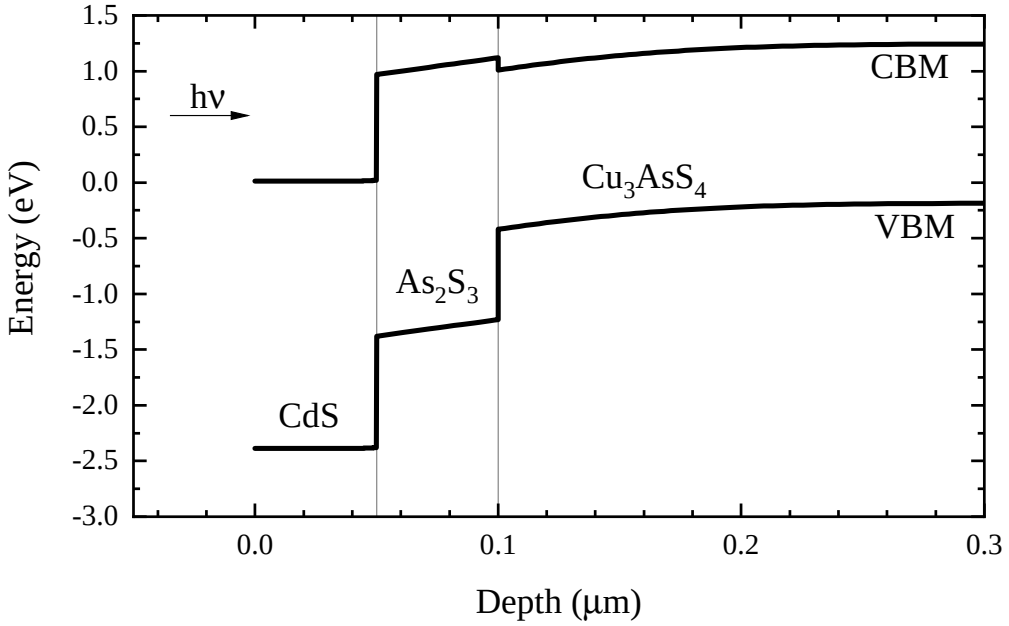

Figure 4.6. ADEPT 2.1 model of the CdS-As_2S_3-enargite band alignment using the parameters listed in Table 4.2. Relative energy values are aligned relative to the CdS CBM.

4.3.3.1 Thermal treatment

Post-deposition thermal treatments were previously investigated for enargite in the context of removing the IR active secondary phase, and concluded through thermogravimetric analysis that those enargite films began to lose mass at approximately 250 °C (McClary, 2019). Therefore, a post-deposition treatment was performed by heating a substrate in an inert atmosphere at 300 °C for 40 minutes. Using mechanical scribing and grain signature mapping, surface-sensitive EDS results were obtained from the two same spots before and after the treatment. These results are displayed in Figure 4.7. Compared to stoichiometric Cu_3AsS_4, these EDS results indicate the surfaces are slightly arsenic and sulfur rich both before and after the thermal treatment, confirming the likelihood of an arsenic sulfide film given that enargite is not known to have an extensive composition field (Maske and Skinner, 1971). Although relative sulfur concentrations are observed to slightly decrease after treatment, arsenic concentration changes are inconclusive. Therefore,

although this method may remove some sulfur, it is likely not removing the entire film. Future efforts may observe better film removal with higher temperatures.

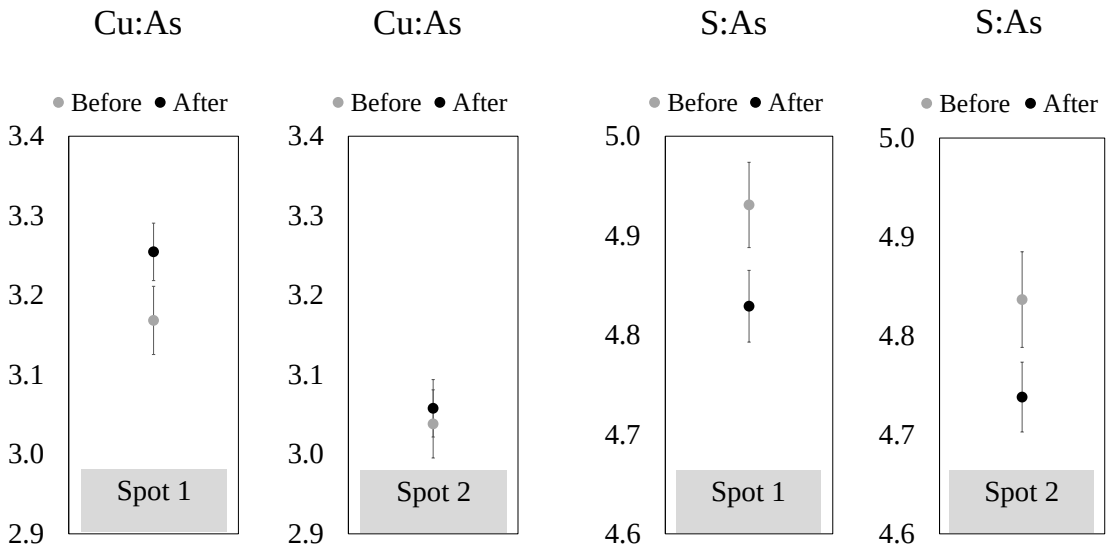

Figure 4.7. Spot-dependent EDS on an enargite film before and after a thermal treatment of 300 °C for 40 minutes in a nitrogen ambient.

4.3.3.2 Selective etching with diammonium sulfide

An alternative method to remove the arsenic sulfide film is to selectively etch the arsenic sulfide with a solvent that dissolves the film without compromising the enargite surface. A selective etch mechanism has been documented which has recommended the use of diammonium sulfide (DAS) to etch the surface of enargite samples (McClary, 2019). This study used a thirty second etching procedure but did not give an indication as to any negative effects on enargite of prolonged exposure to DAS. Figures 4.8 (a) – (d) demonstrate the effect of etching time on observed granular damage. Up to two minutes of etching in DAS does not yield noticeable damage to the enargite surface. After five minutes of etching, there are observable granular features on small particles and on the edges of faceted particles. The location of these features is indicative of excess reactivity, where the etchant preferentially reacts with the highest energy granular particles (on small particles and facet edges). In other words, this behavior is expected from a traditional etchant, but excessive

reaction time is counterproductive. From these observations, it is recommended to stay below approximately 2 minutes for DAS etching of enargite thin films.

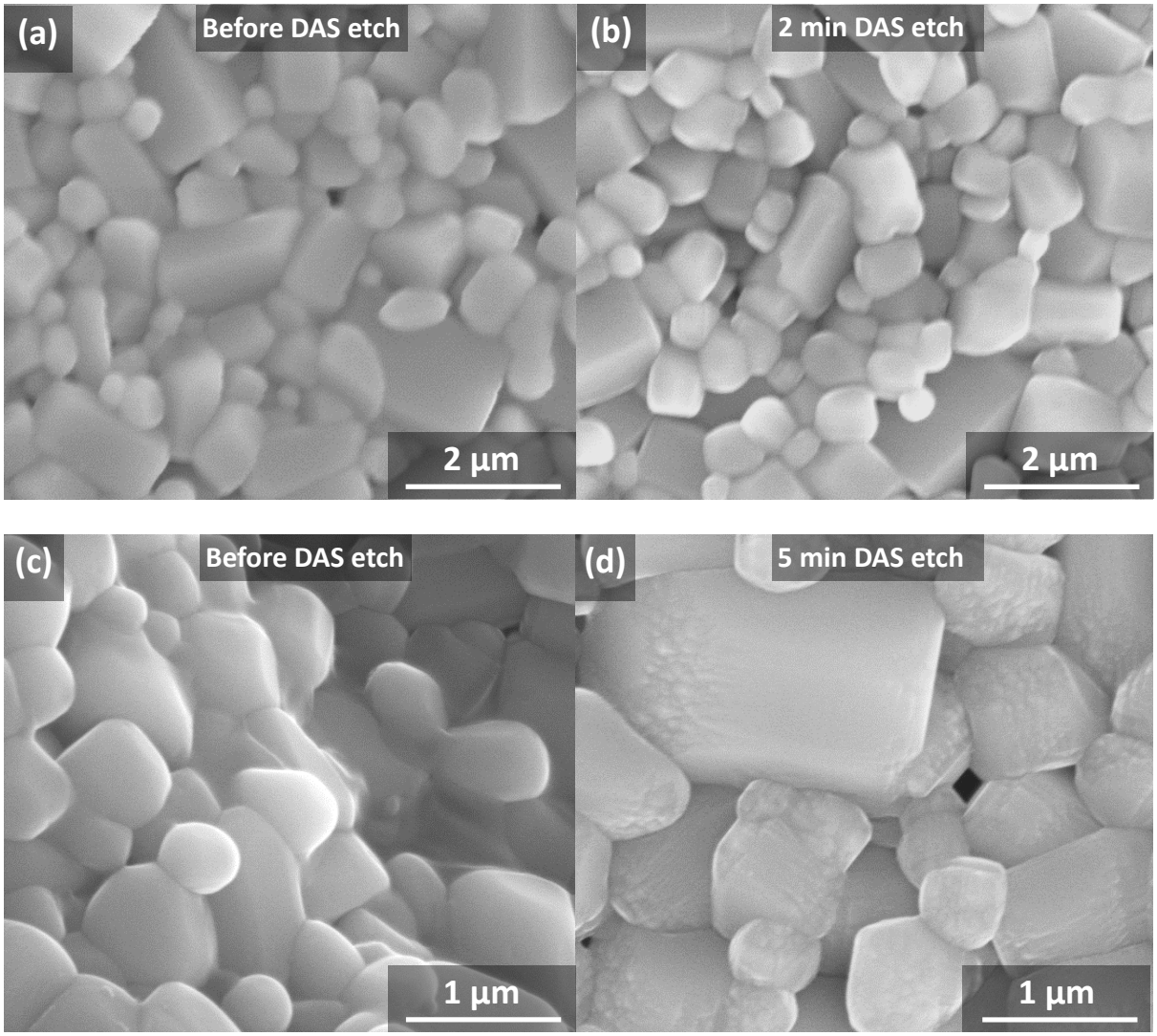

Figure 4.8. Plan-view SEM images of enargite films (a) (c) before and (b) (d) after an etch in diammonium sulfide.

4.3.4 Cu_3AsS_4 enargite device characteristics with post deposition treatment

Using the results from the previous section, an analysis was completed correlating the etching duration with cell performance. As a method to monitor the efficacy of DAS on the

device properties, one enargite film with five marked areas was slowly lowered into a vial filled with DAS solution. The marks indicated the five regions that would be exposed to DAS solution for a different length of time. Regions 5, 4, 3, and 2 were submerged for 130, 100, 70, and 40 seconds, respectively. The first region was not directly exposed to DAS solution; it was only exposed to vapors. All other processing conditions between this sample and the sample referenced in Section 4.3.3. were kept constant besides a slight variation in the added sulfur to arsenic ratio (2.6 in this scenario instead of 2.3). The resulting device characteristics are listed in Table 4.4 and demonstrate the current record device efficiency for enargite-based photovoltaic devices. These cells demonstrate a pronounced increase of the average cell efficiencies, mostly due to an increase in the short circuit current. We note that Region 1, which was not submerged in DAS, has characteristics comparable to those in the previous cell study. The similar short circuit current with the rest of the cells may indicate DAS is interacting with intergranular arsenic sulfide through capillary action. This migration mechanism will likely not influence the open circuit voltage because the surface, which is the location of the p-n junction, may remain covered with an arsenic sulfide film. Under the assumption of intergranular arsenic sulfide, DAS migration through capillary action is also consistent with a decreasing series resistance relative to the sample without a DAS etch. These data support the understanding that arsenic sulfide persists throughout the film, inhibits a robust p-n junction, and can be removed through a post deposition etching procedure with DAS.

External quantum efficiency (EQE) measurements were completed to ensure the photogenerated current is due enargite instead of other semiconducting layers. This analysis in Figure 4.9 demonstrates that enargite accounts for at least 70% of the overall short circuit current in the device, as the only material that has a band gap low enough to absorb photons that have a greater wavelength than approximately 500 nm is enargite. The steady increase in photocurrent with increasing energy most likely reflects the higher absorption coefficient in enargite with higher energy photons (Yu et al., 2013). The sharp increase in EQE between 400 and 500 nm is attributed parasitic absorption from window and buffer layers. However, one notable feature is a step-like photocurrent generated along the absorption edge, which is indicative of band tail behavior similar to that studied in perovskite thin films (Sutter-Fella et al., 2017). These band tails are typically

Table 4.4. *Device characteristics of films fabricated with minimal porosity and without the previously identified IR-active secondary phase. Films additionally had a post deposition treatment in diammonium sulfide.*

Region Number	**Voc (V)**	**Jsc (mA/cm2)**	**Fill Factor (%)**	**Efficiency (%)**	**R_{Sh} (Ω)**	**R_S(Ω)**
1	0.08	8.2	25.7	0.17	290	15
2	0.19	8.3	34.3	0.54	310	24
3	0.20	7.9	32.0	0.51	210	14
4	0.16	7.8	30.7	0.39	230	12
5	0.18	8.8	33.1	0.52	80	14
Average	0.16	8.2	31	0.43	220	16
Standard deviation	0.04	0.4	3	0.14	80	4

introduced from defect states that fluctuate the local electronic structure and lead to recombination of the minority carriers, which reduces the extracted photocurrent. To determine how to prevent these defect states, more analysis is required to identify their nature. In the next section, temperature dependent photoluminescence is completed to verify and understand these defects states.

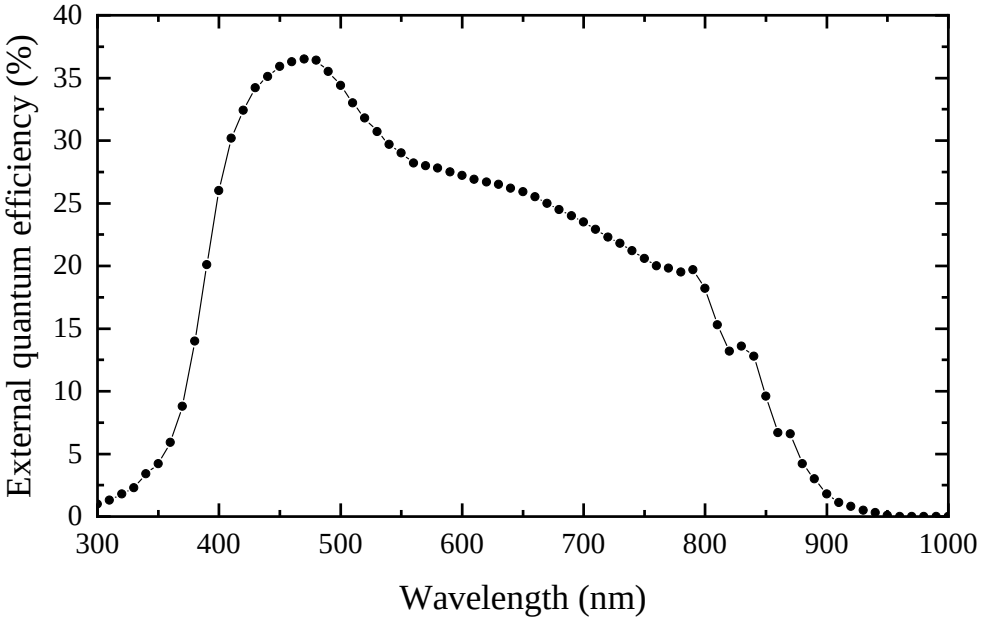

Figure 4.9. EQE measurements on the cell from Region 5

4.3.5 Temperature dependent film analyses

In chapter 3 we demonstrated the PL characteristics of films made from CuS and Cu_2S were largely similar, but films from Cu_2S had a larger relative photoemission from shallow defects which results in a more asymmetrical appearance of the band-to-band emission. Here, temperature dependent photoluminescence was performed to verify the identified band tails and determine the nature of these defect states. These films were fabricated from Cu_2S precursor films and were not etched with DAS.

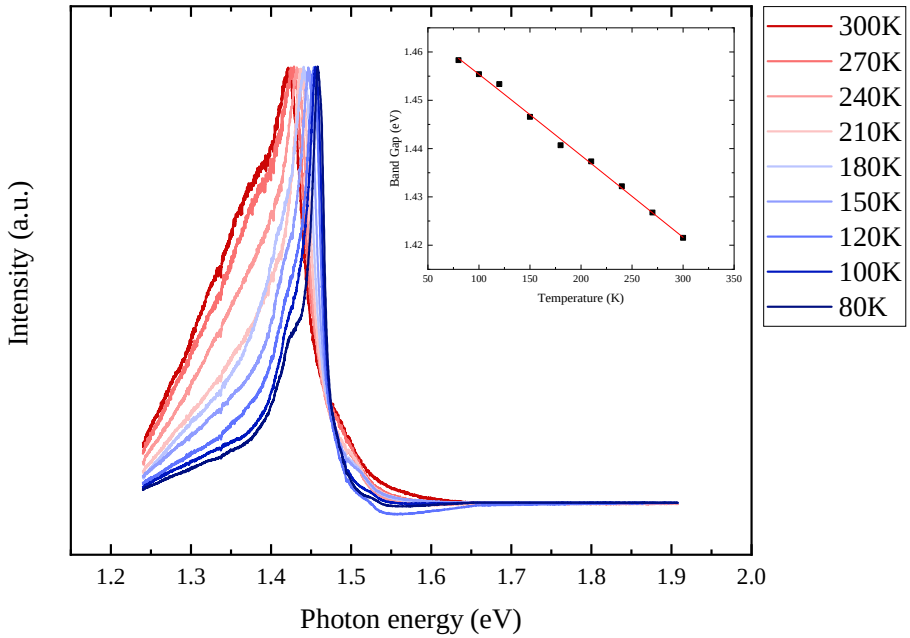

Figure 4.10. Normalized temperature-dependent photoluminescence measurements on an enargite film. The inset shows the change in peak energy as a function of temperature with a Varshni fit.

Figure 4.10 illustrates the TDPL data near the band edges, which indicate a decreasing relative emission from band-to-band recombination compared to a shallow mid-band defect state. This defect state is distinctly photoactive at 80 K but is observed as only a shoulder upon heating. This effect can be understood as a thermal redistribution of the carriers, exciting initially trapped carriers into the band before recombination. However, an emergence of another shallow defect state occurs at about 270 K. Based on data from enargite films from nanoparticle precursors at 4 K (McClary et al., 2019), it is possible this peak corresponds to a different defect state. An increasing relative photoemission from this peak may correspond to an increase in defect concentration. A photoactive defect state in either the conduction or valence band is observed at an energy about 0.02 eV into the band. A defect state with this energy has also been observed in nanoparticle-based films at 4 K (McClary et al., 2019). This photoactivity corresponds in energy to the band tail observed in EQE measurements, verifying this defect is responsible for carrier recombination

that decreases photocurrent. Whether these defects are surface-induced can be inferred from wavelength-dependent TRPL data, but this study has not yet been completed. The temperature dependence of the band gap has also been determined, and has been fit using the Varshni relation (Varshni, 1967):

$$E_g(T) = E_0 - \frac{\alpha T^2}{T+\beta}$$

where $E_g(T)$ is the measured band gap, E_0 is the calculated band gap at 0 K, T is temperature, and α and β are empirically fit constants. This relationship is presented in the inset of Figure 4.10, where Values of E_0 = 1.469 eV, α = 1.71E-4 eV K^{-1}, and β = 20 K are reported. Although these data do not directly influence the development of enargite thin films, the calculated band gap at 0 K can be useful for comparing modeling methods such as density functional theory that assume a system is in its ground state.

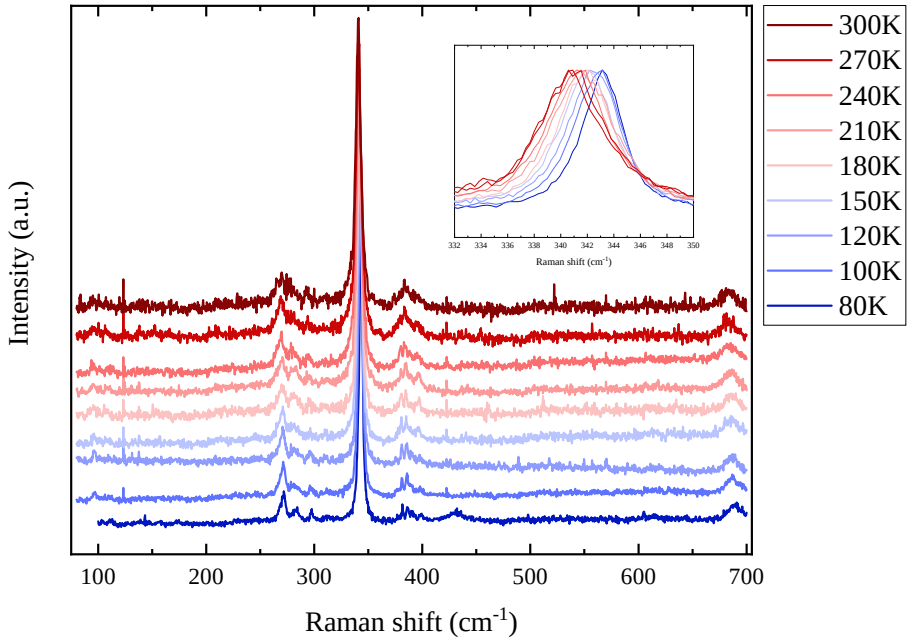

Figure 4.11. Temperature-dependent Raman spectroscopy on an enargite film. The inset shows normalized data indicating a continuous shift in peak energy and FWHM as a function of temperature.

The emerging peak at about 270 K in TDPL spectra could be due to the increase in defect densities with elevated temperature, which may influence the phonon activity within the lattice. With the hypothesis that a sharp increase in defect density may result in a discontinuous shift in the vibrational states of the film, temperature dependent Raman data were also collected with the TDPL data. These TDRS data are presented in Figure 4.11. A continuous redshift of the primary peak is observed with increasing temperature together with a continuous broadening of the full width at half max (FWHM). Although it has been suggested this mode is due to arsenic sulfide bonds (Balow et al., 2017), minimal modeling of enargite vibrational modes are available in literature so the source of the redshift is inconclusive. However, a broadening of the FWHM is commonly attributed to a dephasing of the bond vibrations most likely due to interactions with phonons (Abdula et al., 2008). The continuous shift in the Raman peak does not offer support for the hypothesis that the defects associated with the shallow defects observed in PL result from a discontinuous increase in defect density.

Figure 4.12 illustrates the TDPL data collected with an InGaAs detector on the same sample as above. These data indicate a shifting of photoemission within deep level mid-band states (≈ 0.45 – 0.7 eV from the band edge), most likely due to thermal redistribution of charge carriers. A similar broad photoemission is observed in nanoparticle-derived enargite films at 4 K, but the source of these states is currently unknown. The wave-like shape to the photoemission spectrum is also peculiar, as their energy spacing indicates evenly distributed defect states, instead of a broad range of states observed in other systems (Cherns et al., 2018, Willian De Souza Lucas et al., 2017). These states are repeatedly observed for enargite films but are not observed in other films in our lab, ruling out the possibility of a detector artifact. A constant photoemission energy of these states between approximately 0.8 and 1 eV indicate they are shifting together with the band edge such that the transition energy between states is a constant value. The possible implication may be that the nature of these states is correlated with either the conduction band or valence band states, but a comparison to defect calculations is needed before conclusions are drawn. As these states are photoactive, they will contribute to a degradation of the device performance. Identification and elimination of these defects will assist with the fabrication of high efficiency enargite thin films.

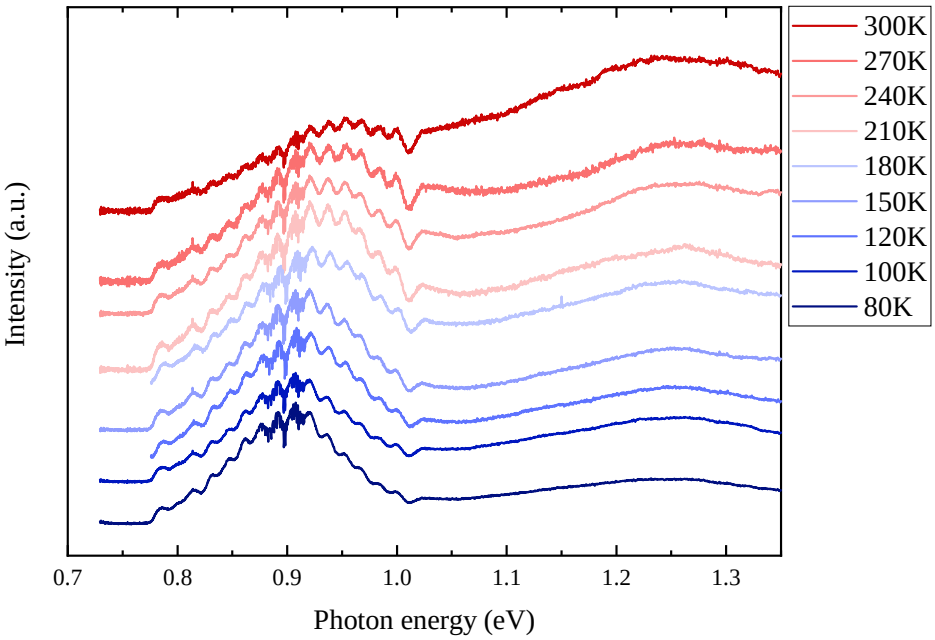

Figure 4.12. Temperature-dependent photoluminescence measurements on an enargite film.

4.3.6 Conclusions and future directions

This chapter was dedicated to understanding the influence of the processing parameters on the resulting film qualities. The hypothesis that changing the elemental composition of the added powder will systematically change the morphology, porosity, and orientation was only convincing regarding texturing of the films. However, an inverse relationship was established between mound-like morphology and large, faceted particles from films fabricated from arsenic (III) sulfide powder and sulfur flakes. The initial cell demonstrated properties comparable to those of the nanoparticle-based precursors, indicating the porosity and IR-active secondary phase observed in those films were not the main limitations of the device. A post deposition treatment with DAS was shown to remove the surface arsenic sulfide layer which facilitated the formation

of a robust p-n junction that resulted in the current record device efficiency for enargite in a solar cell architecture. EQE measurements were collected to ensure enargite was responsible for the improved device qualities opposed to window and buffer layers. This analysis revealed photoactive band tails along the absorption edge that were confirmed in PL. From comparison of the analyses in this section to enargite films fabricated from nanoparticle precursors, films formed from evaporated copper demonstrate similar characteristics to nanoparticle-based films.

4.3.7 Acknowledgements

J.A. would like to acknowledge financial support from the NSF under grant #1144843 (Purdue-Tuskegee IGERT on globally sustainable electronics) and laboratory support from the NSF under grant #1534691-DMR (DMREF: Rapid Design of Earth Abundant Inorganic Materials for Future PVs). He thanks Dr. Scott McClary for XRD, Raman, and EQE training and assistance, Dr. Chris Gilpin and Jameson Root for assistance and training with scanning electron microscopy, Dr. Brian Graeser, Dr. Xianyi Hu, Essam Alruqoba, and Jonathan Turnley for training and assistance with providing molybdenum-coated soda-lime glass, David Rokke for assistance and training with PL, Kyle Weideman for assistance and training on the thermal evaporator, Ryan Ellis, Swapnil Deshmukh, Essam Alruqoba, Apurva Pradhan, and Jonathan Turnley, for their assistance with E-beam depositions, and Alexei Lagoutchev for insights regarding TDRS. He would especially like to thank Apurva Pradhan and David Rokke for their assistance with setting up and collecting data for the temperature-dependent characterization performed in this section.

4.4 References

Abdula, D., Ozel, T., Kang, K., Cahill, D. G., and Shim, M. (2008). Environment-Induced Effects on the Temperature Dependence of Raman Spectra of Single-Layer Graphene. *Journal of Physical Chemistry C*, 112(D):20131–20134.

Balow, R. B., Miskin, C. K., Abu-Omar, M. M., and Agrawal, R. (2017). Synthesis and Characterization of Cu3(Sb1-xAsx)S4 Semiconducting Nanocrystal Alloys with Tunable Properties for Optoelectronic Device Applications. *Chemistry of Materials*, 29(2):573–578.

Cherns, D., Griffiths, I. J., Jones, L., Bishop, D. M., Lloyd, M. A., and McCandless, B. E. (2018). Direct Observation of High Densities of Antisite Defects in Ag 2 ZnSnSe 4. *ACS Applied Energy Materials*, 1(11):6260–6267.

Chirilă, A., Buecheler, S., Pianezzi, F., Bloesch, P., Gretener, C., Uhl, A. R., Fella, C., Kranz, L., Perrenoud, J., Seyrling, S., Verma, R., Nishiwaki, S., Romanyuk, Y. E., Bilger, G., and Tiwari, A. N. (2011). Highly efficient Cu(In,Ga)Se2 solar cells grown on flexible polymer films. *Nature Materials*, 10(11):857–861.

Gray, J., Wang, X., Vamsi, K. C. R., Sun, X., Kanti, A., and John, R. W. (2011). ADEPT 2.1.

Madelung, O. (2004). *Semiconductors: Data Handbook 3rd edition*.

Maske, S. and Skinner, B. J. (1971). Studies of the Sulfosalts of Copper I. Phases and Phase Relations in the System Cu-As-S. *Economic Geology*, 66:901–918.

McClary, S. A. (2019). *SYNTHESIS AND CHARACTERIZATION OF COPPER ARSENIC SULFIDE FOR SOLUTION-PROCESSED PHOTOVOLTAICS*. PhD thesis, Purdue University.

McClary, S. A., Andler, J., Handwerker, C. A., and Agrawal, R. (2017). Solution-processed copper arsenic sulfide thin films for photovoltaic applications. *Journal of Materials Chemistry C*, 5(28):6913–6916.

McClary, S. A., Li, S., Yin, X., Dippo, P., Kuciauskas, D., Yan, Y., Baxter, J. B., and Agrawal, R. (2019). Optoelectronic Characterization of Emerging Solar Absorber Cu3AsS4. In *IEEE Photovoltaics Specialists Conference Proceedings*, pages 3–7.

Sutter-Fella, C. M., Miller, D. W., Ngo, Q. P., Roe, E. T., Toma, F. M., Sharp, I. D., Lonergan, M. C., and Javey, A. (2017). Band tailing and deep defect states in CH3NH3Pb(I1-xBrx)3 perovskites as revealed by sub-bandgap photocurrent. *ACS Energy Letters*, 2(3):709–715.

Tsiulyanu, D. (2004). CHAPTER 2 - Heterostructures on Chalcogenide Glass and Their Applications. In Fairman, R. and Ushkov, B., editors, *Semiconducting Chalcogenide Glass III*, volume 80 of *Semiconductors and Semimetals*, pages 57–101. Elsevier.

Varshni, Y. P. (1967). Temperature dependence of the energy gap in semiconductors. *Physica*, 34(1):149–154.

Wallace, S. K., Svane, K., Huhn, W. P., Zhu, T., Mitzi, D. B., Blum, V., and Walsh, A. (2017). Candidate photoferroic absorber materials for thin-film solar cells from naturally occurring minerals: enargite, stephanite, and bournonite. *Sustainable Energy & Fuels*, 1(6):1339–1350.

Willian De Souza Lucas, F., Peng, H., Johnston, S., Dippo, P. C., Lany, S., Mascaro, L. H., and Zakutayev, A. (2017). Characterization of defects in copper antimony disulfide. *Journal of Materials Chemistry A*, 5(41):21986–21993.

Yu, L., Kokenyesi, R. S., Keszler, D. A., and Zunger, A. (2013). Inverse design of high absorption thin-film photovoltaic materials. *Advanced Energy Materials*, 3(1):43–48.

CHAPTER 5. PROGRESS TOWARDS BAND ALIGNMENT IN Cu_3AsS_4 ENARGITE-BASED PHOTOVOLTAICS

5.1 Introduction

The previous chapter demonstrated films suitable to test the hypothesis that an IR-active secondary phase and porosity were significant limitations to the initial device performance of Cu_3AsS_4 solar cells. Although device efficiencies were improved with a post-deposition etch with diammonium sulfide, the efficiencies of this material remain limited to below 1%. The negative results of this hypothesis indicate the most probable limiting factor is the conduction band alignment with the n-type junction pair, although notable photoactive defects were identified at the absorption onset in this system.

Although the p-n junction presents a limitation to device performance, it is also possible the band alignment with the back contact is an equally limiting factor. A poor alignment with the back contact will increase minority carrier diffusion away from the depletion region, which can result in undesirable recombination that reduces photocurrent. Although the decreased photocurrent can limit device performance, this band alignment has not yet been addressed. The opening part of this chapter presents the first model for the band alignment of enargite with both a molybdenum and molybdenum sulfide back contact.

The conduction band alignment for the initially fabricated devices with cadmium sulfide as the n-type layer has recently been modeled to be a low-performing junction pair (McClary et al., 2019). Suitable n-type materials such as ZnS, ZnTe, and WO_3 have been identified in literature but have not yet been integrated into a device architecture (McClary et al., 2019, Wallace et al., 2019). The second half of this chapter focuses on the insights gained from processing of ZnS thin films applied as the n-type layer on enargite thin films towards high-efficiency devices.

5.2 Experimental Methods

5.2.1 Materials

The chemicals used to complete the investigations in this chapter are listed in Table 5.1.

5.2.2 Band alignment modeling

Adept 2.1 was used to model the band alignments in this study (Gray et al., 2011). The parameter values used to model the Cu_3AsS_4-Mo and Cu_3AsS_4-MoS_2-Mo interfaces are tabulated in Table 5.2. In both cases, the front layer (Layer 1 in Adept) is always modeled with Cu_3AsS_4 and the backmost layer is modeled with Mo. The Absorption, Global, and Simulation parameter defaults were not altered because their values do not influence the modeled Cu_3AsS_4-Mo interface and insights regarding photoactivity were not sought. Due to the fermi level arbitrarily placed at -4.5 eV in the program, all results were shifted to -5.0 eV in this study to align with the work function of the molybdenum $\{110\}$ planes that are representative of the textured films deposited through physical vapor deposition in our lab.

5.2.3 Chemical bath deposition

Four chemical bath deposition recipes (Rec1 – Rec4) for ZnS thin films have been used in this investigation and their respective experimental details are listed in Table 5.3.

5.2.4 Buffer and window layer deposition

Between 40 and 150 nm of slightly n-type ZnO was deposited through RF sputtering with an ambient oxygen content of 2% in argon. Approximately 220 nm ITO was deposited with the same sputter system, but fully in an argon ambient. For experiments using FTO glass, this conducting oxide was purchased as described in Table 5.1.

Table 5.1. *List of products used in this chapter*

Chemicals / equipment	**Purity / type**	**Source**	**Quantity***
Ammonium hydroxide	28-30%	Sigma-Aldrich	≈ 20-130 mL / ZnS deposition
Dimethyl sulfoxide (DMSO)	>99.9%	Sigma-Aldrich	≈ 18 mL / ZnS deposition
Fluorine-doped tin oxide (on glass)	≈ 13 Ω/sq.	Sigma-Aldrich	≈ 0.02 mg / 1"x1" substrate
Indium oxide (ITO) target	>99.99%	Kurt J Lesker	≈ 1 mg / 220 nm**
Hydrogen sulfide (H_2S) gas	1% and 3% bal. Ar	Airgas	Tanks used indefinitely
Pyridine	>99.8%	Sigma-Aldrich	≈ 0.3 mL / 1.6 cm^2 cell
Sulfur flakes	99.99%	Sigma-Aldrich	≈ 0.3-0.6 g / treatment
Thiourea	>99% ACS	Sigma-Aldrich	≈ 1-14 g / ZnS deposition
Ultrapure water	18.2 MΩ-cm	Direct-Q3 UV (in-house)	≈ 0-150 mL / ZnS deposition
Zinc chloride	>99.995%	Sigma-Aldrich	≈ 0.4 g / NP synthesis
Zinc nitrate hexahydrate	>98%	Sigma-Aldrich	≈ 3.9 g / NP synthesis
Zinc oxide target	>99.9%	Kurt J Lesker	≈ 0.3 mg / 80 nm**
Zinc sulfate heptahydrate	>99%	Sigma-Aldrich	≈ 0.5-6 g / ZnS deposition

**Hexane, IPA, water, soap, and nitric acid used for glassware cleaning between each synthesis is not included. Quantities with ranges are described more in the text.*

***Assumed deposition area is a 1"x1" substrate. Waste material not included.*

Table 5.2. *List of values and sources used for modeling the band structure with ADEPT 2.1.*

Parameter	**Value (Mo)**	**Source**	**Value (MoS_2)**	**Source**	**Value (Cu_3AsS_4)**	**Source**
Layer thickness (μm)	0.8	SEM	0.04	SEM	1	SEM
Doping type	n-type	assumption	n-type	assumption	p-type	Hot probe
Dopant dens. (cm^{-3})	5E22	(Lin et al., 2012)	1E16	(Kim et al., 2012)	8E15	(McClary, 2019)
Band gap (eV)	0	assumption	1.23	(Kam and Parkinson, 1982)	1.43	PL
Electron affinity (eV)	5.0	(Scheer and Fine, 1969)	4.2	(Shimada et al., 1994)	3.61	(McClary, 2019)
Dielectric Constant	1	assumption	10	(Yan et al., 2015)	5.83	(Wallace et al., 2017)
CB eff. DOS (cm^{-3})	1E23	assumption	1E18	assumption	1E18	(McClary, 2019)
VB eff. DOS (cm^{-3})	1E23	assumption	1E17	assumption	1E19	(McClary, 2019)
Electron mobility ($cm^2\ V^{-1}\ s^{-1}$)	10	(Lin et al., 2012)	30-500	(Pham and Yeom, 2016)	7	(McClary, 2019)
Hole mobility ($cm^2\ V^{-1}\ s^{-1}$)	1E-5	assumption	25	assumption	1.5	(McClary, 2019)
SRH electron lifetime (ns)	1E10	assumption	0.1	(Ganatra and Zhang, 2014)	1.8	TRPL and assumption
SRH hole lifetime (ns)	0.1	assumption	0.01	assumption	18	assumption
Auger electron recomb. coef ($cm^6\ s^{-1}$)	0	assumption	0	assumption	0	assumption
Auger hole recomb. coef ($cm^6\ s^{-1}$)	0	assumption	0	assumption	0	assumption
Radiative recomb. coef ($cm^3\ s^{-1}$)	0	assumption	0	assumption	0	assumption
Acceptor energy (eV)	0	assumption	0	assumption	0	assumption
Donor energy (eV)	0	assumption	0	assumption	0	assumption

Table 5.3. *Comparative conditions for four chemical bath depositions used to deposit Zn(O,S) thin films. Water, zinc sulfate, ammonium hydroxide, thiourea, DMSO, and soda-lime glass are abbreviated as W, ZN, AH, T, D, and SLG, respectively.*

Variable	**Rec1**	**Rec2**	**Rec3**	**Rec4**
Jacketed beaker setpoint	80 °C	75 °C	76.5 °C	85 °C
Pre-treatment sample conditions	Soak in water	Soak in water	Soak in 14% NH_4OH in H_2O	Soak in water
Ultrapure water, H_2O	150 mL	-	69.9 mL	60 mL
Zinc sulfate, $ZnSO_4$	22 mL; 0.2 M	13.4 mL; 2.5 M	11.3 mL; 3 M	45.0 mL; 0.075 M
Ammonium hydroxide, NH_4OH	28.3 mL; 7.46 M	127.75 mL; 7 M	64.3 mL; 7 M	68.0 mL; 7 M
Thiourea, $SC(NH_2)_2$	22 mL; 0.75 M	83.84 mL; 1.6 M	79.5 mL; 0.6 M	120 mL; 1.5 M
Dimethyl sulfoxide (DMSO)	-	-	-	18 mL
Mix order	W+ZS, T, wait 60 s, add AH	ZN, T, wait 90s add AH	W, heat >66 °, ZS, T, wait 90s add AH	W, T, ZS, D, wait 14 min, add AH
Sample addition time relative to AH	- 60 sec	- 30 sec	- 30 sec	+ 0 sec
Stir rate	100 rpm	100 rpm	100 rpm	60 rpm
Beaker coverage	no	no	no	yes
In-situ monitoring	Temp and pH	Temp and pH	Temp and pH	Temp and pH
Duration after AH addition	45 min	45 min	22 min	13-20 min
Rinse	H_2O	NH_4OH in H_2O then H_2O	NH_4OH in H_2O then H_2O	NH_4OH in H_2O then H_2O
Drying procedure	120 min; 200 °C	8 min; 200 °C	5 min; 200 °C	N_2 gun; vacuum
Deposition surface	SLG	SLG	SLG and enargite	SLG and enargite
Repetitions	1	1	2	2
Onset of cloudiness relative to AH	≈ 40 min	≈ 30 min	≈ 5 -10 min	≈ 10 min

5.2.5 ZnS nanoparticle syntheses

Nanoparticles were prepared through using two different zinc precursors, zinc chloride and zinc nitrate. These compounds dissolved readily in water and were added to a two-neck round bottom flask. One neck was attached to a Schlenk line and the other was sealed with a penetrable red rubber septum, used to bubble hydrogen sulfide into the flask. The flow rate of hydrogen sulfide for these reactions is approximately 10 sccm for 30 minutes. The concentration of the gas used with $ZnCl_2$ was 1% and the concentration used with $Zn(NO_3)_2$ was 3%. These reactions were observed to produce a cloudy white suspension a few minutes after H_2S began bubbling, indicating the formation of zinc sulfide. Both reactions precipitate nanoparticles and form a strong acid supernatant, which is separately neutralized before disposal.

Zinc sulfide nanoparticles prepared with a zinc chloride precursor used 397.4 $\pm$ 0.2 mg $ZnCl_2$ dissolved in 29.2 $\pm$ 0.6 mL ultrapure water to make a 0.1 M suspension. These nanoparticles were pipette onto glass and copper substrates and were analyzed with XRD and SEM-EDS, respectively. Zinc sulfide nanoparticles prepared with a zinc nitrate hexahydrate precursor used 3.8689 $\pm$ 0.0002 g $Zn(NO_3)_2$ $6H_2O$ in 38.7 $\pm$ 0.7 mL reverse osmosis water to make a 0.34 M suspension. These nanoparticles were poured into a tube and centrifuged at 14000 rpm for 5 min. The supernatant was discarded, and the nanoparticles were subsequently washed with approximately a 30% ammonium hydroxide solution under the same centrifugation parameters. After discarding the supernatant, the nanoparticles were stored in a variety of solvents including water, 30% ammonium hydroxide, and pyridine. Aliquots were removed before washing, after the ammonium hydroxide wash, and after storing in these solutions to monitor any change in the nanoparticle structure or Zn:S ratio. We note the centrifuging detailed above creates compact nanoparticle agglomerates that are difficult to redisperse, so less aggressive centrifugation should be completed if large nanoparticle agglomerates are not desired.

5.2.6 Deposition of ZnS nanoparticles onto enargite thin films

The concentration of nanoparticles in suspension was characterized by drop casting, drying, and weighing a known quantity of dispersed nanoparticles. Approximately 0.3 mL of 5 mM ZnS

nanoparticles suspended in pyridine was spin cast onto an enargite thin film. The spin rate was approximately 2000 rpm for 30 seconds, and two 0.15 mL coats were applied during this time. Samples were then heated on a hotplate at 100 °C for 5 minutes and the spin coating and drying processes were repeated one time. The enargite films were adhered to a glass substrate throughout this process. All activities and subsequent film storage occurred in a nitrogen ambient.

5.2.7 Characterization details

A FEI quanta 3D dual-beam field emission scanning electron microscope (SEM) was used to capture film morphology. Energy-dispersive X-ray spectroscopy (EDS) for Figures 5.4 and 5.8 was collected with an accelerating voltage of 5 kV and 20 kV, respectively, on the same SEM with a silicon drift detector. Elemental compositions were determined through AZtec software using standardless quantitative analysis. X-ray diffraction (XRD) data were collected on a Rigaku SmartLab diffractometer using a copper Kα X-ray source in parallel beam mode with a grazing incidence angle of 0.5°. A Hanna Instruments electrode (# HI1296D) was used for all pH and in-situ chemical bath deposition measurements. Th electrode was doubly calibrated less than 45 minutes before each test begins with calibration buffer solutions of 4.01 pH (# HI6004) and 7.01 pH (# HI6007) for Rec1 and solutions of 7.01 pH (# HI6007) and 10.01 pH (# HI6010) for Rec2-Rec4.

5.3 Results and discussion

5.3.1 Investigation into the Mo-Cu_3AsS_4 interface

The band alignment at the p-n junction has been identified as the most probable explanation for the low efficiency observed in enargite-based solar cells (McClary et al., 2019). However, investigation of the band alignment at the back interface has received little attention. According to the band diagram in Figure 5.1 (a), the Cu_3AsS_4-Mo $\{110\}$ interface demonstrates an ideal ohmic behavior where holes can freely migrate to the interface to recombine with injected electrons.

Furthermore, an electron depleting bend is calculated in the conduction band, limiting electron migration to the back interface and subsequent parasitic recombination. This behavior is contrast to the CIGSe-Mo interface where a Schottky barrier forms and allows electrons to diffuse to the back contact which increases parasitic recombination in the device (Hsiao et al., 2013). However, this behavior is mitigated by the formation of $MoSe_2$ during selenization, which has a relatively small valence band offset with CIGSe that does not impede hole transfer. Since this layer is more resistive than molybdenum it will increase the series resistance in the device, so an optimal thickness exists that balances this negative attribute with the band bending benefits. The optimal thickness will change depending on system characteristics, but one study has found a minimum sheet resistance with approximately a 10 nm $MoSe_2$ layer (Klinkert et al., 2016).

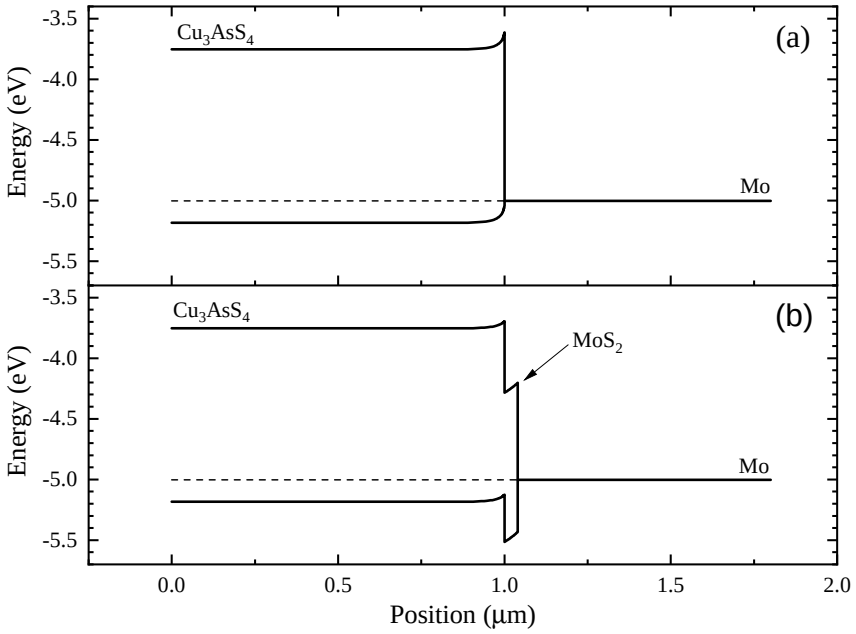

Figure 5.1. ADEPT 2.1 model of the enargite band alignment with (a) Mo and (b) MoS_2 using the parameters listed in Table 5.2. Absolute energy values are aligned relative to the Mo $\{110\}$ planes.

It is currently unconfirmed if an analogous MoS_2 layer is formed during the sulfurization processes required to form enargite. However, some samples offer support for this possibility through means of a contrast difference in side-view SEM images. Figure 2.7 reveals contrast

difference extending to almost 100 nm into the molybdenum substrate. If this layer forms, Figure 5.1 (b) demonstrates a non-ideal band alignment at the Cu_3AsS_4-MoS_2 interface that results in approximately a 0.4-0.5 eV Schottky barrier to holes. For CIGSe solar cells, this is approximately the energy range where notable reduction in the modeled optoelectronic properties begin (Hsiao et al., 2013). Contrary to the formation of $MoSe_2$ for CIGSe solar cells, MoS_2 is detrimental to device properties. It is unclear if this layer significantly hinders the current device properties, but analysis of recombination behavior through wavelength dependent TRPL should demonstrate a decreasing dependence on this interface as the thickness of the sample increases, which is an avenue for future investigation.

5.3.2 Chemical bath deposition towards Zn(O,S) buffer layers

Chemical bath deposition (CBD) is a widely used technique to deposit a buffer layer onto solar cells. Most CBD processes to fabricate thin film solar cells use CdS, however we have demonstrated this material is not ideal for enargite-based photovoltaics. Recently, buffer layer compositions have started decreasing the amount of cadmium used in their processes, and zinc has been a common replacement. Therefore, CBD processes for Zn(S,O) thin films reported in literature guided initial processes. The reactions were modeled after several studies that use different precursors, operating temperatures, and washing techniques (Araoz, 2009, Hong et al., 2018, Steirer et al., 2015). These differences have demonstrated optimized layer properties in other systems: A greater concentration of thiourea has been shown to incorporate a higher amount of sulfur into resulting Zn(O,S) films (Wu et al., 2018). A post deposition rinse in ammonium hydroxide will deplete the wet surface layer of free zinc ions that otherwise would form zinc hydroxide on the surface if rinsed with water (Araoz, 2009). The addition of DMSO to the solution has been found to increase device performance in kesterite CZTSe, but its mechanisms are not currently explained (Steirer et al., 2015). The reaction kinetics remain similar for these slightly different approaches: ammonium hydroxide reacts with a dissolved zinc salt to form a zinc complex, which reacts with sulfur from decomposing thiourea to precipitate zinc sulfide (Araoz, 2009, Hariskos et al., 2012).

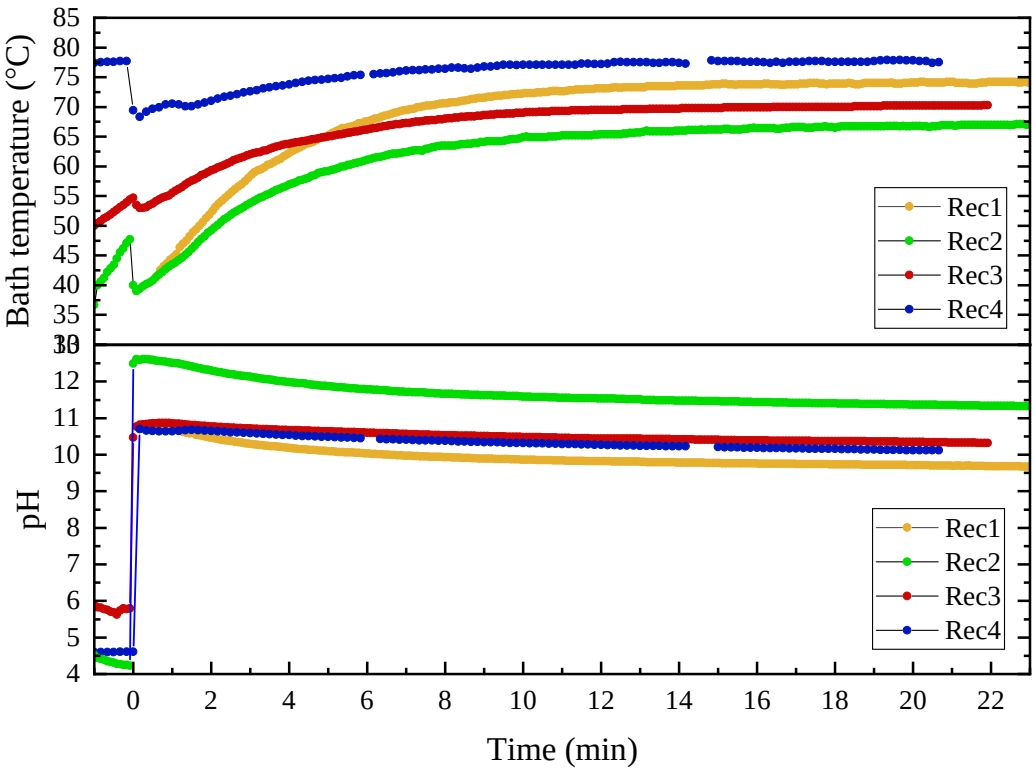

Figure 5.2. XRD data for the material deposited on SLG for the indicated Zn(O,S) recipes.

The pH of the bath is ideally maintained between about 10-12 (Hariskos et al., 2012) to balance deposition time and secondary phase formation. A pH that is too low favors the precipitation of $Zn(OH)_2$, but a pH that is too high introduces superfluous hydroxide ions that coordinate with zinc and inhibit the formation of ZnS. A bath temperature between approximately 70 - 90 °C also balances deposition time and secondary phase formation, but through slightly different mechanisms (Araoz, 2009). As the deposition of ZnS is controlled by the rate of decomposing thiourea and zinc complexes, a higher temperature will increase the decomposition of species within the solution and lead to an increase reaction rate. However, a higher temperature will increase the driving force for NH_4OH evaporation which will decrease the pH and consequently increase the driving force for $Zn(OH)_2$ precipitation. Like other process variables, the concentration

of the reactants also balance deposition rate with secondary phase formation. A more concentrated solution will lead to a faster deposition rate, but too many free zinc ions increases the driving force for $Zn(OH)_2$ precipitation. A relatively too high concentration of NH_4OH will decrease the deposition rate as the hydroxide ions will coordinate with zinc. These insights were used to design the set of reactions presented in Table 5.3. The bath temperature and pH was monitored to ensure the reactions were maintained within the above parameters. These data are presented in Figure 5.2.

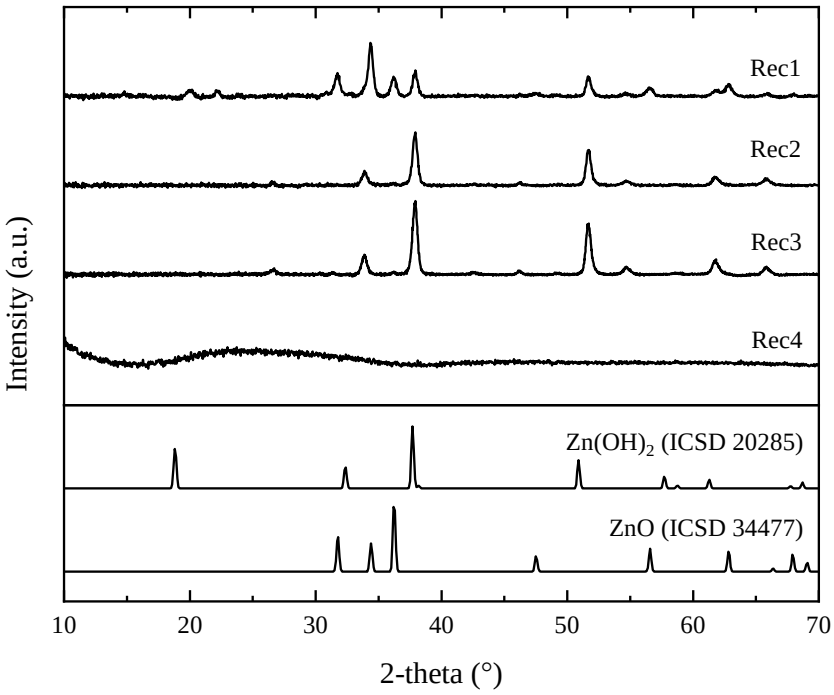

Figure 5.3. XRD data for the material deposited on SLG for the indicated Zn(O,S) recipes.

Resulting Zn(O,S) thin films from CBD generally exhibit low crystallinity and are seldom reported (Ahn and Um, 2015, Wu et al., 2018). Of the recipes examined in this chapter, a low crystallinity was only observed for Rec4. Figure 5.3 demonstrates the commonly observed XRD pattern resulting for many of these reactions. This pattern does not correspond to the commonly formed compounds of ZnS, ZnO, or $Zn(OH)_2$. Interestingly, a similar XRD pattern has been

reported as a textured wurtzite ZnS thin film from magnetron sputtering (Islam et al., 2012). However, a different pattern was obtained under similar conditions in a separate study (Hwang et al., 2012). Since the sphalerite phase of ZnS is more stable under these conditions, it is unlikely oriented wurtzite was deposited on glass substrates. Solar cells made with this unknown structure demonstrated zero efficiencies without evidence of a diode. Therefore, an investigation into the chemical composition and other properties of this material was not completed as it likely is not suitable as the n-type layer for enargite-based solar cells. We note an additional formation of zinc oxide was observed in Rec3, which is presumably due to the extended drying procedure in an oxygen ambient.

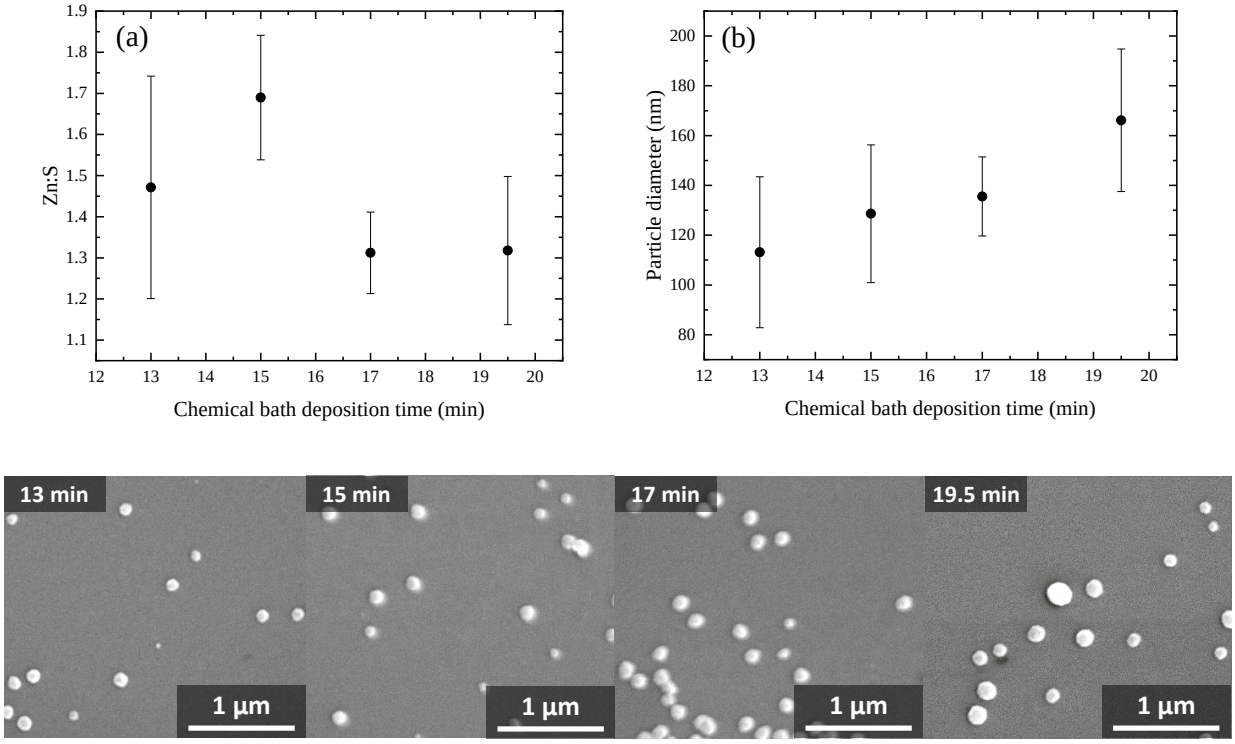

Figure 5.4. (a) composition data and (b) particle size data for CBD Zn(O,S) formed through Rec4. The SEM images are a visual aid supporting the size comparison data.

Films were further analyzed for Rec4 and devices were made following this procedure. First, this procedure was applied to glass substrates. As the deposition proceeds, the evaporation of

ammonium hydroxide from the bath reduces the pH which increases the driving force for $Zn(OH)_2$ nucleation and incorporation into the film (Araoz, 2009). This process may result in a relatively sulfur-poor film as deposition time proceeds. However, the chemical composition does not appear to change following this trend, indicating deposition times of up to 20 minutes are possible without a noticeable decrease in sulfur concentration. The Zn(S,O) nanoparticles adhered to the glass in Figure 5.4 demonstrate an increasing size with CBD time. Since the chemical composition is not corresponding to the increase in grain size, it is likely the particles are the result of a nucleation and growth mechanism instead of from a density change.

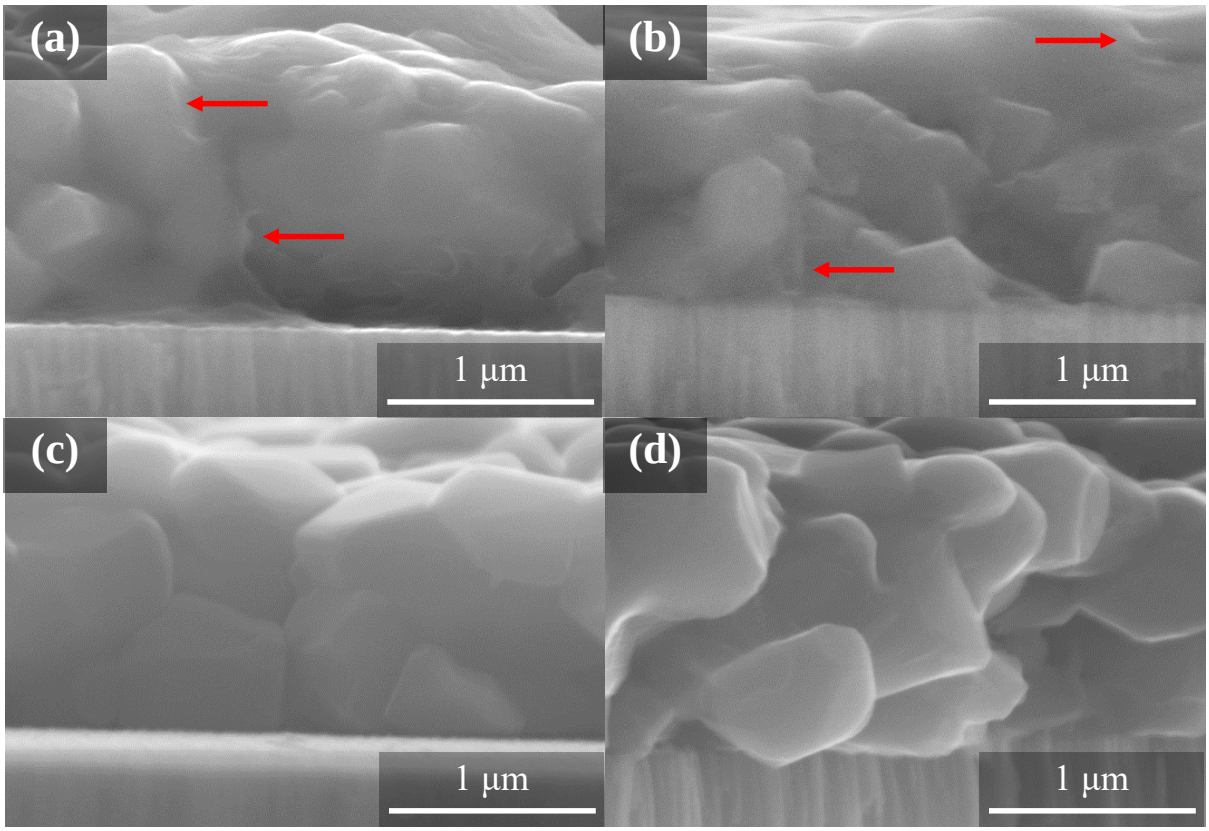

Figure 5.5. Side-view SEM images of an enargite film after a Rec4 CBD corresponding to (a) 13- (b) 15- (c) 17- and (d) 20-minute deposition times.

On enargite thin films, it is unclear if deposition was successful. There is evidence in the 13- and 15-minute samples of a thin film on the surface, designated by red arrows in Figures 5.5

(a) and (b). However, this evidence is not present in the latter samples. XRD and Raman analyses demonstrate no noticeable change in enargite. Devices made from this deposition technique resulted in no efficiency and were mostly resistors opposed to diodes. Although this deposition technique was internally performed on CIGSe devices and produced diodes, it is unclear if that behavior is a direct result of a deposited Zn(S,O) film or subsequent device layers. Therefore, the hypothesis that ZnS will be a better n-type junction pair cannot be tested with the films made in the section.

5.3.3 Sulfurization of ZnO thin films

ZnO films were deposited with RF magnetron sputtering and treated in a H_2S gas. XRD results are provided in Figure 5.6 that demonstrate the relative amount of conversion to ZnS is a function of the H_2S flow rate, film thickness, and treatment duration. Incomplete conversion to ZnS is observed for all conditions tested, but near complete conversion is achieved on a 40 nm ZnO film with a 100 sccm flow rate. Like the copper films in chapter 3, it is probable the reaction is occurring from the top surface down toward the film. Therefore, an incomplete conversion from the ZnO phase indicates the enargite front junction is most likely still formed with ZnO instead of ZnS. We hypothesize that increasing the H_2S flow rate, decreasing the thickness of the film, and extending the treatment conditions will result in films that achieve full conversion to a ZnS film. It is unclear if the resulting ZnS film is a sphalerite or a textured wurtzite. The broad peak around 52° suggests it may be an oriented wurtzite phase, but TEM analyses will confirm the structure. Since sphalerite is typically formed through ZnS deposition techniques like CBD, investigating ZnS films formed from this route may lead to a processing route capable of forming wurtzite n-type junction pairs. However, it is currently unclear which phase will be best for enargite devices. The reaction temperature and gas concentration were not changed during this analysis, but these quantities are expected to also influence the film characteristics. It is unclear if a 400 °C treatment condition will negatively affect the enargite film, so investigations at lower temperatures will be necessary for application to device structures. We note at 120 °C for 45 minutes with a 40 sccm 1% H_2S flow no partial conversion was observed.

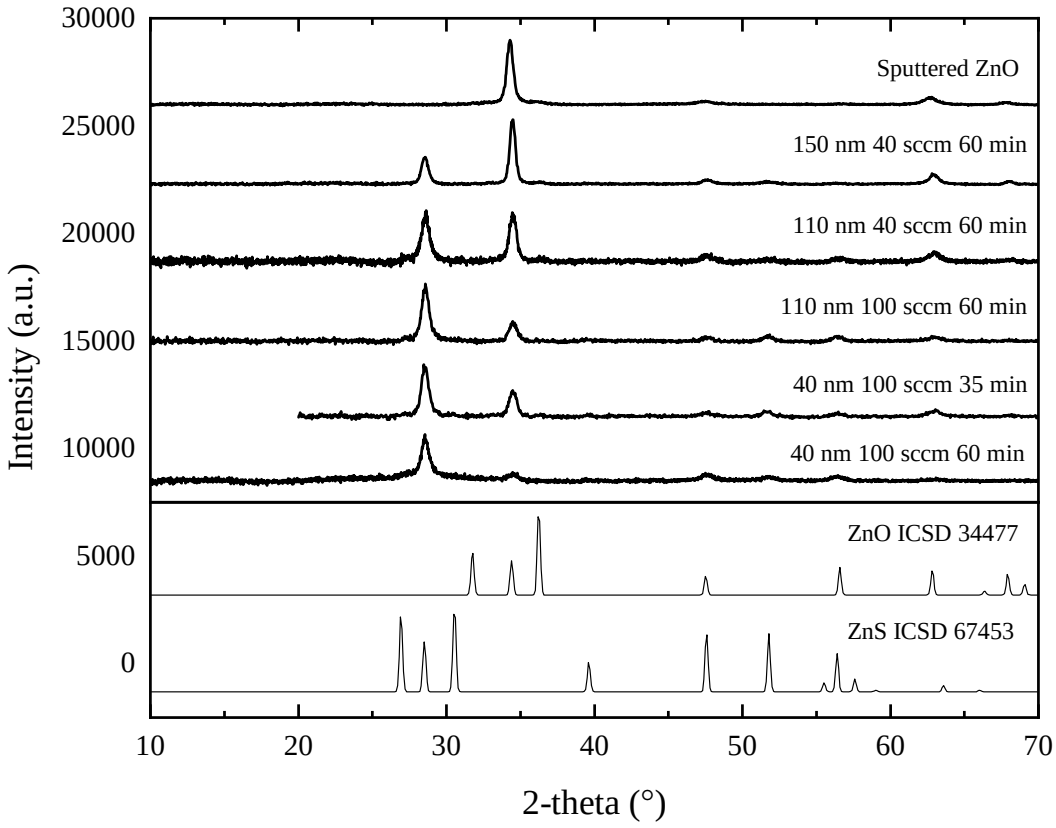

Figure 5.6. XRD data of sputtered ZnO films treated in 1% H_2S at 400 °C. Partial conversion to ZnS is observed for all conditions tested.

5.3.4 ZnS nanoparticle synthesis and deposition onto enargite thin films

Another method to produce a ZnS n-type junction is to synthesize nanoparticles and cast them onto an enargite thin film. Two methods were explored using different zinc precursors, zinc chloride and zinc nitrate. XRD patterns for the two methods are given in Figure 5.7 where an approximation of crystallite size using peak FWHM yields sizes of approximately 4 and 3 nm for ZnCl and $Zn(NO_3)_2$, respectively. The estimation of crystallite size for nanoparticles synthesized from ZnCl precursors was performed without using the primary peak around 28 degrees due to the notable asymmetry present in the diffraction pattern.

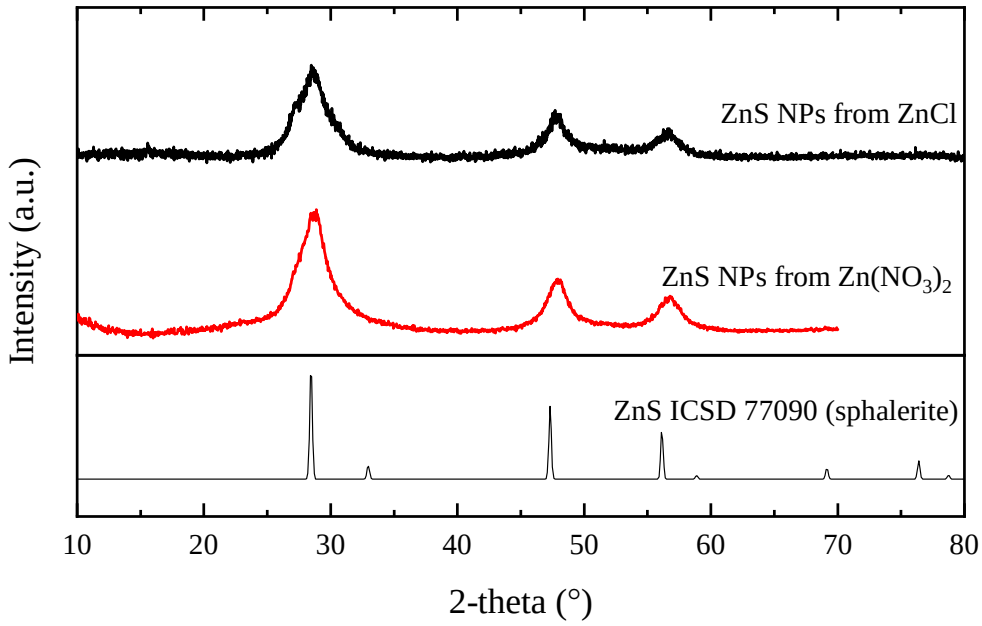

Figure 5.7. XRD data of ZnS nanoparticles synthesized through bubbling H_2S gas through a solution of either ZnCl or $Zn(NO_3)_2$ dissolved in water.

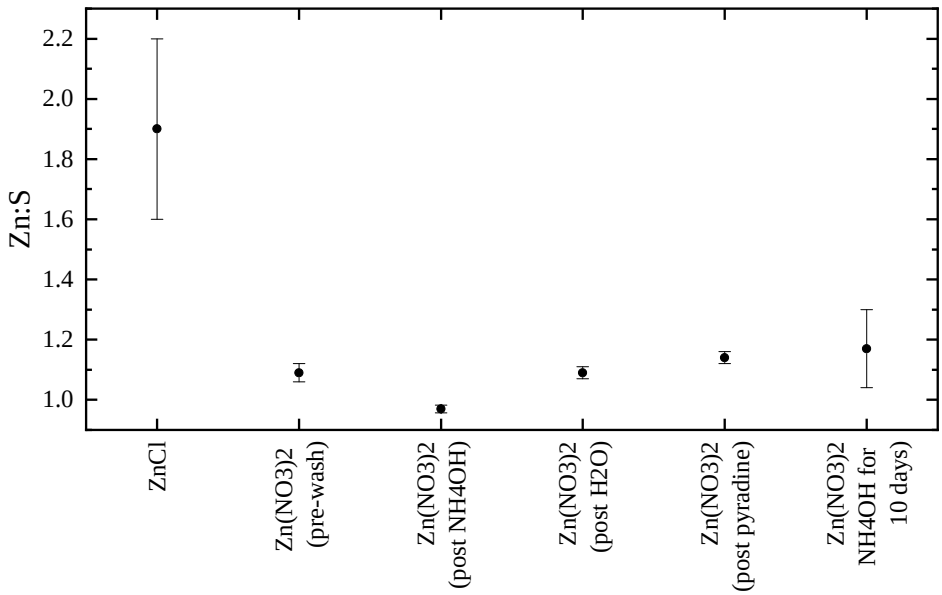

Figure 5.8. SEM-EDS data of ZnS nanoparticles synthesized through ZnCl and $Zn(NO_3)_2$ precursors and suspended in different solutions.

Table 5.4. *Characteristics of solvents investigated for suspending and coating ZnS nanoparticles.*

Solution	Enargite wettability	Colloidal stability
Water	Less wet	Several hours
Ammonium hydroxide (in water)	Less wet	Several hours
Dimethyl sulfoxide (DMSO)	Less wet	-
Acetonitrile	More wet	Few seconds
Pyridine	More wet	Several hours
Formamide	Less wet	-

Chemical composition data from SEM-EDS in Figure 5.8 indicate more contamination from ZnCl precursors for these reaction conditions due to the incorporation of chlorine into the nanoparticles. Nanoparticles synthesized from zinc nitrate exhibited less contamination, so these particles were analyzed further. The Zn:S ratio is observed to change for these nanoparticles depending on the storage solution. NH_4OH storage solutions are observed to reduce this ratio, possibly due to the dissolution of zinc hydroxide which increases in solubility with increasing pH (Araoz, 2009). If NH_4OH leaves the system through vaporization, the pH will decrease and increase the driving force for $Zn(OH)_2$ to precipitate or incorporate into the nanoparticles. This mechanism may explain the nanoparticle concentrations observed after being stored in NH_4OH in a sealed, but not airtight, container.

To form a p-n junction, these nanoparticles must be dispersed and cast onto an enargite film. Details for the solutions tested are provided in Table 5.4. Wetting behavior was determined relatively by pipetting the same volume of liquid onto the surface of an enargite film and monitoring the spread of the solution. Colloidal stability was determined by exposing two of the same suspensions to a light, where one suspension had just been vortexed and the other had been left untouched. If the solutions were observed to scatter light similarly, they were determined to have colloidal stability for that length of time. Once the suspensions began to show different light scattering capabilities, this time was chosen to be the extent of the stability. Times investigated were on the order of seconds, minutes, one hour, and several hours. Considering ZnS colloidal stability and enargite wettability, pyridine was chosen as the dispersing solution for these nanoparticles. Devices made from casting ZnS nanoparticles suspended in pyridine onto enargite films resulted in device efficiencies of zero percent, although some diode-like behavior was noted.

5.4 Conclusions and future directions

This chapter focused on achieving improved band alignment in enargite-based solar technology. First, modeling of the enargite interface at the back contact was completed and demonstrates a near-ideal alignment with molybdenum. However, the formation of MoS_2 is expected to be detrimental to device properties, contrary to $MoSe_2$ formation in CIGSe technology. Future efforts can either aim to ensure minimal formation of MoS_2 or use a different back contact with a similar work function to the $\{110\}$ planes of molybdenum, like gold or nickel.

Regarding the p-n junction, three routes were explored for the formation of ZnS thin films on enargite thin films. The chemical bath deposition route was inconclusive regarding the formation of Zn(S,O), but devices made from the synthesized material did not demonstrate diode-like behavior. A promising route for ZnS thin film formation is to convert sputtered ZnO films through exposure to H_2S gas at elevated temperatures. The challenge will be attaining complete conversion of the ZnO phase without compromising the enargite film. Low temperature, long treatments with a high flow rate over thin films should be investigated in future efforts. Lastly, ZnS nanoparticle syntheses were investigated to directly cast the appropriate phase onto enargite films. Future studies can further optimize dispersing solution and casting method to ensure an even coating is applied over the film. The hypothesis that ZnS will be able to form a high-efficiency enargite-based solar cell could not be tested, since the formation of a robust p-n junction was never achieved with the conditions described. Alternatively, high-efficiency enargite-based photovoltaic technology may be achievable through the deposition of other identified n-type junction pairs such as ZnTe or WO_3 (Wallace et al., 2019).

5.5 Acknowledgements

J.A. would like to acknowledge financial support from the NSF under grant #1144843 (Purdue-Tuskegee IGERT on globally sustainable electronics) and laboratory support from the NSF under grant #1534691-DMR (DMREF: Rapid Design of Earth Abundant Inorganic Materials for Future PVs). He thanks Dr. Scott McClary for XRD and Raman training and assistance as

well as informative discussions during the development of this chapter, Dr. Chris Gilpin and Jameson Root for assistance and training with scanning electron microscopy, Dr. Brian Graeser, Dr. Xianyi Hu, Essam Alruqoba, and Jonathan Turnley for training and assistance with providing molybdenum-coated soda-lime glass, Weideman for assistance and training on the thermal evaporator, and Ryan Ellis, Swapnil Deshmukh, Essam Alruqoba, Apurva Pradhan, and Jonathan Turnley, for their assistance with E-beam depositions.

5.6 References

Ahn, H. and Um, Y. (2015). Post-annealing Effects on ZnS Thin Films Grown by Using the CBD Method. *Journal of the Korean Physical Society*, 67(6):1045–1050.

Araoz, R. S. (2009). *Chemical bath deposition of Zn(S,O) buffer layers and application in Cd-free chalcopyrite-based thin-film solar cells and modules*. PhD thesis, Freien Universitat Berlin.

Ganatra, R. and Zhang, Q. (2014). Few-Layer MoS2 : A Promising Layered Semiconductor. *ACS Nano*, (5):4074–4099.

Gray, J., Wang, X., Vamsi, K. C. R., Sun, X., Kanti, A., and John, R. W. (2011). ADEPT 2.1.

Hariskos, D., Menner, R., Jackson, P., Paetel, S., Witte, W., Wischmann, W., Powalla, M., Bürkert, L., Kolb, T., Oertel, M., Dimmler, B., and Fuchs, B. (2012). New reaction kinetics for a high-rate chemical bath deposition of the Zn(S,O) buffer layer for Cu(In,Ga)Se2-based solar cells. *Progress in Photovoltaics: Research and Applications*, 20(January):534–542.

Hong, J., Lim, D., Eo, Y. J., and Choi, C. (2018). Chemical bath deposited ZnS buffer layer for Cu(In,Ga)Se 2 thin film solar cell. *Applied Surface Science*, 432:250–254.

Hsiao, K.-J., Liu, J.-D., Hsieh, H.-H., and Jiang, T.-S. (2013). Electrical impact of MoSe2 on CIGS thin-film solar cells. *Physical Chemistry Chemical Physics*, 15:18174–18178.

Hwang, D. H., Ahn, J. H., Hui, K. N., Hui, K. S., and Son, Y. G. (2012). Structural and optical properties of ZnS thin films deposited by RF magnetron sputtering. *Nanoscale Research Letters*, 7(26):1–7.

Islam, M. A., Hossain, M. S., Aliyu, M. M., Sulaiman, Y., Karim, M. R., Sopian, K., and Amin, N. (2012). COMPARATIVE STUDY OF ZnS THIN FILMS GROWN BY CHEMICAL BATH DEPOSITION AND MAGNETRON SPUTTERING. In *2012 7th International Conference on Electrical and Computer Engineering*, pages 86–89. IEEE.

Kam, K. K. and Parkinson, B. A. (1982). Detailed Photocurrent Spectroscopy of the Semiconducting Group VI Transition Metal Dichalcogenides. *Journal of Physical Chmistry*, 86:463–467.

Kim, J. H., Rho, H., Kim, J., Choi, Y.-J., and Park, J.-G. (2012). Raman spectroscopy of ZnS nanostructures. *Journal of Raman Spectroscopy*, 43:906–910.

Klinkert, T., Theys, B., Patriarche, G., Jubault, M., Donsanti, F., Guillemoles, J.-F., and Lincot, D. (2016). New insights into the Mo/Cu(In,Ga)Se2 interface in thin film solar cells: Formation and properties of the MoSe2 interfacial layer. *The Journal of Chemical Physics*, 154702.

Lin, Y. C., Yen, W. T., and Wang, L. Q. (2012). Effect of substrate temperature on the characterization of molybdenum contacts deposited by DC magnetron sputtering. *Chinese Journal of Physics*, 50(1):82–88.

McClary, S. A. (2019). *SYNTHESIS AND CHARACTERIZATION OF COPPER ARSENIC SULFIDE FOR SOLUTION-PROCESSED PHOTOVOLTAICS*. PhD thesis, Purdue University.

McClary, S. A., Li, S., Yin, X., Dippo, P., Kuciauskas, D., Yan, Y., Baxter, J. B., and Agrawal, R. (2019). Optoelectronic Characterization of Emerging Solar Absorber Cu3AsS4. In *IEEE Photovoltaics Specialists Conference Proceedings*, pages 3–7.

Pham, V. P. and Yeom, G. Y. (2016). Recent Advances in Doping of Molybdenum Disulfide: Industrial Applications and Future Prospects. *Advanced Materials*, 28:9024–9059.

Scheer, M. D. and Fine, J. (1969). Electron Affinity of Lithium. *J. Chem. Phys.*, 50:4343.

Shimada, T., Ohuchi, F. S., and Parkinson, B. A. (1994). Work Function and Photothreshold of Layered Metal Dichalcogenides. *Japanese Journal of Applied Physics*, 33:2696–2698.

Steirer, K. X., Garris, R. L., Li, J. V., Dzara, M. J., Ndione, P. F., Ramanathan, K., Repins, I., Teeter, G., and Perkins, C. L. (2015). Co-solvent enhanced zinc oxysulfide buffer layers in Kesterite copper zinc tin selenide solar cells. *Physical Chemistry Chemical Physics*, 17(23):15355–15364.

Wallace, S. K., Butler, K. T., Hinuma, Y., and Walsh, A. (2019). Finding a junction partner for candidate solar cell absorbers enargite and bournonite from electronic band and lattice matching. *Journal of Applied Physics*, 125(5):1–8.

Wallace, S. K., Svane, K., Huhn, W. P., Zhu, T., Mitzi, D. B., Blum, V., and Walsh, A. (2017). Candidate photoferroic absorber materials for thin-film solar cells from naturally occurring minerals: enargite, stephanite, and bournonite. *Sustainable Energy & Fuels*, 1(6):1339–1350.

Wu, W., Shen, H., Chen, J., Shang, H., Li, J., Yang, W., and Li, Y. (2018). Impact of thiourea concentration on the properties of sol–gel derived Zn(O,S) thin films and Cu(In,Ga)Se2 solar cells. *Journal of Sol-Gel Science and Technology*, pages 266–273.

Yan, X., Zhu, L., Zhou, Y., E, Y., Wang, L., and Xu, X. (2015). Dielectric property of MoS2 crystal in terahertz and visible regions. *Applied Optics*, 54(22):6732–6736.

CHAPTER 6. ENVIRONMENTAL AND HUMAN HEALTH ANALYSES OF Cu_3AsS_4 PHOTOVOLTAIC TECHNOLOGY

A version of this chapter has been published in two prior publications: a journal article Andler, J., Mathur, N., Sutherland, J., Zhao, F., and Handwerker, C. *Guiding the environmental design of a novel solar absorber through life cycle assessment by identifying anticipated hot spots.* doi: 10.1016/j.jclepro.2020.120847 (Andler et al., 2020) and a conference paper Andler, J., Mathur, N., Zhao, F., and Handwerker, C. *Assessing the Potential Environmental Impact of Cu_3AsS_4 PV Systems.* doi: 10.1109/PVSC40753.2019.8981146 (Andler et al., 2019). These papers have been merged with the supporting information, sections have been added, and figures have been adapted where appropriate. References to Appendix B reflect Appendix B referenced in the journal publication.

6.1 Introduction

Purposeful engineering during a product's design stage can mitigate potential human and environmental concerns associated with that product (Giudice et al., 2004, Lewis et al., 2017). Therefore, identifying products that may have life cycle concerns is important so that environmental screening can inform product design. Environmental screening can take the form of quantitative environmental analysis such as life cycle assessment (LCA), which is a technique widely used to quantify life cycle impacts of a product or process through attributing impacts to predetermined material flows in a life cycle inventory (LCI). The results from LCAs can be used to identify potential hot spots and determine opportunities where design changes can be made to affect improvement. Specific examples of design changes include identifying key areas to reduce waste, increase process efficiency, or search for material alternatives. Promising technologies that may exhibit significant environmental concerns should be identified and assessed at early stages to reduce their anticipated life cycle impacts. Regarding emerging photovoltaic (PV) technology, many assessments have been completed to identify notable areas of improvement on a variety of absorber materials (Chatzisideris et al., 2016).

We have identified Cu_3AsS_4 polymorphs enargite and luzonite as promising solar absorbers. However, having arsenic as a constituent leads to concern over toxicity, carcinogenicity, and other life cycle impacts. Similar concerns were raised during the development of cadmium telluride (CdTe) solar technology (Fthenakis and Moskowitz, 1995, Fthenakis, 2004), but these concerns have been mitigated through careful life cycle analyses and identifying strategies for responsible life cycle management (Held and Ilg, 2011, Sinha and Wade, 2018). Here, reducing the potential life cycle impact will be investigated through the completion of an LCA aimed at influencing the design of Cu_3AsS_4 technology.

The main goals and supporting goals of this paper are to:

(G1) Assess the potential life cycle impacts of Cu_3AsS_4 technology.

(G1.1) Compare Cu_3AsS_4 PV with CdTe, $Cu(In,Ga)Se_2$ (CIGS), and multicrystalline silicon (mc-Si) technology.

(G1.2) Identify significant contributors to the anticipated life cycle impact of Cu_3AsS_4 PV systems.

(G1.3) Identify significant contributors to the calculated range of life cycle impacts of Cu_3AsS_4 PV systems to determine inputs where focused effort can most effectively reduce uncertainty in future research.

(G1.4) Quantify the extent that product performance, mounting decisions, and available radiation affect the calculated life cycle impact of Cu_3AsS_4 PV systems.

(G2) Use these assessment results to offer design considerations for the development of Cu_3AsS_4 technology.

Towards (G1), a cradle-to-grave LCA on prospective Cu_3AsS_4 photovoltaic technology is completed in Section 6.3.3. These results are supplemented with a contribution analysis in Section 6.3.4., a sensitivity analysis in Section 6.3.5., and scenario analyses in Section 6.3.6. Towards (G2), design considerations based on the results of these analyses are discussed in Section 6.5.

6.2 Research motivation and methodology

6.2.1 Motivation to assess Cu_3AsS_4 technology

The motivation to assess this technology from a material property perspective is detailed in Section 1.2 of this dissertation. Regarding life cycle concerns, no LCA literature exists addressing the environmental impacts of copper arsenic sulfide semiconductors.

One approach to reduce environmental concerns in Cu_3AsS_4 technology is to substitute arsenic with other group V elements (P, Sb). Indeed, studies have shown promise for these materials as well (Banu et al., 2016, Franzer et al., 2014, Yin et al., 2019). However, the defect nature of these materials has not yet been studied and it is unknown at this time which group V elements will exhibit superior performance. Mid-band gap defects are known to vary by element and electronic structure (Huang et al., 2019, Sai Gautam et al., 2018), so changing group V elements in this system is expected to influence the defect nature of these materials. Whether these defects are benign, detrimental, or can be easily passivated is an area of increasing concern in related solar cell materials (Fiducia et al., 2019, Huang et al., 2014, Savory and Scanlon, 2019, Yu and Carter, 2016, Yuan et al., 2015). Therefore, a direct substitution during this early research stage is not yet justified.

6.2.2 Methodology concerning life cycle assessment for a prospective Cu_3AsS_4 PV system

LCAs are comprised of four main components that include: defining the goal and scope, performing an inventory analysis, generating an impact assessment, and interpreting the data in the context of the goal and scope. The first three components are discussed in Sections 6.2.2.1., 6.2.2.2., 6.2.2.3., respectively. The interpretation of these data is completed with an uncertainty analysis, sensitivity analysis, and scenario analyses in sections 6.2.2.4., 6.2.2.5., and 6.2.2.6., respectively. Many variations of life cycles that are encompassed by the LCA exists. One of these variations is called a cradle-to-grave LCA, which specifies the environmental impact from

the extraction, purification, manufacturing, use, and disposal stages of the product. This study performs a cradle-to-grave LCA.

6.2.2.1 Assessment scope and key assumptions

For LCA studies in general, the purpose of defining the goal is to clearly state the motivation of completing the LCA so that the reader can easily follow the data and arguments provided in the paper. The purpose of defining the scope is to clearly justify what is included in and excluded from the analysis in terms of system bounds, assumptions, and limitations so the study is transparent and repeatable. By defining these bounds and the functional unit, the study can more effectively be compared to other studies or adapted to suit other specific applications. The system bounds define the scope of the work and clearly outline what processes or part of the life cycle is accounted for in the study. Assumptions made and limitations that result from defining these bounds should be included. In this LCA, the study goal, system bounds, functional unit, and key assumptions are provided below. The limitations of this study are detailed in Section 6.2.2.8.

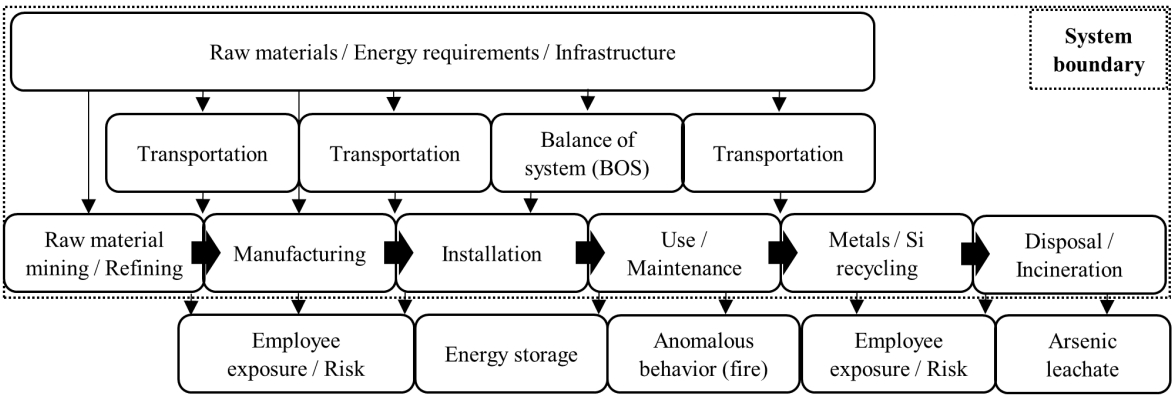

Figure 6.1. The system boundary for this cradle-to-grave assessment.

The system bounds for this cradle-to-grave assessment are illustrated in Figure 6.1. A functional unit for comparison to other technologies is chosen to be the generation of 1 kWh of electricity, averaged over the total amount of energy produced during the system lifetime. Note that this functional unit is different than 1 kWh of dispatchable electricity; energy storage and other

backup methods can considerably influence calculated impact results (Bilich et al., 2017) but are not addressed here. For decommissioning of the PV system, transportation is included to a local municipal waste facility where the energy requirements for panels recycling are included based on CdTe data for all thin film PV panels (Held and Ilg, 2011) and polycrystalline silicon data for mc-Si PV panels (Corcelli et al., 2017). Plastics are assumed to be incinerated and energy credits are only given for plastics in solar panels according to CdTe data (Held and Ilg, 2011). Printed circuit boards from inverters are assumed to be disassembled and smelted for metals recovery with no recycling credits. Recycled silicon credits are applied assuming recovery rates of 90% (Komoto and Lee, 2018) and a substitution ratio of 95% (Corcelli et al., 2017). Glass and bulk metals from the balance of system (BOS) and frame are assumed to be recycled based on standard material flows (European Commission, 2019). The system boundary and decommissioning assumptions are similar for all PV technologies assessed in this LCA.

The LCA has been completed according to ISO 14040 (ISO/TC 207, 2006a), ISO 14044 (ISO/TC 207, 2006b), and International Energy Agency recommendations for implementing LCAs on PV technology (Frischknecht et al., 2016) with key assumptions outlined in Figure 6.2. Similar LCA studies have used photoconversion efficiencies (Sengül and Theis, 2011) and/or panel lifetimes (Celik et al., 2016, García-Valverde et al., 2010) not yet achieved in a module to make comparisons with other PV technologies by assuming reasonable technological development of the respective absorber. Likewise, Cu_3AsS_4 is compared with CdTe, CIGS, and mc-Si solar cells by assuming a future scenario where Cu_3AsS_4 PV modules have efficiencies commensurate with these technologies. For this study, initial panel efficiencies of 18.6%, 18.6%, 19.2%, and 19.9% are assumed for Cu_3AsS_4, CdTe, CIGS, and mc-Si, respectively, reflecting champion panel efficiencies for the respective technologies (First Solar, 2015, Green et al., 2019, First Solar, 2018). Degradation to 80% of the initial efficiency over the lifetime of the module leads to an assessed average efficiency of 16.7%, 16.7%, 17.3%, and 17.9%, respectively. Other differences between the LCI for PV systems come from cell- and panel-specific data, mc-Si decommissioning and recycling credits and requirements, or when conservation of mass would otherwise be violated (e.g., CIGS LCI data suggest these solar modules are slightly heavier than CdTe modules, and therefore transportation impacts will not be the same between these two systems). BOS materials

(Jungbluth et al., 2012) are assumed to be the same for all PV technologies, but values reflect mass and area (efficiency) dependent inputs. Transportation distances for thin film modules are based on First Solar's Series 6 manufacturing capacities (First Solar, 2019).

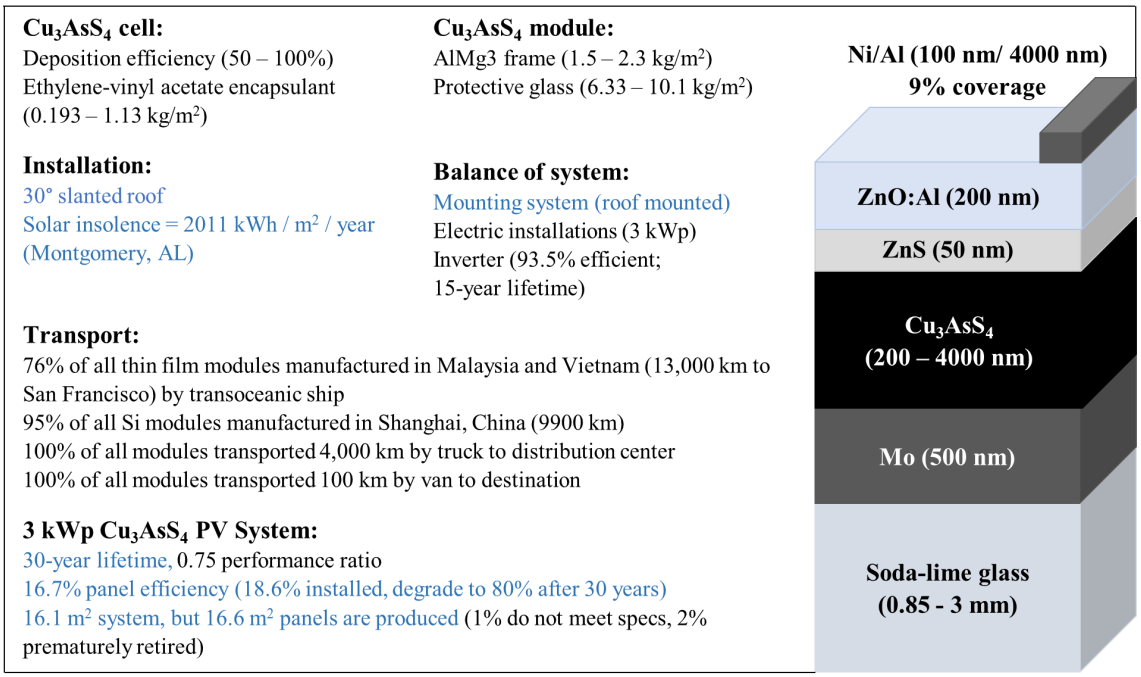

Figure 6.2. Snapshot of the key assumptions made in this study. Assumptions highlighted in blue are modified in Section 6.3.6.

6.2.2.2 Life cycle inventory

A life cycle inventory is a quantitative collection of all the inputs and outputs of a system, including all solid, liquid, and gaseous chemicals, catalysts, and byproducts. With this information, assessing where substantial amounts of toxins, carcinogens, or other waste is being generated and expelled in a system is straightforward. This information is a necessary preceding step to the impact analysis portion of the LCA.

Ecoinvent v3.5 has been used to model most unit processes for the LCI. Ecoinvent v2.2 has been used for unit processes like arsenic trioxide that do not exist in v3.5 and for inputs like

decommissioning that are assumed to take place in the United States. Input tables for Cu_3AsS_4, CdTe, CIGS, and mc-Si PV systems are included in Appendix B.1 of the journal publication and reflect recent LCI inventories for CdTe, CIGS, and mc-Si PV modules (Frischknecht et al., 2015, Sinha and Wade, 2018). A thorough description of how the LCI values were determined is available in Section 6.2.2.2. In short, because no commercial method of fabricating Cu_3AsS_4 solar modules exists, the LCI was developed from assumptions made about future manufacturing routes from current processing techniques. Many of these assumptions are revisited in the sensitivity analysis, but LCI ranges are used to capture possible impact scenarios instead of single values.

6.2.2.2.1. Cell architecture

A standard substrate for solar cells is glass 2-3 mm thick, but thinner (0.85 mm) glass substrates have been demonstrated (Dziedzic and Inglot, 2017). Polymer substrates can be used when PV materials are synthesizable at temperatures below about 200 °C, but since suitable Cu_3AsS_4 thin films have only been synthesized after processing at temperatures above 400 °C (McClary et al., 2017), glass was chosen as the substrate material for this solar cell. The range of substrate thickness in this study is 0.85 mm to 3 mm. Molybdenum is a common back contact for thin film solar cells like CIGS with a substrate architecture; a thickness of 500 nm is assumed. The optimal thickness for Cu_3AsS_4 thin films will vary based on absorption and minority carrier diffusion length, the latter of which is dependent on the minority carrier lifetime and mobility. Because these parameters are not fully characterized, a conservative estimate of 0.2-4 μm is calculated using available data (McClary et al., 2019, Yu et al., 2013). For n-type buffer layers, it is common for other thin film solar cells to apply approximately 50 nm CdS, however, ZnS is comparatively a better material concerning conduction band alignment (McClary et al., 2019) and is therefore modeled in this study. Common transparent conducting oxides used in thin film solar cells with a substrate architecture are doped ZnO and ITO. Considering long term market stability, doped ZnO has been chosen in this study to avoid the large competing market and relative scarcity of indium (U.S. Department of Energy, 2011). Ni/Al top contacts represent a standard grid for substrate architectures.

6.2.2.2.2. Semiconductor component deposition efficiency

It is assumed for thin film processing that deposition efficiencies of 50% are necessary for economic manufacturing processes (Zweibel, 1998) so that the total range of assessed LCI inputs is varied from the lowest necessary value (100% deposition efficiency) to twice this value (i.e. the calculated absorber range necessitates 0.29 – 5.73 mg of sulfur for stoichiometric Cu_3AsS_4 films ranging from 0.2-4 μm, but 0.29 – 11.5 mg of sulfur is assessed). These LCI input ranges are uniformly distributed and are tabulated in Appendix B.1 of the journal publication. Note that uniformly distributed mass distributions require a 1/x dependence on deposition efficiency, where the deposition efficiency is 67% for the mean value. For example, if a 100% deposition efficiency results in 10 g of material deposited, a 50% deposition efficiency results in 20 g of material deposited. However, depositing 15 g of material requires a deposition efficiency of 67%.

6.2.2.2.3. Auxiliary processes

Due to the tendency of arsenic and sulfur to volatilize at processing temperatures of 300-500 °C, we assume that processing conditions after copper deposition will more likely resemble CdTe processes such as close-space sublimation and vapor transport deposition than CIGS processes like co-evaporation and selenization. For this reason, auxiliary input processes such as isopropanol and other miscellaneous chemicals are taken from the LCI of CdTe and extended to 50% for LCI ranges. Inputs that are shared between CdTe and CIGS such as ethylene-vinyl acetate encapsulant and electricity are given a range that is bounded 50% below the lowest value and 50% above the highest value.

6.2.2.2.4. Other panel inputs

Frame inputs are modeled from CIGS data where ranges are made to encompass values from two reports (Frischknecht et al., 2015, Jungbluth et al., 2012). Protective glass must withstand

harsh environments and is assumed in this study to be tempered and range in thickness from 2.5 – 4 mm.

6.2.2.2.5. Transportation

Transportation for thin film modules is based on First Solar's Series 6 manufacturing capacities (First Solar, 2019) and assumes 82% (1.2 GW out of 6.6 GW are produced in Perrysburg, Ohio) of panels are shipped via transoceanic ship from Saigon, Vietnam and Kulim, Malaysia (13,000 km) to San Francisco, CA. Panels are then shipped by truck to Birmingham, AL, (4,000 km from San Francisco; 1,000 km from Perrysburg, Ohio) where they are transported 100 km by van to the final destination of Montgomery, AL.

6.2.2.3 Life cycle impact assessment

SimaPro version 8.5.2.0 has been used to complete the life cycle impact assessment by utilizing TRACI 2.1 version 1.04 with US 2008 as the normalization set (Ryberg et al., 2014). To calculate environmental and human health impacts from LCI input data, standard methodologies and control models for ten distinct impact categories are used and cited below. These impact categories and quantification methods are:

(ODP) Ozone Depletion Potential

(GWP) Global Warming Potential

(MIR) Maximum Incremental Reactivity; smog

(AP) Acidification Potential (Norris, 2002)

(EP) Eutrophication Potential (Norris, 2002)

(CA) Carcinogenics; human health (USETox)

(N-CA) Non-carcinogenics; human health (USEtox)

(RE) Respiratory Effects; human health; (PM2.5) criteria pollutants (Humbert, 2009)

(ETP) Ecotoxicity Potential; (USEtox)

(FFD) Fossil Fuel Depletion

Apart from fossil fuel depletion, all above indicators are controlled through legislation or international agreements and are used because reliable models have been built for the fate, transport, and potency of these indicators (Bare, 2012). ODP, GWP, and USEtox are internationally used, whereas criteria pollutants and MIR apply only to North America and the United States, respectively. Non-site-specific models exist for acidification and eutrophication through the increase in hydrogen ion potential and excess phosphorous and nitrogen concentration, respectively. Resource depletion is noted as the most controversial impact category because similar indicators do not yet exist (Bare, 2012).

6.2.2.4 Uncertainty in PV system modelling

Assumptions are made to simplify calculations and increase throughput where added effort may be unnecessary regarding the outcome of the calculations. For example, linearity is a typical assumption in LCA studies that assumes a linear relationship between a unit process and its environmental impact. Non-linear relationships can include effects from various quantities such as packaging, transportation, and energy usage. Although these physical relationships will change the calculated impact, linearity assumes these relationships contribute negligibly to the calculated impacts so that effort in this calculation space is unnecessary. In some systems with significant correlated processes, this assumption may introduce significant uncertainty into the reported values. In this early-stage study, the uncertainty attributed to assuming linearity is expected to be much lower than the variability associated with modelling different possible scenarios and probable unit process quantities. This distinction is described more in detail in the next section.

6.2.2.4.1. Uncertainty analysis

Many types of uncertainty exist in LCA analyses, and the reader is directed here for thorough analyses distinguishing types of uncertainty (Björklund, 2002, Hauschild et al., 2017, Huijbregts, 1998, Ries and Lloyd, 2007). The largest sources of uncertainty in this LCA are assumed to be parameter and scenario uncertainty. Parameter uncertainty for Cu_3AsS_4 modules

is attributed to epistemological uncertainty and is considered by assuming uniformly distributed LCI input ranges to account for the variability in possible inputs. Parameter uncertainty for other PV modules is attributed to a combination of basic parameter uncertainty and a lack of data quality, represented as a data quality indicator (DQI). Basic parameter uncertainty is a predefined uncertainty value assigned to each parameter (Weidema et al., 2013) that accounts for the imprecise nature of the reported parameter value. DQIs, in ecoinvent methodology, are the numeric result of subjective weighting calculated through the pedigree approach (Weidema et al., 2013). DQIs consider temporal, spatial, and other sources of uncertainty. DQIs and basic uncertainty are jointly propagated for CdTe, CIGS, and mc-Si module inputs to calculate the uncertainty of these systems. The traditional approach for uncertainty propagation is the use of Monte Carlo methods that randomly sample values from a predefined distribution representative of the input parameter (typically lognormal in LCA studies) and generate a distribution of probable impacts. Information gleaned from these distributions yields valuable insights about the life cycle impacts and uncertainty of a system but can be time consuming and are not accessible on all versions of LCA software. Alternatively, a transparent and high throughput approach to generating variance information from a set of distributions in the context of LCA is an analytical method derived from a first-order approximation using a Taylor series expansion (Heijungs, 2010, Hong et al., 2010, Imbeault-Tétreault et al., 2013, Jung et al., 2014). In systems with low uncertainty (coefficient of variation, CV $\approx$ 5%) and linear behavior, this method has been shown to accurately approximate impacts compared to sampling methods such as Monte Carlo analyses (Bisinella et al., 2016, Groen et al., 2014, Heijungs and Lenzen, 2014). As calculated in Appendix B.2. of the journal publication, CdTe, CIGS, and mc-Si systems have a calculated CV less than 7% regarding relative uncertainty. We note the assumed linearity and non-correlation between inventory vector components are limitations of this study. Nevertheless, this analytical uncertainty propagation method is used for CdTe, CIGS, and mc-Si PV systems. We note that inventory inputs with the same values such as BOS components, infrastructure, and most transportation, do not contribute to relative uncertainty and are excluded from the uncertainty propagation.

Opposed to DQIs for modeling parameter uncertainty, Cu_3AsS_4 modules are modeled with uniform distributions to capture the expected impact range due to parameter variability. Variability

is expected to influence the reliability of reported life cycle impacts of Cu_3AsS_4 modules, especially for electricity, substrate glass, and transportation, due to the discrete values dependent on solution vs vacuum processing, flexible vs standard substrate glass, and subsequent domestic vs international shipping with discrete module weights. Although these variable inputs are propagated with Monte Carlo simulations (distributions below) the calculated mean may not be representative of the anticipated life cycle impacts of the system much like a 50% mean probability is insufficient to describe the anticipated outcome of a coin flip. Therefore, a direct comparison between the mean calculated for Cu_3AsS_4 systems and other PV systems should be done cautiously. Furthermore, propagation of the range of impacts yields a distribution curve that is not to be interpreted the same as the lognormal distribution with 95% confidence intervals for CdTe, CIGS, and mc-Si PV systems. For Cu_3AsS_4 PV systems, the distribution represents the range of variability for calculated life cycle impacts due to the use of different input values, instead of distributions in other systems that represent uncertainty due to temporal, spatial, and technical parameters. Quantification of uncertainty in Cu_3AsS_4 PV systems like that carried out for CdTe, CIGS, and mc-Si PV systems is left for future research when industrial processing routes and input values are documented.

Cu_3AsS_4 life cycle impacts are reported as a range to capture input variability and with a mean to compare relative influence of location, efficiency, and lifetime in Section 6.3.6. Since uniform ranges can be propagated using mean values, this analysis does not fundamentally alter the calculated system impact compared to traditional life cycle impact assessment methods. However, uncertainty between these two methods is handled differently, as described above.

6.2.2.4.2. Matlab code and resulting distributions

Monte Carlo simulations were executed to generate 3200 data points using Matlab R2018b. These graphs were generated using the following code with ozone depletion potential as an example. Because the calculated values only consider inventory inputs that contribute to the impact range, BOS inputs are not propagated. Therefore, the x-axis bins in Figure 6.3 are not expected to reflect the total calculated impact range. Referencing Table 6.2, impact categories that are dominated

by a single contribution appear more trapezoidal (GWP and RE PM2.5) than those with equally contributing impactors (ODP, MIR, and FFD).

```
>>ODPR = []                          #create variable corresponding to the
                                     #magnitude of the range of possible ODP
                                     #impacts; copy output data from Excel
                                     #into variable (# rows = # LCI inputs)

ODPLB = []                           #create variable corresponding to the
                                     #lowest bound of the range for ODP
                                     #impacts; copy data from Excel into
                                     #variable (# rows = # LCI inputs)

TotODP = []                          #create numeric variable to store data

for j = 1:3200                       #number of iterations

k = 0                                #reset k for every new iteration

for i = 1:N                          #N = number of inputs; correlated
                                     #inputs are co-propagated

                                     #choose a random value in the possible
                                     #ODP range for each LCI input and add
k = k + rand()*ODPR(i) + ODPLB(i)    #to the low bound (ODPLB).
                                     #Cumulatively store in k to calculate a
                                     #single impact from the 44 inputs
end
TotODP[i] = k                        #add k value as an input into the variable
end
```

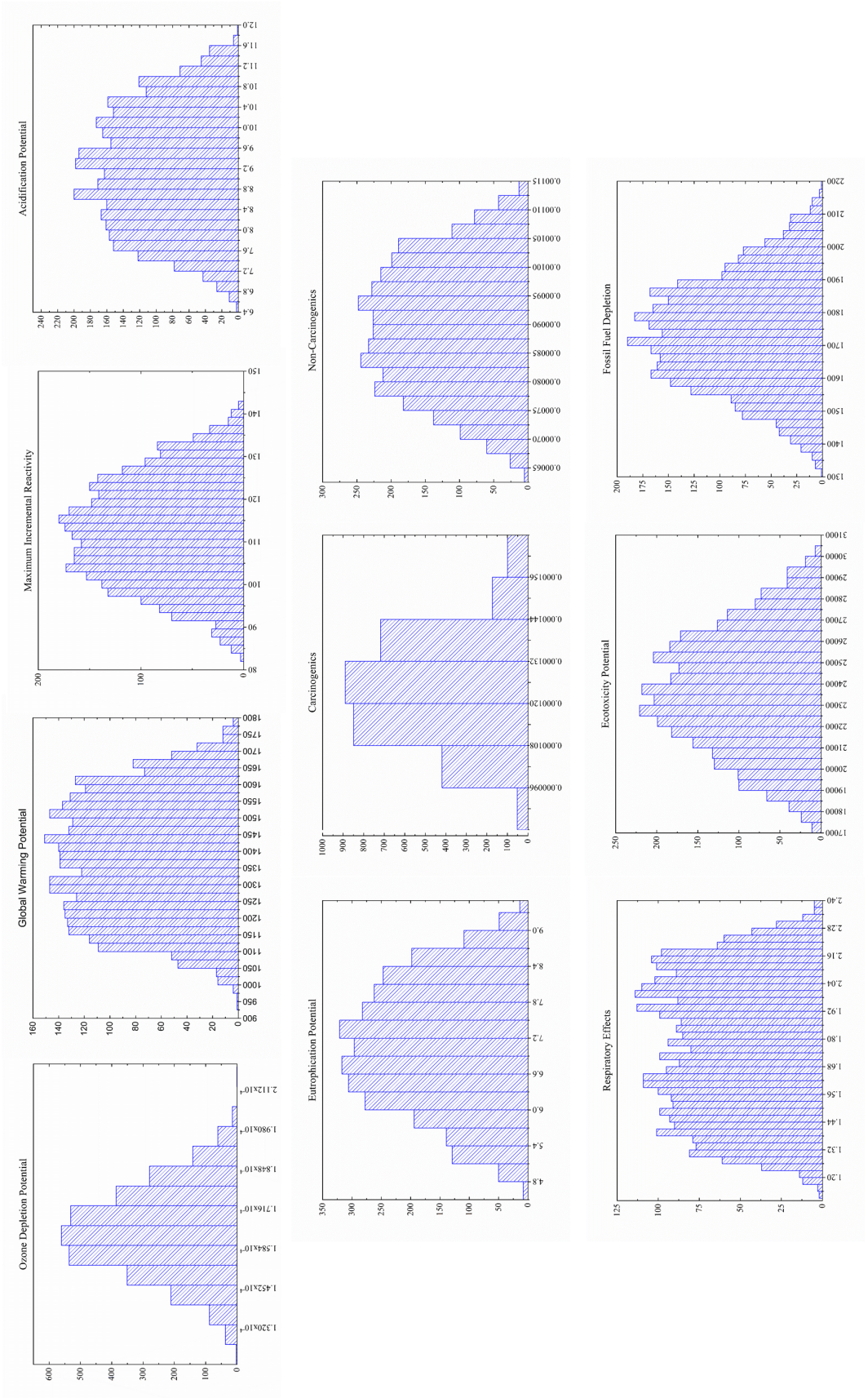

Figure 6.3. Distributions calculated from LCI input ranges for Cu_3AsS_4 PV modules

6.2.2.5 Sensitivity analysis

Two goals of the sensitivity analysis are to understand the inputs that are responsible for the greatest contribution to the impact range in the present study and to understand the inputs that may contribute most to the uncertainty in future research. For each of these goals, a variation of a contribution (dominance) analysis is completed. For the former goal, individual contributions to the impact range are calculated by dividing the input impact range by the total range (Appendix B.3. of the journal publication). The motivation to additionally analyze contributions to the uncertainty in future research is due to the arbitrary nature of the assigned impact ranges and distributions. These ranges and distributions have been shown to influence the identification of key variables in early-stage LCAs (Lacirignola et al., 2017). Consequently, the ranges and distributions originally assigned to Cu_3AsS_4 module components might be expected to influence the identification of most contributing inputs. Therefore, for the second goal of this sensitivity analysis, there is a need to identify key variables while remaining unbiased from the initial ranges and distributions assumed. A bias is defined here to be a distinction between the variable and system coefficient of variation (CV), since these variations have no physical basis. To ensure initial assumptions do not bias the sensitivity analysis, a common CV can be assumed for all inputs. Since a sensitivity analysis for inputs with a common CV simplifies to a contribution analysis, this approach simply identifies the dominant contributors to the module impacts. The results of this common CV approach are compared in Section 6.3.5. to the results of the former contribution analysis. This approach is typically not used for systems with known inventory values and distributions since there is a physical basis for variable CVs, such as data that is dissimilar spatially, technically, or temporally. Therefore, since the basis for variable CVs in future research is not known, this approach identifies inputs whose values should be documented with a fair amount of certainty before beginning a study so that uncertainty is kept to a minimum.

6.2.2.6 Scenario assessment

As mentioned in Section 6.2.2.4.1., a mean is not necessarily reflective of the expected life cycle impacts of Cu_3AsS_4 systems. However, it can still be useful for quantifying the influence of variables such as system location, efficiency, and lifetime that affect the energy generation of PV

systems but are not influenced by LCI inputs. Since comparative life cycle impacts are normalized to total energy generation, these variables will influence the calculated system mean. The practical limitations that may govern the efficiency and lifetime are not yet known, but since these variables will affect the calculated life cycle impacts, a range of values (10 - 25% and 15 – 40 years) are studied.

6.2.2.7 Defining environmental hot spots

This study aims to identify environmental hot spots in Cu_3AsS_4 PV systems to determine opportunities where design changes can be made to affect improvement. According to Flagship Project 3a of the United Nations Environment Programme and the Society of Environmental Toxicology and Chemistry, hot spot analysis is a framework that allows for rapid analysis of data from a range of information sources (Barthel et al., 2014). Defining "hot spot" is difficult because of vastly different stakeholder perspectives, inconsistent system boundaries, and available information included with each analysis (Barthel et al., 2014). However, definitions within groups or communities are helpful to remain self-consistent. Qualitative definitions for hot spots vary from identifying primary impactors like "the most important sources of environmental impact" (Nielsen and Wenzel, 2002) to grouping impactors like "hot, hotter, and hottest" (Ye et al., 2003). Quantitative definitions for hot spots use predefined criteria-based methods that compare data points to standards or averages and define a threshold that, when exceeded, indicates a hot spot. Some of these methods are demonstrated through continuous monitoring of nuclear reactors (Gandini, 2011), geospatial statistics used in commercial software such as ArcGIS (Getis and Ord, 1992), and end-of-life resource management (Ardente and Mathieux, 2014). Variations of these definitions could be applied here, for example, by determining the average impact in an impact category and calculating outliers based on standard deviation. However, there is no basis for a unimodal distribution of unit impacts and if wide or bimodal-like distributions are present, a large standard deviation may limit the number of outliers identified. Still, quantitative definitions for hot spot thresholds are helpful in this study to target key impactors while keeping impactor options broad (i.e., having a predefined method that does not arbitrarily choose the top N = 1, 2, etc. sources of concern).

A more general hot spot threshold definition suggested by UNEP/SETAC is to establish an arbitrary value, such as 25%, where a single parameter that influences more than 25% of the impact category is determined to be a hot spot (Barthel et al., 2014). However, since there are a growing number of hot spot analyses that include either additional quantified data or information as they become available (Barthel et al., 2014), it is helpful to have a definition that can correspondingly adapt to additional terms. As implied above, it is also helpful in some situations to have a definition that is not influenced by the degree of variability in the data. Lastly, this threshold should equal 100% when n=1 (an input is a hot spot in a system where it is the only input), should not converge, and should only identify hot spots when parameter impacts are significantly greater than the average. With these criteria in mind, we define a hot spot as satisfying the following condition:

$$\%\ impact \geq 100 * n^{-0.5}$$

where n is the number of foreground input parameters. For example, if an LCA has 100 LCI inputs, a hot spot is defined as one input that contributes to at least 10% of the total impact in at least one category. Since the number of inputs in an LCA study can be arbitrarily extended, here we define foreground inputs as those over which manufacturers have direct control. For example, a solar manufacturer will have direct control over the amount of copper that is used in each module, but not the amount of fuel used to purify the copper. With this definition, hot spots identified will be directly relevant to the manufacturer. Note that the exponent is ultimately arbitrary and can be increased to lower the threshold and include more hot spots. For comparison, using the standard deviation hot spot identification method results in equivalent exponents between 0.43 and 0.59 depending on impact category. The cumulative 80% threshold results in equivalent exponents between 0.49 and 0.9.

6.2.2.8 Limitations

6.2.2.8.1. Sources of uncertainty

Main sources of uncertainty not included in this study are from two forms of model uncertainty: linearity and characterization factors. Linearity refers to the inherent assumption that sources of error, including parameter uncertainty, are treated independently. Characterization factors consider the emission modification to the impact unit (i.e., the uncertainty associated with transforming kg CH_4 emissions into global warming potential, which has a unit of kg CO_2-eq). Therefore, this study does not capture the complex interdependencies of non-linear relationships in LCI data and characterization factors, nor does it consider inherent uncertainty associated with characterization factors. For these reasons, the uncertainty in this study does not capture the uncertainty necessary to report absolute life cycle impacts. Impacts in this study are to be interpreted relatively.

6.2.2.8.2. Film deposition waste

We note here that company information for CIGS molybdenum LCI data is calculated to require a film of approximately 600 nm (Frischknecht et al., 2015). We believe these data do not consider the waste associated with the sputter deposition process. In-house calculations on lab-scale equipment estimate a material utilization efficiency of approximately 0.1% during this process but can be improved to approximately 4% if high ($\geq$75%) target utilization methods are used. In this case, impacts due to molybdenum (and other sputtered material) can justifiably be modeled to contribute 20x more to life cycle impacts than current methods. If deposition waste (beyond the 50% lower bound) is considered in this LCA, Cu_3AsS_4 PV system impacts are increased by approximately 2% in the worst case for all materials other than molybdenum. Considering deposition waste for molybdenum increases impacts by at least 10% in every impact category. To remain consistent with the CIGS LCI, and since molybdenum impacts are of poor

data quality, additional deposition waste below 50% for sputtering and evaporation processes are not considered.

6.2.2.8.3. Allocations

Molybdenum is obtained from roasting molybdenite, which is produced both as a co-product in copper production and as a primary product. LCIs for molybdenite roasting are not available and zinc production is used as a proxy (Classen et al., 2009), which is noted as a crude approximation. Co-product allocations are assumed to be economically based, and since molybdenum to copper costs have remained approximately in the same proportion since the allocation last used in ecoinvent v2.1 (Classen et al., 2009, Nuss and Eckelman, 2014), the allocation percentage has not changed. However, using zinc production as a proxy is indicative of poor data quality, so molybdenum impacts in this study are communicated with reservations.

Arsenic trioxide is obtained as a by-product from copper production, so allocation is necessary. Both mass and economic allocations for impacts attributable to arsenic are calculated and compared. Arsenic is produced as a by-product from copper smelting where 0.07 kg As_2O_3 is extracted for every 1 kg Cu (Nuss and Eckelman, 2014). For a mass allocation, 0.07 / (1 + 0.07) $\approx$ 6.5% of impacts are allocated to arsenic trioxide.

When allocating economically, arsenic trioxide has been reported to and is used in the ecoinvent software as yielding 0.5% of the environmental impacts (Nuss and Eckelman, 2014). This allocation will change depending on the cost per kg, arsenic content in extracted ores, and primary product, which are addressed separately here. When this allocation was made, copper was US $6.7 per kg and arsenic trioxide was US $0.46 (Nuss and Eckelman, 2014). From the United States Geological Survey, the current prices are US $3.0 per kg and US $0.59 (average of US $0.75 from Morocco and US $0.42 from China) per kg of copper and arsenic trioxide, respectively (Reilly II and Bernhardt, 2019). These updated prices will increase arsenic allocations by a factor of roughly ($0.59/$3.0)/($0.46/$6.7) $\approx$ 3. Regarding arsenic content in extracted ores, the Bou Azzer mine, Morocco, is reported to have arsenic concentrations of at most 300 ppm (Ahmed et al., 2009), which accounts for 50% of US imports of arsenic trioxide

(Reilly II and Bernhardt, 2019). Considering data from ecoinvent, arsenic concentrations in copper concentrate is approximately 0.75% (Nuss and Eckelman, 2014). Since copper concentrate has approximately 30% copper content (Classen et al., 2009) and copper is mined from ores that contain approximately 1% (0.2% - 2%) copper, arsenic concentrations in these ores are assumed to be approximately $1\% * 0.75\%/30\% = 0.025\%$, or 250 ppm. This calculation assumes arsenic is concentrated in the same proportion as copper. Therefore, since 250 ppm is modeled in ecoinvent and concentrations in the Bou Azzer mine are at most 300 ppm, the arsenic concentrations are not assumed to influence the arsenic allocation. Lastly, the Bou Azzer mine produces cobalt, instead of copper. Since cobalt has approximately ten times greater cost per kg than copper (Reilly II and Bernhardt, 2019), the allocated impact for arsenic will decrease by a factor of ten from Morocco imports. Because Morocco imports account for 50% of total imports, arsenic allocations will decrease by a factor of roughly 5, assuming China's production of arsenic trioxide is from copper production. Therefore, a factor of 3 from updated copper and arsenic costs and a factor of 0.2 from cobalt and copper cost comparisons suggest that the arsenic allocation in ecoinvent (0.5%) is approximately consistent with the assumptions in this study that include updated economic calculations. For the calculations in this study, allocation is based on mass to avoid underestimating arsenic contributions to the life cycle impacts.

6.3 LCA on prospective Cu_3AsS_4 systems

In line with (G1), it is possible Cu_3AsS_4 thin films may find application in optoelectronic applications other than PV systems. Broadening the environmental analysis of Cu_3AsS_4 semiconductors, an upstream assessment on copper, arsenic, and sulfur as source materials is completed in Section 6.3.1.

6.3.1 Upstream environmental assessment for Cu_3AsS_4 thin films

The scope of this investigation includes processes and waste associated with mining, purification, and transport of copper, arsenic, and sulfur in stoichiometric ratios. Raw materials and energy requirements for the infrastructure needed to source the material is considered. This

assessment does not include processing of these materials to form a Cu_3AsS_4 crystal or the disposal of these materials at the end of life, even though these procedures are expected to influence the calculated life cycle impacts. The extent to which these parameters affect the impacts will vary depending on application, and an example application for solar cells is demonstrated in Section 6.3.3. This assessment assumes a material utilization efficiency of 100%.

6.3.1.1 Assumptions

Copper is a primary metal assumed to be mined from sulfidic ores that contain a mix of 0.2 – 2% wt. copper. Sulfur is assumed to be recovered from a combination of petroleum refining operations and natural gas production in the form of hydrogen sulfide and sulfur dioxide, which is converted to elemental sulfur through the Claus process (Sassi and Gupta, 2008). Arsenic is vaporized during smelting of nonferrous metal ores and is typically removed in the form of arsenic trioxide through electrostatic precipitation (Carapella, 2002, Dalewski, 1999). Current economic allocation of arsenic trioxide as a byproduct of copper production is consistent with information available in the database and is discussed in Section 6.2.2.8.3. Arsenic trioxide is used in this study as a proxy for As_2S_5, which is an arsenic source used in the processing of enargite Cu_3AsS_4 thin films (McClary et al., 2017). Transportation for copper and sulfur are included in the LCI unit process for the market product and are based on average transport distances based on commodity flow surveys through the United States Department of Transportation's Bureau of Transportation Statistics. Transportation is not inherently included in arsenic trioxide's unit process. Transportation inputs are included to account for arsenic trioxide's transportation to and within the United States; 50% imported from Morocco and 50% from China (Reilly II and Bernhardt, 2019). The transportation distances used are approximations made by the authors. All input values are calculated in Appendix B.4 of the journal publication.

6.3.1.2 Upstream environmental assessment for a Cu_3AsS_4 thin film

The goal of this investigation is to identify upstream life cycle impacts tied to the constituent elements of stoichiometric Cu_3AsS_4 and relate these impacts to real systems. Furthermore, we hope to quantify the influence of the choice of allocation on the calculated contribution in this

case scenario. Both economic and mass allocations have been documented in Table 1, with mass allocations in bold.

Case 1 calculates the percentage contribution to life cycle impacts from only copper, arsenic trioxide, sulfur, and transportation (transportation values are calculated in Appendix B.4. of the journal publication). To relate these results to real systems, Case 2 presents an analysis of impacts that have been completed on a system composed of a 3 μm Cu_3AsS_4 thin film with a 2 mm thick SLG substrate.

Table 6.1. *Relative impacts in upstream Cu_3AsS_4 systems. Case 1: Impact contributions of copper, arsenic, and sulfur to a Cu_3AsS_4 system. Case 2: Impact contributions of SLG, copper, arsenic, and sulfur to a Cu_3AsS_4 system with a 2 mm SLG substrate. Italicized percentages reflect calculated values with an economic allocation; bolded percentages reflect calculated values with a mass allocation.*

		ODP	GWP	MIR	AP	EP	CA	N-CA	RE	ETP	FFD
Case 1: Cu_3AsS_4 only	Contribution (%) of **Cu_3AsS_4** to system impacts	100	100	100	100	100	100	100	100	100	100
	Contribution (%) of **Cu** to system impacts	97 **96**	95 **82**	94 **57**	98 **87**	94 **11**	94 **21**	94 **21**	96 **55**	94 **11**	77 **66**
	Contribution (%) of **As_2O_3** to system impacts	0.5 **1.5**	2.8 **17**	5.2 **43**	1.3 **12**	6.4 **89**	5.8 **79**	5.7 **79**	3.7 **45**	6.4 **89**	2.3 **12**
	95% confidence interval range (%), lognormal	9.8	9.8	9.8	9.8	9.8	9.8	9.8	9.8	9.8	9.8
Case 2: Cu_3AsS_4 + 2 mm SLG	Contribution (%) of **SLG** to system impacts	94	99	98	95	63	75	40	94	43	99
	Contribution (%) of **Cu_3AsS_4** to system impacts	5.8	1.0	1.6	4.7	37	25	60	6.1	57	1.1
	Contribution (%) of **Cu** to system impacts	5.6 **5.6**	1.0 **0.8**	1.5 **0.9**	4.6 **4.0**	35 **3.9**	24 **5.0**	57 **12**	5.9 **3.2**	53 **5.8**	0.8 **0.5**
	Contribution (%) of **As_2O_3** to system impacts	0.03 **0 .09**	0.03 **0.2**	0.08 **0.7**	0.06 **0.6**	2.4 **33**	1.5 **20**	3.4 **47**	0.2 **2.7**	3.6 **51**	0.03 **0.1**
	95% confidence interval range (%), lognormal	9.8	9.8	9.8	9.8	9.8	9.8	9.8	9.8	9.8	9.8

ODP, ozone depletion potential; GWP, global warming potential; MIR, maximum incremental reactivity; AP, acidification potential; EP, eutrophication potential; CA, carcinogenic; N-CA, non-carcinogenic; RE, respiratory effects; ETP, ecotoxicity potential; FFD, fossil fuel depletion; SLG, soda-lime glass.

As this system is expanded to include a substrate, the relatively small amount of absorber material still has a significant contribution to the life cycle impacts in many impact categories. Even though this thin film is comparatively about three orders of magnitude thinner than the substrate, it still contributes to over 50% of the impacts in N-CA and ETP impact categories. Therefore, using a small amount of material does not justify omitting Cu_3AsS_4 films from calculations. Furthermore, using a mass allocation increases the percent impacts attributable to arsenic trioxide between three and 14 times depending on impact category. Therefore, the choice of allocation procedure must be justified when using arsenic trioxide as an arsenic source, since this choice is not expected to produce negligibly different results.

The results of this assessment demonstrate that impacts attributable to Cu_3AsS_4 are not expected to be negligible, even though the film is only a few micrometers thick. Furthermore, the choice of allocation procedure (mass vs economic) is shown to influence impacts attributable to arsenic by up to 80% in eutrophication and ecotoxicity impact categories. We therefore urge practitioners to justify choice of allocation when using arsenic trioxide in future studies.

6.3.2 Defining reporting differences compared to traditional life cycle assessment studies

The remainder of this study details the results of integrating Cu_3AsS_4 films into a PV system. As this life cycle assessment of Cu_3AsS_4 PV systems is completed when knowledge of industrial processes is minimal, the analysis will subtly change to address the larger uncertainty of inventory inputs. Figure 6.4 illustrates these changes along with the corresponding analysis section.

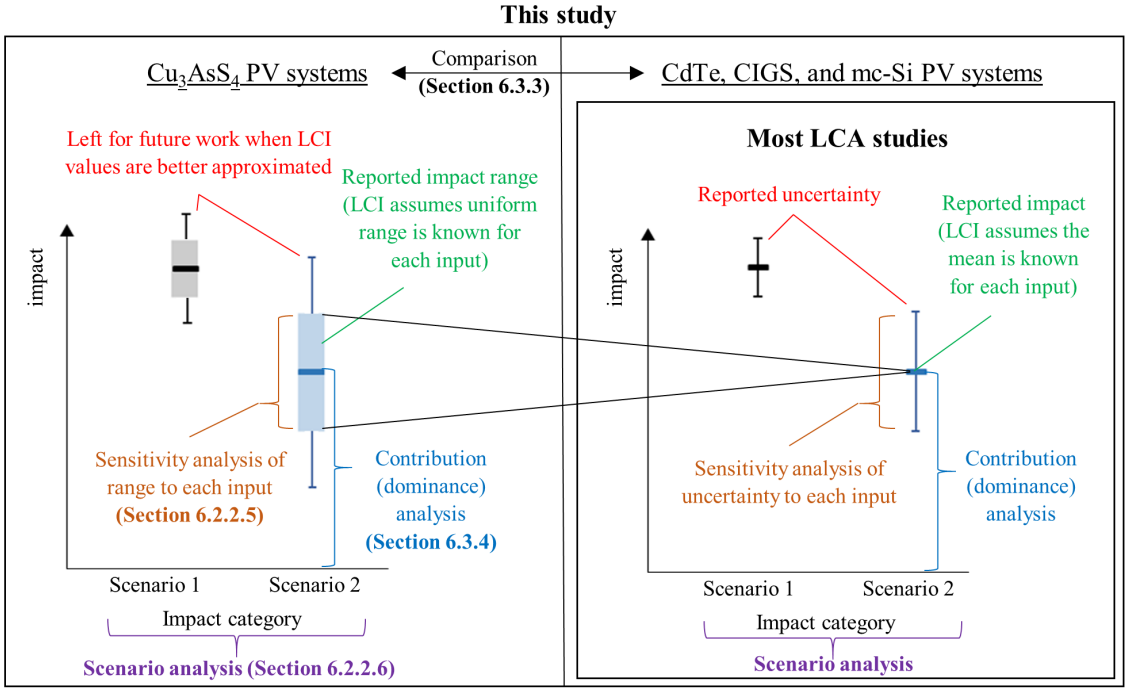

Figure 6.4. Conceptual comparison between the analysis for this study and most other LCA studies.

6.3.3 Comparison to other PV systems

In line with (G1.1), Figure 6.5 presents relative impacts for all PV systems examined in this study. Impact ranges calculated for Cu_3AsS_4 systems are consistent with other thin film technologies and are expected to be lower than mc-Si impacts in all impact categories for the scenario outlined Figure 6.2. The 95% confidence intervals obtained from analytical uncertainty propagation for CdTe, CIGS, and mc-Si PV systems are calculated in Appendix B.2 of the journal publication. The distributions calculated from Monte Carlo simulations for Cu_3AsS_4 modules are shown in Figure 6.3. Cu_3AsS_4 impacts overlap both CdTe and CIGS impacts in most categories except CA, N-CA, and ETP where the lowest projected Cu_3AsS_4 impact still exceeds CdTe. This result is primarily due to the molybdenum back contact used in both these and CIGS absorbers. The excess sulfidic tailings associated with mining of molybdenum has a significant impact in

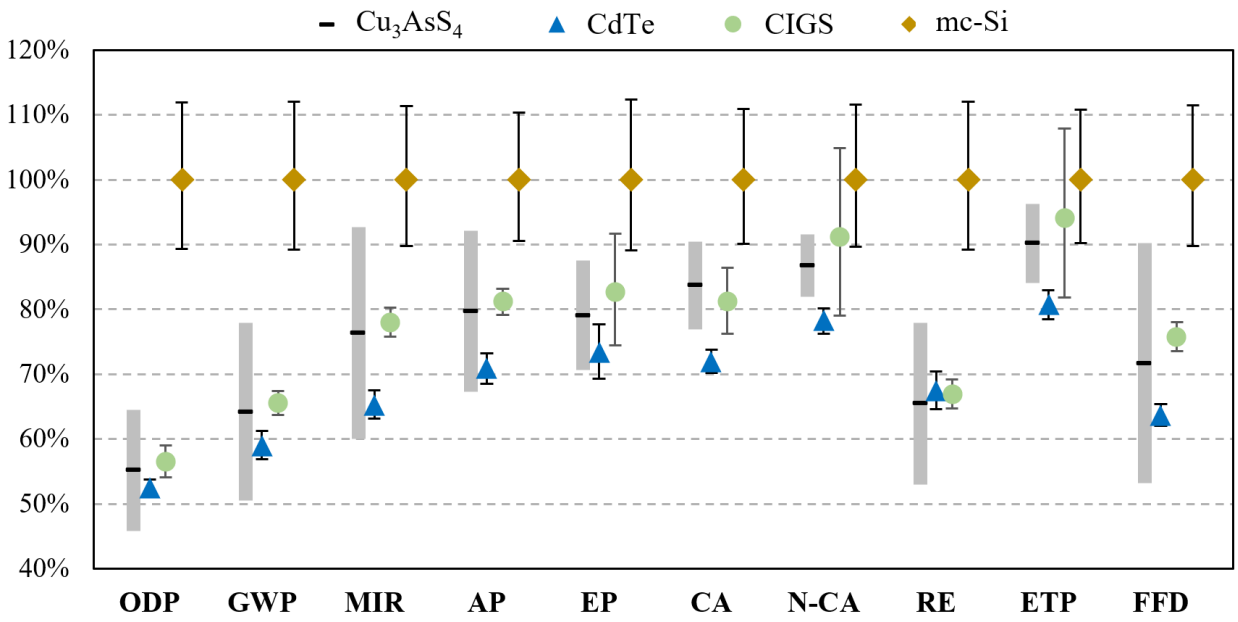

Figure 6.5. Roof-mounted 3 kWp PV system relative impacts per kWh. The range of impacts calculated for Cu_3AsS_4 PV systems is expressed as a gray bar while a 95% confidence interval calculated through AUP is denoted by capped error bars. Note that the mean value for Cu_3AsS_4 may not be directly comparable to other systems (see Section 6.2.2.4.1.). Impact categories: Ozone Depletion Potential (ODP), Global Warming Potential (GWP), Maximum Incremental Reactivity (MIR), Acidification Potential (AP), Eutrophication Potential (EP), Human Health – Carcinogenics (CA), Human Health – Non-carcinogenics (N-CA), Human Health – PM 2.5 Respiratory Effects (RE), Ecotoxicity Potential (ETP), and Fossil Fuel Depletion (FFD).

Table 6.2. *Calculated life cycle impacts associated with Figure 6.5. See Figure 6.3 for Cu_3AsS_4 distributions. μ = mean value; GSD^2 = squared geometric standard deviation.*

PV technology (distributions)	Distribution parameters	Ozone Depletion Potential (µg CFC-11-eq)	Global Warming Potential (g CO_2-eq)	Maximum Incremental Reactivity (g O_3-eq)	Acidification Potential (g SO_2-eq)	Eutrophication (g N-eq)	Carcinogenics (CTUh) (µg C_6H_6-eq)	Non-Carcinogenics (CTUh) (µg toluene-eq)	Respiratory Effects (mg PM2.5-eq)	Ecotoxicity (CTUe) (kg 2,4-D-eq)	Fossil Fuel Depletion (kJ surplus)
Cu_3AsS_4 (see Section 6.2.2.4.2.)	Avg.	**3.24**	**23.1**	**1.75**	**0.201**	**0.221**	**4.70**	**46.2**	**33.1**	**1.03**	**24.9**
	Min	**2.68**	**18.2**	**1.36**	**0.169**	**0.195**	**4.34**	**43.4**	**26.6**	**0.953**	**18.8**
	Max	**3.79**	**28.0**	**2.13**	**0.233**	**0.246**	**5.11**	**49.0**	**39.7**	**1.10**	**31.0**
CdTe (lognormal)	μ	**3.08**	**21.2**	**1.49**	**0.178**	**0.204**	**4.47**	**41.9**	**34.2**	**0.922**	**22.1**
	GSD^2	**1.01**	**1.02**	**1.02**	**1.02**	**1.04**	**1.02**	**1.02**	**1.03**	**1.02**	**1.02**
CIGS (lognormal)	μ	**3.32**	**23.7**	**1.79**	**0.205**	**0.233**	**4.83**	**49.1**	**34.3**	**1.08**	**26.2**
	GSD^2	**1.03**	**1.05**	**1.04**	**1.04**	**1.10**	**1.06**	**1.14**	**1.06**	**1.14**	**1.03**
mc-Si (lognormal)	μ	**5.96**	**36.6**	**2.34**	**0.257**	**0.287**	**6.00**	**54.2**	**52.0**	**1.16**	**34.3**
	GSD^2	**1.12**	**1.12**	**1.10**	**1.10**	**1.12**	**1.11**	**1.12**	**1.12**	**1.11**	**1.10**

categories and is also reflected in the relatively large uncertainty for CIGS. Cu_3AsS_4 N-CA impacts are expected to be lower than CIGS mostly due to the avoidance of volatile zinc emissions from extracting indium from zinc concentrates. All calculated impacts corresponding to Figure 6.5 are tabulated in Table 6.2. The contribution broken into main system components is discussed and illustrated below along with a brief description of the decommissioning assumptions as a supplement to the description in Section 6.2.2.1.

The impacts in Figure 6.5 are separated by component in Figure 6.6. Two inverters, mounting, and cabling requirements are included for BOS impacts and are tabulated in Appendix B.1 of the journal publication along with other component impacts. Decommissioning impacts include transportation to a recycling facility and electricity and chemical requirements for separating the glass and semiconductor materials. Environmental credits for decommissioning impacts are generated from the recovery of energy from module plastics incineration and avoided aluminum, copper, and steel production. Decommissioning impacts from metals are calculated by subtracting the SimaPro impact (generated from LCI inputs listed in Appendix B.1. of the journal publication with SimaPro version 8.5.2.0) from the Product Environmental Footprint Category Rules (PEFCR) modeling impact (European Commission, 2019). The PEFCR modeling impact has the previously recycled proportion (referred to as R1 in Section 5.11 using values in Tab. 6.10 of the PEFCR report) modified to match the recycled proportions assumed in the ecoinvent v3.5 database. These calculations are available in Appendix B.5 of the journal publication. The smelting of printed circuit boards is also included without additional credits. The system characteristics are slightly different at the high and low extreme of the impact range (BOS and recycling have a greater contribution for the low extreme), so Cu_3AsS_4 impacts are split into two distinct impact scenarios that represent calculations from the low and high values of the impact range: Cu_3AsS_4 L and Cu_3AsS_4 H, respectively. There are multiple factors contributing to the $>10\%$ decommissioning contribution of mc-Si for FFD. Most significantly is the credits from avoiding the production of high purity silicon. Additionally, the electricity requirements per square meter for recycling mc-Si modules are modeled to be almost three times lower than thin film solar cells (Appendix B.1. of the journal publication) due to differences in calculation methods for determining the necessary requirements (Corcelli et al., 2017, Held and Ilg, 2011).The relatively high electricity

requirements for thin film solar cells results in a minimum (but still negative) loss in fossil fuel depletion impacts. Precise values are tabulated in Appendix B.6 of the journal publication.

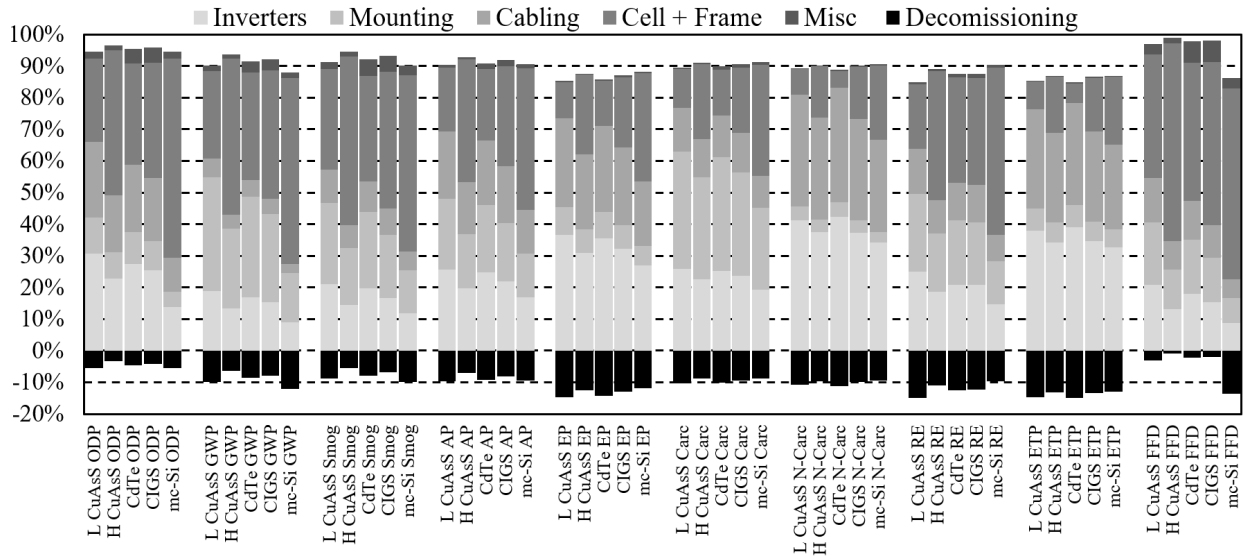

Figure 6.6. Roof-mounted 3 kWp PV system relative impacts based on system component.

6.3.4 Contribution analysis

In line with (G1.2), Table 6.3 tabulates the percent contribution to the mean of the life cycle impacts in Table 2 for Cu_3AsS_4 PV systems for all inputs that contribute to at least 1% in any impact category. Hot spots are identified using three different techniques to remove the inherent bias of any single technique. Another method calculates the average impact and variation for a given impact category and identifies the contributors above the second standard deviation from the mean. The last method defines the most relevant contributors by ranking impactors and identifying those that cumulatively contribute to the top 80% of total impacts in that category (Zampori and Pant, 2019).

Table 6.3. *Contribution to life cycle impacts by impact category and individual input. Boxed inputs identify the greatest impactor in each impact category. The cut-off contribution for chart inclusion is 1%.*

PV Component	Region	Ozone Depletion Potential (µg CFC-11-eq)	Global Warming Potential (g CO_2-eq)	Maximum Incremental Reactivity (g O_3-eq)	Acidification Potential (g SO_2-eq)	Eutrophication (g N-eq)	Carcinogenics (CTUh) (µg C_6H_6-eq)	Non-Carcinogenics (CTUh) (µg toluene-eq)	Respiratory Effects (mg $PM_{2.5}$-eq)	Ecotoxicity (CTUe) (kg 2,4-D-eq)	Fossil Fuel Depletion (kJ surplus)
Cell		**22.2%**	**27.0%**	**31.0%**	**21.3%**	**17.6%**	**10.7%**	**11.2%**	**25.1%**	**12.5%**	**34.4%**
‡§•Electricity	{RoW}	5.9%	14.8%	12.5%	11.0%	8.3%	5.3%	1.8%	16.9%	2.6%	11.1%
•Ethylene-vinyl acetate	{GLO}		1.0%								3.9%
•Glass (substrate)	{GLO}	2.4%	2.7%	3.6%	2.7%				1.5%		4.0%
Heat, industrial, gas	{GLO}										1.3%
•Molybdenum	{GLO}					6.9%	2.8%	7.6%	1.6%	8.0%	
•Silicone	{GLO}	2.7%									1.0%
§•Transport (truck)	{GLO}	6.9%	3.8%	6.5%	2.2%				1.7%		8.3%
•Transport (ship)	{GLO}	1.7%	1.1%	4.5%	2.5%				1.0%		2.0%
Panel		**14.5%**	**15.0%**	**14.1%**	**11.3%**	**4.2%**	**9.2%**	**2.4%**	**11.1%**	**2.9%**	**16.2%**
Light fuel oil*	{US}										1.3%
§•Aluminum (AlMg3)	{GLO}	9.0%	8.7%	6.8%	5.9%	3.4%	8.5%	2.0%	8.2%	2.5%	6.3%
§•Glass (protective)	{GLO}	4.0%	4.6%	6.2%	4.6%				2.5%		6.8%
Tempering (glass)	{GLO}										1.4%
Inverters		**27.4%**	**17.1%**	**18.5%**	**24.4%**	**38.8%**	**26.8%**	**43.7%**	**24.5%**	**41.9%**	**16.6%**
Capacitor (electrolyte)	{GLO}		1.1%								
Capacitor (film)	{GLO}	1.5%	1.7%	2.1%	1.6%	2.2%	1.3%	2.2%	1.8%	2.2%	1.7%
‡§•Copper	{GLO}	15.3%	2.8%	5.9%	14.1%	21.4%	9.8%	27.0%	9.7%	24.8%	3.9%
Electricity	{US}								1.8%		
Inductor (choke type)	{GLO}		1.3%	1.0%					1.2%		1.2%
•Integrated circuit (logic)	{GLO}	2.7%	2.5%	2.6%	1.5%	7.8%	3.4%	8.3%	2.2%	8.5%	2.2%
•Steel (low-alloyed)	{GLO}		1.2%				6.2%		1.4%		
Wire drawing (copper)	{GLO}							1.1%		1.0%	
Mounting System		**10.2%**	**32.3%**	**22.7%**	**21.0%**	**9.3%**	**38.2%**	**4.7%**	**24.1%**	**7.7%**	**15.6%**
‡§•Aluminum (wrought)	{GLO}	8.3%	28.8%	20.4%	19.3%	7.5%	28.6%	3.3%	21.1%	5.9%	12.9%
•Extrusion (aluminum)	{GLO}		1.5%	1.1%			7.9%	1.2%	1.8%	1.3%	
•Steel (low-alloyed)	{GLO}		1.6%								1.4%
Electric Installations		**21.5%**	**5.4%**	**9.1%**	**20.2%**	**29.8%**	**14.2%**	**37.5%**	**14.0%**	**34.5%**	**11.1%**
‡§•Copper	{GLO}	20.4%	3.8%	7.8%	18.8%	28.5%	13.1%	36.0%	13.0%	33.0%	5.2%
•Polyethylene (high density, granulate)	{GLO}										4.8%
Wire drawing (copper)	{GLO}					1.2%		1.4%		1.4%	
BOS (misc.)		**4.1%**	**3.2%**	**4.5%**	**1.7%**	**0.4%**	**0.8%**	**0.4%**	**1.1%**	**0.5%**	**6.1%**
•Transport (van)*	{US}	3.6%	2.9%	3.8%	1.5%						5.5%

**Input from ecoinvent database v2.2*
‡Impact hot spot identified through the technique described in Section 6.2.2.7
§Impact hot spot identified by exceeding two standard deviations from the mean
•Impact hot spot identified by including greatest impactors that cumulatively exceed 80% of the overall impact (Zampori and Pant, 2019)

All three hot spot identification techniques identify copper (inverters and electrical wiring), aluminum (mounting), and electricity (module processing) to be a hot spot in at least one impact category. Approximately 50 - 70% of impacts are directly attributable to BOS components across all impact categories. About 50% of PV system impacts in the eutrophication, non-carcinogenic, and ecotoxicity impact categories are directly attributable to the treatment of tailings from copper mining associated with inverter and electrical wiring. Module truck transportation, protective glass, aluminum frames, and processing of aluminum are also notable contributors to the life cycle impacts. Approximately 80% and 12% of the module mass is attributed to glass and aluminum, respectively (Appendix B.1. of the journal publication), which indicates that these inputs are mostly responsible for transportation impacts as well.

6.3.5 Sensitivity analysis

In line with (G1.3), Table 6.4 tabulates the percent contribution to the range of the life cycle impacts in Table 6.2 for Cu_3AsS_4 module inputs that contribute to at least 1% in any impact category. Hot spots are identified using the same approach as in Section 6.3.4. As explained in Section 6.2.2.5., it is possible the initially estimated impact ranges for each input may bias the identification of inputs that may contribute most to the uncertainty of Cu_3AsS_4 modules in future research. Therefore, values are presented for both the biased and unbiased techniques, where the biased technique uses the LCI ranges tabulated in Appendix B.1. of the journal publication, and the unbiased technique assumes the same mean as the biased technique but additionally assumes the same coefficient of variation for each input. The goal of the latter is to identify the most important inputs to acquire accurate data to reduce uncertainty in future studies.

Table 6.4. *Contribution to uncertainty by impact category and individual input. Values represent the contribution to the impact range from unbiased (biased) data by assuming an identical CV (initial CV). Values without parentheses can also be interpreted as a percent contribution to the total module impacts. Boxed inputs identify the greatest impactor in each impact category. Hot spots correspond to unbiased data. Cut-off contribution for chart inclusion is an unbiased 1%.*

PV Component	Region	Ozone Depletion Potential (µg CFC-11-eq)	Global Warming Potential (g CO_2-eq)	Maximum Incremental Reactivity (g O_3-eq)	Acidification Potential (g SO_2-eq)	Eutrophication (g N-eq)	Carcinogenics (CTUh) (µg C_6H_6-eq)	Non-Carcinogenics (CTUh) (µg toluene-eq)	Respiratory Effects (mg PM2.5-eq)	Ecotoxicity (CTUe) (kg 2,4-D-eq)	Fossil Fuel Depletion (kJ surplus)
Cell		**55% (72%)**	**60% (77%)**	**63% (78%)**	**62% (79%)**	**79% (89%)**	**52% (71%)**	**80% (88%)**	**67% (84%)**	**79% (87%)**	**61% (76%)**
Arsenic trioxide*	{US}					1.2% (2.6%)		2.1% (5.2%)		1.9% (4.7%)	
Disposal, municipal to sanitary landfill*	{US}									2.4% (3.1%)	
‡§•Electricity	{RoW}	14% (21%)	33% (46%)	25% (37%)	32% (45%)	38% (51%)	26% (41%)	13% (20%)	45% (60%)	16% (25%)	20% (27%)
•Ethylene-vinyl acetate	{GLO}	1.3% (2.3%)	2.3% (3.8%)	1.4% (2.4%)	1.3% (2.1%)	1.1% (1.8%)	1.0% (1.9%)		1.3% (2.0%)		7.0% (12%)
•Glass (substrate)	{GLO}	5.8% (8.1%)	6.1% (7.8%)	7.4% (10%)	7.9% (10%)	1.7% (2.1%)	1.4% (2.1%)	1.3% (1.9%)	3.9% (4.8%)	1.2% (1.7%)	7.2% (9.3%)
Glass fiber reinforced polyamide	{GLO}		1.2% (1.3%)								1.6% (1.9%)
Heat, industrial, gas	{GLO}	1.3% (1.6%)	1.1% (1.3%)								2.3% (2.7%)
‡§•Molybdenum	{GLO}			2.0% (1.6%)	1.2%	31% (24%)	14% (12%)	55% (48%)	4.4% (3.2%)	50% (43%)	
Photovoltaic panel factory	{GLO}	1.2% (1.4%)	1.7% (2.0%)	1.5% (1.8%)	2.0% (2.4%)	1.1% (1.2%)	2.9% (3.8%)	2.1% (2.7%)	1.6% (1.7%)	1.4% (1.8%)	1.3% (1.5%)
•Silicone	{GLO}	6.6% (13%)	1.3% (2.5%)								1.8% (3.4%)
‡§•Transport truck)	{GLO}	17% (15%)	8.4% (7.0%)	13% (11%)	6.4% (5.4%)	1.9% (1.5%)	2.8% (2.6%)	3.1% (2.9%)	4.5% (3.6%)	2.8% (2.6%)	15% (12%)
•Transport (ship)	{GLO}	4.1% (3.6%)	2.4% (2.0%)	9.1% (7.9%)	7.5% (6.3%)				2.8% (2.2%)		3.5% (2.9%)
Panel		**36% (19%)**	**33% (17%)**	**29% (15%)**	**33% (17%)**	**19% (9.3%)**	**44% (25%)**	**17% (9.6%)**	**30% (14%)**	**18% (10%)**	**29% (15%)**
Light fuel oil*	{US}	1.9% (1.1%)	1.4%								2.2% (1.2%)
‡§•Aluminum (AlMg3)	{GLO}	22% (12%)	19% (9.4%)	14% (7%)	17% (8.5%)	15% (7.4%)	41% (23%)	14% (7.9%)	22% (10%)	16% (8.5%)	11% (5.5%)
§•Glass (protective)	{GLO}	9.9% (5.6%)	10.3% (5.5%)	12.5% (7.0%)	13.4% (7.2%)	2.8% (1.5%)	2.4% (1.4%)	2.2% (1.3%)	6.6% (3.3%)	2.0% (1.2%)	12% (6.5%)
Tempering (glass)	{GLO}	1.8% (1.0%)	1.7%	1.6%	1.7%						2.5% (1.4%)
Installation		**6.5% (5.9%)**	**4.6% (3.8%)**	**6.1% (4.9%)**	**3.2% (2.6%)**	**1.3% (1.1%)**	**2.7% (2.4%)**	**2.0% (1.9%)**	**1.9% (1.5%)**	**1.8% (1.7%)**	**7.0% (5.9%)**
•Transport (van)*	{US}	5.7% (5.0%)	4.1% (3.4%)	4.9% (4.3%)	2.7% (2.3%)	1.2%	2.4% (2.2%)	1.9% (1.7%)	1.7% (1.3%)	1.7% (1.6%)	6.2% (5.2%)
Decommissioning		**2.9% (2.6%)**	**2.2% (1.9%)**	**2.5% (2.2%)**	**1.4% (1.2%)**	**0.6%**	**1.2% (1.3%)**	**1.0%**	**0.9%**	**1.0% (1.0%)**	**3.1% (2.6%)**
Transport (van)*	{US}	2.8% (2.5%)	2.1% (1.7%)	2.5% (2.2%)	1.4% (1.2%)		1.2% (1.1%)				3.1% (2.6%)

**Input from ecoinvent database v2.2*
‡Impact hot spot identified through the technique described in Section 6.2.2.7
§Impact hot spot identified by exceeding two standard deviations from the mean
●Impact hot spot identified by including greatest impactors that cumulatively exceed 80% of the overall impact (Zampori and Pant, 2019)

A comparison between the biased and unbiased results demonstrates the range of values for panel inputs in this study were relatively small compared to cell inputs, as their contributions to the range of impacts are modeled to be almost half their contribution to the mean impact. If only the biased results were interpreted, the aluminum frame would not have been identified as contributing most to the range of impacts in any impact category. However, the unbiased interpretation suggests acquiring accurate data for the aluminum frame should be the highest priority for reducing uncertainty in future Cu_3AsS_4 PV module studies for ODP and CA impact categories. Of course, Table 3 suggests acquiring accurate data for copper wiring and mounting aluminum is the highest priority to reduce the uncertainty for the overall PV system.

All three hot spot identification techniques identify electricity, molybdenum, truck transportation, and aluminum to be a hot spot in at least one impact category. Additionally, both substrate and protective glass can be significant contributors to the uncertainty in future studies in about half the impact categories. Moreover, since about 80% of the module mass is attributable to glass, determining the type, quality, and thickness of these glasses will reduce uncertainty in transportation impacts as well as their respective inputs.

6.3.6 Scenario analyses

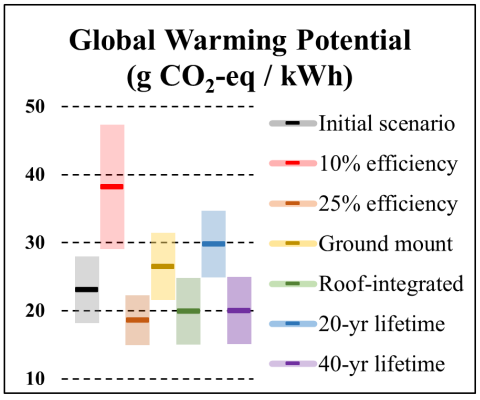

Figure 6.7. Influence of various scenarios on global warming potential impact results compared to the initial scenario.

Table 6.5. *Description of the various scenarios assessed and their influence on the calculated impacts.*

Scenario Modified	Initial Assumption (Section 6.2.2.1)	New Input	GWP Impact ($g CO_2$-eq) Low	Mean	High	Notes
			Initial Scenario			
			18.2	23.1	28.0	
Initial Efficiency	18.6%	10%	29.1	38.2	47.4	• Normalized to total energy generated (≈122MWh over 30 years) • 10% efficient panel produces 9% / 16.7% ≈ 54% of the energy of the initial system. Scale panel and mounting area by 1 / 54% + 3% ≈ 1.9x (3% for defective and failing panels). Use the same procedure for the 25% panel. • Requirements for change in wiring due to the change in panel area is taken from table 5.6.1.1 of (Frischknecht et al., 2015). • Mounting area, panel area, and decommissioning credits and burdens are assumed to scale linearly.
		25%	14.9	18.6	22.3	
Mounting	Roof-mounted	Ground Mount	21.6	26.5	31.4	• The difference in mounting contribution impacts calculated from the LCI (Jungbluth et al., 2012) is added to the initial scenario. • Decommissioning credits and burdens are scaled to the difference in Al and steel required (7.21 kg, 0.2 kg, and 1.5 kg steel and 3.98 kg, 2.25 kg, and 2.84 kg Al for ground mounted, roof-integrated, and roof-mounted systems, respectively). • Avoided burden of roof tiles are included
		Roof-Integrated	15.0	19.9	24.8	
Lifetime	30 years	20 years	24.9	29.8	34.7	• Normalized to total energy generated over 30 years (i.e. lifetimes apply to the module, not the system). • Conceptual methodology: one and a half 20-year modules are needed to generate the same electricity as the baseline system. These systems necessarily cover a slightly smaller area than the baseline scenario since the second 20-year panel will generate more electricity on average than the first system (used only for ten years so less degradation). A smaller area leads to lower mounting impacts, but a shorter lifetime necessitates more impacts from panel manufacturing, decommissioning, and recycling. • Similar logic applies for longer lifetime systems but note that a slower degradation rate consequently leads to more average energy generation, so the area is also slightly smaller for these systems.
		40 years	15.1	20.0	25.0	

In line with (G1.4), Figure 6.7 illustrates the influence of varying the module performance and mounting requirements on global warming potential for these systems. The initial scenario is the same as that tabulated in Table 6.2. Each scenario is described in Table 6.5 with an explanation of how the calculations were altered from the initial scenario. Scaling to the functional unit was

completed for each of these scenarios. We assume module credits and burdens can be linearly scaled, which means that if a system covers twice the area, the impacts attributed to the module double. The decrease in efficiency, installation of ground mounted systems, and increase in lifetime necessitate additional panels, more structural materials, and a third inverter, respectively. In addition to these causal impacts the calculations consider consequential impacts (e.g., transportation and recycling) to fully capture the scenario characteristics.

6.3.6.1 Factors influencing impact calculations

Subtle factors influencing the calculated impacts are the mounting angle and choice of location. Because these calculations assume the same energy production, the amount of incident energy will influence the calculations with a higher solar insolence scenario resulting in a comparatively smaller impact since less modules need to be made to generate the same amount of energy. Montgomery, Alabama has been chosen in this study to roughly represent the approximate average annual US solar insolation with 2011 kWh/m^2 for the conditions outlined in Figure 6.2, generated from NREL's PVWatts Calculator. Since this model initially assumes a 30-degree mounting angle, these calculations more closely represent plane of array opposed to global horizontal irradiance (0 degrees). This change in tilt angle will increase the calculated life cycle impacts by about 1%, 5%, and 13% for 20-degree, 10-degree, and 0-degree tilts, respectively. Regarding location, calculated impacts increase for Ithaca, NY (1606 kWh/m^2) and decrease for Phoenix, AZ (2420 kWh/m^2) by about 20%. These results are not included in Figure 6.7 because they do not offer further insight into concept design of this PV system, even though these factors affect the calculated impacts.

6.3.6.2 Global warming potential impacts as a function of efficiency and lifetime

The scenarios illustrated in Figure 6.7 independently modify the initial system. However, the initially modeled module efficiency and lifetime has not yet been demonstrated so a continuous range of values are possible. Therefore, we modeled the combined effect of both efficiency (10 – 25%) and lifetime (15 – 40 years) on the calculated GWP impact, illustrated in Figure 6.8. These data are generated from evaluating GWP at efficiency and lifetime intervals of 0.1, As shown in

Table 6.6. Like the scenarios described in Table 6.5, these calculations scale the energy generated to the functional unit to calculate impacts. By equating the partial derivatives of the surface, these data distinguish the efficiency-lifetime domains where researchers can justifiably prioritize increasing one variable over the other, from an environmental perspective. Since Cu_3AsS_4 enargite is a stable mineral, we do not expect cell-based sensitivity to oxygen, moisture, or light to be a limiting factor in these PV systems. Therefore, we expect these PV systems to be in the domain where the pursuit of efficiency increase is of primary importance until module-based or other lifetime limitations are demonstrated.

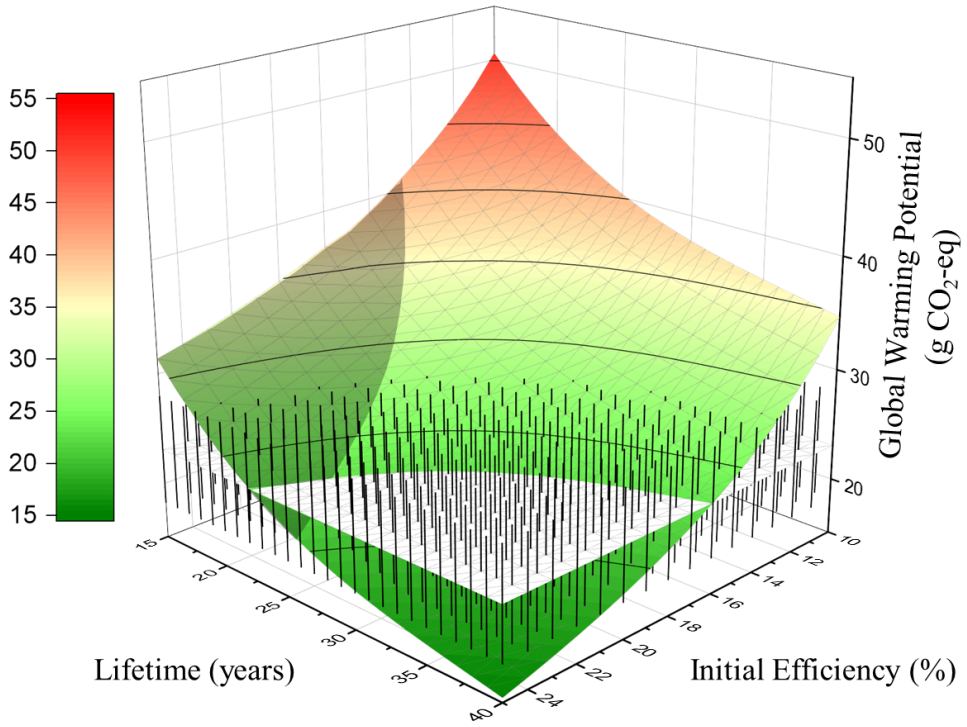

Figure 6.8. Influence of efficiency and lifetime on calculated global warming potential (GWP) impacts. The white plane and error bars represent the calculated impact range for the 18.6% efficient, 30-year PV system initially assumed in Section 6.2.2.1. The shaded region denotes where the partial derivative with respect to efficiency is smaller than the partial derivative with respect to lifetime (i.e. if Cu_3AsS_4 PV systems are expected to last 20 years but the initial efficiency is less than about 18%, it is justifiable in terms of GWP to focus on increasing efficiency rather than increasing lifetime). For reference, mc-Si PV systems are calculated to have a GWP impact of 36.6 $\pm$ 1.1 g CO_2-eq (Table 6.2)

Table 6.6. *Calculated global warming impact dependency on efficiency and lifetime assuming the same energy is generated over the lifetime of the system. The calculated fit as a function of efficiency is: Impact = 228.3730*(Efficiency)$^{-0.7821665}$ and the calculated fit as a function of lifetime is: Impact = -0.000793*(lifetime)^3 + 0.0898*(lifetime)^2 - 3.6533*(lifetime) + 73.409. Units are g CO_2-eq emissions.*

Lifetime (years)	**Efficiency (%)**															
	10	**11**	**12**	**13**	**14**	**15**	**16**	**17**	**18**	**19**	**20**	**21**	**22**	**23**	**24**	**25**
15	50.6	47.9	45.6	43.6	41.9	40.2	38.8	37.5	36.7	35.7	34.8	34.0	33.3	32.6	31.9	31.3
16	49.2	46.5	44.2	42.2	40.5	38.8	37.3	36.0	35.3	34.3	33.4	32.6	31.8	31.1	30.5	29.9
17	47.9	45.1	42.8	40.9	39.1	37.5	36.0	34.7	34.0	33.0	32.1	31.2	30.5	29.8	29.2	28.6
18	46.6	43.9	41.6	39.6	37.9	36.2	34.8	33.5	32.7	31.7	30.8	30.0	29.3	28.6	27.9	27.3
19	45.5	42.8	40.5	38.5	36.7	35.1	33.6	32.3	31.6	30.6	29.7	28.9	28.1	27.4	26.8	26.2
20	44.4	41.7	39.4	37.4	35.7	34.2	32.8	31.6	30.5	29.5	28.6	27.8	27.1	26.4	25.7	25.1
21	43.4	40.7	38.4	36.4	34.7	33.2	31.8	30.6	29.5	28.6	27.7	26.8	26.1	25.4	24.7	24.1
22	42.5	39.8	37.5	35.6	33.8	32.3	30.9	29.7	28.6	27.7	26.8	25.9	25.2	24.5	23.9	23.3
23	41.7	39.0	36.7	34.7	33.0	31.5	30.1	28.9	27.8	26.8	25.9	25.1	24.4	23.7	23.0	22.4
24	41.0	38.3	36.0	34.0	32.3	30.7	29.4	28.2	27.1	26.1	25.2	24.4	23.6	22.9	22.3	21.7
25	40.3	37.6	35.3	33.3	31.6	30.1	28.7	27.5	26.4	25.4	24.5	23.7	22.9	22.3	21.6	21.0
26	39.7	37.0	34.7	32.7	31.0	29.4	28.1	26.9	25.8	24.8	23.9	23.1	22.3	21.6	21.0	20.4
27	39.1	36.4	34.1	32.1	30.4	28.9	27.5	26.3	25.2	24.2	23.3	22.5	21.8	21.1	20.4	19.8
28	38.6	35.9	33.6	31.6	29.9	28.4	27.0	25.8	24.7	23.7	22.8	22.0	21.2	20.6	19.9	19.3
29	38.1	35.4	33.1	31.1	29.4	27.9	26.5	25.3	24.2	23.3	22.4	21.5	20.8	20.1	19.4	18.8
30	37.7	35.0	32.7	30.7	29.0	27.5	26.1	24.9	23.8	22.8	21.9	21.1	20.4	19.7	19.0	18.4
31	37.3	34.6	32.3	30.3	28.6	27.1	25.7	24.5	23.4	22.4	21.5	20.7	20.0	19.3	18.6	18.0
32	37.0	34.3	32.0	30.0	28.2	26.7	25.4	24.2	23.1	22.1	21.2	20.4	19.6	18.9	18.3	17.7
33	36.6	33.9	31.6	29.6	27.9	26.4	25.0	23.8	22.7	21.8	20.9	20.0	19.3	18.6	17.9	17.3
34	36.3	33.6	31.3	29.3	27.6	26.1	24.7	23.5	22.4	21.4	20.5	19.7	19.0	18.3	17.6	17.0
35	36.0	33.3	31.0	29.0	27.3	25.8	24.4	23.2	22.1	21.2	20.3	19.4	18.7	18.0	17.3	16.7
36	35.8	33.1	30.8	28.8	27.0	25.5	24.2	23.0	21.9	20.9	20.0	19.2	18.4	17.7	17.1	16.5
37	35.5	32.8	30.5	28.5	26.8	25.2	23.9	22.7	21.6	20.6	19.7	18.9	18.1	17.4	16.8	16.2
38	35.2	32.5	30.2	28.2	26.5	25.0	23.6	22.4	21.3	20.3	19.5	18.6	17.9	17.2	16.5	15.9
39	35.0	32.3	30.0	28.0	26.2	24.7	23.4	22.2	21.1	20.1	19.2	18.4	17.6	16.9	16.3	15.7
40	34.7	32.0	29.7	27.7	26.0	24.4	23.1	21.9	20.8	19.8	18.9	18.1	17.3	16.6	16.0	15.4

6.3.6.3 Comparison of different PV absorbers

Scenarios analyses were performed by comparing the allocation assumption for arsenic (Figure 6.9) and changing the Cu_3AsS_4 absorber with other semiconductor devices (Figure 6.10). The purpose of these comparisons, respectively, is to put into context the influence of the mass or economic allocation assumption on PV impacts, and to directly compare three micrometer films based on life cycle impact integrated into an assessment with standard assumptions (lifetime, efficiency, etc.). The figures compare the impact relative to Cu_3AsS_4 PV systems (0% in all categories) to other assessed scenarios.

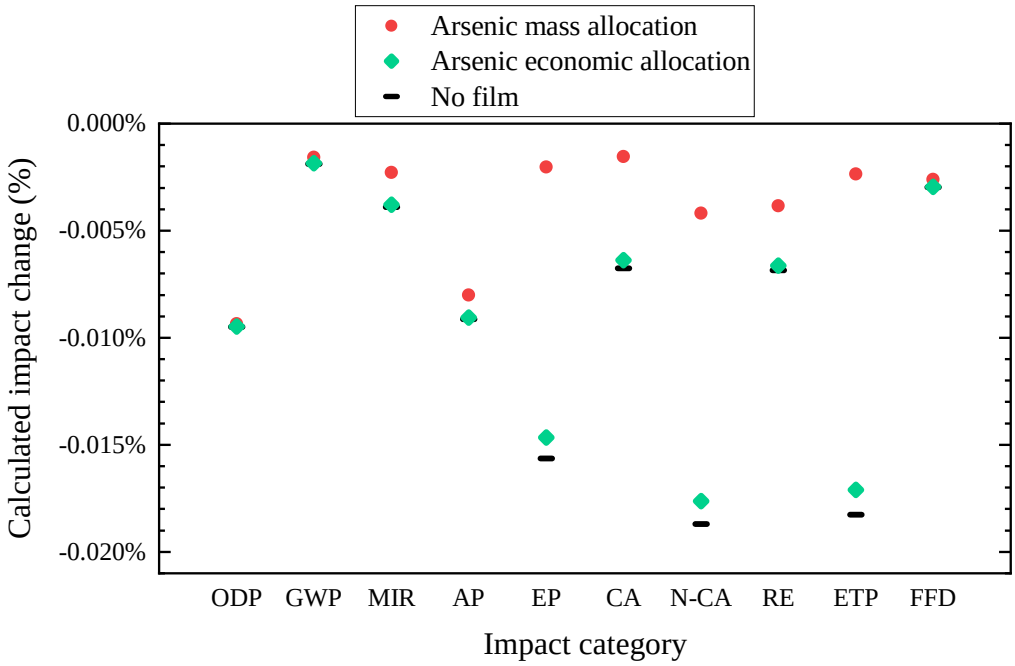

Figure 6.9. A comparison of the impact that a mass or economic allocation assumption has in the context of PV life cycle impacts. ODP, ozone depletion potential; GWP, global warming potential; MIR, maximum incremental reactivity; AP, acidification potential; EP, eutrophication potential; CA, carcinogenic; N-CA, non-carcinogenic; RE, respiratory effects; ETP, ecotoxicity potential; FFD, fossil fuel depletion

As concluded in Section 6.3.1.2., the expected life cycle impacts of systems that include arsenic are expected to be significantly different between an economic and mass allocation assumption. Therefore, the motivation behind the calculations demonstrated in Figure 6.9 is to

confirm the validity of this claim in the context of this study. The black lines indicate the relative impact of removing the entire semiconductor layer in each impact category. Of course, removing this layer in practice would eliminate the functionality of the device and render the efficiency near zero. However, these values are meant to help distinguish the relative impact of the allocation assumption. The green diamonds (red circles) represent the calculated impacts of the system in the case where arsenic is the only component of Cu_3AsS_4 films included in the calculations according to an economic (mass) allocation. We note this allocation decision has a minimal influence ($>0.015\%$) on the impacts attributable to arsenic for this system. Therefore, even though the impacts attributable to arsenic was expected to be significantly different between mass and economic allocations, we have shown that the difference is minimal in the case of this study.

The relative impacts reported in Figure 6.10 assume everything about the system described above is the same as the Cu_3AsS_4 system except the absorber layer is replaced by other chalcogenide absorbers. The architecture assumed for these other solar absorbers may not be optimal for high efficiency devices, but the relatively small change indicates the life cycle impact is expected to be influenced more significantly from other components of the PV system, such as manufacturing electricity usage, balance of systems, or other semiconductor layers. The small change of CIGS and CdTe systems compared to the difference calculated in Figure 6.5 support this hypothesis.

It is interesting to note that the (copper) antimony chalcogenides have a more pronounced environmental impact than all other thin films studied in the ecotoxicity impact category, since it is generally assumed these materials are non-toxic (Dufton et al., 2012, Ramasamy et al., 2014, Wen et al., 2017). The toxicity calculated here is a result of upstream processes, specifically, from zinc released via waterways as a result of treating sulfidic tailings from extracting antimony from its ores. This toxicity is not associated with direct handling of the material, which may be an unstated assumption in these studies. In this case, this assumption should be specified in future research provided the non-toxicity of antimony compounds is indeed determined, which is not necessarily agreed upon (Cooper and Harrison, 2009, World Health Organization, 2003).

The large burden associated with CIGS thin films in the non-carcinogenic impact category is mainly attributed to the release of zinc into the air from extracting indium from zinc production

concentrates. Overall, the relative contribution from the thin film absorber to the PV life cycle impact is small compared to BOS and other module inputs. To the best of our knowledge, these data provide the first life cycle screening of these emerging thin film chalcogenide absorber materials.

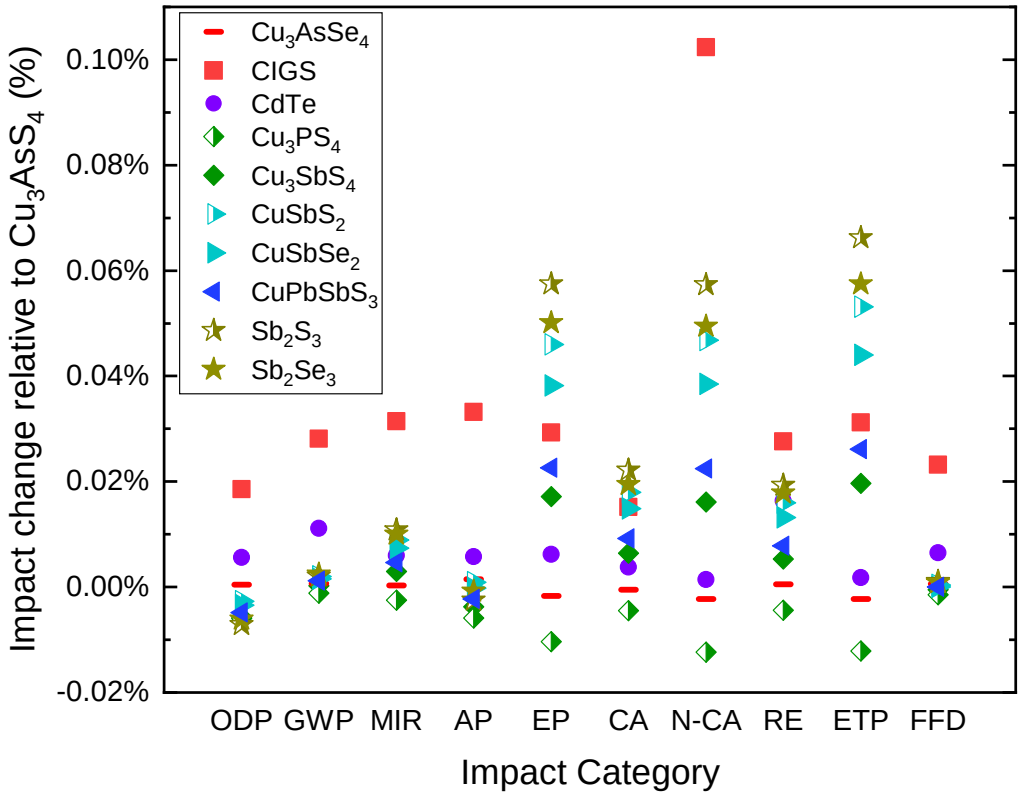

Figure 6.10. Comparison of the life cycle impacts attributable to various chalcogenide absorbers when integrated into the PV system described above. All films are assumed to be fully dense and 3 micrometers thick; calculations consider difference in density. ODP, ozone depletion potential; GWP, global warming potential; MIR, maximum incremental reactivity; AP, acidification potential; EP, eutrophication potential; CA, carcinogenic; N-CA, non-carcinogenic; RE, respiratory effects; ETP, ecotoxicity potential; FFD, fossil fuel depletion

6.4 Simulating possible arsenic exposure

6.4.1 Arsenic emission from rooftop PV fire

Although we have determined the relative impacts of arsenic to be low in Cu_3AsS_4 PV systems, this result does not inherently imply the nonexistence of risk nor the assured adherence to safety protocol. Before commercialization, a risk analysis must be performed with appropriate manufacturing techniques to determine the viability of this technology in an industrial setting. However, regardless of manufacturing technique, this technology has the possibility of exposing customers to arsenic by means of uncommon events such as a fire. Following the methodology an International Energy Agency report, here we calculate an estimated level of human health risk associated with Cu_3AsS_4 PV technology that burns in a small house fire (Sinha et al., 2018). Adapted from page 13 of this report, the maximum concentration of arsenic in air downwind from a small house fire can be calculated as

$$Maximum\ Airborne\ Concentration = \frac{MHNC \times PF \times M \times A \times RE}{AT}$$

where MHNC is the maximum one-hour normalized concentration ($\mu g/m^3$ per g/s), PF is the persistence factor, M is the mass of arsenic per unit area (g/m^2), A is the area of the PV system (meters), RE is the release efficiency (%), and AT is the averaging time (seconds). Maximum concentrations are compared to Acute Exposure Guideline Levels taken from the U.S. Environmental Protection Agency website. Table 6.7 lists the values used in the calculation of expected maximum airborne concentration of arsenic from Cu_3AsS_4 PV modules. Figure 6.11 displays the results of this calculation with two release efficiencies, 1% and 100%. Although these values are unknown, the expected release efficiency is on the order of 1% since softened glass is observed to incorporate many of the elements from burning semiconductor layers (Fthenakis et al., 2005). The cited study found the release efficiency of cadmium from a portion of a CdTe module to be approximately 0.5%, which is expected to be a conservative estimate due to their choice of small module size.

Table 6.7. *Assumptions made and values used for determining the maximum concentration of arsenic exposure anticipated for a small house fire with mounted Cu_3AsS_4 PV modules.*

Variable	Value(s)	Reference
Maximum one-hour normalized concentration (MHNC) [μg/m^3 per g/s]	96	(Sinha et al., 2018) modeling with SCREEN3 (US EPA, 1995)
Persistence Factor (PF) [unitless]	1.43, 1, 1, 0.9, 0.7	(Sinha et al., 2018)
Mass per unit area (M) [g/m^2]	2.51	Calculation of average arsenic quantity from Figure 6.2
Area (A) [m^2]	16.1	Provided in Figure 6.2
Release Efficiency (RE) [%]	1, 100	Unknown variables
Averaging times (AT) [Minutes]	10, 30, 60, 240, 480	Corresponds to Acute Exposure Guideline Level times

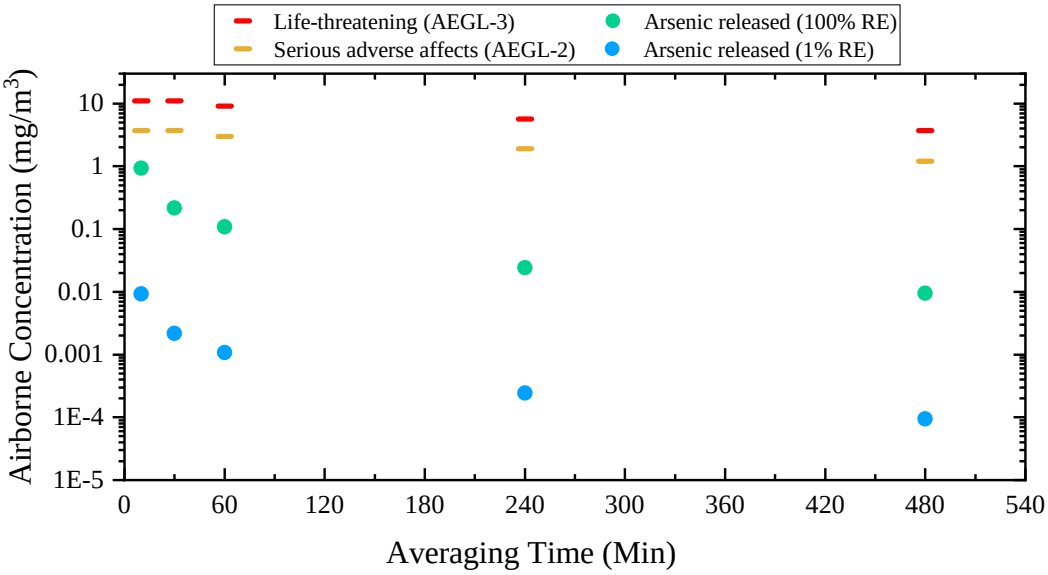

Figure 6.11. Calculated airborne arsenic concentration compared to Acute Exposure Guideline Levels (AEGL) 2 and 3, which indicate serious adverse effects and life-threatening exposure, respectively. RE = release efficiency.

6.4.2 Toxicity Characteristic Leaching Procedure

The Toxicity Characteristic Leaching Procedure (TCLP) has been performed to determine the extent of leaching from end-of-life disposal of Cu_3AsS_4 solar cells in a landfill environment. If enough arsenic leaches from these cells, these modules may be classified as hazardous waste. Hazardous waste requires adhering to more strict disposal requirements, per the U.S. EPA (Hansen et al., 1994). It is the hope of the authors that quantitatively understanding this concern may motivate improved design for end-of-life management, either by avoiding the amount of arsenic leached, decreasing the amount of arsenic used, or finding a replacement for arsenic.

This study is scaled down due to processing and infrastructure constraints which limit the analysis to less than 1 gram of solar material instead of the minimum required 100 grams for a certifiable TCLP study (US EPA, 1992). Besides the scaling aspect, all other processes follow Method 1311 protocol (US EPA, 1992). Briefly, Cu_3AsS_4 solar cells were placed in a slightly acidic (pH = 4.89 $\pm$ 0.02) extraction fluid 20 times the weight of the solid phase and turned end-over-end at 29 $\pm$ 1 rpm for 19 hours in a borosilicate glass vessel. The extraction fluid was comprised of ultrapure water (Millipore Sigma; Direct-Q 3), glacial acetic acid (Sigma-Aldrich; 695092), and sodium hydroxide (Macron Fine Chemicals; 1310-73-2). The filtered extractant was used to form 5% w/w nitric acid (Fisher Scientific; A200212) solutions and the leachate was analyzed with inductively coupled plasma optical emission spectroscopy. Matrix spikes (Exaxol; PLAS1, PLCU1, PLMO1, PLNI1, and PLZN1) were used for instrument calibration and a blank was used for comparison. Samples with different transparent conducting oxide (TCO) layers: tin-doped indium oxide (ITO) and ZnO (to represent ZnO:Al, etc.), were analyzed in this study to investigate if the amount of leaching may be dependent on the TCO.

The results of this leaching test are presented in Table 6.8 and demonstrate that concentrations below the TCLP regulatory level for arsenic were measured. However, we note two limitations with these data. First, this procedure was carried out in a scaled environment where only a small amount of material was used. A more rigorous future study should produce a larger sample size compliant with the TCLP standards mentioned above. Second, the TCLP may not accurately represent long-term leachability in this system. The slow dissolution of arsenic

Table 6.8. *TCLP data determined through analyzing leachate fluid with inductively coupled plasma optical emission spectroscopy*

Element	ZnO as TCO (mg/L)	Relative Standard Deviation (%)	ITO as TCO (mg/L)	Relative Standard Deviation (%)	TCLP Regulatory level (mg/L)
As	0.145	5.5	0.135	2.5	5.0
Cu	<0.01	18	0.022	3.4	-
Ni	0.120	0.8	0.1355	0.5	-
Mo	4.38	0.6	7.39	0.5	-
Zn	5.68	0.6	0.596	0.8	-

from enargite has been documented (Gupta, 2010, Padilla et al., 2005), but never demonstrated in a simulated landfill environment. As we show here, the slow dissolution may influence the amount of arsenic leached in this 19-hour extraction procedure. Therefore, Long-term investigations are recommended when probing arsenic leachability from Cu_3AsS_4 thin films for end-of-life policy determination.

6.5 Design considerations for Cu_3AsS_4 PV systems

In line with G2, the purpose of this section is to offer design considerations from an environmental perspective for the development of Cu_3AsS_4 technology.

6.5.1 Balance of systems

Most of the anticipated impacts for Cu_3AsS_4 PV systems are from BOS contributions. Most notably, the aluminum and copper used for mounting and as part of the electrical system (including the inverters) are the main contributors to the life cycle impacts. One approach to reduce the impacts from these metals is to reduce the quantity that is used while maintaining functionality. For the mounting system, an integrated roof configuration requires less aluminum compared to a traditional mounting configuration. The data in Table 6.5 indicate this change may marginally reduce the calculated impacts by approximately 15%. However, considering utility scale systems constitute much of the market (Masson et al., 2018), limiting the configuration to

integrated rooftop may not be appealing economically. Another approach to reduce the impact of BOS metals is to implement reusing and recycling of these components. Since decommissioning and recycling of aluminum, steel, and copper is calculated to be an environmental benefit in every impact category (Figure 6.6), designing a reusable mounting configuration or using metals with a high recycled content is expected to reduce life cycle impacts of BOS components.

6.5.2 Module components

Regarding module inputs, frame aluminum, molybdenum, electricity, glass, and transportation are the main contributors to the life cycle impacts. As mentioned for BOS, if reducing the amount of material limits functionality, life cycle impacts due to the aluminum frame may be reduced by designing a reusable frame and using aluminum with high recycled content. Reducing the amount of material may be more feasible for molybdenum and other processes involving modifiable material utilization efficiencies. Opposed to BOS metals which are mostly utilized, solution processing and sputtering waste material when it does not become incorporated into the cell. Increasing target utilization during molybdenum sputtering, for example, can reduce life cycle impacts but may require more electricity consumption. This trade-off can be quantified with the data in Tables 6.2, 6.4 and Appendix B.1 of the journal publication. For example, the uniform range of molybdenum utilization (Appendix B.1. of the journal publication) is 2.57 g/m^2, so a decrease in molybdenum losses of 0.1 g/m^2 represents a decrease in input range of 0.1/2.57 = 3.9% because the deposition efficiency is assumed to range from 100 - 50%. Regarding N-CA impact, since molybdenum is modeled to contribute to 48% (Table 6.4) of the (49.0 – 43.4 =) 5.6 μg toluene-eq. (Table 6.2) range, an absolute change of 3.9%*(5.6*48%) = 0.1 g toluene-eq. emissions is calculated for the PV system if molybdenum utilization changes by 0.1 g/m^2. Since electricity is modeled with a range of 50.2 kWh/m^2, and contributes to 20% of the impact range, these emissions are matched for electricity when increased by 0.1/(5.6*20%)*50.2 $\approx$ 4.5 kWh/m^2. Therefore, these calculations demonstrate that it is an equivalent N-CA trade-off to invest in a 4.5 kWh/m^2 more energy-intensive sputtering process if a 0.1 g/m^2 increase in molybdenum utilization is achieved (note that both areas refer to cell production, so these calculations are independent of

module efficiency and lifetime). Industrially, this trade-off may equate to investing in a sputtering process that, if initially requires 15 kWh/m^2, uses 4.5/15 = 30% more energy to achieve a 0.1 g/m^2 increase in molybdenum utilization. For an original deposition efficiency of 50% this molybdenum utilization is equivalent to increasing the deposition efficiency to 2.57/(5.14-0.1) = 51.0%, but for an original deposition efficiency of 75% this is the same as increasing the deposition efficiency to 2.57/(3.43-0.1) = 77.3% (molybdenum requirements have a 1/x dependence on utilization efficiency). Any process that uses less (the same) power to achieve the same (increased) molybdenum utilization will be a N-CA benefit. However, in the case of MIR (Table 6.4), a 0.1 g/m^2 decrease in molybdenum losses will only be a benefit if the increase in energy consumption is less than 0.1*(50.2/2.57)*(1.6%/37%)= 0.08 kWh/m^2.

Because the impact from electricity varies regionally, the exact trade-off for a manufacturing facility is expected to differ, but the method for calculating these trade-offs is generally applicable for processes involving modifiable material utilization efficiencies.

Regarding electricity consumption, a recent investigation on CZTS PV modules found that solution processing may require less energy compared to vacuum-based processes, but the environmental impact becomes dependent on the amount of additional precursors used and the associated waste (Mokhtarimehr et al., 2018). Using the methodology described above, a trade-off in Cu_3AsS_4 PV systems for solution and vacuum processing can be quantified considering electricity requirements, material utilization, and process waste. However, since neither electricity requirements, material utilization efficiency, nor precursor solutions are known, quantification of this trade-off is left for future work.

Protective and substrate glass are closely tied to transportation impacts for PV modules. Without including electrical connections, glass contributes to over 80% of the module mass (Appendix B.1. of the journal publication). About 99% of the mass is accounted for if the aluminum frame, ethylene-vinyl acetate encapsulant, and silicone sealant are additionally included. Reducing life cycle impacts for both transportation and glass depend on reducing the amount of material used. Developing roll-to-roll compatible technologies on thin, flexible substrates may facilitate mass reduction for substrate glass, but as demonstrated in Section 6.3.6., any process that contributes to a shortened lifetime will be an environmental detriment. Therefore, it is important that both a thin substrate as well as protective glass maintains the durability of the PV system.

6.5.3 Other notes

Calculated impacts are dependent on both lifetime and efficiency of PV systems. The dependency is quantified in Figure 6.8 for GWP and demonstrates the domains where pursuit of one variable over the other is environmentally justifiable. Since the scaling methodology does not have implicit assumptions concerning impact category, a similar lifetime-efficiency influence is expected for all other impact categories. Since Cu_3AsS_4 PV systems are not expected to suffer from ambient stability issues, engineering for efficiency improvement is more environmentally worthwhile than engineering for lifetime until stability limitations are demonstrated. Of course, contributions to improving both variables are preferred.

Arsenic (with associated transportation) is not expected to contribute to more than 1% of the life cycle impacts in any impact category calculated with both a mass and economic allocation (Section 6.3.6.3.). However, we note that the impact methodology used herein may not accurately predict direct exposure during manufacturing and decommissioning since specific processing conditions were not modeled. Although low end-of-life leachability of arsenic from Cu_3AsS_4 enargite thin films has been demonstrated (Andler et al., 2019), limiting exposure during these steps relies on managing emissions during specific processes. Like other PV systems, risk assessments (Fthenakis and Zweibel, 2003, Fthenakis, 2012, Sinha et al., 2018), including identifying the hazards of feasible manufacturing routes (Eisenberg et al., 2013), should be completed on Cu_3AsS_4 systems when these devices are viable for large-scale production to mitigate potential human exposure to arsenic.

6.6 Conclusions

This work establishes a basis for understanding potential Cu_3AsS_4 technologies from an environmental perspective. Specifically,

(G1.1) Cu_3AsS_4 PV system impacts are expected to be commensurate with CdTe and CIGS solar cells.

(G1.2) We have used three hot spot identification methods to identify mounting aluminum, copper electrical wiring, copper in the inverter, and module production electricity as

the main contributors to PV system impacts. Molybdenum, inverter integrated circuits, frame aluminum, glass, and module ground transportation are also notable contributors.

(G1.3) Electricity, molybdenum, frame aluminum, glass, and module ground transportation have been found to contribute most to the range of impact. Additionally, accurate values for these inputs should be acquired to minimize uncertainty in future studies concerning Cu_3AsS_4 PV modules.

(G1.4) GWP dependency on lifetime and PV system efficiency are quantified in Figure 6.8 and Table 6.6. BOS mounting configuration influences calculated impacts by approximately $\pm 14\%$. Near-plane of array calculated impacts are approximately 13% lower than global horizontal irradiance impacts. Choice of location can influence impacts $\pm 20\%$ for the continental United States.

(G2) Environmental design considerations are listed in Table 6.9. Because Cu_3AsS_4 thin films and other semiconducting layers have a relatively low contribution to PV system impacts, the design considerations with the largest influence on life cycle performance are applicable to other PV systems.

Assuming high efficiency devices are achieved, future studies should model direct arsenic flows with specific manufacturing and decommissioning processes. Furthermore, since many of the design considerations are inherently tied to economic incentives and social implications, future studies may include quantifying trade-offs between environmental, economic, and social perspectives to assess Cu_3AsS_4 sustainability.

6.7 Acknowledgements

The authors would like to acknowledge Melissa McCarthy for help with gathering LCI information and Cory Tatarzyn and Matt Triebe for early conceptual structuring. We would also like to acknowledge the reviewers of this manuscript who have provided valuable critiques. This work is supported by the National Science Foundation [grant number #1144843 (Purdue-Tuskegee IGERT on globally sustainable electronics)].

Table 6.9. *Environmental design considerations for the development of Cu_3AsS_4 PV systems.*

Key design considerations
Balance of Systems
Use aluminum, copper, and steel with high recycled content and design reusable BOS components.
Module Manufacture
For materials with modifiable utilization efficiencies during deposition (like sputtering or solution processing), reduce waste as much as possible during those processes, especially for molybdenum.
As in Section 6.5.2, calculate trade-offs to determine if it is environmentally justifiable to increase electricity consumption to decrease processing waste. These calculations will depend on the local electricity grid mix.
Reduce supply chain transportation distances and weight of transported components; investigate lightweight substrates.
Module Performance
Although engineering towards both high PV system efficiency and lifetime is necessary, prioritize cell and module efficiency improvements.

6.8 References

Ahmed, A. H., Arai, S., and Ikenne, M. (2009). Mineralogy and Paragenesis of the Co-Ni Arsenide Ores of Bou Azzer ,. *Economic Geology*, 104:249–266.

Andler, J., Mathur, N., Sutherland, J., Zhao, F., and Handwerker, C. (2020). Guiding the environmental design of a novel solar absorber through life cycle assessment by identifying anticipated hot spots. *Journal of Cleaner Production*, 258:120847.

Andler, J., Mathur, N., Zhao, F., and Handwerker, C. (2019). Assessing the Potential Environmental Impact of Cu3AsS4 PV Systems. In *2019 IEEE 46th Photovoltaic Specialist Conference (PVSC)*, Chicago, IL.

Ardente, F. and Mathieux, F. (2014). Identification and assessment of product's measures to improve resource efficiency: The case-study of an Energy using Product. *Journal of Cleaner Production*, 83:126–141.

Banu, S., Ahn, S. J., Ahn, S. K., Yoon, K., and Cho, A. (2016). Fabrication and characterization of cost-efficient CuSbS2 thin film solar cells using hybrid inks. *Solar Energy Materials and Solar Cells*, 151:14–23.

Bare, J. (2012). Tool for the Reduction and Assessment of Chemical and other Environmental Impacts (TRACI) version 2.1 USER'S MANUAL. Technical report, U.S. EPA.

Barthel, M., James, K., Guinness, J., Barker, C., Fava, J., Valdivia, S., Khan, S., Harnanan, C., Smerek, A., Adibi, N., Valdivia, S., and Khan, S. (2014). UNEP/SETAC Life Cycle Initiative -Flagship Project 3a (Phase 1). Technical report.

Bilich, A., Langham, K., Geyer, R., Goyal, L., Hansen, J., Krishnan, A., Bergesen, J., and Sinha, P. (2017). Life cycle assessment of solar photovoltaic microgrid systems in off-grid communities. *Environmental Science and Technology*, 51(2):1043–1052.

Bisinella, V., Conradsen, K., Christensen, T. H., and Astrup, T. F. (2016). A global approach for sparse representation of uncertainty in Life Cycle Assessments of waste management systems. *International Journal of Life Cycle Assessment*, 21(3):378–394.

Björklund, A. E. (2002). Survey of approaches to improve reliability in LCA. *International Journal of Life Cycle Assessment*, 7(2):64–72.

Carapella, S. (2002). Arsenic and Arsenic Alloys. In *Kirk-Othmer Encyclopedia of Chemical Technology*, volume 3, pages 262–274.

Celik, I., Song, Z., Cimaroli, A. J., Yan, Y., Heben, M. J., and Apul, D. (2016). Life Cycle Assessment (LCA) of perovskite PV cells projected from lab to fab. *Solar Energy Materials and Solar Cells*, 156:157–169.

Chatzisideris, M. D., Espinosa, N., Laurent, A., and Krebs, F. C. (2016). Ecodesign perspectives of thin-film photovoltaic technologies: A review of life cycle assessment studies. *Solar Energy Materials and Solar Cells*, 156:2–10.

Classen, M., Althaus, H.-j., Blaser, S., Tuchschmid, M., Jungbluth, N., Doka, G., Faist, E. M., and Scharnhorst, W. (2009). Life Cycle Inventories of Metals. Technical report, Swiss Centre for Life Cycle Inventories, Dubendorf, CH.

Cooper, R. and Harrison, A. (2009). The exposure to and health effects of antimony. *Indian Journal of Occupational and Environmental Medicine*, 13(1):3–10.

Corcelli, F., Ripa, M., and Ulgiati, S. (2017). End-of-life treatment of crystalline silicon photovoltaic panels. An emergy-based case study. *Journal of Cleaner Production*, 161:1129–1142.

Dalewski, F. (1999). Removing arsenic from copper smelter gases. *The Journal of the Minerals, Metals & Materials Society (TMS)*, 51(9):24–26.

Dufton, J. T. R., Walsh, A., Panchmatia, P. M., Peter, L. M., Colombara, D., and Islam, M. S. (2012). Structural and electronic properties of CuSbS2 and CuBiS2: potential absorber materials for thin-film solar cells. *Phys. Chem. Chem. Phys.*, 14:7229–7233.

Dziedzic, J. and Inglot, M. (2017). Ultrathin glass for the photovoltaic applications. *Acta Physica Polonica A*, 132(1):176–178.

Eisenberg, D. A., Yu, M., Lam, C. W., Ogunseitan, O. A., and Schoenung, J. M. (2013). Comparative alternative materials assessment to screen toxicity hazards in the life cycle of CIGS thin film photovoltaics. *Journal of Hazardous Materials*, 260:534–542.

European Commission (2019). PEFCR - Photovoltaic modules used in photovoltaic power systems for electricity generation. Technical report.

Fiducia, T. A. M., Mendis, B. G., Li, K., Grovenor, C. R. M., Munshi, A. H., Barth, K., Sampath, W. S., Wright, L. D., Abbas, A., Bowers, J. W., and Walls, J. M. (2019). Understanding the role of selenium in defect passivation for highly efficient selenium-alloyed cadmium telluride solar cells. *Nature Energy*.

First Solar (2015). First Solar Achieves World Record 18.6 % Thin Film Module Conversion Efficiency.

First Solar (2018). First Solar 2017 Annual Report. Technical report.

First Solar (2019). First Solar Series 6^{TM} NEXT GENERATION THIN FILM SOLAR TECHNOLOGY.

Franzer, N. D., Paudel, N. R., Xiao, C., and Yan, Y. (2014). Study of RF sputtered Cu3SbS4 Thin-film Solar Cells. In *iEEE 40th Photovoltaic Specialist Conference (PVSC)*, pages 2326–2328.

Frischknecht, R., Heath, G., Raugei, M., Sinha, P., and de Wild Scholten, M. (2016). *Methodology Guidelines on Life Cycle Assessment of Photovoltaic Electricity 3rd edition*, volume IEA PVPS T.

Frischknecht, R., Itten, R., Sinha, P., de Wild-Scholten, M., Zhang, J., Fthenakis, V., Kim, H. C., Raugei, M., and Stucki, M. (2015). *Life Cycle Inventories and Life Cycle Assessments of Photovoltaic Systems. Report IEA-PVPS T12-04:2015*. Number PVPS Task 12, Report T12-04:2015.

Fthenakis, V. and Zweibel, K. (2003). CdTe PV: Real and Perceived EHS Risks. In *National Center for Photovoltaics and Solar Program Review Meeting*, number May, pages 1–3.

Fthenakis, V. M. (2004). *Life cycle impact analysis of cadmium in CdTe PV production*, volume 8.

Fthenakis, V. M. (2012). *Overview of potential hazards*. Elsevier Ltd.

Fthenakis, V. M., Fuhrmann, M., Heiser, J., Lanzirotti, A., Fitts, J., and Wang, W. (2005). Emissions and encapsulation of cadmium in CdTe PV modules during fires. *Progress in Photovoltaics: Research and Applications*, 13(8):713–723.

Fthenakis, V. M. and Moskowitz, P. D. (1995). Thin-film Photovoltaic Cells: Health and Environmental Issues in their Manufacture Use and Disposal. *Progress in Photovoltaics: Research and Applications*, 3(5):295–306.

Gandini, A. (2011). Hot point detection method. *Annals of Nuclear Energy*, 38(12):2843–2847.

García-Valverde, R., Cherni, J. A., and Urbina, A. (2010). Life cycle analysis of organic photovoltaic technologies. *Progress in Photovoltaics: Research and Applications*, 18(7):535–538.

Getis, A. and Ord, J. K. (1992). The Analysis of Spatial Association. *Geographical analysis*, 24(3):189–206.

Giudice, F., La Rosa, G., and Risitano, A. (2004). Materials selection in the Life-Cycle Design process: A method to integrate mechanical and environmental performances in optimal choice. *Materials and Design*, 26(1):9–20.

Green, M. A., Dunlop, E. D., Levi, D. H., Hohl-Ebinger, J., Yoshita, M., and Ho-Baillie, A. W. (2019). Solar cell efficiency tables (version 54). *Progress in Photovoltaics: Research and Applications*, 27(7):565–575.

Groen, E. A., Heijungs, R., Bokkers, E. A., and de Boer, I. J. (2014). Methods for uncertainty propagation in life cycle assessment. *Environmental Modelling and Software*, 62:316–325.

Gupta, M. Z. (2010). *An investigation into the leaching of enargite under atmospheric conditio*. Master's thesis, Queen's University.

Hansen, J., Reed, C., Scudese, M., Lazarus, L., and Park, F. (1994). Technical Assistance Document for Complying with the TC Rule and Implementing the Toxicity Characteristic Leaching Procedure (TCLP). Technical report, U.S. EPA.

Hauschild, M. Z., Rosenbaum, R. K., and Olsen, S. I. (2017). *Life Cycle Assessment: Theory and Practice*.

Heijungs, R. (2010). Sensitivity coefficients for matrix-based LCA. *International Journal of Life Cycle Assessment*, 15(5):511–520.

Heijungs, R. and Lenzen, M. (2014). Error propagation methods for LCA - A comparison. *International Journal of Life Cycle Assessment*, 19(7):1445–1461.

Held, M. and Ilg, R. (2011). Update of environmental indicators and energy payback time of CdTe PV systems in Europe. *Progress in Photovoltaics: Research and Applications*, 19:614–626.

Hong, J., Shaked, S., Rosenbaum, R. K., and Jolliet, O. (2010). Analytical uncertainty propagation in life cycle inventory and impact assessment: Application to an automobile front panel. *International Journal of Life Cycle Assessment*, 15(5):499–510.

Huang, B., Chen, S., Deng, H. X., Wang, L. W., Contreras, M. A., Noufi, R., and Wei, S. H. (2014). Origin of reduced efficiency in Cu(In,Ga)Se2 solar cells with high ga concentration: Alloy solubility versus intrinsic defects. *IEEE Journal of Photovoltaics*, 4(1):477–482.

Huang, M., Xu, P., Han, D., Tang, J., and Chen, S. (2019). Complicated and Unconventional Defect Properties of the Quasi-One-Dimensional Photovoltaic Semiconductor Sb 2 Se 3. *ACS Applied Materials & Interfaces*, 11:15564–15572.

Huijbregts, M. A. (1998). Application of Uncertainty and Variability in LCA, Part I: A General Framework for the Analysis of Uncertainty and Variability in Life Cycle Assessment. *The International Journal of Life Cycle Assessment*, 3(5):273–280.

Humbert, S. (2009). Geographically Differentiated Life Cycle Impact Assessment of Human Health. *UC Berkeley Electronic Theses and Dissertations*.

Imbeault-Tétreault, H., Jolliet, O., Deschênes, L., and Rosenbaum, R. K. (2013). Analytical propagation of uncertainty in life cycle assessment using matrix formulation. *Journal of Industrial Ecology*, 17(4):485–492.

ISO/TC 207 (2006a). International Standard 14040:2006. *International Organization*, 2006:1–11.

ISO/TC 207 (2006b). International Standard 14044:2006. *The International Journal of Life Cycle Assessment*, 2006(7):652–668.

Jung, J., Von Der Assen, N., and Bardow, A. (2014). Sensitivity coefficient-based uncertainty analysis for multi-functionality in LCA. *International Journal of Life Cycle Assessment*, 19(3):661–676.

Jungbluth, N., Stucki, M., Flury, K., Frischknecht, R., and Busser, S. (2012). Life Cycle Inventories of Photovoltaics. Technical report, ESU-services Ltd.

Komoto, K. and Lee, J.-S. (2018). *End-of-Life Management of Photovoltaic Panels: Trends in PV Module Recycling Technologies*. International Energy Agency Photovoltaic Power Systems Program.

Lacirignola, M., Blanc, P., Girard, R., Pérez-López, P., and Blanc, I. (2017). LCA of emerging technologies: addressing high uncertainty on inputs' variability when performing global sensitivity analysis. *Science of the Total Environment*, 578:268–280.

Lewis, H., Gertsakis, J., Grant, T., Morelli, N., and Sweatman, A. (2017). *Design + Environment*. Routledge, New York, NY.

Masson, G., Kaizuka, I., Cambie, C., and Brunisholz, M. (2018). 2018 Snapshot of Global Photovoltaic Markets, Report IEA-PVPS T1-33:2018. Technical report.

McClary, S. A., Andler, J., Handwerker, C. A., and Agrawal, R. (2017). Solution-processed copper arsenic sulfide thin films for photovoltaic applications. *Journal of Materials Chemistry C*, 5(28):6913–6916.

McClary, S. A., Li, S., Yin, X., Dippo, P., Kuciauskas, D., Yan, Y., Baxter, J. B., and Agrawal, R. (2019). Optoelectronic Characterization of Emerging Solar Absorber Cu3AsS4. In *IEEE Photovoltaics Specialists Conference Proceedings*, pages 3–7.

Mokhtarimehr, M., Forbes, I., and Pearsall, N. (2018). Environmental assessment of vacuum and non- vacuum techniques for the fabrication of Cu 2 ZnSnS 4 thin film photovoltaic cells. *Jpn. J. Appl. Phys.*, 57.

Nielsen, P. H. and Wenzel, H. (2002). Integration of environmental aspects in product development: A stepwise procedure based on quantitative life cycle assessment. *Journal of Cleaner Production*, 10(3):247–257.

Norris, G. A. (2002). Impact Characterization in the Tool for the Reduction and Assessment of Chemical and Other Environmental Impacts - Methods for Acidification, Eutrophication, and Ozone Formation. *Journal of Industrial Ecology*, 6(3-4):79–101.

Nuss, P. and Eckelman, M. J. (2014). Life Cycle Assessment of Metals: A Scientific Synthesis. *PLOS ONE*, 9(7):e101298.

Padilla, R., Girón, D., and Ruiz, M. C. (2005). Leaching of enargite in H2SO4–NaCl–O2 media. *Hydrometallurgy*, 80:272–279.

Ramasamy, K., Sims, H., Butler, W. H., and Gupta, A. (2014). Selective nanocrystal synthesis and calculated electronic structure of all four phases of copper-antimony-sulfide. *Chemistry of Materials*, 26(9):2891–2899.

Reilly II, J. F. and Bernhardt, D. (2019). *Mineral Commodity Summaries*. U.S. Department of the Interior.

Ries, S. and Lloyd, S. M. (2007). Characterizing, Propagating, and Analyzing Uncertainty in Life-Cycle Assessment: A Survey of Quantitative Approaches. *Journal of Industrial Ecology*, 11(1).

Ryberg, M., Vieira, M. D. M., Zgola, M., Bare, J., and Rosenbaum, R. K. (2014). Updated US and Canadian normalization factors for TRACI 2.1. *Clean Technologies and Environmental Policy*, 16(2):329–339.

Sai Gautam, G., Senftle, T. P., and Carter, E. A. (2018). Understanding the Effects of Cd and Ag Doping in Cu 2 ZnSnS 4 Solar Cells. *Chemistry of Materials*, 30(14):4543–4555.

Sassi, M. and Gupta, A. K. (2008). Sulfur Recovery from Acid Gas Using the Claus Process and High Temperature Air Combustion (HiTAC) Technology. *American Journal of Enviromental Sciences*, 4(5):502–511.

Savory, C. N. and Scanlon, D. O. (2019). The complex defect chemistry of antimony selenide. *Journal of Materials Chemistry A*, pages 10739–10744.

Sengül, H. and Theis, T. L. (2011). An environmental impact assessment of quantum dot photovoltaics (QDPV) from raw material acquisition through use. *Journal of Cleaner Production*, 19(1):21–31.

Sinha, P., Heath, G., Wade, A., and Komoto, K. (2018). *Human Health Risk Assessment Methods for PV Part 1 : Fire Risks*.

Sinha, P. and Wade, A. (2018). Addressing Hotspots in the Product Environmental Footprint of CdTe Photovoltaics. *IEEE Journal of Photovoltaics*, 8(3):793–797.

U.S. Department of Energy (2011). Critical materials strategy. Technical report.

US EPA (1992). Method 1311 - Toxicity Characteristic Leaching Procedure. Technical report.

US EPA (1995). SCREEN3 Model User's Guide. Technical report.

Weidema, B. P., Bauer, C., Hischier, R., Mutel, C., Nemecek, T., Reinhard, J., Vadenbo, C. O., and Wernet, G. (2013). *Overview and Methodology: Data quality guideline for the ecoinvent database version 3*. Number 1(v3). Swiss Centre for Life Cycle Inventories, St. Gallen.

Wen, X., He, Y., Chen, C., Liu, X., and Yang, B. (2017). Magnetron sputtered ZnO buffer layer for Sb2Se3 thin film solar cells. *Solar Energy Materials and Solar Cells*, 172:74–81.

World Health Organization (2003). Antimony in Drinking-water. Background document for development of WHO Guidelines for Drinking-water Quality. Technical report.

Ye, Q., Glantz, M. H., Song, L., Sun, G., and Pan, X. (2003). Urban drought: a potential environmental hotspot in the western region development of China. *Ecosystems Dynamics, Ecosystem-Society Interactions, and Remote Sensing Applications for Semi-Arid and Arid Land*, 4890:466.

Yin, X., McClary, S. A., Song, Z., Zhao, D., Graeser, B., Wang, C., Shrestha, N., Wang, X., Chen, C., Li, C., Subedi, K. K., Ellingson, R. J., Tang, W., Agrawal, R., and Yan, Y. (2019). A Cu3PS4 nanoparticle hole selective layer for efficient inverted perovskite solar cells. *Journal of Materials Chemistry A*, 7(9):4604–4610.

Yu, K. and Carter, E. A. (2016). Elucidating Structural Disorder and the Effects of Cu Vacancies on the Electronic Properties of Cu2ZnSnS4. *Chemistry of Materials*, 28(3):864–869.

Yu, L., Kokenyesi, R. S., Keszler, D. A., and Zunger, A. (2013). Inverse design of high absorption thin-film photovoltaic materials. *Advanced Energy Materials*, 3(1):43–48.

Yuan, Z. K., Chen, S., Xiang, H., Gong, X. G., Walsh, A., Park, J. S., Repins, I., and Wei, S. H. (2015). Engineering Solar Cell Absorbers by Exploring the Band Alignment and Defect Disparity: The Case of Cu- and Ag-Based Kesterite Compounds. *Advanced Functional Materials*, 25(43):6733–6743.

Zampori, L. and Pant, R. (2019). *Suggestions for updating the Product Environmental Footprint (PEF) method*.

Zweibel, K. (1998). Thin Film Photovoltaics. In *Technology's Critical Role in Energy and Environmental Markets*, pages 1–10.

CHAPTER 7. INSIGHTS INTO DENSE Cu_3AsSe_4 THIN FILMS TOWARDS TANDEM PHOTOVOLTAICS

7.1 Introduction

As silicon and thin film technology continually decrease consumer costs and aim for global grid parity, it is possible novel single-junction thin film technology may not be able to compete unless notable capital, processing, or installation costs are eliminated. Alternatively, tandem photovoltaics have the potential to generate more electricity per unit area, making these technologies ideal candidates for area-constrained applications. The motivation for this chapter comes from the idea that an increased energy yield from tandem devices may be able to compete with mature solar technologies.

The compound Cu_3AsSe_4 has a calculated band gap between 0.3-0.9 eV (Yu et al., 2013, Berger and Prochukhan, 1969), which may make this material suitable for infrared technology or as the bottom layer in tandem PV applications. This material has also demonstrated promising preliminary thermoelectric properties (Balow et al., 2016) and its glasses have been studied for data storage applications (Karuppannan et al., 2011). Towards planar diode applications, the purpose of this chapter is to provide insight that may facilitate the development of dense Cu_3AsSe_4 thin films.

Section 7.3.1. is dedicated to determining the formation pathway of Cu_3AsSe_4 nanoparticles. This section analyses the phase present in the reaction vessel before and during the nucleation of the Cu_3AsSe_4 phase. Due to synthesis irregularities described in the text, the Cu_3AsSe_4 nanoparticles formed in this section are notably more oriented and faceted than those reported in previous literature (Balow et al., 2016). Sections 7.3.2. and 7.3.3. describe the observed instability of nanoparticles produced following the reported synthesis procedure. Therefore, the characterization results reported in these sections for are not a result of the synthesis irregularities reported in Section 7.3.1.

7.2 Experimental details

7.2.1 Materials

The chemicals and materials used to complete the investigations in this chapter are listed in Table 7.1.

7.2.2 Nanoparticle fabrication

To minimize contamination, the glassware and stir bars used for the syntheses below are not used for any other reaction systems besides copper-arsenic-antimony-sulfide reactions. Even so, after cleaning with hexane, isopropanol, soap, and water three times, the glassware and stir bars are submerged for at least one day into nitric acid baths that are also dedicated for these and copper-arsenic-antimony-sulfide reactions. After the nitric acid bath, the glassware and stir bars are rinsed with RO water and stored in a non-dedicated drying oven maintained at 60 °C.

7.2.2.1 Synthesis of stock selenium precursor

Selenium powder (1.43 g, 18.1 mmol) is added to a round bottom, single-neck reaction vessel with a magnetic stir bar. 18.1 mL FPT OLA and 1.8 mL ethanethiol are then added in order. The reaction vessel is connected to a Schlenk line and purged five times with argon while being stirred vigorously at 600 rpm. After purging, the reaction vessel is stirred with argon for 15 minutes. Subsequently, a vacuum is introduced, and the contents are stirred for an additional one hour. The reaction vessel with selenium-OLA (Se-OLA) is sealed and transported to nitrogen for storage. If contents are exposed to oxygen, the reaction mixture will turn blue, indicating the stock solution is not usable.

7.2.2.2 Synthesis of Cu_3AsSe_4 nanoparticles

Copper (I) chloride (99.0 mg, 1mmol), 7.0 mL FTP OLA, and 30.1 mL (0.357 mmol) AsCl3 are added with a magnetic stir bar to a three-neck flask in a nitrogen environment. A glass

Table 7.1. *List of products used in this chapter*

Chemicals / equipment	**Purity / type**	**Source**	**Quantity***
ampule (10 mL)	Borosilicate glass	Chemglass Life Sciences	$\approx$ 13 g / treatment
Arsenic (III) chloride ($AsCl_3$)	>99.99	Sigma-Aldrich	$\approx$ 0.03 mL / synthesis
Centrifuge	Allegra X-30	Beckman Coulter	1 used indefinitely
Copper (I) chloride (CuCl)	>99.99	Strem Chemicals	$\approx$ 99 mg / synthesis
1-Ethanethiol	>99%	Acros Organics	$\approx$ 2.2 mL / synthesis
Ethanol	200 proof	Decon Labs	$\approx$ 70 mL / synthesis
Hexanes	>98.5% / ACS	Fisher Scientific	$\approx$ 10 mL / synthesis
1-Hexanethiol	>95%	Sigma-Aldrich	$\approx$ 0.01 mL per treatment
Oleylamine (OLA)**	>98% primary amine	Sigma-Aldrich	$\approx$ 14 mL / synthesis
Selenium pellets < 5 mm	>99.999%	Sigma-Aldrich	$\approx$ 55-70 mg / treatment
Selenium powder, 100 mesh	>99.99%	Sigma-Aldrich	$\approx$ 15-25 mg / treatment $\approx$ 240 mg / synthesis
Stir bar	3/8” PTFE	VWR International	1 used indefinitely
Toluene	>99.5%	Macron Chemicals	$\approx$ 4 mL / synthesis
Vortex Mixer	Analog	VWR International	1 used indefinitely

**Hexane, IPA, water, soap, and nitric acid used for glassware cleaning between each synthesis is not included*
***OLA stock solution was degassed using three freeze-pump-thaw (FPT) cycles and stored under nitrogen*

rod which is long enough to be submerged in the liquid is inserted into one neck of the vessel to monitor the reaction temperature when OLA and a thermocouple is added. This port is not open to the reactants. One neck is closed with a puncturable rubber septa, which is useful for reactions that require aliquots to be taken at specific time-intervals. The last neck is attached to a condenser tube and valve, and the value is connected to a Schlenk line where the line to the valve is purged three times. The valve is then opened, and the reaction contents are purged three additional times with argon. While stirring continuously at 500 rpm, the contents are subsequently heated to 125 – 200 °C depending on the desired reaction conditions which are specified in the main text. When the desired reaction temperature has been reached, 2.8 mL of Se-OLA (stock selenium precursor) is added. The reaction proceeds for up to 60 minutes depending on the desired reaction conditions. After the desired time has passed, the reactants are cooled naturally to approximately 40 °C when the washing procedure begins. This procedure can be scaled up or down depending on the quantity of nanoparticles preferred.

For syntheses requiring aliquot removal, a glass syringe is used. The syringe is purged first with toluene, then with FPT OLA. Nitrogen gas is then used to purge the inner contents of the syringe until the aliquot is ready to be removed from the reaction mixture. At this time, the syringe is filled completely with argon and slowly compressed to maintain a positive pressure with respect to the ambient until the needle is ready to puncture the septa attached to the reaction vessel. The amount of argon remaining in the syringe before puncturing the septa should be comparable to the aliquot volume. The argon is then expelled into the vessel and the aliquot is removed. For aliquot storage, a 4 mL vial with a puncturable cap is used. Between aliquot removal, the exterior is cleaned with hexane and the interior is cleaned as described above.

7.2.2.3 Washing of Cu_3AsSe_4 nanoparticles

The reactants are exposed to ambient and poured into a 20 mL centrifuge tube. The tube is topped with ethanol, vortexed for ten seconds, and centrifuged at 14000 rpm for one minute. The supernatant is discarded, and approximately 5 mL hexane is added. The tube is vortexed for ten seconds and then centrifuged at 14000 rpm for one minute. The supernatant is discarded, and ethanol is added to top off the centrifuge tube. The tube is vortexed for ten seconds and then

centrifuged at 14000 rpm for one minute. The supernatant is discarded and 2 mL OLA and 0.2 mL ethanethiol are added to the tube. After vortexing for ten seconds, the tube is centrifuged at 14000 rpm for one minute. The supernatant is discarded and the same amount of OLA and ethanethiol are added and the procedure is repeated a second time. After the second centrifugation, the supernatant is discarded and the following steps are repeated with the same steps are before: add ethanol, vortex, centrifuge, discard supernatant, add hexane, vortex, centrifuge, discard supernatant, add ethanol, vortex, centrifuge, discard supernatant, add hexane, vortex, centrifuge, and the discard supernatant. Finally, the nanoparticles are resuspended with about 4 mL toluene and stored until used.

7.2.2.4 Differences in the syntheses reported herein

Some differences were noted during the syntheses in this study and are reported below for transparency. Notes from the 140 °C reaction include: the reaction was scaled by 1.5x; the precursor solution in the reaction vessel was slightly blue, indicating moderate oxygen exposure; at 60 °C the vessel was agitated to incorporate bubbles on the side of the reaction vessel. Notes during the 125 °C – 200 °C reaction include: The reaction was scaled by 1.5x; before Se-OLA injection, the syringe was punctured into the vessel and remained in the vapor space above the reactants for thirty seconds before injecting the precursor; 4.0 mL of Se-OLA was used instead of 4.2 mL of Se-OLA; the first hexane wash after the first ethanol wash was omitted.

7.2.3 Film fabrication

Nanoparticles are dried before being resuspended under a continuous flow of nitrogen. The nanoparticles are then suspended in hexanethiol with a concentration of 250 mg per mL in a glass vial. This vial is vortexed for approximately two minutes right before coating onto a molybdenum-coated soda-lime glass substrate using a doctor blade technique with a clean glass rod. The amount of liquid used is dependent on the surface area covered but requires 24.8 mL per square meter of substrate. Typically, a lab scale setting requires anywhere from 4 to 40 μL. The coating procedure proceeds as follows in a fume hood: A substrate is placed with the molybdenum

side facing upwards between home-made taped glass rails that allows the rod to pass over the substrate without making direct contact. The nanoparticle suspension is pipette across the width of one end of the substrate. A glass rod is used to push the nanoparticle suspension across the length of the substrate and is returned to its original position in a process that is repeated once more. The freshly coated substrate is placed upwards at an angle such as to minimize the spreading that occurs due to the build-up of solution where the glass rod had been removed. Drying is determined through visual inspection, but typically lasts several minutes. Afterwards, the substrate is again placed between the glass rails and the coating procedure as above is repeated once more. Unless the films are immediately used, they are stored in a nitrogen environment.

7.2.4 Ampule preparation

Ampules used in this study have a neck diameter of approximately 0.6 cm so nanoparticle-coated substrate samples must be at least this small in one dimension. The substrate sample size used in all ampule treatments mentioned in this chapter is 0.6 cm x 2.5 cm unless otherwise noted. If treatments are performed under a controlled-vapor environment, the appropriate chemicals are first put into the ampule in a nitrogen ambient. The nanoparticle-coated substrates are then loaded into the ampule and sealed from oxygen with a valve. The ampule is then connected to a Schlenk line which is purged three times with argon. The valve is opened and the ampule is purged three times with argon. When under a vacuum of approximately 0.2 torr, a butane torch is used to yield the glass at the neck until an airtight seal is formed. The resulting total volume of the ampule is approximately 13 mL.

7.2.5 Treatments

Most heat treatments occurred inside of an airtight ampule, which is loaded into a horizontal three-zone tube furnace. From one end, a K-type thermocouple protrudes into the center of the three zones. The other end is installed with a pushrod. The furnace is sealed and purged three times with argon. The furnace is then stabilized at operating temperature before the ampule is

pushed into the center of the three zones. Cooling occurs naturally after opening the top of the furnace.

The 450 °C treatment of Cu_3AsSe_4 nanoparticles on silicon occurred under a flowing argon environment. This sample was not sealed in an ampule, but instead was placed in the center of an open graphite box. The box was pushed into the furnace after it had stabilized at 450 °C. The sample was allowed to cool naturally after five minutes.

7.2.6 Characterization

A FEI quanta 3D dual-beam field emission scanning electron microscope (SEM) was used to capture nanoparticle and film morphology. Energy-dispersive X-ray spectroscopy (EDS) was collected with an accelerating voltage of 20 kV on the same SEM with a silicon drift detector. Elemental compositions were determined through AZtec software using standardless quantitative analysis. SEM images of nanoparticles and films were captured with an accelerating voltage of 5 kV and 10 kV, respectively. EDS measurements were completed with an accelerating voltage of 20 kV. X-ray diffraction (XRD) data were collected on a Rigaku SmartLab diffractometer using a copper Kα X-ray source with a Kβ filter in Bragg-Brentano mode. Raman spectra were collected using a Horiba/Jobin-Yvon LabRAM HR800 confocal microscope system with a 17 mW 633 nm He:Ne laser. Thermogravimetric analysis (TGA) was conducted using a TA Instruments SDT Q600 system in a 50 mL/min helium flow with a ramp rate of 10 °C/min. Wulff plots were generated using the Equilibrium Wulff Shape Generator (Garcia et al., 2014).

7.3 Results and discussion

7.3.1 Formation pathway of Cu_3AsSe_4 nanoparticles

In pursuit of the goal to provide insight towards the formation of dense Cu_3AsSe_4 thin films, this section investigates the conditions present for and the formation pathway of Cu_3AsSe_4

nanoparticles. The formation of nanoparticles through hot-injection has been documented (Balow et al., 2016), but insights into the mechanism of formation and explanation of secondary phase formation has not yet been documented. Briefly, Se-OLA is injected at 125 °C into a solution of OLA, CuCl, and AsCl3, and ramped to 200 °C for 30 minutes. The synthesis in this section is a slightly altered form of the reported procedure (see Section 7.2.4.), and thus the discussion in this section is distinct from the discussion in following sections.

7.3.1.1 Reaction aliquots at 140 °C

To investigate the conditions present before the formation of Cu_3AsSe_4 nanoparticles, the reaction mixture was heated to approximately 130 °C for hot injection. The temperature profile for the solution during this experiment is provided in Figure 7.1 with the Se-OLA injection time as t = 0. Note the temperature decreased approximately 5 °C after injection but continued to rise steadily. This notable increase in temperature is standard and attributed to non-optimal PID controls, since the injection occurs during heating instead of after stabilization. Therefore, the curve is not entirely attributable to exothermic behavior from the reaction. Aliquots were removed from the reaction vessel at 0.5, 3, 5.6, 8, and 10.4 minutes after injection of the Se-OLA precursor to monitor changes in the phases present before the formation of Cu_3AsSe_4 nanoparticles.

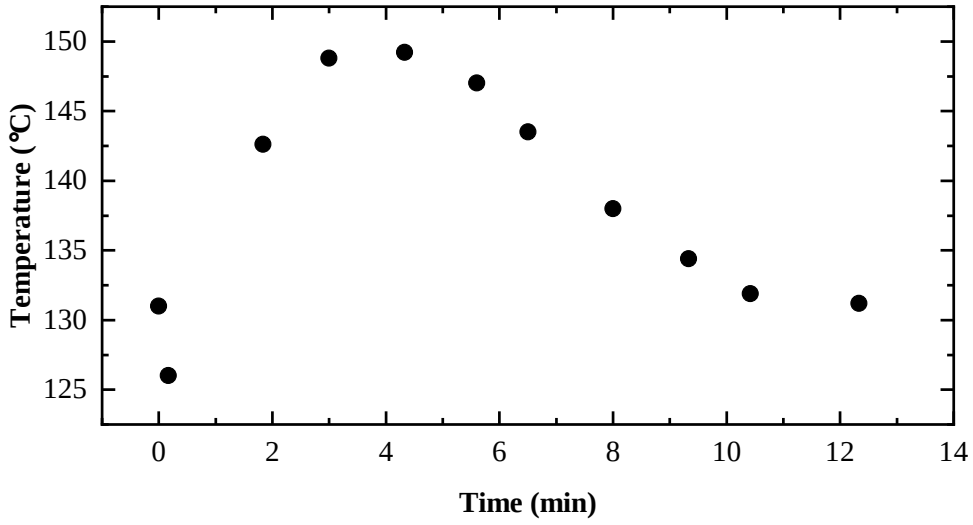

Figure 7.1. Temperature profile of the reaction solution during the "140 °C" aliquots

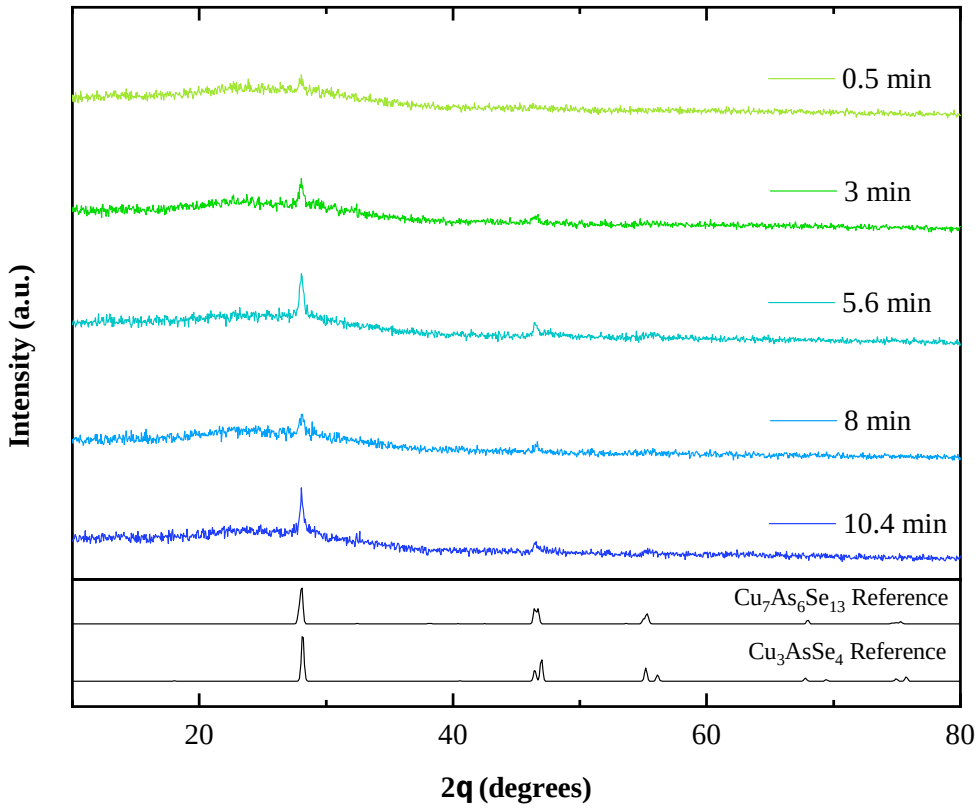

Figure 7.2. XRD spectra of the solutions removed from the reaction vessel corresponding to the "140 °C" aliquots. For reference, $Cu_7As_6Se_{13}$ (ICSD collection code 15235) and Cu_3AsSe_4 (ICSD collection code 610361) are provided.

Figure 7.2 displays XRD data for these aliquot samples. Structurally, the phases do not appear to change over the first ten minutes of reaction. However, conclusive evidence is limited due to the low signal-to-noise ratio. The peaks present in the sample indicate the possibility of the formation of a $Cu_7As_6Se_{13}$ or Cu_3AsSe_4 phase, but it does not appear to have strong crystallinity.

Regarding characteristic infrared activity, the Raman spectra corresponding to the aliquots are provided in Figure 7.3. The stretches do not correlate to any known copper-arsenic-selenide ternary or either one of the common binaries. The amorphous and crystalline arsenic selenides from compositions ranging from $Cu_{45}Se_{55}$ - $Cu_{25}Se_{75}$ do not have peaks corresponding to the broad peaks around 90 or 180 cm^{-1} and the peaks around 250 cm^{-1} are generally not well defined

except in the case of crystalline samples which also have peaks closer to 200 cm^{-1} (Ewen, 1978, Finkman et al., 1974). The copper selenides do not have peaks around 240 cm^{-1} except for $CuSe_2$ which also has peaks around 150 and 450 cm^{-1}. Therefore, it is likely the peaks observed in this reaction correspond to both binary systems, with the peaks around 90, 180, and 260 cm^{-1} corresponding to copper-rich copper selenides and the peak-shoulder between 230-240 cm^{-1} corresponding to arsenic selenide glasses. We note here that a ternary copper arsenic selenide phase is also possible, but lack of available Raman data on these ternary systems makes this assertion speculative.

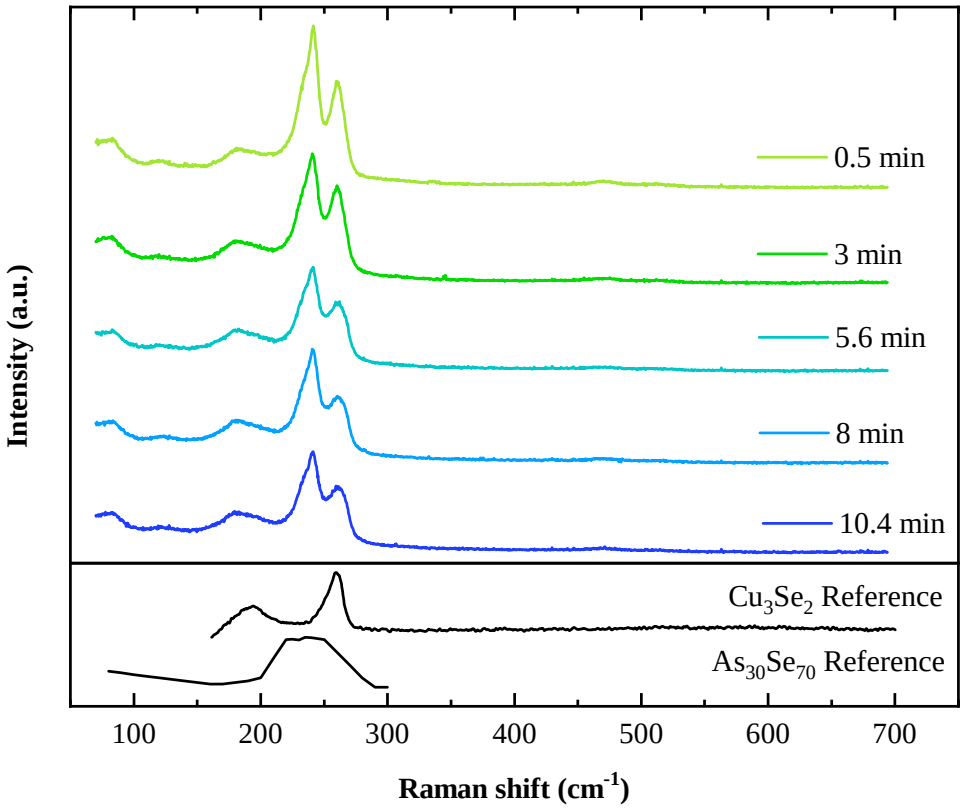

Figure 7.3. Raman spectra of the solutions removed from the reaction vessel corresponding to the "140 °C" aliquots. The Cu_3Se_2 reference corresponds to rruff ID R070019, and the data for $As_{30}Se_{70}$ are adapted from Figure 6.13 of this source (Ewen, 1978).

7.3.1.2 Reaction aliquots after ramping from 125 °C to 200 °C

To detail the reaction pathway to form Cu_3AsSe_4 nanoparticles, the reaction proceeded as previously documented (Balow et al., 2016) except aliquots were taken at short time intervals to monitor the change in Cu_3AsSe_4 formation. The reaction mixture was heated to 200 °C, and Se-OLA was injected at approximately 129 °C. The temperature profile for the solution during this experiment is provided in Figure 7.4 with the Se-OLA injection time as t = 0, as with the experiment described above. Aliquots were removed from the reaction vessel at 4, 7.5, 10, 12.9, and 15.6 minutes after injection of the Se-OLA precursor, which corresponds to 0, 3.5, 6, 8.9, and 11.6 minutes after the reaction reached 200 °C, respectively.

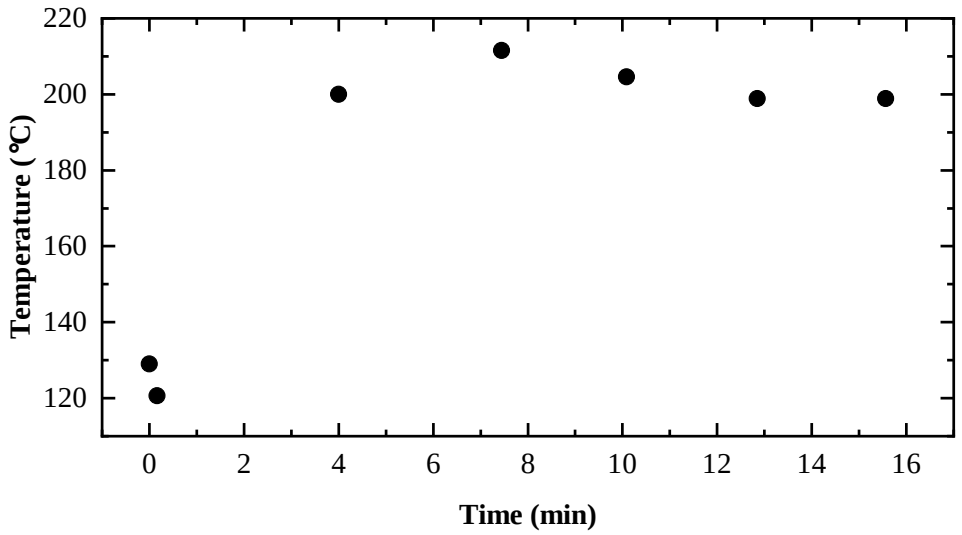

Figure 7.4. Raman spectra of the solutions removed from the reaction vessel corresponding to the "125 - 200 °C" aliquots.

Figure 7.5 displays XRD data for the aliquots taken during the 125 – 200 °C reaction. Phase-pure Cu_3AsSe_4 is observed, confirming the previous report (Balow et al., 2016). (Balow et al., 2016). However, one notable difference observed between the earlier report is the orientation along the {112} planes, which becomes more defined with reaction time. The nature of this orientation was investigated with scanning electron microscopy, and the observed nanoaggregates and faceted mesoparticles are displayed in Figure 7.6. Orientation of Cu_3AsSe_4 mesoparticles is

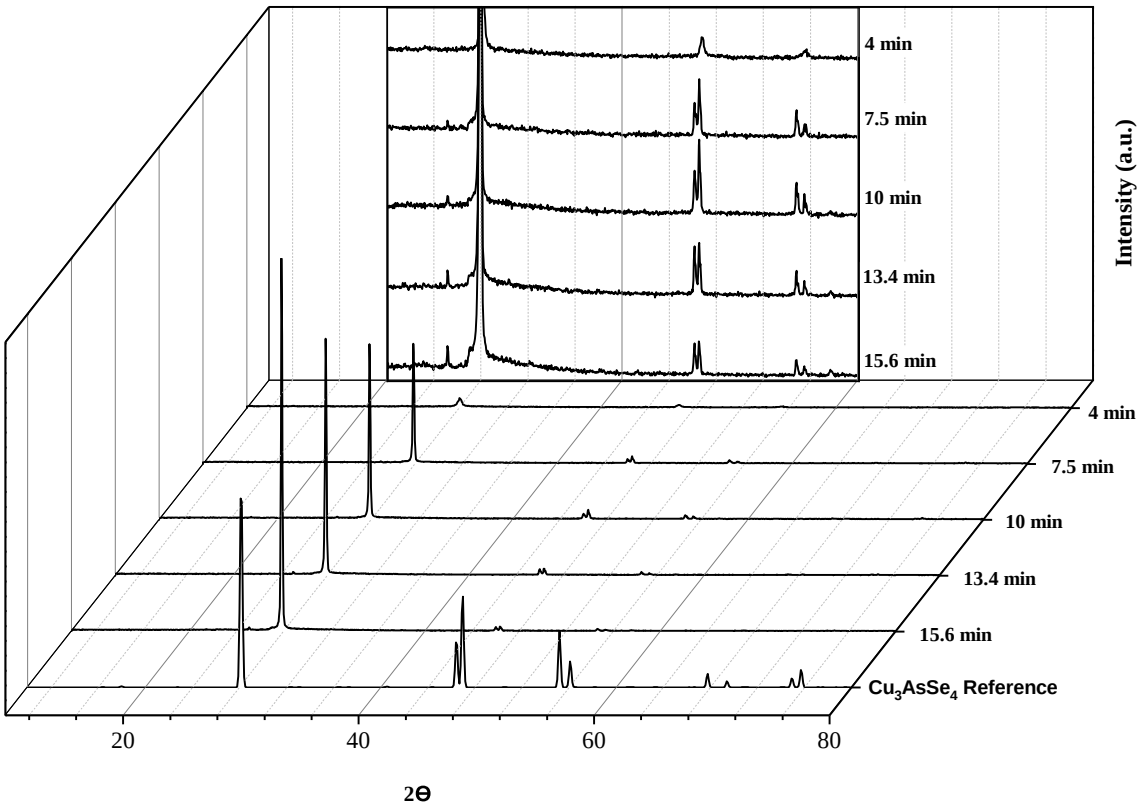

Figure 7.5. XRD spectra of the solutions removed from the copper-arsenic-selenide reaction vessel corresponding to the "125 – 200 °C" aliquots. The inset shows the same spectra but illustrates the detail on planes other than the primary $\{112\}$ planes. The small peak at 25.1 2θ is incomplete filtering of k-β from the primary peak. The Cu_3AsSe_4 reference is from ICSD collection code 610361.

correlated with what appear to be self-assembled triangular prisms. Triangular prisms, given their threefold symmetry, are not an equilibrium shape for the tetragonal crystal structure of Cu_3AsSe_4 with fourfold symmetry. Therefore, modelling of equilibrium shapes was completed and the resulting Wulff plots are depicted in Figure 7.7. These plots demonstrate that thin tetragon-like morphologies are the expected equilibrium shape for this system when strong preferred orientation exists along the $\{112\}$ planes. Triangular prisms can appear to exist when two neighboring particles form a common low-energy plane by redistributing mass from their nearest vertices, such as what is depicted by the arrow in Figure 7.7 (b). This explanation agrees with the observations of

strong preferred orientation along the {112} planes and triangular-like particles. However, it is also possible several low energy, slow growth planes that are not active in XRD cause a flattening of the equilibrium structure parallel to the triangular face. For example, the {100} and {001} planes are not active planes in XRD, but their relative energies are observed to change the equilibrium shape in Figure 7.7. Both explanations cannot be ruled out with the data provided. The cause of this tetragon-like formation during synthesis was not investigated, however, notable differences in reaction conditions are detailed in Section 7.2.2.4. Furthermore, we note the XRD and SEM characterization was performed after the particles were suspended in toluene for at least twenty-one days, suggesting a possible microstructural and orientation relationship with the solvent system.

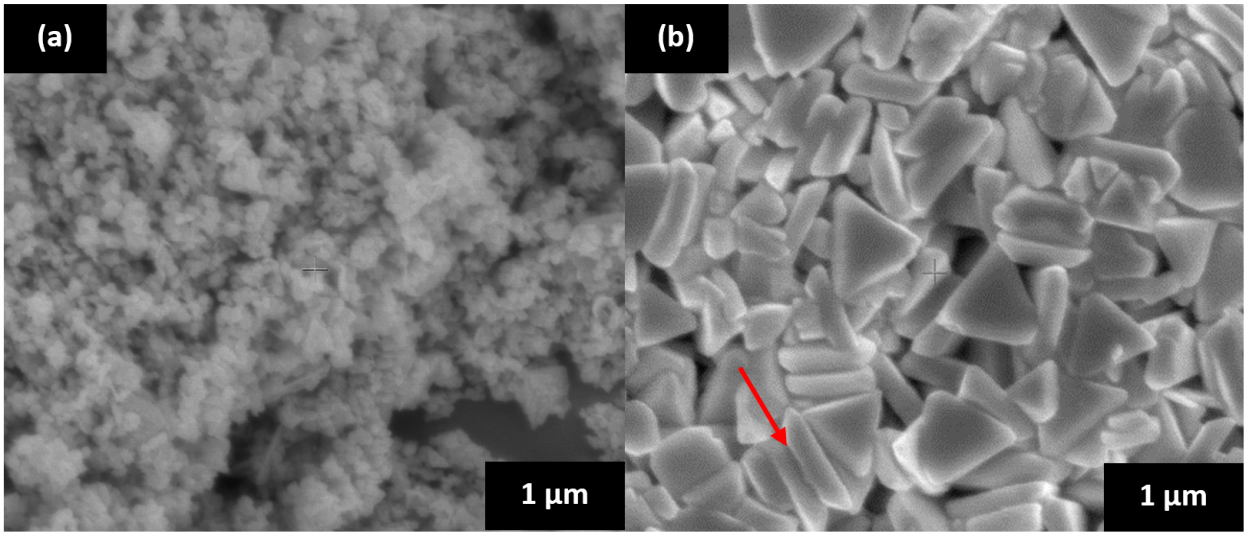

Figure 7.6. SEM images of mesoparticles removed from the "125 – 200 °C" aliquot study at the timestamp of (a) 4 minutes and (b) 15.6 minutes. The arrow in (b) indicates a low energy plane formed between two particles in place of expected vertices.

The Raman spectra of this aliquot synthesis are shown in Figure 7.8. The similar XRD pattern and bond stretches between the 4 minute aliquot and the "140 °C" aliquots suggests the same arsenic selenide and copper selenide binaries are present during the early stages of the 200 °C treatment. After several minutes, concurrent with the structural transformation, the bonding characteristics are found to stabilize with the Cu_3AsSe_4 phase. Together with the data above, these findings suggest a Cu_3AsSe_4 formation pathway beginning with a mixture of binary arsenic selenides and copper selenides.

Table 7.2. *Relative surface energies corresponding to those modeled in Figure 7.7.*

Surface	**Color**	**Relative energy**					
		7(a)	7(b)	7(c)	7(d)	7(e)	7(f)
{112}	Red	2	1.5	1	0.5	0.5	0.5
{100}	Tan	1	1	1	1	1	1
{001}	Green	1	1	1	1	1	1

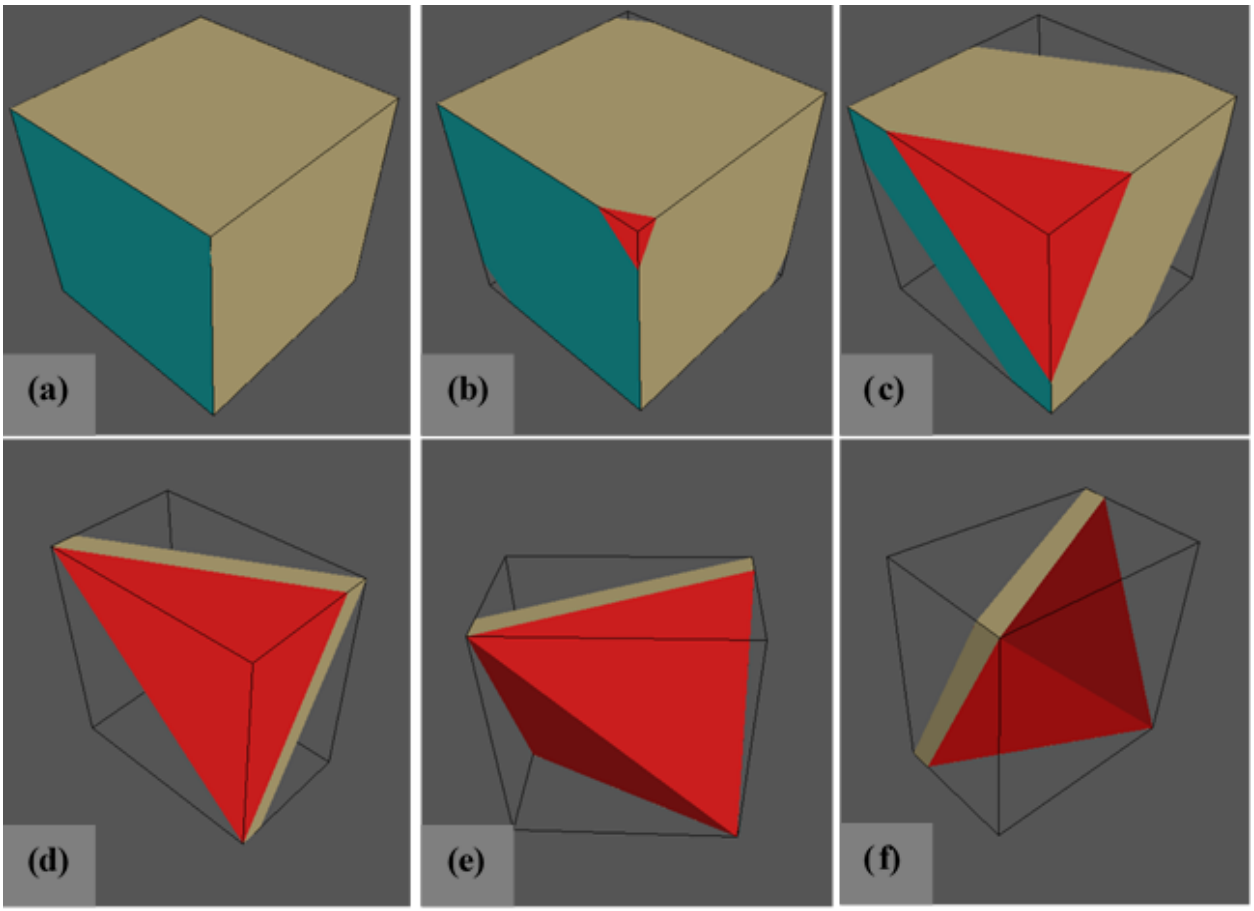

Figure 7.7. Wulff plots depicting 112 planes (red) gradually becoming relatively lower energy planes in a tetragonal crystal structure with $I\bar{4}2m$ symmetry, corresponding to Cu_3AsSe_4. Relative energies for (a), (b), (c), and (d) – (f) are 2:1:1, 1.5:1:1, 1:1:1, and 0.5:1:1, respectively for {112}:{100}:{001} planes, tabulated in Table 2. Figures (d) – (f) depict only a rotational transformation as relative energies are identical.

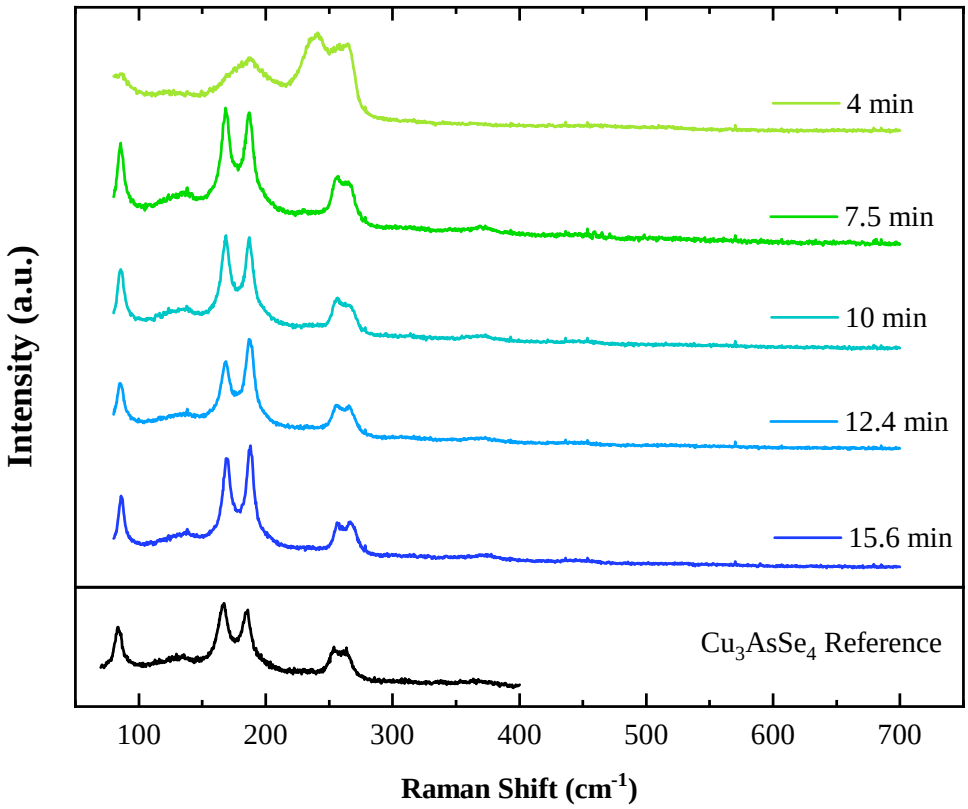

Figure 7.8. Raman spectra of aliquots taken from a copper-arsenic-selenide reaction mixture heated from 125 - 200 °C. The data correspond to the time after the Se-OLA precursor was hot-injected at 125 °C, where 4 minutes indicates the time the reactants first reached 200 °C. The Cu_3AsSe_4 reference is from (Balow et al., 2016).

7.3.2 Thermal instability of Cu_3AsSe_4 nanoparticles

In pursuit of the goal to provide insight towards the formation of dense Cu_3AsSe_4 thin films, this section investigates the instability region for Cu_3AsSe_4 nanoparticles. The nanoparticles studied in this section are fabricated using the reported synthesis (Balow et al., 2016), and results should not be misinterpreted as a follow-up investigation of the faceted nanoparticles detailed in the section above.

The Cu_3AsSe_4 phase has been documented to melt congruently at temperatures as high as 500 °C, presumably in an atmosphere of arsenic and selenium (Cohen et al., 1995). It has also been

documented to melt congruently around 477 °C, with a polymorphic transition to a cubic phase at 442 °C (Mashadieva et al., 2018). In an evacuated environment, Cu_3AsSe_4 has been reported to melt as low as approximately 460 °C (Liang et al., 1974, Rao et al., 1996).

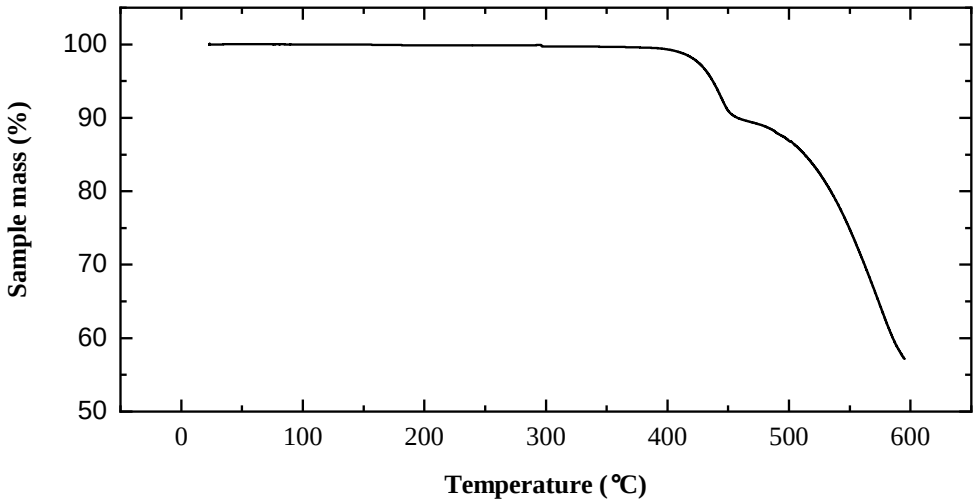

Figure 7.9. Thermogravimetric analysis of Cu_3AsSe_4 nanoparticles.

Due to the higher surface energy of nanoparticles compared to millimeter-size samples, the melting point for Cu_3AsSe_4 is expected to be lower than previous reports. Here, thermogravimetric analysis (TGA) in Figure 7.9 indicates nanoparticles of this phase begin to lose mass after the sample pan exceeds 400 °C. The stabilization at approximately 450 °C indicates the presence of a non-congruent melting or a multiphase system. As demonstrated in Figures 7.10 and 7.11, the only XRD and Raman phases observed for these nanoparticles is the same as that previously reported for this synthesis technique (Balow et al., 2016) which demonstrated phase-pure nanoparticles. Since we also observe phase-pure nanoparticles, we reason non-congruent melting is observed for this phase under the TGA conditions reported: 10 °C/min ramp rate with 100 mL/min He flow. As $CuAsSe_2$ has a reported melting point of 415 °C (Liang et al., 1974, Rao et al., 1996), we speculate this phase may undergo partial thermal decomposition into $CuAsSe_2$.

To test this hypothesis, we heated these nanoparticles on a silicon substrate at 450 °C for 5 minutes before cooling to room temperature. The flow rate of argon during this procedure was 10

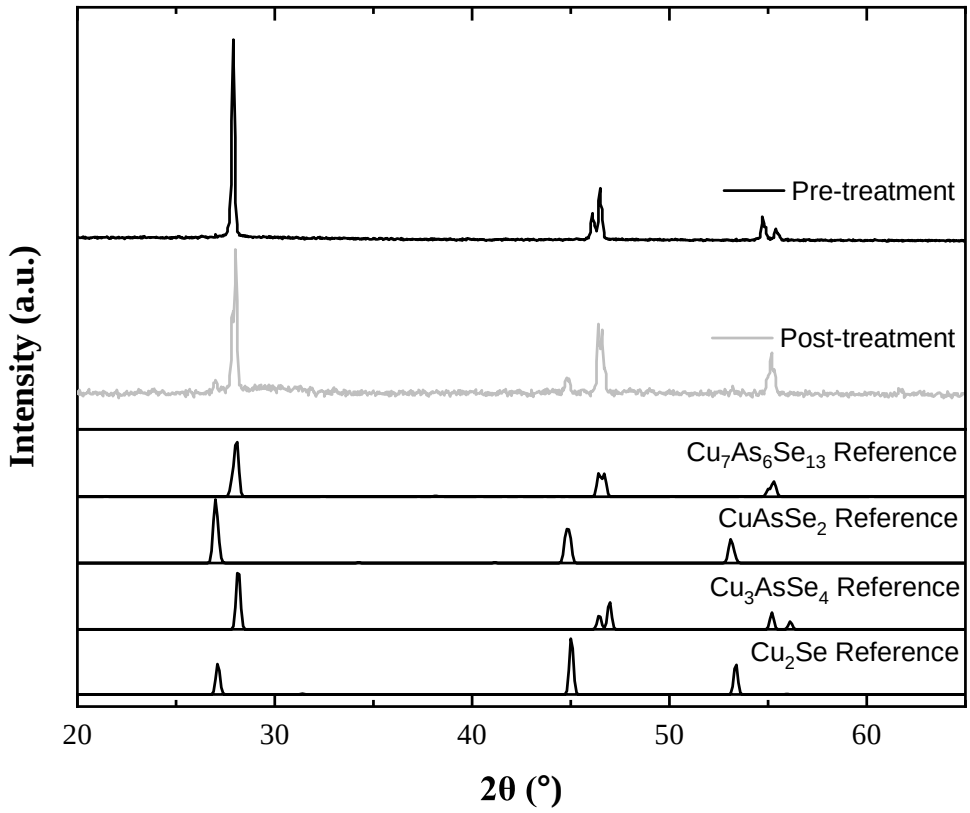

Figure 7.10. XRD spectra of Cu_3AsSe_4 nanoparticles. Spectra were obtained before and after a 5 minute, 450 °C treatment under 10 sccm argon flow. For reference, $Cu_7As_6Se_{13}$ (ICSD collection code 15235), $CuAsSe_2$ (ICSD collection code 42884), and Cu_3AsSe_4 (ICSD collection code 610361) are provided.

sccm. We note that red condensation was observed outside of the three zones of the furnace, which is indicative of selenium evaporating from the sample. We observed a structural transformation of the nanoparticles (Figure 7.10) and a change in characteristic IR activity (Figure 7.11). XRD analyses suggest structural transformation into a $Cu_7As_6Se_{13}$ phase and either a copper selenide binary or $CuAsSe_2$ phases. Raman analyses demonstrate bond activity not consistent with the famatinite Cu_3AsSe_4 nanoparticles, and have been identified in previous literature as an unknown phase that requires higher processing temperatures to form (Balow et al., 2016), which is consistent with our finding. These characteristic bonding frequencies, especially at 156 cm^{-1}, were not found by the authors to be identified in previous reported literature when searching copper selenides,

arsenic selenides, and copper-arsenic-selenide ternaries. However, similar frequencies were identified and attributed to $CuAsSe_2$ (Rödl, 2012). We note that Raman spectra for $Cu_7As_6Se_{13}$ was not found in our search. Although chemical analyses were not completed to quantify the amount that vaporized, we note selenium was observed to leave the system. These data support the hypothesis that the observed phase is a relatively selenium-poor phase that forms due to the volatility of (arsenic and) selenium. With the information above, we speculate this Raman spectrum may be attributable to $Cu_7As_6Se_{13}$ or a mixture of this phase with copper selenide or $CuAsSe_2$, but further chemical and analyses must be completed for confirmation.

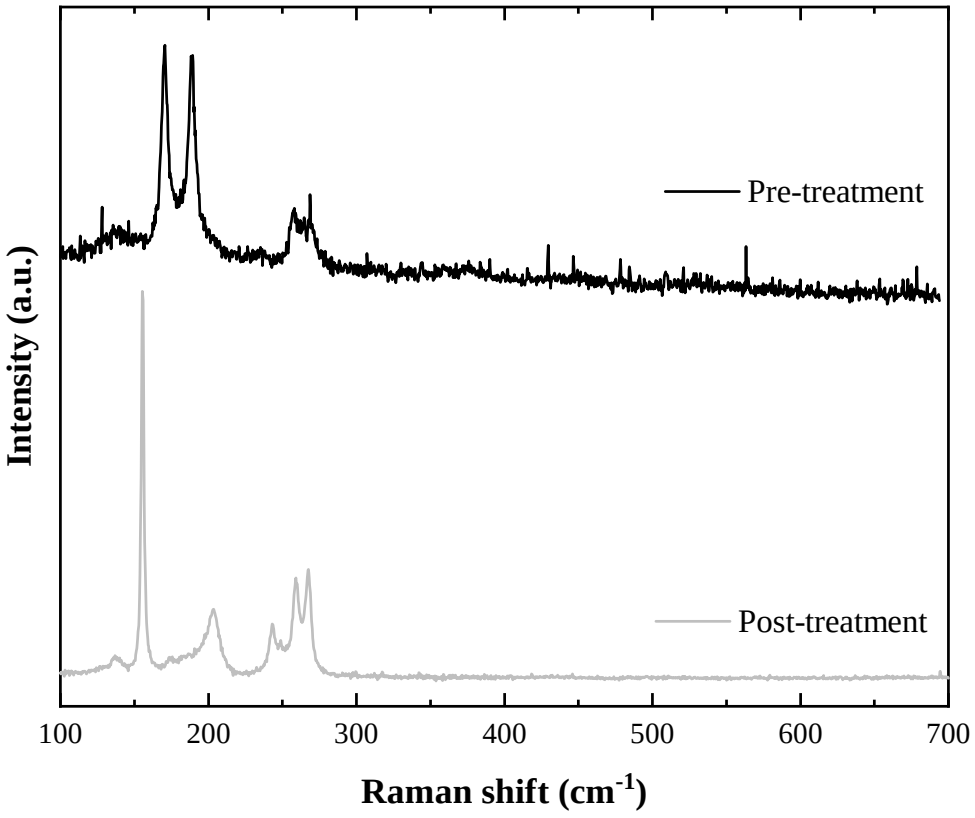

Figure 7.11. Raman spectra of Cu_3AsSe_4 nanoparticles. Spectra were obtained before and after a 5 minute, 450 °C treatment under 10 sccm argon flow.

7.3.3 Selenium-induced arsenic volatility during nanoparticle treatments

In pursuit of the goal to provide insight towards the formation of dense Cu_3AsSe_4 thin films, this section investigates treatments of Cu_3AsSe_4 nanoparticles in a selenium atmosphere. A previous report treated Cu_3AsSe_4 nanoparticles in a selenium pellet environment and observed traditional densification of the nanoparticle film via sintering (Balow et al., 2016). However, the film was still porous, and the grain size remained smaller than one micrometer. A porous film with numerous grain boundaries perpendicular to the light absorption plane is not ideal for a light absorber solar cell layer due to low absorption and increased recombination at these boundaries that limit minority carrier diffusion length. Therefore, insights are provided in this section to guide future experiments in this research space.

To investigate the role of selenium on the densification of the nanoparticle film, films were exposed to selenium in different forms at 250 °C and 340 °C. The forms used in this investigation were from powder and pellet sources, where powder is expected to volatilize more quickly than pellet sources to fill the vapor space more rapidly and condense on the film in a greater quantity. These studies were performed in an ampule and their preparation is described in Section 7.2.4. These samples were exposed slightly different conditions, which are listed in Table 7.3.

Scanning electron microscopy images are provided in Figures 7.12 (a)-(d). Increased non-uniformity is observed for samples that have been exposed to selenium powder compared to samples that have been exposed to a selenium pellet, even though less selenium is seen by the film at equilibrium conditions, indicating the influence of condensed selenium during early stages of heating. At 250 °C, regions devoid of particles are observed and indicated with an arrow. We speculate these voids are caused by heterogeneous condensation of selenium on the surface of the film that causes rearrangement of the particles through phase segregation of selenium and Cu_3AsSe_4. As time proceeds, the selenium evaporates to fill the vapor space and leaves an area void of particles. Grains over one micron in size were observed to form at 340 °C with a selenium powder environment, in contrast to the grains observed here and reported previously when selenium pellets were used at that temperature (Balow et al., 2016).

For investigating elemental composition differences between the samples, EDS data are provided in Figures 7.13 (a)-(d). As the reactivity at 250 °C is expected to be small, the slightly

Table 7.3. *List of conditions the respective samples were exposed to.*

Sample	Selenium source	Amount	Treatment conditions
(a)	powder	20.8 mg	250 °C, 30 minutes
(b)	powder	21.0 mg	340 °C, 30 minutes
(c)	pellet	66.4 mg	250 °C, 30 minutes
(d)	pellet	60.6 mg	340 °C, 30 minutes

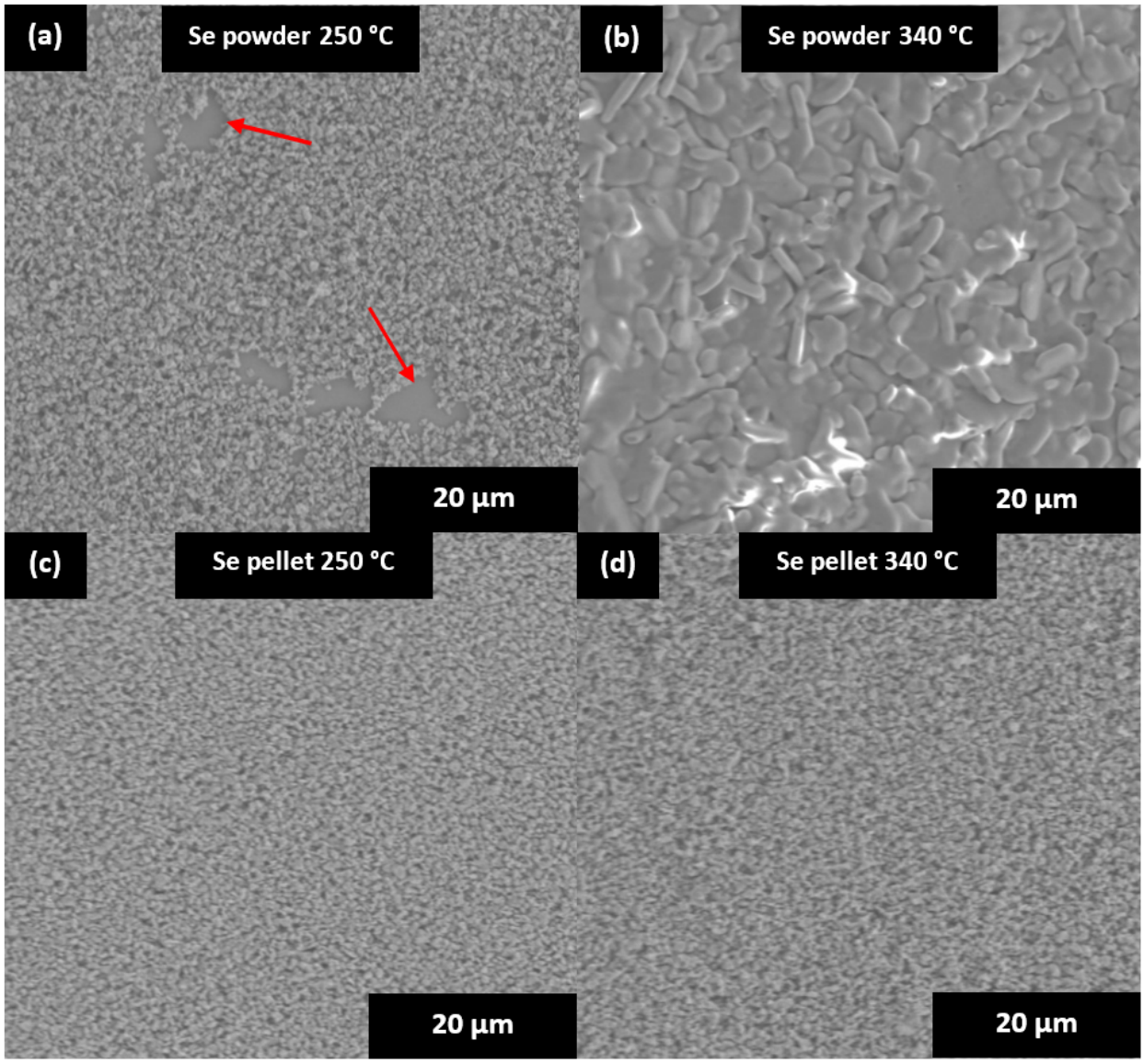

Figure 7.12. SEM images of Cu_3AsSe_4 nanoparticles treated under a Se atmosphere at different conditions.

copper poor data reflect the slightly copper poor synthesis conditions that are supposed to inhibit the formation of copper selenide secondary phases. Since the molybdenum back contact was detected in all EDS measurements with an accelerating voltage of 20 kV on an approximately one micrometer thick film, we attribute the arsenic deficiency for powder-based samples to a volatilization of arsenic. Given that the temperatures in this study are lower than the temperature in which these nanoparticles are observed to lose mass (Figure 7.9), we conclude the arsenic volatility is most likely due to the excess selenium on the surface of the film Therefore, these data demonstrate that excess selenium increases the arsenic volatility in this system.

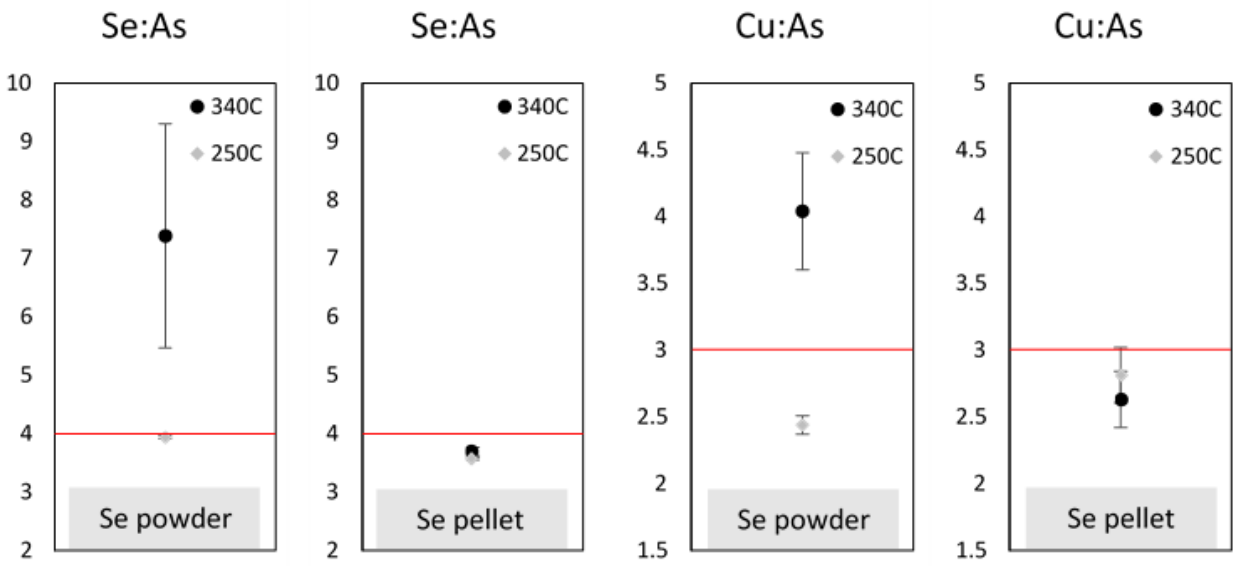

Figure 7.13. EDS data corresponding to Cu_3AsSe_4 nanoparticles that have been treated under a Se atmosphere at different conditions. The red lines indicate the stoichiometric ratios for Se:As and Cu:As. Error bars for all data indicate the standard deviation from measurements taken from two different parts of the film.

For sample (b), XRD analyses were inconclusive due to the very low signal to noise ratio, indicating the lack of an observable crystalline structure throughout the film. We note that copper arsenic selenides are known to be glassy in nature (Cohen et al., 1995, Karuppannan et al., 2011, Liang et al., 1974), so these data do not provide insight into additional film qualities such as the prevalence of binary or ternary phases. Raman analyses indicate the characteristic bonds in the film are no longer that of Cu_3AsSe_4, but determination of prevalent phases is also inconclusive

as the characteristic stretches measured were spatially inconsistent. From the SEM, EDS, Raman, and XRD data obtained, we conclude that excess selenium reacts with the copper in Cu_3AsSe_4 at 340 °C to form relatively large, glassy particles of material relatively rich in copper and selenium.

7.4 Conclusions and future directions

This chapter has provided insights into the formation route for Cu_3AsSe_4 nanoparticles, when and how these nanoparticles thermally decompose, and structural and chemical instability due to condensed selenium. It has been determined that nanoaggregates of copper selenide and arsenic selenide binaries form quickly and are stable in solution before the formation of the ternary Cu_3AsSe_4. Strong orientation behavior has been observed with a variation of the procedure reported in literature, but the source of this orientation has not been studied here. The faceted mesoparticles are modeled and agree with XRD data indicating strong orientation along the $\{112\}$ planes for these particles. The melting temperature for Cu_3AsSe_4 is inconsistently reported in literature, and here we demonstrate incongruent melting of nanoparticles under helium flow at a temperature exceeding 400 °C but less than 450 °C. When heated in a vacuum to 450 °C, we demonstrate these nanoparticles no longer retain a tetragonal Cu_3AsSe_4 structure and most likely transform into a selenium-poor phase due to elemental volatility. At temperatures well below where these nanoparticles are expected to lose structural and chemical integrity, excess selenium deposited on the surface of the film during the initial stages of heating has been shown to decrease uniformity and increase arsenic losses from the film, most likely through the formation of a copper selenide phase.

Since arsenic selenide and copper selenide binaries are found to be precursors to Cu_3AsSe_4 formation, it is possible that the formation of a dense film of this material can bypass a nanoparticle precursor, much like was observed for Cu_3AsS_4 in earlier chapters of this dissertation. However, future investigations into the formation of dense thin films of Cu_3AsSe_4 should note the arsenic and selenium volatility observed here and anneal under an atmosphere of these elements. The formation of persistent copper selenide ternary phases can be hindered by synthesizing with copper poor conditions. Although the formation of persistent arsenic selenide phases has not yet been

observed, it may be possible perform a post-deposition treatment of films to eliminate this phase, much like what has been demonstrated for removing persistent arsenic sulfide phases from Cu_3AsS_4 in earlier chapters of this dissertation.

7.5 Acknowledgements

J.A. would like to acknowledge financial support from the NSF under grant #1144843 (Purdue-Tuskegee IGERT on globally sustainable electronics) and laboratory support from the NSF under grant #1534691-DMR (DMREF: Rapid Design of Earth Abundant Inorganic Materials for Future PVs). He would like to thank Dr. Scott McClary for providing TGA data and assistance and training on Raman spectroscopy, and Dr. Chris Gilpin and Jameson Root for assistance and training with scanning electron microscopy, and Dr. Brian Graeser, Dr. Xianyi Hu and Essam Alruqoba for training and assistance with providing molybdenum-coated soda-lime glass.

7.6 References

Balow, R. B., Tomlinson, E. P., Abu-Omar, M. M., Boudouris, B. W., and Agrawal, R. (2016). Solution-based synthesis and characterization of earth abundant Cu3(As,Sb)Se4 nanocrystal alloys: towards scalable room-temperature thermoelectric devices. *Journal of Materials Chemistry A*, 4(6):2198–2204.

Berger, L. I. and Prochukhan, V. D. (1969). *Ternary diamond-like semiconductors*. Consultants Bureau, New York.

Cohen, K., Rivet, J., and Dugue, J. (1995). Description of the Cu-As-Se ternary system. *Journal of Alloys and Compounds*, 224:316–329.

Ewen, P. J. S. (1978). *THE RAMAN SPECTRA AND STRUCTURE OF GLASSES IN THE ARSENIC-SULPHUR AND ARSENIC-SELENIUM SYSTEMS BY Thesis presented for the degree of Doctor of Philosophy of the University of Edinburgh October 1978*. Ph.d., Edinburgh.

Finkman, E., DeFonzo, A. P., and Tauc, J. (1974). Raman Studies of the Crystallization of As2Se3. In Pilkuhn, M. H., editor, *Proceedings of the Twelfth International Conference on the Physics of Semiconductors*, pages 1022–1026, Wiesbaden. Vieweg+Teubner Verlag.

Garcia, R., Marques, P., and Freire, F. (2014). Life-cycle assessment of electricity in Portugal. *Applied Energy*, 134(2014):563–572.

Karuppannan, R., Ganesan, V., and Asokan, S. (2011). Electrical Switching in Cu-As-Se Glasses. *International Journal of Applied Glass Science*, 2(1):52–62.

Liang, K. S., Bienenstock, A., and Bates, C. W. (1974). Structural studies of glassy CuAsSe2 and Cu-As2Se3 alloys. *Physical Review B*, 10(4):1528–1538.

Mashadieva, L. F., Gasanova, Z. T., Yusibov, Y. A., and Babanly, M. B. (2018). Phase Equilibria in the Cu2Se–Cu3AsSe4–Se System and Thermodynamic Properties of Cu3AsSe4. *Inorganic Materials*, 54(1):8–16.

Rao, N. R., Rabinal, M. K., Sangunni, K. S., and Gopal, E. S. R. (1996). Devitrified phases in CuAsSe glasses. *Physica B*, 225:274–282.

Rödl, T. (2012). *Addukte der Gruppe 11 Halogenide mit Phosphor- und Arsenchalkogeniden Molekulare Aspekte in Festkörpern Dissertation*. PhD thesis, University of Regensburg.

Yu, L., Kokenyesi, R. S., Keszler, D. A., and Zunger, A. (2013). Inverse design of high absorption thin-film photovoltaic materials. *Advanced Energy Materials*, 3(1):43–48.

CHAPTER 8. INFLUENCE OF THE IGERT PROGRAM ON EMERGING LEADERS

The technical portion of this dissertation focuses on the development of Cu_3AsS_4 and Cu_3AsSe_4 as an absorber layer in photovoltaic materials. Dissertations in the engineering discipline often overlook both technical and non-technical contributions to the field, especially from humanities disciplines. In a growing interdisciplinary and intercultural world, it is useful to acknowledge, utilize, and build on progress in all practices. The Purdue-Tuskegee Integrative Graduate Education and Research Traineeship (IGERT) program on sustainable electronics not only advances technical knowledge in this space, but it also concentrates on training next-generation leaders in the scientific community.

Insights into the global electronics supply chain from domestic and international workshops are discussed in Sections 8.1.2. and 8.1.3., respectively. Understanding qualities of resilient systems are discussed in Section 8.1.4. in the context of social processes that have been significantly perturbed from steady-state conditions, with Puerto Rico after Hurricane Maria analyzed as a case study. Regarding emerging leaders, a technique to increase their cultural competency and ability to acknowledge bias is studied in Section 8.2.1. Insights into instilling leadership qualities such as motivation is discussed in Section 8.2.2. Lastly, practicing these leadership qualities as a mentor to high school teachers is discussed in Section 8.3.

8.1 Introduction to the IGERT program

The IGERT program is an NSF-funded traineeship that prepares graduate students to enter the workforce by focusing on collaborative, interdisciplinary training. A five-year traineeship was established at Purdue and Tuskegee Universities, and is focused on sustainable electronics. All graduate students working for this traineeship have projects dedicated to performing research in this field. Each cohort of graduate students takes four classes over two years and performs dedicated research concurrent with their thesis research. Two cohorts of graduate students from these universities were already mentored by faculty at their respective universities and are still involved with this traineeship. Eight students from Purdue University and two students from

Tuskegee University participated in this traineeship as part of the third and last cohort, of which I am included.

8.1.1 Class structure

The trainees are required to take four classes that focus on sustainable electronics. The first two classes served as the foundation for our learning. The concepts that were covered are important for all IGERT trainees, because this knowledge is necessary to make well-informed decisions about the sustainability of any product or process that we will spend time evaluating. The third class focused on understanding the environmental and economic implications of products by monitoring all inputs and outputs of a system. This class emphasizes life cycle assessment (LCA) fundamentals by quantitatively understanding the impacts that products and processes have on the environment. The fundamentals learned in the first three classes culminated in the final IGERT class, which focused on applying this knowledge to the specific research or topic of interest that each of the IGERT trainees are involved with. The objective of this last class is to expand the scope of understanding regarding topics learned in the first three classes by introducing the trainees to comprehensive examples of innovative research on these topics.

8.1.1.1 Introductory classes

The first classes serve as the introduction to fundamental ideas that are later expanded upon in subsequent research/classes. The first semester introduces basic concepts including the pillars of sustainability, polarity management, the Ostrom framework, tragedy of the commons, and circular economies. We learn about these concepts in the context of supply chain management, anthropological thinking, and life cycle assessments. For this semester, the focus of the final project was on value recovery of material components in hard disc drives.

During the second semester, these basic concepts are applied to sustainable development and product design for a circular economy. We were first taught about polymer design, formulation, and recyclability, which allowed us to use quantitative structure-activity relationships (QSARs) to perform risk analysis on a wide range of polymer chemistries. QSARs are a quantitative way

to make predictions about the possible danger a newly synthesized chemical may have on the environment based on its structure. Next, were given a deeper understanding of the amount of information necessary for a thorough life cycle inventory by considering the inputs and outputs of a typical metal extraction process. We then thoroughly explored supply chain management concepts including ideal supply chain structures, bullwhipping effects, and risk pooling. Lastly, we were introduced to the impacts that governmental policy have on local and national environments and how the concepts we learned tie into creating good policy, including using anthropological thinking to more fully understand a situation and apply the right kind of policies.

8.1.1.2 LCA class

The third class gave the cohort an in-depth understanding of how to perform a life cycle assessment, which is used for understanding the environmental impact of a product or process by examining the impact from every input into and output from the system, referred to as a life cycle inventory (LCI). We began discussing fundamental ideas including functional units, reference flows, system bounds, system processes, and unit processes, which are necessary to define or clarify in every LCA that is performed. We then discussed inventory databases (US-LCI, Ecoinvent, GaBi), impact databases (TRACI, USEtox, ReCiPe), and impact quantification (global warming potential, greenhouse gasses, etc.), which are useful for completing an LCI and finishing the impact assessment. The last component of an LCA consists of interpretation and analysis, which was demonstrated by completing both sensitivity and uncertainty analyses on a 36-process life cycle inventory manually built from the US-LCI database.

The versatility and effectiveness of LCA concepts were demonstrated through the introduction of different models. For a quick approximation of environmental impact for established sectors or new technologies, an economic input-output (EIO) model can be used in the absence of LCI information. EIO models assign an environmental impact per specified dollar amount, so an impact can be directly estimated from established or proposed economic flows. If an LCI is available, this information can also be used to determine the economic feasibility of a new technology, which can provide valuable information to the decision-making process for businesses or governments when deciding on what products to design, fund, or implement. These

valuable assessments are called techno-economic analyses (TEAs), which are most effectively used in early-stage assessments to understand the economic feasibility of various technologies. A more recent development in LCAs for comprehensive sustainability research is a social life cycle assessment (S-LCA). S-LCAs tie social impacts related to worker exploitation, community conditions, etc. to each LCI flow. This type of LCA is still in preliminary stages of development, but it has a potential to make considerable insights on human injustice throughout a product supply chain, which could substantially influence governmental or company policies.

8.1.1.3 Design for global sustainability

The final class was specifically designed to create a symbiotic teaching/learning environment between the IGERT trainees. Instead of a traditional lecture-style class, this class was developed to enhance learning and discussion by having each class taught by one of the trainees in a facilitating environment. The trainees presented lectures, discussion topics, and/or other interactive material directly related their main thesis work to the rest of the cohort, and clearly presented how the material learned in the previous courses were able to enhance their research. These in-depth, relevant topics helped the trainees expand on their knowledge formulated in the three previous courses.

A major portion of the class focused on the designing stage of electronic product development. We first considered design thinking as it relates to artificial intelligence, and how blue ocean strategies are an example of how to sustainably design a product. Biomimicry was discussed in relation to product design, and what specific role this design technique plays in existing products. We examined eco-design methods of a novel material, and how industrial symbiosis as a design goal is an innovative and effective sustainability strategy. Anthropological concepts were also discussed: understanding our and others' inherent biases, how products are designed, how to identify flaws, and how all these concepts relate to electronic product sustainability.

Other portions of the class addressed governmental influence on sustainability, and how electronic products affect different stakeholders. We learned about drafting and implementing of policies and the possible role we have in modifying them. We used this knowledge to lobby for

STEM in a group call to a staffer for a member of the U.S. House of Representatives. We lastly learned about the electronic recycling initiative in Guiyu, China, where one of the IGERT students visited. Guiyu has consistently been one of the largest e-waste sites in the world and is notorious for informal (usually dangerous or unhealthy) recycling. This city has been trying to improve its recycling reputation since 2010 when it began construction on a circular economy industrial park. Many improvements have been made regarding reducing the environmental impact and employee health hazards, but it still has room for improvement according to the student.

8.1.2 Indianapolis cohort field trip

After the second semester of classes, the students and faculty from Purdue and Tuskegee Universities met in Indianapolis to tour three businesses: Cascade Asset Management, Heritage Environmental Services, and DIVSYS International. The goal was to understand the electronics supply chain and the role of sustainability each of the companies. DIVSYS is a woman-owned international printed circuit board (PCB) manufacturer that makes PCBs for electronic devices, especially light emitting diodes (LEDs). They perform tests on PCBs in the manufacturer-distributor supply chain to independently collect data for the supplier as well as the customer to ensure quality products are distributed. Recently, DIVSYS paired with Heritage Environmental Services to decrease their hazardous waste emissions. Heritage exercises a sustainable business model by practicing green chemistry, where they perform research with the goal of turning hazardous waste into useful products. Their innovative solution to using the hazardous waste generated by DIVSYS had led to the collaboration that warranted our visit: The hazardous waste electrolyte solution from manufacturing PCBs at DIVSYS was sent to Heritage, where nutrients for animal feed were produced by filtering the waste and high-purity copper was extracted to sell back to DIVSYS. The remaining solution was no longer hazardous. This end-of-life hazardous waste recycling collaboration is a prime example of how to make the electronics supply chain more sustainable. Another method is employed by Cascade Asset Management, which recycles hard disc drives (HDDs) and other electronic products like televisions and computers that are nearing the end of their life. They separate valuable and non-valuable components of electronic materials

through manual disassembly and shredding. The most valuable components per pound found in HDDs in terms of revenue are the magnets, since they can be reused for similar applications and their constituent elements are not easily extracted from the earth's crust. Contrary to intuition, there is not much economic benefit from selling plastics or casing around most recycled electronic materials. This field trip was important for the IGERT cohort as it was the first physical exposure to electronics manufacturing, recycling, and business strategy.

8.1.3 India workshop

May 15th through May 29th, 2017 was spent touring different companies and organizations in India to learn more about electronics manufacturing, policy, and recycling. We met with chief officers, owners, directors, workers, and students from various businesses, colleges, and non-governmental organizations near New Delhi, Jaipur, and Udaipur. We learned how electronic materials are made, how electronic elements are mined and recycled, what it takes to build a successful business, how organizations give back to the community, and other related topics. To gain an appreciation and deeper understanding of what was learned or experienced throughout the day, we would discuss and record critical incident assessments as a group. These assessments consisted of structured discussion on a specific event that had some memorable or lasting impact where we thought valuable lessons could be learned or interesting insights could be shared. By the end of the trip, we had insightful discussions on almost every aspect of the trip including similarity in corporate models, differences in culture, and inspiring businesses with a dedication to the community in relation to economic, environmental, or social sustainability.

In New Delhi, we visited Deki Electronics, Toxics Link, Chintan, and Barco. Deki Electronics is an industrial film capacitor manufacturer that is growing in the light emitting diode (LED) industry. They informed us how the business was formed from a niche in the Indian market, since imported capacitors were taxed 60%, but the constituent materials were only taxed 40%. On one hand, they demonstrated a successful closed-loop material system by using their waste materials to make bricks, however, these bricks do not undergo certification and may have the potential to expose the users to hazardous chemicals. Intrapersonal bias was identified in the

cohort after speaking with the company after discussion on a comment made citing they do not hire women because they do not want to pay for maternity leave, which is a practice that is viewed differently from many of our backgrounds. Toxics Link is a non-governmental organization (NGO) dedicated to environmental justice. This company taught us about various strategies concerning public awareness, influencing corporations, and building a trustworthy reputation. Because many people of the community seek their help regarding health evaluations, their public awareness strategy is to educate nurses about toxins in the environment so these nurses can inform their patients. To influence companies to act more sustainably, they gather data from industry competitors and publicize comparable toxicity information, which motivates companies to reduce their toxic waste to increase public perception of the company. Building a trustworthy reputation relies on refusing company funding, which demonstrates their toxicity data is not influenced by financial incentives. Chintan is a recycling business that generates a revenue from items found in discarded waste. Although we were previously informed of their specialization in electronics recycling, we learned they make most of their revenue from aluminum cans. They offered free education for the children of their employees, which is admirable given these children may not otherwise receive an education. However, their company had a noticeable dichotomy in social structure: only women rummaged through waste, and only men oversaw the business and composting areas. Barco is a PCB and display technologies manufacturing company that focuses on customer connection through enhanced visualization performance. They informed us about corporate social responsibility (CSR), which is an ethical regulation imposed on companies that is aimed at improving the quality of life of the community where the companies are located. Barco's CSR initiative focuses on helping children from low-income backgrounds get into schools for a quality education. All these companies provided information that generated valuable discussion within the IGERT group on social structure, business strategies, and community outreach projects, which deepened our understanding of the global electronics industry. We particularly resonated with the stance many companies have on expanding access to education.

We next made our way to Jaipur, where we met with Deep Pandey and visited the Rajasthan Pollution Control Board, Barefoot College, and Jaipur Foot. These experiences focused our attention on how companies and organizations, with forceful orders and/or international

collaboration, can positively influence communities and the environment across the globe. Deep Pandey is the Principal Chief Conservator of Forests for the Rajasthan Government Forest Department and is an influential advocate for agroforestry. With his leading efforts to clean Rajasthan streets, parks, and forests of trash, he shut down about 1500 companies until they complied with regulations and agreed to improve their inadequate pollution habits. He is also a retired member of the Rajasthan Pollution Control Board, which enforces environmental policy that conforms to, but is independent from, the Indian Government. Their focus is on industrial waste, and they audit companies and NGOs by in-person visits and/or with sensors when appropriate. The board has shut down businesses for unacceptable handling of waste, and they recently implemented a ban on all plastic carry bags because of excessive plastic waste throughout the region. Many years ago, they worked closely with Teddy Roosevelt and the United States government to create closely related forest department programs. A similar display of international collaboration is also apparent in the next place we visited, Barefoot College. Not a traditional college, Barefoot is an organization promoting the equal status of women and rural people in developing communities across the world. They recruit older, poor women of tribes and communities, and teach these "solar mamas" how to operate and fix a solar lantern. The goal is to send these women back to their communities with a helpful wealth of knowledge and equipment that will help the community generate necessary electricity for many years. Aside from solar education, these mamas are also educated on a variety of subjects including health, economics, trade skills, gender and human rights, and social interaction with people that have different customs and beliefs. Older women are specifically chosen to enhance community connection; so the information is not kept to men in traditionally chauvinistic cultures, and so the younger generation does not use the knowledge for their own benefit and sell the equipment for their personal gain or leave their community to seek further education. The importance of a strong community connection is necessary for a growing economy, which is made clear with the last company visited in Jaipur. Jaipur Foot is an interesting and inspiring company that makes prosthetic limbs at a greatly reduced price compared to traditional prosthetics. Most employees have either received a limb from the business or are a part of the community and work to support the cause. After an individual was introduced to the company and their services many years ago, they informed

professors at Stanford University of their purpose. These professors agreed to help design a cheaper but durable prosthetic limb. Using plaster, wood, and rubber, Jaipur Foot makes customized prosthetic limbs for about $50 per limb (compared to about $10,000 in the United States) that are just as durable as a prosthetic limb made in the United States, but with a much higher turnaround time of less than 3 days (compared to a few months in the United States). Many people who get a limb from this company are not wealthy enough to afford to pay for all of it, even at this greatly reduced price. Since Jaipur Foot does not advertise, they generally rely on donations from either companies or private parties to support the financial aspect of the company. Like the companies in New Delhi, the companies in Jaipur provided the IGERT cohort with valuable discussion material. These discussions specifically focused on the influence of policies, education, and international collaboration on communities and the environment.

Lastly, we traveled to Udaipur where we visited Pyrotech Electronics, Hindustan Zinc Limited, Secure Meter, and the Indian Institute of Management. The meetings with these companies stimulated conversation about the display of appropriate treatment of employees in the workplace. Pyrotech Electronics is a manufacturing company and supplier for control panels, LED drivers/displays, sensors, and instruments for process control. A few examples of fair employee values in this company include employing more women than men to foster social gender equality and promoting employees from within instead of externally hiring upper management positions, which ultimately leads to longer retention rates. Employees also reported being satisfied with their working conditions, which may be reflected in the quality products sold by the company. Pyrotech's satisfaction of their products is shown in their eagerness to reveal that they created control panels for many companies, one of which is Hindustan Zinc Limited. Hindustan Zinc is a leading industry focused on the mining and production of lead, silver, cadmium, and zinc. This company exhibits employee rights through partnering with Dupont to stress a comprehensive safety training and culture. This safety culture is necessary in an industry that exposes its workers to hazardous metals such as lead and cadmium, and minerals like jarosite that contain varying amounts of these elements that can leach into the surrounding environment. Hindustan Zinc currently has five separate CSR projects focused on children, young children, adults, farmers, and women. The success of their company is self-attributed to four employee pillars that include

employee stewardship, strong relationships, effective communication, and sharing of values. These four necessary intracompany pillars can be compared with the four intercompany pillars that Secure Meter considers necessary for sustainable business design, which include marketplace, workplace, environment, and society. Secure Meter is an electric and gas metering company aimed at reducing the amount of energy wasted by energy-users, both commercial and private. They are proud to boast zero-waste and zero-discharge of wastewater with the use of their biogas plant, even as they explore various research and design projects. Their CSR consists of the construction of a "third space" (after home and work/school) that links science, art, and culture in an area where people want to spend their time but are still motivated to invoke their curiosity to question nature and learn about the world. They treat their employees reverently by having mandatory breaks every two hours, giving yearly pay raises to all employees, and by offering a suggestion box to improve aspects of the company that rewards employees for their ideas if they become implemented. The last venue the IGERT cohort visited was the Indian Institute of Management, which is a graduate school for some of the brightest students in the country. We visited a new location still under construction and met with the director of the university. We toured the living areas for students on campus, and noted the spacious, open, and inviting living conditions. The design of the campus is to be energy and water neutral, so there is significant investment in renewable energy, and a man-made lake that will provide the school's water needs. An interesting feature of the university is that every incoming student is required to live in poverty for two weeks before beginning classes to understand the problems faced by the poor, so they may begin to think about ways to offer solutions to these problems when they become leaders. All the places we visited in Udaipur gave the IGERT cohort a solid understanding of the employee-employer relationship and allowed us to have constructive discussions comparing practices in the United States.

The purpose of the India trip was to gain an understanding and appreciation of all the stakeholders in the global electronics supply chain. Meeting with people from NGOs, businesses, and other organizations gave the IGERT cohort a thorough understanding of the work necessary to build electronic products, uphold policies, or manage international businesses. Not only was discussing business logistics with upper management and observing the labor of employees educational from an academic perspective, but the meetings also allowed us to appreciate the

influence of CSR on the community. An equally important aspect of the trip were the discussions, both extemporaneous and those generated by the critical incident assessment forms. The perspectives introduced in these discussions were not always similar, and it was valuable to have an educated, constructive conversation about the shared experiences. By the conclusion of the trip, the IGERT cohort was able to gain an understanding of employee-employer relationships, effective corporate models, and the impact of policies and education on the environment. These lessons directly relate to our understanding of electronics sustainability – socially, economically, and environmentally.

8.1.4 Puerto Rico workshop

June 9th – June 13th, 2019 was spent in Puerto Rico touring various places to learn about resiliency and how companies and ecosystems bounced back after Hurricane Maria. From a big picture, the purpose was to understand how people, companies, and ecosystems recovered from a major perturbation to an established routine, supply chain, or life cycle. It is possible to model a sustainable system and predict what is important, but it is more difficult to model unexpected, notably impactful scenarios. Most of our IGERT experiences to this point were modelling and understanding a steady-state system, or learning how to incorporate and minimize unpredictability (especially for supply chain management). Specifically, the purpose of the trip was to engage in discussion with various stakeholders and learn about how the hurricane impacted them personally and what was necessary for reestablishing a business or life cycle, so that we could learn and apply these discussions to have a better grasp on how to better prepare systems to facilitate the construction of more resilient systems from the beginning.

The preparation for this Puerto Rico workshop was notably different than our India and Indianapolis experiences. The students took initiative to plan learning objectives, contact various stakeholders, and managing discussions during the workshop. This student-led programming was unlike previous experiences, which were mostly planned and executed by the professors. Practice planning the learning objectives, logistics, and meetings was a practical means of exposure to planning similar education-based workshops in the future. These soft skills are often overlooked

in Ph.D. programs but are a useful asset for emerging leaders to experience. An immediate benefit of planning the learning objectives for the trip was apparent through the notable increase in spontaneous learning experiences on this trip. Since the students had a complete grasp on the purpose of the trip and had built an expectation of acquired knowledge through self-motivated research, it facilitated unplanned, effective conversation from the students with local citizens.

The first conversation I had was with a student I met at a conference one month prior to the workshop, which initiated self-motivated seminar material that ultimately led to the cohort meeting with academics from the University of Puerto Rico. The purpose of this meeting was to gain insight into the academic and governmental initiatives into integrating a renewable energy portfolio into the Puerto Rican economy as a step toward electricity resiliency. The rationale for a renewable-based grid was apparent after Hurricane Maria in 2017 when distribution line damage resulted in most of the population losing access to electricity. In the case of renewable energy-based microgrids that may operate independently, power can be restored much more quickly since distribution is not localized to a single source. We learned that collaboration with academic-led research is difficult with the electricity monopoly on the island, but progress is being made towards a renewable energy-based grid through legislation. However, concerns with accountability have been raised since there is not a governing body to ensure compliance with self-mediated policies. In the case of resiliency against unstable circumstances, it may be more advantageous to design resilient systems opposed to subsequently adapting them.

In addition to meeting with stakeholders in the electricity sector, we met with representatives associated with El Yunque National Forest. The purpose of this meeting was to gain insight into how ecosystems naturally recover to inspire biomimicry in interdependent systems. One noteworthy aspect of natural systems is their persistent transformation. After an unanticipated event, natural systems do not bother restoring themselves to a previous state. Rather, they simply adapt to the present circumstance. Therefore, systems that are amenable to adaptation are inherently more resilient.

Throughout the workshop, students met with various industries, academics, entrepreneurs, and community members. Like in the examples above, these stakeholders provided valuable insight into resilient systems. One last factor for resilient systems gleaned from these stakeholders

is the importance of social capital. When external perturbations disrupt system norms, the social network of those affected can determine their resiliency more than established system processes. We were told countless anecdotes about the Puerto Rican communities orchestrating change through synergistic collaboration. Systems with social components can exercise resiliency through continued enhancement of social capital. As discussed more in Section 8.2. below, the workshop was found to be a success in teaching skills that are valuable for future leaders to employ. Through formulating the learning objectives, contacting stakeholders of interest, and conducting in-person meetings, the interdisciplinary, student-led initiatives were valuable for establishing intercultural competency. Systems with increased resiliency to external perturbations should consider designing adaptability and enhancing social capital.

8.2 Empowering leaders in interdisciplinary groups though intercultural experiences

The IGERT program in sustainable electronics seeks to empower leaders through cultivation of the necessary technical and personal skills in an increasingly global society. Although dissertations are technical in nature, less emphasis has traditionally been placed on personally preparing students for the intrinsically intercultural and interdisciplinary working environment they will be exposed to. Personal preparation through critical reflection of incidents is useful for increasing identification of bias and may lead to more productive encounters when projects, interactions, or experiences do not go as planned. Although these encounters happen regularly, there is an increased likelihood for these events in the context of intercultural and interdisciplinary groups. Productive encounters are an avenue for leaders to gain respect from their peers. These interactions can be enhanced from *intra*personal learning though *inter*personal reflection leading to increased cultural competence and identification of miscommunication. However, tools to develop these reflective skills in a systematic way are often not introduced to students. One tool employed by the sustainable electronics IGERT program is the critical incident assessment technique, which is adapted from [cite] and designed to build cultural competency through critical self-reflection. This technique is designed to help students grow personally by having them gain a deeper understanding of complex interactions during intercultural experiences. With the intention

of refining this technique, the third IGERT cohort studied the most useful practices for effective group discourse, discussed more in Section 8.2.1. below.

In addition to identifying personal bias, preparation for leaders in future workplace environments consists of building a motivated, cohesive team. The third cohort exhibited an unusually high degree of self-motivation and cohesiveness compared to the other IGERT cohorts that resulted in the group seeking additional educational experiences and opportunities. As this proactive, collaborative attitude is a desirable component regarding productive group dynamics, the cohort sought to identify specific factors present in their education and traineeship that may have acted as a catalyst for group efficacy. Through integrating self-determination theory and the expectancy-value model, four factors were analyzed by the third sustainable electronics IGERT cohort: value, competence, autonomy, and relatedness. Using these four factors as indicators, suggestions for enhancing motivation in interdisciplinary groups are identified in Section 8.2.2.

8.2.1 Reflecting on intercultural experiences

The study referenced in this section is Korey, M., Clarkson, C., Frost, K., Andler, J., Wang, Y., Reeves, M., and Handwerker, C. *Critical incident assessment as a tool to reflect on students' emotional response during international experiences.* ASEE Annual Conference & Exposition, Montreal, Canada, 2020.

A survey consisting of matrix, Likert, ranking, and open-ended questions was developed and sent to students from all cohorts associated with the sustainable electronics IGERT program. Responses were grouped into "agree" and "did not agree" categories which were analyzed statistically by means of a chi squared analysis. Open-ended questions were assessed to provide context for the analysis. The critical incident assessment technique was found to be useful for identifying personal biases and increasing cultural competence. It was found the technique was most useful in an environment where participants showed enthusiasm towards participating, like after instances where they felt misunderstood or when they emotionally sought different perspectives to gain insight into an interaction. Regarding technique logistics, the following recommendations were found: having a group size of approximately 5-10 people where everyone

feels they have an opportunity but not an obligation to have their opinions heard, time between 30-60 minutes (which is expected to change depending on the length and specificity of questions) in the afternoon, in a private area where passersby without context are not able to overhear discussion, and in an arrangement where participants can face one another. It is recommended to use these insights when structuring similar personal intercultural growth exercises.

8.2.2 Enhancing student motivation towards shared goals

The study referenced in this section is Wang, Y., Clarkson, C., Andler, J., Korey, M., Frost, K., Reeves, M., and Handwerker, C. *Lessons learned from the NSF IGERT program: cultivating student motivation in the interdisciplinary and international context.* ASEE Annual Conference & Exposition, Montreal, Canada, 2020.

A survey consisting of matrix, Likert, ranking, and open-ended questions was developed and sent to students from the sustainable electronics IGERT program who were involved in both the originally planned India workshop as well as the student-organized Puerto Rico workshop. As the number of participants were relatively small, statistical quantification was not justified. The IGERT traineeship was found during the student-organized workshop to be successful in nurturing competence, autonomy, and relatedness. These three factors were found to be integrated during the originally planned workshop and the self-designed academic course. The fourth factor, value, was found to be integrated at different points for individuals throughout the program.

The student-organized workshop was prepared after experiencing a successfully designed workshop and learning the practical skills of foresight, organization, and implementation during the execution of a student-led academic course. In theory, after having first-hand exposure to these skills, students will no longer these "unknown" logistics as a barrier to planning which may increase their competence and autonomy. Regarding cultural competence and identifying personal biases, as mentioned in section 8.2.1., having reflective discourse can expose misconceptions. Sharing perspectives and misunderstandings can then lead to increased group cohesiveness, as long as personal identities are not threatened. Underlying the development of these factors is the necessity of having shared values in the context of the program. This is to say that students

are expected to disagree on the journey, but if they agree on the destination, they can leverage these experiences to build competence, autonomy, and relatedness toward a shared goal. These values may be incorporated through early and regular exposure to other students while designing value-oriented goals, such as what is introduced during group projects. Successfully incorporating these values is the task of the faculty involved, primarily at early stages. It was determined that extrinsic motivation from faculty drove participation during the early stages of the program, but peer-influenced extrinsic motivation drove participation during later stages of the program. A self-motivating learning community was thus observed in the third cohort of the sustainable electronics IGERT program.

8.3 Research experience for teachers

8.3.1 Introduction to the program

The goal of the RET program on sustainable electronics is to provide high school teachers with the knowledge and skills they need to help their students begin to think critically about how products should be designed or used to reduce the negative human impact or environmental damage caused by the product. This program pairs graduate students with teachers for six weeks during the summer term to complete research on a project related to electronic sustainability. Most of the students from cohort three worked on a project with a high school teacher from around the same region of the US (Purdue students worked with teachers from Indiana, and Tuskegee students worked with teachers from Alabama). All these teachers integrated what they had learned during the summer into their curriculum for the following school year.

From only the first year of the program in 2016, approximately 1293 students received instruction related to sustainability, chemistry, governmental policy, or environmental impact of electronics disposal. Teachers' knowledge of science standards related to electronic sustainability improved by participating in this professional development program, and they reported increased confidence in their ability to integrate environmental design thinking into their curricula. The

expectation is that these students, having learned about up-to-date research in the electronics sustainability field, will be able to discuss (and possibly prioritize) sustainability concepts in their future careers. Many teachers have been educated through the RET program since its inception, and many more students have been impacted because of this experience.

8.3.2 Research

I worked on a life cycle assessment project with a science teacher during the summer of 2017. The main idea of this project was to begin developing a life cycle assessment for a novel semiconductor material, Cu_3AsS_4. The high school teacher did much of the background research focused on building the life cycle inventory that is necessary as a fundamental component of an LCA. She specifically investigated the smelting processes for copper and was able to get a sense for standard industrial material flows. These flows mainly include energy flows, but also include byproducts such as sulfur dioxide and arsenic salts, which are assumed to be used as feedstock in binary arsenic sulfide production that is necessary for thin-film Cu_3AsS_4 formation. LCI data was collected and assessed for this part of the manufacturing stage of the semiconductor life cycle. Work was also completed on the last stage of the semiconductor life cycle, which specifically investigated the leachability of these solar cells. Although no experiments were performed on this material by the conclusion of the program, she had compiled information on standard leaching test results from other photovoltaic technologies through researching the leaching methodology common in the hazardous waste field and finding relevant literature.

8.3.3 Knowledge transferred to students

The purpose of the RET program is to give teachers the knowledge necessary to educate students enough these students can begin to think critically about the impacts of all (electronic) materials. The specific purpose of the LCA research is to understand how to sustainably design a new absorber for photovoltaic applications by minimizing the life cycle impacts this PV system has. Students benefit from this work by being introduced to a hands-on activity where they get

to fabricate a dye-sensitized solar cell made from berry juice. With the accompanying lecture(s), this activity exposes the students to lab research, solar cell development, and the understanding of product environmental impacts. Hopefully, this knowledge will stimulate the students' curiosity and inspire them to critically analyze the life cycle of products during the design stage to optimize technical and life cycle performance from the start.

8.4 Conclusions

The IGERT program successfully communicated sustainability aspects of the electronic supply chain to three cohorts of interdisciplinary graduate students and developed them into emerging leaders in their respective disciplines, which was the goal of the program. However, from it emerged a unique feature that resulted in increased student motivation and performance. Although many programs are dynamic to incorporate new insights or developments, this IGERT program became shaped by the students it was training. These students demonstrated organized behavior aligned with IGERT values that exceeded originally structured programming.

From a leadership position, instilling motivation aligned with specified values is a useful tool for a team leader to practice. Having recognized the usefulness of this feature, the students organized survey questions, acquired data, and analyzed the program to determine key aspects that may have been most beneficial for instilling intra- and inter-personal value and motivation. It was found that extrinsic motivation from faculty drove participation during the early stages of the program, but peer-influenced extrinsic motivation drove participation during later stages. Peer-driven motivation may have been instilled through routine exposure to team exercises aligned with the values of the program. It may also have been instilled while identifying personal biases during critical incident assessment group discussions. Shared experiences are beneficial to develop rapport, but also can be used to teach leadership skills such as mentoring, organization, and communication. It is possible the soft skills developed in the beginning of this program established the confidence necessary to facilitate autonomous behavior near the end of the program. From the identified components of the IGERT program, the students recommend implementing similar strategies in future interdisciplinary graduate education training.

8.5 Acknowledgements

J.A. would like to acknowledge financial support from the NSF under grant #1144843 (Purdue-Tuskegee IGERT on globally sustainable electronics). He would like to acknowledge the professors associated with the IGERT program for orchestrating a successfully executed interdisciplinary traineeship, and the students associated with the program for broadening his perspective in countless ways.

CHAPTER 9. SUMMARY AND OUTLOOK

9.1 Conclusions and future efforts in Cu_3AsS_4-based photovoltaics

Dense, single-phase enargite films have been synthesized through reactive deposition with a thermally evaporated copper film. A champion device efficiency of 0.54% was achieved following a DAS post deposition etching procedure on these enargite films, which is the current record for enargite-based photovoltaic technology. However, the relatively low efficiency indicates the porosity and observable secondary phases were not limiting to initial nanoparticle-based device performances. This conclusion supports the hypothesis that band alignment issues with the current device architecture are the primary limiting factor for high efficiency devices.

The enargite band alignment with Mo and MoS_2 was modeled and suggests the formation of MoS_2 is detrimental to device performance, contrary to the formation of $MoSe_2$ in CIGS- or CZTS-based solar cells. If MoS_2 is formed, a hole barrier of approximately 0.4 – 0.5 eV is calculated, which is comparable to the ≈ 0.7 eV cliff offset calculated for the Cu_3AsS_4-CdS diode interface. Zinc sulfide has been identified among other potential candidates as an enargite junction pair that may achieve an appropriate band alignment. A path to developing these thin films through CBD, sputtering, and nanoparticle techniques has been established, but a diode has not yet been achieved.

Enargite films synthesized through evaporated copper thin films do not have observable secondary phases. This attribute makes these films ideal candidates for determining intrinsic properties such as carrier density, mobility, and the nature of deep and shallow defects. Majority carrier density and mobility are typically determined through hall effect measurements but require a crack-free film on an insulating substrate, which has not yet been achieved through this synthesis route. Films prepared on various glass substrates either demonstrate severe cracking or complete delamination, so these measurements are pending the formation of dense thin films on insolating substrates. Recombination behavior can be elucidated through wavelength- and voltage-dependent TRPL which can determine the extent the lifetime is governed by surface recombination. The

nature of these defects can be identified through temperature-dependent TRPL, capacitance-voltage, and admittance spectroscopy measurements which can determine lifetime dependence on shallow trap states, electrically active defects, and defect activation energies, respectively.

The advancement of enargite-based photovoltaics currently depends on finding an effective deposition approach that facilitates carrier transport throughout the device. Regarding the back contact, it should be determined if and to what extent MoS_2 is forming. Due to the overlapping characteristic energies of these elements, compositional techniques such as EDS and XRF introduce relatively high uncertainty and may not be conclusive. High-resolution TEM should reveal this information from a change in crystal structure. Regarding the p-n junction, the ZnS film formation processes described herein should be expanded. For CBD routes, it may help to provide a seed layer of ZnS to assist with deposition, either through converted sputtered ZnO, ZnS nanoparticles, or other methods such as sequential ionic layer adsorption and reaction (SILAR) or atomic layer deposition (ALD). A seed layer through transformation of sputtered ZnO may be adequately prepared with thin films, long H_2S treatment times, and high flow rates. should be attainable through long deposition Other n-type junction pairs such as WO_3 or ZnTe should be additionally investigated.

9.2 Conclusions and future efforts in Cu_3AsSe_4-based photovoltaics

The formation of Cu_3AsSe_4 nanoparticles in solution has been analyzed through aliquot analysis and suggest a formation pathway consisting of binary copper and arsenic selenides. Textured mesoparticles along the $\{112\}$ planes have been synthesized by adapting the reported procedure and display a triangular morphology. Separately, thermal degradation of non-textured Cu_3AsSe_4 nanoparticles has been addressed and structural and chemical instability due to condensed vapor during selenization has been identified.

Since arsenic selenide and copper selenide binary phases are precursors to Cu_3AsSe_4 formation, it is possible that the formation of a dense film of this material can bypass a nanoparticle precursor, much like was observed for Cu_3AsS_4. However, future investigations into the formation of dense thin films of Cu_3AsSe_4 should note the arsenic and selenium volatility observed here and

anneal under an atmosphere of these elements. The formation of persistent copper selenide ternary phases can be hindered by synthesizing with copper poor conditions, and the observed arsenic volatility indicates a high partial pressure of arsenic may be needed to achieve stoichiometric films. Although the formation of persistent arsenic selenide phases has not yet been observed, it may be possible to perform a post-deposition treatment of films to eliminate this phase, much like what has been demonstrated for removing persistent arsenic sulfide phases from Cu_3AsS_4.

9.3 Conclusions and future efforts toward sustainable Cu_3AsS_4 PV technology

Three assessments were completed regarding the life cycle performance and risk associated with Cu_3AsS_4 PV technology. A life cycle assessment was completed to compare significant impactors and identify characteristics unique to this system. This analysis was performed early in the development stage to guide the evolution of this technology through an environmental lens. By identifying hot spots, notable design considerations were established that include minimizing waste associated with deposition techniques that have modifiable utilization efficiencies such as molybdenum, designing reusable balance of system components, investigating roll-to-roll compatible substrates, and prioritizing module efficiency improvements. Additionally, two preliminary risk assessments on the release of arsenic into the environment were completed concerning module fires and end-of-life leaching in a landfill through a scaled TCLP. Both analyses indicate a low expected quantity of arsenic released into the environment, but more rigorous examinations should be performed with experimental measurements for module fires and longer extraction times for landfill leaching.

The LCA performed during this dissertation considers a prospective scenario of Cu_3AsS_4 technology and presumes technological advancements have been made that result in a competitive product. However, an assessment of the waste produced on the lab scale has not been completed. Future research can investigate lab-scale deposition techniques to inform developers of the technology which materials or processing routes may lead to supply chain environmental hot spots. The motivation is to avoid a scenario where the development of the technology is more negatively impactful than the potential benefits of developing the technology. Furthermore, as a primary path

for arsenic exposure may come during the manufacturing or decommission phases of a product's life cycle, modelling employee risk should be completed as soon as potential commercial deposition routes are better understood. Since an overarching goal of these assessments is to enable the development of an environmentally sustainable photovoltaic technology, exploring avenues to promote a circular economy through recycling should also be investigated. Lastly, sustainable products concern economic and social implications, so assessments such as cost-benefit, technoeconomic, and social-LCA can identify areas towards Cu_3AsS_4 sustainability.

VITA

Education

2020 Ph.D. in Materials Engineering, Purdue University (GPA 3.66) Synthesis and environmental assessment of arsenic containing copper chalcogenides for photovoltaic applications. Advisors: Carol Handwerker and Rakesh Agrawal

2015 Bachelor of Science in Physics Marietta College (GPA 3.83)

Publications

2020 **J. Andler**, N. Mathur, J. W. Sutherland, F. Zhao, C. A. Handwerker. Environmental design of a novel solar absorber through life cycle assessment and hot spot analysis. J. Clean Prod., 258, 120847. DOI: 10.1016/j.jclepro.2020.120847

2020 C. Wang, C. Clarkson, **J. Andler**, M. Korey, K. Frost, M. Reeves, C. Handwerker. Lessons learned from the NSF IGERT program: cultivating student motivation in the interdisciplinary and international context. 2020 ASEE Annual Conference & Exposition, Montreal, Quebec, Canada, accepted

2020 M. Korey, C. Clarkson, K. Frost, **J. Andler**, C. Wang, M. Reeves, C. Handwerker. Critical Incident Assessment as a Tool to Reflect on Student's Emotional Response During International Experiences. 2020 ASEE Annual Conference & Exposition, Montreal, Quebec, Canada, accepted

2019 **J. Andler**, N. Mathur, F. Zhao, C. A. Handwerker. Assessing the Potential Environmental Impact of Cu3AsS4 PV Systems. Photovoltaic Specialists Conference (PVSC), 2019 IEEE 46th, DOI: 10.1109/PVSC40753.2019.8981146

2017 S. A. McClary, **J. Andler**, C. A. Handwerker, and R. Agrawal, Solution-processed copper arsenic sulfide thin films for photovoltaic applications. Journal of Materials Chemistry C, 5, 6913-6916, DOI: 10.1039/c7tc01920c

Presentations

2019 **J. Andler**, N. Mathur, R. Agrawal, J. W. Sutherland, F. Zhao, C. A. Handwerker. Assessing the Environmental Performance of Potential Solar Absorber Cu3AsS4. Oral, 2019 MRS Spring Meeting & Exhibit, Phoenix, AZ

2019 **J. Andler**, N. Mathur, F. Zhao, C. A. Handwerker. Assessing the Potential Environmental Impact of Cu3AsS4 PV Systems. Poster, 46th IEEE Photovoltaic Specialists Conference, Chicago, IL

2019 **J. Andler**, N. Mathur, R. Agrawal, J. W. Sutherland, F. Zhao, C. A. Handwerker. Life cycle assessment on arsenic-containing solar absorber for thin-film photovoltaics. Poster, 26th CIRP Life Cycle Engineering Conference, Purdue University

2018 **J. Andler**, I. Hua, M. McCarthy, M. Cardella, M. Curry, and C. A. Handwerker, Research Experiences for Teachers: Sustainable Electronics Professional Development Program for High School Curriculum Enhancement. Poster, Cascade Asset Management open house, Indianapolis, IN

2017 **J. Andler**, X. Hu, E. Stach, C. A. Handwerker, and R. Agrawal, Luzonite Nanoparticle to Enargite Grain Polymorphic Transition for Thin-film Photovoltaics. Poster, Crystal Growth and Assembly, Gordon Research Conference, University of New England, Biddeford, ME

2016 **J. Andler**, C. Miskin, R. Agrawal, et al., Solution-Processed Thin-Film Photovoltaics via Nanocrystal Inks and Molecular Solutions for Scalable, Low-Cost Manufacturing. Poster, Regional Clean Energy Innovation Forum, Purdue University

2016 **J. Andler**, S. A. McClary, B. Graeser, J. Grommet, C. A. Handwerker, and R. Agrawal, Growth of Solution-Processed Cu-V-VI Thin-films for Photovoltaic Applications. Poster, Ceramics, Solid State Studies in, Gordon Research Conference, Mount Holyoke College, South Hadley, MA